# Non-relativistic collisionless shocks in Laboratory Astrophysics

Quentin Moreno-Gelos

## To cite this version:

Quentin Moreno-Gelos. Non-relativistic collisionless shocks in Laboratory Astrophysics. Astrophysics [astro-ph]. Université de Bordeaux, 2018. English. NNT : 2018BORD0427 . tel-02053276

# Université de Bordeaux

**Spécialité doctorale “Sciences physiques et de l’ingénieur”**
**Laboratoire Centre Lasers Intenses et Applications**

## Thèse de Doctorat

*présentée et soutenue publiquement par*

**Quentin MORENO-GELOS**

le 19 décembre 2018

# Non-relativistic collisionless shocks in Laboratory Astrophysics

Directeur de thèse : **Emmanuel D’HUMIÈRES**
Co-directeur de thèse : **Xavier RIBEYRE**
Co-encadrant de thèse : **Mark Erik DIECKMANN**

**Jury**

| | | |
|---|---|---|
| **V. T. Tikhonchuk,** | Professeur | Président du jury |
| **A. Marcowith,** | Directeur de Recherche | Rapporteur |
| **A. Macchi,** | Chercheur | Rapporteur |
| **L. Gremillet,** | Chercheur | Examinateur |
| **M. E. Dieckmann,** | Professeur associé | Encadrant de thèse |
| **X. Ribeyre,** | Chercheur | Directeur de thèse |
| **E. d’Humières,** | Professeur | Directeur de thèse |

*Á mes parents,*

## Remerciements

Dans un premier temps, je souhaite remercier l'ensemble du jury pour son travail et sa participation.

J'ai pu faire cette thèse grâce au financement d'une ANR, nom de code MACH, composée de personnes brillantes, sympathiques et bienveillantes avec qui j'ai eu beaucoup de plaisir à échanger. Je remercie donc Alexandre Marcowith, Laurent Gremillet, Michael Grech, Antoine Bret, Martin Lemoine, Guy Pelletier, Bertrand Lembège... Je souhaite aussi remercier Philip Korneev avec qui j'ai apprécié boire du vin, collaborer et boire du vin.

Merci à Vladimir Tickonchuk pour tous ses conseils, nos discussions, et son soutien durant cette thèse. Je suis plus qu'heureux et impatient de pouvoir continuer notre collaboration à Prague.

Manu et Xavier, sans vous je n'aurais jamais eu l'occasion de faire cette thèse. Trois ans pleins de rembondissements, avec des hauts et des bas (bien plus de hauts que de bas). Je suis heureux de vous avoir eu comme directeurs, cette thèse fut le point d'encrage/ancrage de notre amitié et d'une collaboration qui je l'espère pourra continuer dans un futur plus ou moins lointain.

J'aimerais bien évidement te remercier Mark. La réussite de cette thèse t'est dû en grande partie, tout comme ma nouvelle aptitude à descendre des bières. Ma visite en Suède fut l'expérience la plus enrichissante de ce parcours, et aujourd'hui grâce à cela, je ne souhaite qu'une chose, continuer dans la recherche. Je ne pourrais jamais te remercier assez pour ton aide, ta patience et ta gentillesse. Merci Mark.

Je souhaite remercier le fakeOffice.com #Beuton#Clergerie#Duluc#Girot#Maillet(#Xavier). Ces trois années de thèse ont vraiment été géniales en votre compagnie, comme le seront les prochaines années, malgré la distance.

Merci à Pierre Hericourt, Teddy Pichard, Kevin Gaudfrin pour avoir entretenu la température intenable du bureau B13 (et pour leur sympathie!).

Benjamin, Guilhem, Dimitri, Bertrand, Arno, on se revoit bientôt, à une conf ou dans la rue.

Petit clin d'oeil au m(z)otule qui m'a permis plus d'une fois de décompresser autour d'une bière(s) durant toutes mes études, toujours présent, toujours debout.

Merci à la blockout.team, une secte en perpétuel essor. J'ai eu grand plaisir à grimper avec vous tous durant ces trois ans, et les plus belles montagnes n'attendent que nous.

Merci à tous ceux que j'ai oublié de remercier dans ces remerciements.

Je souhaite remercier ma famille et plus particulièrement mes frères Pierre, Simon, Guillaume pour ce qu'ils sont et ce qu'ils m'apportent au quotidien.

Enfin, je veux remercier mes parents. Leur amour m'a porté jusqu'ici, toujours à me soutenir, toujours à m'accompagner dans les moments difficiles. J'espère pouvoir vous rendre fiers. Je vous aime.

# Abstract

Les chocs sans collision sont omniprésents dans l'Univers, notamment dans les restes de supernova, et sont formés via diverses instabilités plasmas dépendant essentiellement de la vitesse et de la magnétisation des flux de plasmas. La description de tels chocs nécessite une approche cinétique, tant analytique que numérique. Dans cette thèse, nous avons étudié, au travers de simulations Particle-In-Cell (PIC), les processus sous-jacents par lesquels les instabilités rentrent en compétition les unes avec les autres. Nous avons montré que la diminution du rapport des masses entre ions et électrons, souvent utilisée en simulations numériques pour accélérer la dynamique des chocs, peut avoir de fortes conséquences sur le transfert d'énergie entre particules durant la phase non-linéaire des instabilités. Ces dernières, comme l'instabilité acoustique ionique (IAI) amènent sous certaines conditions à la formation de chocs électrostatiques, pouvant donner naissance à la formation de trous dans l'espace des phases, se propageant dans la région aval du choc, et accélérant ce dernier. L'ajout d'un champ magnétique externe conduit à un changement de médiation du choc, pouvant varier entre l'IAI et les ondes magnéto-soniques lente ou rapide en fonction de l'obliquité entre le champ magnétique et la normale au choc. De plus, nous avons montré que l'orientation du champ magnétique permet de choisir entre une dispersion convexe ou concave des ondes plasma conduisant à la création d'ondes précurseurs dans les régions amont ou aval du choc. Ces chocs magnétisés se trouvent être correctement représentés par le modèle magnétohydrodynamique (MHD) tant qu'ils restent laminaires et que leur potentiel dans la région aval n'est pas suffisamment grand pour réfléchir les particules du milieu amont. Nous avons montré que même pour des chocs sous critiques, une fraction d'ions réfléchis, ne pouvant pas être représentés par la MHD, est suffisante à la croissance d'ondes solitaires en amont du choc, conduisant à l'accélération de ce dernier, mais pas à un processus d'auto-reformation comme pour les chocs super critiques. Bien que les échelles spatio-temporelles soient très différentes, les lois d'échelle rendent possible l'étude de tels phénomènes en laboratoire. Nos études numériques ont été faites dans un cadre de type tube à choc pouvant être testé expérimentalement. A ce titre, nous proposons dans cette thèse une expérience sur la création d'îlots magnétiques, formés par l'interaction de plasmas générés par l'irradiation de cibles par laser baignant dans un champ magnétique externe, et conduisant à la formation de tels chocs. Enfin, nous avons démontré expérimentalement et numériquement la formation de chocs électromagnétiques sans collisions par le biais de l'instabilité de Weibel stimulée par l'instabilité de batterie Biermann, conduisant à l'accélération de particules par le mécanisme de Fermi. Ce nouveau type d'expérience pourrait expliquer l'origine du rayonnement cosmique provenant des restes de supernova.

Collisionless shocks are ubiquitous in the Universe, especially in the supernova remnants, and are formed via various plasma instabilities mainly depending on the speed and magnetization of plasma flows. The description of such shocks requires a kinetic approach, both analytical and numerical. In this thesis, we have studied, through Particle-In-Cell (PIC) simulations, the underlying processes by which instabilities compete with each other. We have shown that the reduction of the ion-to-electron mass ratio, often used in numerical simulations to accelerate the dynamics of shocks, can have strong consequences on the energy transfer between particles during the non-linear phase of instabilities. These instabilities, like the ionic acoustic instability (IAI) lead under certain conditions to the formation of electrostatic shocks, which can give rise to phase space holes formation, propagating in the downstream shock region, and accelerating the shock. The addition of an external magnetic field leads to different shock mediation, which can vary between the IAI to the slow or fast magneto-sonic waves as a function of the obliquity between the magnetic field and the shock normal. Furthermore, we have shown that the orientation of the magnetic field makes it possible to choose between a convex or concave dispersion of the plasma waves leading to the creation of precursor waves in the upstream or downstream shock regions. These magnetized shocks are correctly represented by the magnetohydrodynamic (MHD) model as long as they remain laminar and their potential in the downstream region is not large enough to reflect the particles of the upstream medium. We have shown that even for sub-critical shocks, a fraction of reflected ions, which cannot be modeled by the MHD, is sufficient for the growth of solitary waves upstream of the shock, leading to the acceleration of the latter, but not to a process of 'self-reformation' as for super-critical shocks. Although spatio-temporal scales are very different, scaling laws make possible the study of such phenomena in the laboratory. Our numerical studies have been done in the context of shock tubes that can be experimentally tested. As such, we propose in this thesis an experiment on the creation of magnetic islands, formed by the interaction of plasmas generated by the irradiation of laser targets bathed in an external magnetic field, leading to the formation of such shocks. Finally, we experimentally and numerically demonstrated the formation of collisionless electromagnetic shocks through the Weibel instability stimulated by the Biermann Battery instability, and leading to particle acceleration by the Fermi mechanism. This new type of experiment could explain the origin of cosmic radiation from supernova remnants.

# Contents

# Introduction

Shock waves led several generations of scientists to investigate these physical phenomena and, still give rise, thus far, to numerous questions. The first study on shocks deals with the perturbations which a projectile could produce in a gas flowing at a high speed. More than a century ago, (Mach and Wentzel, 1884) were the first to define the shock formation condition, in the course of their experiments on a bullet propagating in a transparent though very viscous fluid. This latter condition, stipulating that a shock wave forms whenever the relative drift speed between a gas flow and a projectile, called $v$, is larger than the sound speed in the gas, called $c_s$. The ratio between these two speeds, $\mathrm{M} = v/c_s$, is at this day referred to as the Mach number, and $\mathrm{M} > 1$ as the 'sine qua non' condition for the shock formation. The Mach experiment, motivated by military purposes, is at this day one example among many others of observable shock on Earth. The most famous one is probably today, the Mach cone which can be seen on the backside of military aircrafts, breaking the sound barrier.

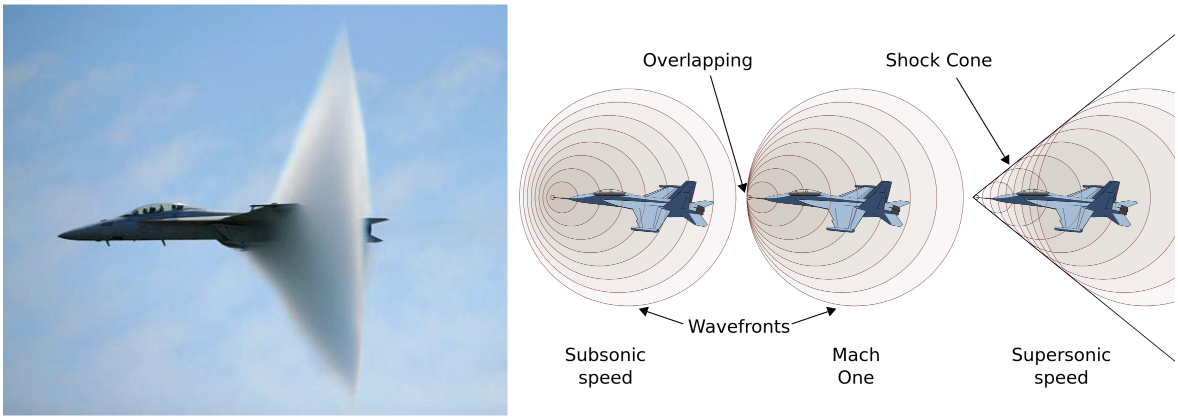

Figure 1 – Photography of the condensation Mach cone at the backside of an aircraft propagating beyond the sound speed (left). The sketch of the shock is shown in the right panel. Circles illustrate sound waves (or other types of waves) being emitted by a moving source (Doppler effect). The shock propagates orthogonal to the cone. The shock is produced for a Mach number $\mathrm{M} > 1$. Picture from a website.

The condensation cone arises, in Figure 1, only during the initial forming of the shock wave, when the pressure immediately behind the leading edge of the steepening sound wave drops due to rarefaction. Once the shock forms and is stable, the density, pressure, and temperature downstream (i.e., behind the shock) are higher than those upstream (i.e., beyond the shock). The profile of the shock can be constructed from the characteristic geometry of sound wave around the aircraft (cf. Figure 1 right). In the downstream region the subsonic flow bends around the obstacle. Since retardation implies that the volume of a flow element is reduced, the density downstream of the shock is increased above the density upstream of the shock and the flow energy is converted into the heat. This growth in temperature along the shock discontinuity increases disorder and thus implies that entropy is generated at the shock making the whole process irreversible. Obviously, these parameters slowly equilibriate with the surrounding medium far enough away from the shock, but in the immediate vicinity, the shock resembles a step function.

A shock can be represented as a wave that became highly nonlinear. Considering this wave as a one-dimensional sinusoidal disturbance of the gas velocity V, moving in the gas background at the velocity $V_0$, the velocity is largest at the maxima of the wave. Since the wave maxima move faster than the remaining parts of the wave profile, the wave steepens until the gradients become so steep that the wave breaks out and collapses, the wave starts forming a ramp corresponding to a shock front. A schematic representation of the wave breaking process is shown in (Balogh and Treumann, 2011). The breaking can be avoided by additional processes which set on when the wavelength of the ramp becomes very short. In the wave propagation equation (1) the terms of higher-order derivatives in the velocity need to be taken into account if the ramp becomes to steep.

Equation describing of the wave propagation is given by

$$\frac{\partial V}{\partial t} + \frac{\partial V}{\partial x} = \frac{\partial}{\partial x} D \frac{\partial V}{\partial x} - \beta \frac{\partial^3 V}{\partial x^3}, \tag{1}$$

where $D(x)$ represents a diffusion coefficient and $\beta$ is the lowest-order contribution of wave dispersion to the evolution of the wave shape and amplitude (The higher-order gradients in the velocity have been neglected). The nonlinear equation (1), shows that the wave profile can be prevented from breaking, if diffusive or dispersive terms balance the nonlinearity steepening, thus permitting to form a stationary shape wave. That equation can be simplified in two extreme cases. The first case is that of purely diffusive compensation of the nonlinear steeping by neglecting the last term in eq. (1), leading to the Burgers' Dissipative Shock Solution (Burgers, 1948) which is commonly used in fluid mechanics. The second case is obviously the purely dissipative compensation of the nonlinear steeping, when neglecting the diffusion coefficient $D(x)$, leading to the Korteweg-de Vries Dispersion Effects (Korteweg and de Vries, 1895). The latter equation accepts the so-called soliton solution, which describes a stationary bell-shaped solitary wave pulse propagating at a certain velocity in a particular direction without any change of form. This solution will be discussed in detail in Chapter 4 of this thesis. However, it is important to note that dispersion does not provide dissipation and entropy generation, and only diffusion can provide these, which means that a wave described by the Korteweg-de Vries equation will be able to prevent the breaking, but not to form a shock.

A shock wave is thus a longitudinal propagative wave, as a sound wave, with a nonlinear wave front reaching an equilibrium between deformation and dissipation via dispersion and diffusion. The energy dissipation mechanism, allowing to convert kinetic energy into thermal heating as discussed before, is one of the most important characteristics of a shock. Majoritarly, the dissipation comes from microscopic processes, depending of conduction, viscosity, and other gas properties. On Earth, almost all gas are collisionnal, the interactions between molecules are mediated by binary collisions, leading to heating and entropy generation. The shock boundary is sharp and well-defined only as long as binary collisions between the particles of the gas occur frequently on the characteristic time scale of the gas flow. If this is not the case then the width of its transition layer widens. This scenario is frequently encountered in outer space where the particle density is low.

### Collisionless shocks in astrophysics

Shocks are not only present on Earth, they are ubiquitous in the Universe and are of particular importance in astrophysics. The gases, close to stars and planets, reach temperatures substantially exceeding the ionisation energy threshold are essentially ionized, and evolve in their plasma states, where the two components, electrons and ions, are independent populations that are coupled primarily through the forces of electrostatic attraction. This baryonic matter (99.9 % of the matter which can be detected by our current technology, which represents 4–5% of the universe average density, the rest being covered by the dark matter and dark energy) is largely much less dense than on Earth and consists of particles moving much faster, leading to a very low binary collisions frequency. The Coulomb mean free path, for fast particles, $l_C \propto v^4$ increases rapidly with $v$ and, for thermal particles, $l_C \propto T^2$ increases with temperature. In interplanetary space this length is of the order of several AUs (Astronomical Units), and any shock of lesser width must therefore be completely collisionless. Shocks developing under such conditions are called collisionless shocks, since binary collisions are not efficient anymore for the shock dissipation. The widths of collisionless shocks are much less than the collisional mean free path, and any dissipative process must be attributed to mechanisms based not on collisions but on collective processes capable to warrant the production of entropy. The dissipative mechanisms that lead to the heating of a plasma that crosses a collisionless shock and to the increase of its entropy must involve collective processes. More than one such process exist. Several of them can be at work at the same time and they can even couple to other processes on spatio-temporal scales that differ by orders of magnitude. Transition layers of collisionless shocks can thus display a more complex behaviour than those of their collisional counterparts.

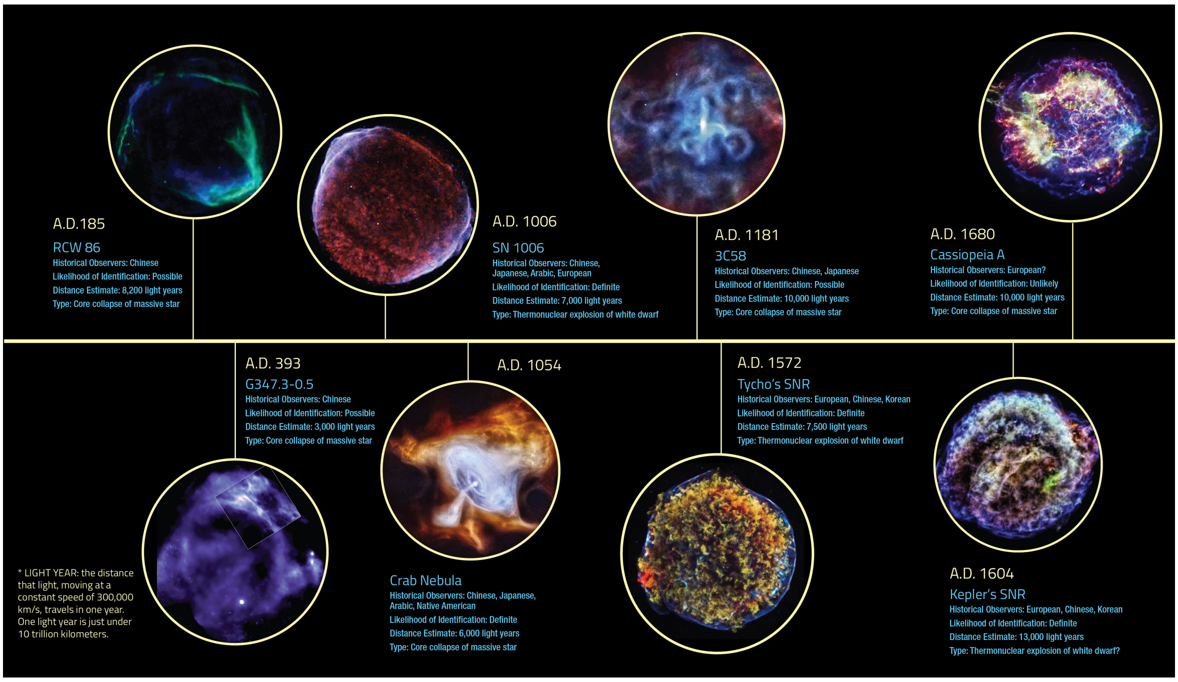

Figure 2 – A timeline of historic supernova candidates. The historical observators, the likelihood of identification, the distance estimate, as well as the type of supernovae are given in legend. This picture comes from the Chandra X-ray Observatory, Credit NASA/CXC/SAO. The majority of these pictures have been taking by the X-ray Chandra satellite, as the ones for the Tycho SNR or the G347.3-0.5 SNR.

The first observations of stellar events, date back more than a millenium. Supernovae were the stellar objects which have captured the most attention of the scientific community on Earth (cf. figure 2), since they are some of the most illuminating phenomena in the Universe. Some of them possess properties which are particularly interesting for the astrophysic community, as the supernovae of type Ia (RCW 86, SN 1006, SN 1572 called Tycho, SN 1604 called Kepler), occuring in binary systems (two stars orbiting one another), which produce consistent peak luminosity. The supernova type Ia explosions are used as standard candles (controversial) to measure the distance to their host galaxies because the visual magnitude of the supernovae depends primarily on the distance.

Furthermore, the supernovae remnants (SNRs), which are diffuse expanding nebula that results from a supernova explosion, seems to be a candidate to collisionless shock formation. During the free expansion of the SNR, a forward shock (or blast wave) moves out supersonically from the explosion through the surrounding medium, either a circumstellar material produced by pre-supernova mass loss in the form of stellar winds or the interstellar medium (ISM) itself. Pressure of the shocked ambient material eventually exceeds the thermal pressure of the ejecta. Ambient medium is accelerated, compressed and heated. It pushes back into the ejecta, creating a reverse shock. This reverse shock is responsible for heating the supernova ejecta to X-ray emitting temperatures. The shock wave also accelerates the ISM into an expanding shell which outputs copious amounts of synchrotron radiation due to the acceleration of electrons in the presence of a magnetic field. This free expansion continues (100-200 years) until the mass of the material swept up by the shock wave exceeds the mass of the ejected material, leading to an adiabatic phase during which instabilities mix the shocked ISM with the supernova ejecta and enhance the magnetic field inside the SNR shell (10,000 - 20,000 years). Finally, the evolution of the SNR ends in a radiative phase during which the shock wave continues to cool and electrons, recombine to form heavier elements, and radiate energy much more efficiently than the thermal X-rays and synchrotron emission produced thus far, further cooling the shock wave which ultimately disperses into the surrounding ISM.

As said before, the reverse shock is maintained by electric and magnetic fields generated collectively in plasma. The magnetization of these shocks, defined as

$$\sigma = \frac{B^2}{4\pi(\gamma_{sh} - 1) n_i m_i c^2}, \tag{2}$$

with $\gamma_{sh} = \sqrt{1 - v_{sh}^2/c^2}$ the Lorentz factor of the shock ($n_i$ and $m_i$ the ion density and the ion mass respectively), exceeds by far the original ISM magnetization, $\sigma_{\rm ISM} \sim 10^{-9}$ ($B_{\rm ISM} \sim \mu$G). The increase of the magnetic field in SNR shocks is often due to the development of electromagnetic instabilities (discussed in detail in Chapter 2) leading to magnetic turbulence, strong enough to isotropize the flows, able to accelerate particles via the Fermi mechanism (discussed in Chapter 5) and to generate nonthermal X-ray emission, which can be observed via the measurements of the cosmic rays (CRs) spectrum on Earth.

G347.3-0.5 (cf. figure 2) is one of three shell-type supernova remnants (SNRs) in the Galaxy whose X-ray spectrum is dominated by nonthermal emission. This puts G347.3-0.5 in the small but growing class of SNRs for which the X-ray emission reveals directly the presence of extremely energetic electrons accelerated by the SNR shock. The bright northwestern peak of the SNR was resolved with the X-ray Chandra satellite consists of bright filaments and fainter diffuse emission, these X-ray filaments are probably controlled by radiative losses (Marcowith and Casse, 2010) as those in SN 1006. From the Chandra data, (Lazendic et al., 2004) explains the broadband emission from G347.3-0.5 with the synchrotron and inverse Compton mechanisms and shows that spectral properties of these regions support the hypothesis that efficient particle acceleration is occurring in the bright SNR filaments. The clumpy morphology of these two SNRs come from the hydrodynamic Rayleigh-Taylor instabilities causing a departure of the ejecta from spherical symmetry.

In younger SNRs, such as Cassiopeia A, Tycho, and Kepler an Alvénic and fast magnetosonic modes damping is the dominant magnetic relaxation process (with a magnetic field ~ 200-300 μG), possibly leading to PeV CR energies (Marcowith and Casse, 2010). In particular, the Tycho SNR (well known for its collisionless shock with the ISM) is represented in figure 2 (Tycho colors: Red 0.95-1.26 keV, Green 1.63-2.26 keV, Blue 4.1-6.1 keV) which shows X-ray emission measured by Chandra (Warren et al., 2005). The thermal plasma ejecta is localized in the center of the SNR (green), and the edge of the expanding shock appears in blue, from the non-thermal particles accelerated at the shock front. Furthermore, $FeK_\alpha$ diagnostics using high-quality X-ray data obtained by the Suzaku satellite revealed efficient collisionless electron heating at the reverse shock of Tycho's SNR (Yamaguchi et al., 2014).

Supernova remnants are not the only stellar objects able to eject plasma at very high speeds and produce large energy X-ray emission. Plasma, in SNRs, expands generally at non-relativistic velocity, but other astrophysical events are much more brutal and drive shocks with relativistic and even ultra-relativistic flows. It is the case of relativistic jets from Active Galactic Nuclei (AGN) or from Gamma Ray Bursts (GRB) reaching relativistic factor up to $\gamma_{sh} \sim 10^3$. Even supernova, can lead to the formation of nebula composed of a plasma accelerated to relativistic speeds by a rapidly rotating, hugely powerful magnetic fields (above 1 TG) that are generated by a spinning pulsar inside the shell of the SNR. These Pulsar wind nebula (PWN), stream into the surrounding ISM, creating a standing shock wave, called termination shock, which decelerates the plasma flows to sub-relativistic speeds, as it is the case for the Crab nebula (cf. figure 2). Strong magnetization of the PWNs leads to different shock formation mechanisms and to alternative acceleration mechanisms (Lyubarsky, 2003; Sironi and Spitkovsky, 2011b) since these shocks do not necessarily produce the level of magnetic turbulence required for Fermi-like acceleration. Description of different collisionless shock mechanisms in the Universe is shown in figure 3, as function of the shock magnetization $\sigma$ and the shock speed $\beta_{sh}$.

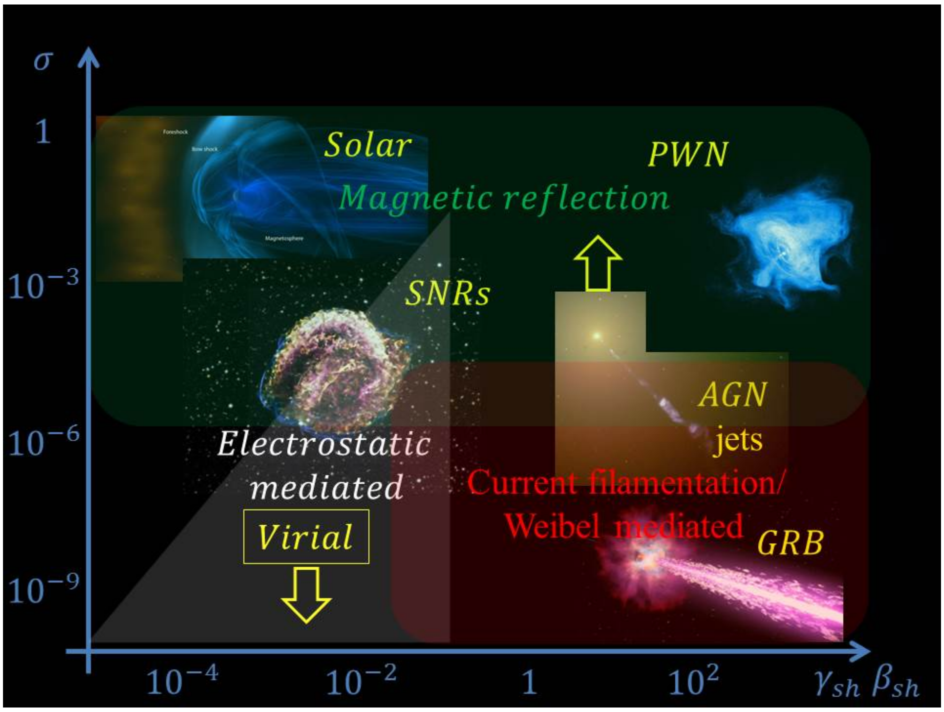

Figure 3 – The landscape of collisionless astro/space shocks, depending of their magnetization $\sigma$ and their energy $\gamma_{sh}\beta_{sh}$. The white transparent part represents electrostatic shocks (including SNRs, virial shock). The red transparent part represents Weibel-mediated shocks (including GRB, AGN jets, and SNRs). The green transparent part represents magnetized shocks (including PWN, Earth bow shock, AGN jets, and SNRs). Adapted from A. Spitkovsky

Relativistic, weakly magnetized flows lead to shocks essentially mediated by the ion Weibel instability (Weibel, 1959) and the following non-linear generation of magnetic turbulence (discussed in Chapter 2 and 5), are the cradle of efficient acceleration (up to 10% of the flow kinetic energy) via a Fermi-like mechanism has been demonstrated by means of numerical simulations (Spitkovsky, 2008b; Sironi and Spitkovsky, 2011a). As said before, the SNR does not necessary mediates a shock via an electromagnetic instability (Weibel instability), but it can also form an electrostatic shock developing in magnetized electron-ion flows and leading to another acceleration mechanism than Fermi, the Shock Surfing Acceleration (Hoshino and Shimada, 2002). A third type of shock mediation is feasible for supernova, with a very high magnetization level, the so called magnetized shock (discussed in Chapter 4). The shock is thus sustained by a magnetic barrier (often referred to as a magnetic reflection shock) that provides the local dissipation and flows isotropization mechanism through the Maser Synchrotron Instability (Zarka et al., 1986; Hoshino and Arons, 1991). In this type of shocks, the Fermi mechanism is suppressed and the acceleration relies on the so-called Shock Drift Acceleration (Amano and Hoshino, 2007; Matsukiyo et al., 2011) in which particles gain energy from the motional electric field driven by the moving magnetic barrier and are found to drift along the shock front surface.

The best understood magnetized shock in a dilute medium is probably the Earth's bow shock (cf. figure 3 solar). The Earth's magnetic field is an obstacle for the solar wind (Goldstein et al., 2016), which is made of particles that escaped from the solar corona. The solar wind is fully ionized and composed of electrons, protons and a minor fraction of heavier ions. It is a good conductor and, hence, it carries with it some of the Sun magnetic field. The relative speed between the Earth's magnetic field and the magnetized solar wind exceeds that of the charge density waves in the solar wind plasma. A shock forms, which separates the solar wind from the Earth's magnetosheath (Lucek et al., 2005). The latter is the downstream region. The shock is approximately stationary in the rest frame of the Earth while the magnetosheath plasma flows around the Earth's magnetic field and escapes in the anti-sunward direction. The bow shock's thickness is about 100 kilometres (Bale et al., 2003). The mean free path of solar wind particles is orders of magnitude larger than that and binary collisions are unlikely to occur in the plasma while it crosses the bow shock. The shock dynamics is regulated instead by interactions of the charge- and current densities carried by the ensemble of the plasma particles with the electromagnetic field. The bow shock is a diffuse hyperbolically shaped region standing at a distance of 90000 km from the Earth surface, in front of the magnetopause. The shock normal can be perpendicular, tangent or parallel to the solar wind magnetic field leading to characterization the bow shock as perpendicular, quasi-perpendicular, or quasi-parallel. The orientation of the macroscopic field is changing, and this affects the shock formation (discussed in Chapter 4) and the acceleration mechanism (Caprioli and Spitkovsky, 2014). The Earth bow shock is the paragon of a magnetized collisionless shock. In-situ studies of the Earth's bow shock by satellites can thus improve our understanding of them. However, the dependence of shocks on plasma bulk parameters like the direction and relative strength of the upstream magnetic field and on the plasma temperature and flow speed (Bale et al., 2005; Burgess et al., 2005) implies that we may not be able to generalize the insight gained from studies of the Earth's bow shock to other collisionless shocks. All these different type of shocks are able by various mechanisms to accelerate particles, electrons and ions, which are observed on the Earth as high-energy cosmic rays.

In this thesis we have focused our attention on shocks of non-relativistic nature, relativistic shocks have been investigated by (Ruyer, 2014; Grassi, 2017).

**Particle acceleration and cosmic ray emission**

Cosmic rays are a very puzzling topic for the scientific community, because of difficulty to explain the energies of the most energetic ultra-high-energy cosmic rays (UHECRs) approaching $3 \times 10^{20} eV$, about $4 \times 10^7$ times the energy of particles accelerated by the Large Hadron Collider (LHC). But these rays are not just interesting from a scientific point of view, since due to their high energy they can impact space missions outside the magnetosphere protection and damage their microelectronics, thus reducing their life. The supernova remnants have long been suspected to generate cosmic rays, but the size of supernovae is not large enough to maintain acceleration above $10^{16}$ eV, making impossible their implication in the generation of Ultra High Energy particles. Telescope Array is looking for possible sources of these Ultra High Energy cosmic rays, as GRBs or colliding galaxies, but the source of these cosmic rays is still unknown. Indeed, the Fermi-like mechanisms seem not efficient enough to describe the spectrum of CRs above $10^8$ GeV even in GRBs. Different theories tried to solve this enigma as (Blasi, 2013) considering a mechanism where a secondary instability driven by the accelerated particles generates stronger magnetic fields able to confine much more particles at the shock front allowing a longer acceleration stage. The latter theory failed to describe CRs above $10^9$ GeV and the problem of generation of very high energy cosmic rays is still unsolved. However, most cosmic rays, do not have such extreme energies, and the energy distribution of cosmic rays peaks around 0.3 GeV, giving a place to the Earth's bow shock or the SNR, in the cosmic rays diagram presented by the (Cronin et al., 1997).

Cosmic rays are composed majoritarly of protons and alpha particles (99%) with a small amount of heavier nuclei, positrons and antiprotons ($\sim$ 1%), and come, generally, from outside the Solar system. These primary cosmic rays generated from the acceleration of high-energy particles in GRBs or AGNs are converted to secondary particles when they interact with the Earth's atmosphere. The processes of primary cosmic rays decay do not include only primary particles or neutrons, but also particles as pions, positrons, and muons, making the observation on Earth very difficult. The CRs are detected using different methods, as the air Cherenkov telescope for energies

< 200 GeV (using the Cherenkov radiation), or the Extensive air shower (EAS) arrays (able to measure much higher-energy cosmic rays). But all these observation methods have some limitations and no direct observations are able to capture unequivocally the physical processes predicted by the theory. This is why, in order to fully understand the underlying physics of CRs, the scientific community has tried, for many decades, to produce some controlled experiments and effectively interpret them.

### Laser facilities to serve world research

Laboratory astrophysics is one of the youngest branches of astrophysics, established to recreate, in the laboratory, conditions relevant to various astrophysical scenarios. It provides the firm laboratory base of atomic, molecular and plasma data necessary to understand and direct observations in space. Laboratory experiments offer the unique possibility to have access to astrophysical phenomena, for which in situ measurements are beyond our reach, in a controlled and well-diagnosed environment.

This field came along new generations of laser facilities which are still undergoing a phase of growing activity. The formation of partially ionised plasma on Earth is common nowadays, as for examples lightning and neon lights, but is is possible, using laser facilities, to form plasmas close to astrophysical conditions (fully ionised and quasi-collisionless).

Interaction of intense lasers with gas or solid targets can ionize the matter and rapidly produce plasmas, under ad hoc experimental conditions. An intensity of $10^{15}$Wcm$^{-2}$ is sufficient to ionize certain atoms via the laser electric field in a single laser period. However, it was very complex until the mid 1980s to go beyond this laser intensity. Amplification of a laser pulse goes through several consecutive stages using series of active media, however its intensity is limited as a laser pulse at intensities $10^{9}$Wcm$^{-2}$ can already cause serious damage to a gain medium through nonlinear processes such as self-focusing and ionisation (Wood, 2003). Plasma formation in experiments was limited by the damages on the laser optical elements. The introduction of the Chirped Pulse Amplification (CPA) by (Strickland and Mourou, 1985), overcame this issue and created the technological bases of the Laboratory astrophysics with improve laser capabilities. This amplification method is now at the basis of the most advanced technology for the production of ultra-intense laser pulses, and received this year in october 2018 the Nobel prize shared by Gérard Mourou, Arthur Ashkin and Donna Strickland. CPA is based on the stretching out in time of an ultrashort laser pulse prior to introducing it to the gain medium using a pair of gratings (or prisms) that arranges the travels of the laser pulse frequency components (the high-frequency component lags behind the low-frequency component and has longer pulse duration than the original), the intensity is sufficiently low, compared with the intensity limit of $10^{9}$Wcm$^{-2}$, to be safely amplified by the gain medium and finally recompressed back to the original pulse width through the reversal process of stretching. This technique achieving orders of magnitude higher peak powers than laser systems could generate before the invention of CPA, made possible, amongst others, the production of femtosecond-duration pulses with intensity above $10^{21}$Wcm$^{-2}$. The CPA method, implemented for some of the most powerful lasers, as an example on PETAL on the Laser Mega-Joule (LMJ), can also not be sufficient for astrophysical experiments, since these pulses even in an unfocused large aperture (after exiting the compression grating) can exceed the threshold of damage. Problems of optic damage and laser pulses degradation are still at this day a very engineering challenges. However, CPA is the current state-of-the-art technique used by all the highest power lasers in the world with powers greater than about 100 TW and pulse duration shorter than 1 ps.

These high power lasers are not only research systems, but have now a large commercial market, like the Ti:sapphire-based systems of 100 GW used in medicine and industry. But the most powerful lasers, reaching the petawatt are, for now, restricted to the academic and military researches. Their number all over the world is limited to the LFEX Petawatt laser at the Gekko XII facility in the Institute of Laser Engineering at Osaka University, the OMEGA EP laser at the University of Rochester's Laboratory for Laser Energetics, the now available PETAL laser at the LMJ facility. Furthermore, a new generation of powerful lasers starts to emerge reaching the multi-Petawatt regime, using the technique of Optical Parametric Chirped Pulse Amplification (Ross et al., 2000), based on a combination of the optical parametric amplification and the CPA method. It is the case of the Vulcan Petawatt Upgrade at the Rutherford Appleton Laboratory's central laser facility, ELI project or the APOLLON petawatt at the Saclay CEA center (CILEX) which will possibly reach 10 PW.

The high power of these lasers is used for achieving particle acceleration to ultra-high energies, as for example via the Target Normal Sheath Acceleration (TNSA) mechanism (Wilks et al., 2001; Passoni et al., 2010) allowing the production of very energetic, multi-tens MeV ion populations. These accelerated ions via TNSA are also commonly used as a diagnostic tool for proton radiography to probe the spatial shape of the magnetic field in experiments. The basic theory of TNSA and related models is described in detail in (Macchi et al., 2013). These lasers are also able to generate intense ultra-short X-rays which can be used in a large range of applications. An example is the PINNACLE project launched in 2017 by Julien Fuchs to investigate with the unique capabilities of the APOLLON laser generation of high flux neutron sources and their interaction with plasmas to reach the nucleosynthesis of heavy elements.

Lasers are usually divided into two main categories: high-power (discussed above) and high-energy lasers. A diagram of the distribution and time evolution of selected high energy and/or high power lasers is shown in figure 4.

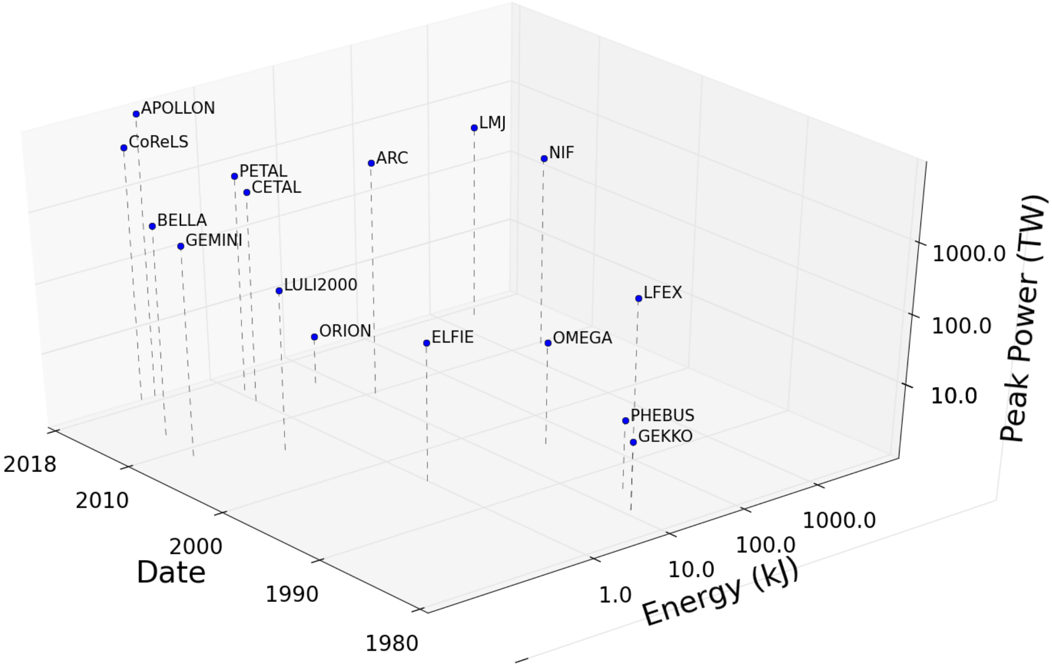

Figure 4 – Diagram of the evolution, of selected laser facilities in the world as a function of their power and energy. The power is calculated from the energy and a pulse duration (not shown), which can be modify. In the case of the LMJ, the current available energy is not yet the one shown in the diagram, but the facility must reach this value in a close future.

High-energy lasers such as the National Ignition Facility (NIF), the LMJ, Gekko XII and Orion are huge facilities primarily dedicated to fusion energy. These facilities are composed of several lasers divided into sets with multiple beams like quads for NIF and LMJ. For these latter facilities, each beam is characterized by long pulses of several nanoseconds, for a power of few TW leading to a focused intensity in a range of $10^{14} - 10^{15}$Wcm$^{-2}$ as detailed in Table 1.

The high-energy lasers have limitations related to optical damage of optic elements on gratings (Wood, 2003) and high construction and operating costs. As for an example, the LMJ facility pos-

| Facility | NIF | LMJ | SG-III | OMEGA | Gekko | ORION |
|---|---|---|---|---|---|---|
| Country | USA | France | Chine | USA | Japon | UK |
| Total Energy | 1.85 MJ | 1.3 MJ | 180 kJ | 30 kJ | 3.5 kJ | 5 kJ |
| Wavelength | 351 nm | 351 nm | 351 nm | 351 nm | 532 nm | 351 nm |
| Number of beams lines | 192 | 176 | 48 | 60 | 12 | 10 |
| Peak Power | 500 TW | 400 TW | 60 TW | 0.5 TW | 0.2 TW | 0.5 TW |
| Pulse duration | 1 – 10 ns | 1 – 10 ns | 3 ns | 0.1 – 4 ns | 1 – 2 ns | 0.1 – 5 ns |
| Creation date | 2009 | 2014 | 2015 | 1995 | 1983 | 2013 |

Table 1 – Highest-energy lasers facilities in the world.

sess a nominal laser energy designed for 30 kJ per quad, but in many cases the CEA experiments are designed with laser energies from 10 to 15 kJ in order to limit damages on optics.

Construction of the largest high laser energy facilities (NIF and LMJ) is a part of projects for replacement of underground nuclear explosion tests and dedicated also to fusion research and high energy density physics. The Sun is a main-sequence star, and thus generates its energy by nuclear fusion. Trying to reproduce a controlling fusion reaction, between the two hydrogen isotopes, deuterium (D) and tritium (T), producing a helium nucleus and emitting a high energy neutron is one of the great scientific challenges of this century. Two approaches are investigated, the magnetic confinement fusion, which uses a tokamak-type device (the ITER facility under construction and JET operational sins 1990s) to produce a low-density plasma over a rather long period, and the Inertial confinement fusion (ICF) which uses high-power lasers (such as the LMJ or its American counterpart, the NIF) to generate very dense plasmas of a very short duration (Atzeni et al., 2005) (cf. figure 5).

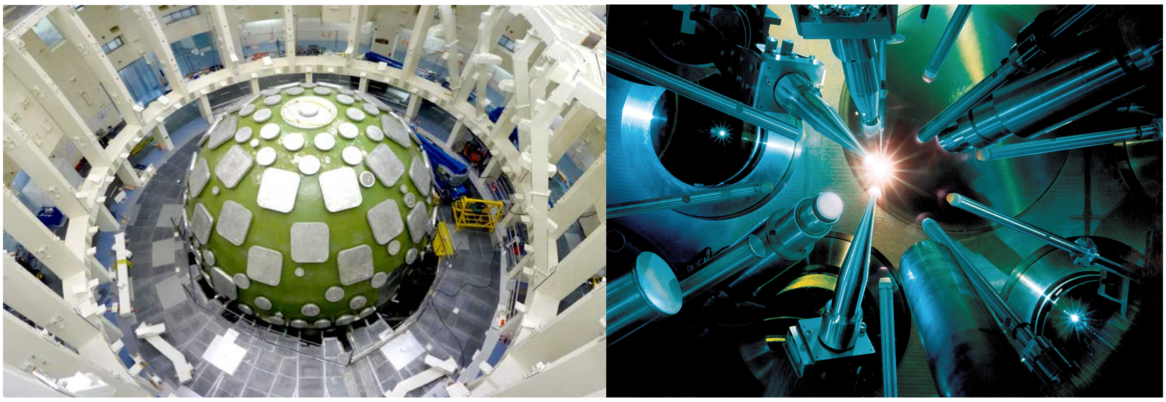

Figure 5 – Experimental sphere of the LMJ facility (left), and artist representation of laboratory astrophysics experiments (right). By mimicking fundamental physics aspects in the lab, researchers hope to better understand violent cosmic phenomena.

More specially, two methods are used to bring about very rapid implosion of a microcapsule. The Indirect-drive inertial confinement fusion, where the laser beams are directed against the inner walls of the gold hohlraum thus microcapsule producing intense X-rays. The radiation is trapped inside this cavity, where the radiation temperature can reach > $10^6$K. It is the X-rays that interact with the microcapsule held inside the hohlraum. In the Direct-drive inertial confinement fusion, the laser delivers its energy directly to the microcapsule, causing a direct interaction between the laser beam and the microcapsule filled with the DT mixture. The Indirect approach of ICF is being used on LMJ and on NIF. Completed in 2009, the NIF failed, at this day, to achieve ignition in part because of parametric and hydrodynamic instabilities (Edwards et al., 2013). The released fusion energy for the moment is about 3% of the NIF laser energy. This recent difficult raises particularly serious questions to the LMJ (which is not yet complete), calculated to achieve ignition with a gain of 10 between the energy produced by the thermonuclear reactions and the laser energy supplied to the target. However, these facilities are not only dedicated to defense purposes, but can also be used for academic researchs.

### Laboratory astrophysics

Laboratory astrophysics constitutes one of subjects investigated on high energy laser facilities. Starting from the warm dense matter physics addressing conditions in the interiors of planets (Koenig et al., 2005), the research passes by the physics of accretion of matter in a strongly magnetized environment as for example in some young pre-main-sequence stars (Hartmann et al., 2016; Revet et al., 2017), and investigates also the physics of shocks (radiative, collisionless, etc) in supernovae (Remington et al., 1999). The fundamental physical processes predicted by quantum electrodynamics (QED) such as the Breit–Wheeler pairs production, appearing during the gravitational collapse leading to the formation of a black hole being observed in Gamma Ray Bursts (GRBs) or in AGN, can be studied in laboratory (Ruffini et al., 2010; Ribeyre et al., 2016, 2018).

Generally, spatial and temporal scales involved in astrophysical processes and those obtained in the laboratory have extremely large differences, but similarity criteria have been identified, the so called 'scaling laws', to ensure the equivalence between the astrophysical conditions and those produced in the experiments (Ryutov et al., 1999; Bouquet et al., 2010; Falize et al., 2011). The latter references concerned radiative hydrodynamic flows, but the 'scaling laws' are different when considering collisionless, non-radiative processes since the similarities will depend of the nature of the instabilities, electrostatic or electromagnetic, (Ryutov et al., 2012). The latter scaling is therefore used to investigate collisionless shocks in the laboratory.

The first experiment on collisionless shocks has been conducted by (Dean et al., 1971), by letting a laser-driven blast shell collide with an ambient plasma. Later, (Bell et al., 1988) studied in the laboratory collision of a laser-driven blast shell with an obstacle, forming an electrostatic shock due to the limited flow velocity of the laser-ablated plasma. Both approaches were the test bed for plenty of other experiments, allowing systematic study of a wide range of collisionless shocks different from those in the solar system which can be reached by satellites. Particularly, thanks to the improvements of experimental diagnostics such as development of the proton radiography using radiochromic films, RCFs (Borghesi et al., 2002), Bremsstrahlung x-ray emissions imaging, or even Thomson scattering measurements, it has been possible to investigate in experiments the three type of shocks described in figure 3

Electrostatic shocks are generally the easiest to produce in experiments and do not require large energy facilities, since their width are on the microscopic scale. Until recently, these shocks have been found to transition to a double-layer structure, in an experiment conducted by (Ahmed et al., 2013) on the VULCAN laser facility (cf. figure 6).

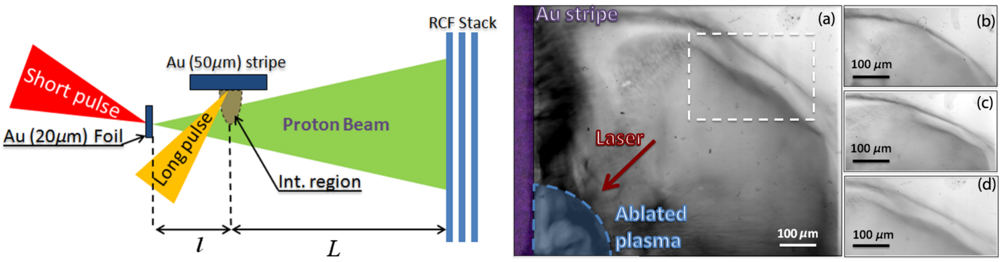

Figure 6 – Left Panel: Experimental setup of (Ahmed et al., 2013). Righe Panel: A proton radiograph of the interaction of the main laser pulse (red arrow) with a gold foil (left purple rectangle) at t=17 ps. Panel b, c and d are zooms of the region high-lighted by the dashed white rectangle in panel a, for proton energies 11.5, 10, and 9 MeV respectively.

More recently (Schaeffer et al., 2017a,b) performed experiments on the OMEGA laser facility and demonstrated the first laboratory generation of high-Mach-number magnetized collisionless shocks created through the interaction of a laser-driven magnetic piston and a magnetized ambient plasma (cf. figure 7).

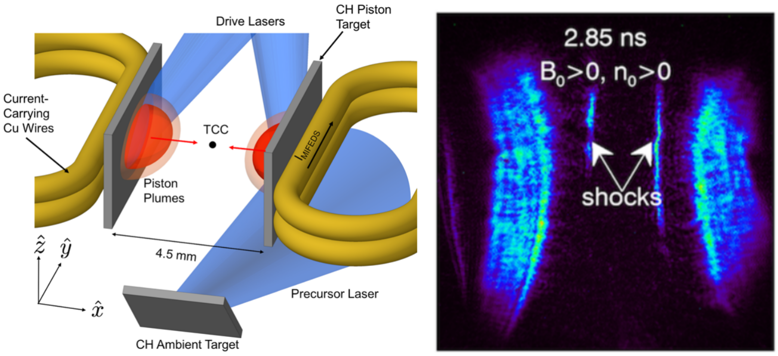

Figure 7 – Left Panel: Experimental setup of (Schaeffer et al., 2017a,b). An ambient plasma generated by laser ablation of a CH target is compressed by two counter-propagating piston plumes also created by CH targets ablation via laser beams. An external magnetic field is provided by current-carrying wires. Right Panel: Angular filter refractometry image, the shock is observed with an external field and ambient plasma at t=2.85 ns.

Weibel-mediated shocks, of electromagnetic nature, result from the long-time non-linear evolution of the ion Weibel-filamentation instability (Weibel, 1959), it is particularly difficult to conduct experiments able to form such shocks because of very large spatio-temporal scales. They require high-energy lasers with long pulse durations to maintain the plasma at high temperature with high drift motion in order to ensure the collisionless nature of the shock (Ross et al., 2017). Experiments conducted on the OMEGA laser facility by (Huntington et al., 2013, 2017), failed to fully form an electromagnetic shock even after 6 ns of interaction, these shocks remain the only collisionless shocks not been demonstrated up to this day in experiments. More details on the nature of these shocks as well as the experiments conducted on them will be discussed in detail in Chapter 5.

It is important to note that the shocks discussed in this Introduction concern only ion-electron collisionless shocks, but in parallel to these shock studies, $e^{+/-}$ pair plasmas collisionless shocks are presently investigated. The recent experiment of (Sarri et al., 2015) has demonstrated the generation of neutral and high-density electron-positron plasmas and numerical kinetic simulation by (Lobet et al., 2015) have then confirmed that soon-available laser facilities might be able to test pair plasma collisionless astrophysics.

**Outline of this manuscript**.

The work performed during this thesis and presented in this manuscript concerns the physics of ion-electron collisionless shocks in several configurations of interest for astrophysics, and often related to the laser-plasma interaction.

In the first Chapter, we present the basic theoretical and numerical tools necessary for modelling and the understanding of collisionless shocks. Starting from the kinetic description of a plasma and discussing the hydrodynamic limit, we detail the shock physics by given the Rankine-Hugoniot conditions and introducing the physics of instability.

Kinetic plasma instabilities necessary for formation of any collisionless shock are discussed in Chapter 2. The underlying processes by which such instabilities compete with each other is studied in details. In particular, the impact of the ion-to-electron mass ratio during the linear and nonlinear growth phase instabilities are investigated (Moreno et al., 2018d).

Chapter 3, then presents the studies of electrostatic collisionless shocks by investigating the thermal expansion of a dense plasma into a dilute plasma in an one-dimensional configuration. The aim of this work is to understand the qualitative effects of an ambient medium on a dense plasma expansion, as it is the case in SNR forward/reverse shocks, by performing a parametric analysis of the density ratio between two clouds (Moreno et al., 2018a).

Chapter 4, is dedicated to the case of magnetized shocks in the context of the Earth's bow shock for a range of plasma parameters able to be reached for laser-plasma experiments. We discuss the MHD approximation in a collisionless plasma and found that kinetic shocks are transient and that the plasma dynamics are eventually regulated by structures that exist also in the single-fluid MHD model (Dieckmann et al., 2017b; Moreno et al., 2018c; Dieckmann et al., 2018b). To analyse the limit of the MHD approximation in a collisionless shock, we investigate different shock regimes with different ion species, to represent processes which are not captured by the MHD model (Moreno et al., 2018e), as specular reflection and shock reformation.

Chapter 5 is dedicated to electromagnetic shocks. We present a recent experiment on the OMEGA laser facility in the context of Laboratory Astrophysics (Li et al., 2019). This experiment aims to reach the formation of High-Alfvenic-Mach-number nonrelativistic electromagnetic collisionless shocks mediated by the ion Weibel instability. We specially analyse the role of the self-generated Biermann battery magnetic fields on the shock formation (Moreno et al., 2018b).

In Chapter 6, we finally present proposals for laboratory experiments on magnetized collisionless shock formation, in the context of strongly magnetized SNR shocks. These experiments are designed for the LULI2000 and for the LMJ laser facility.

# Chapter 1

# Analytical and numerical approach at the interface of the hydrodynamic and the kinetic models of the collisionless shock formation

This chapter presents the basic theoretical background of collisionless shock physics. Two approaches are discussed, starting from the kinetic plasma description and followed by the hydrodynamic approximation. The Rankine-Hugoniot jump conditions at shocks are derived with the shock solutions explicitly given. A general discussion of wave instabilities causing growth of initial disturbances, necessary for the shock formation are discussed thereafter. The last section explains the numerical simulation techniques, hydrodynamic and kinetic, used during this thesis.

## 1.1 Analytic models

The Korteweg-de Vries wave equation discussed in the Introduction is dissipation free and does not directly lead to shock wave solutions. Waves transform gradually to shock whenever processes at short wavelengths cause appearance of anomalous dissipation under the ideal conditions of non-collisionality (Sagdeev, 1966). This statement is a very important, however, it can be justified only within the kinetic theory of microscopic interaction between waves and particles and waves and waves in plasmas far from thermal equilibrium.

### 1.1.1 Basic equations

The kinetic equation which describes collective interactions of charges many particles and electromagnetic fields was introduced by (Vlasov, 1945).

$$\frac{\partial f_s}{\partial t} + \mathbf{v} \cdot \nabla_{\mathbf{r}} . f_s + q_s (\mathbf{E} + \mathbf{v} \wedge \mathbf{B}) \cdot \nabla_{\mathbf{p}} . f_s = 0 \tag{1.1}$$

The Vlasov equation describes evolution of the electron and ion phase space distribution function $f_s$ (index $s$ for the different species), in low density plasmas. This equation can be derived as a smooth version of the Klimontovich equation which describes evolution of the microscopic distribution of punctual charges $q_s$ (Klimontovich, 1967). Each point in the phase space follows a trajectory of a real particle placed at the same point and moving under the action of the electric and magnetic fields **E**, **B** produced by the smooth (Vlasov) charge and current distributions.

It is actually the basis of all kinetic models for particles interacting through long range forces: electromagnetic and gravitational. The collisions in this equation are neglected. This is accurate if the typical scale-lengths of the physical mechanisms of interest are much smaller than the collisional mean-free-path of particles. Since the shocks of interest in this thesis are of collisionless nature this description is well adapted from all points of view. An additional term due to particle-particle interaction can be added on the right side of the Vlasov equation as the Boltzmann collision term, which accounts for binary scattering of the particles. The collisional effects become important when the particles come closer to each other. The Vlasov equation is not sufficient to describe collisional plasmas, it only describes evolution of the distribution function in a scale, larger then the electron Debye length $\lambda_{De} = \sqrt{\epsilon_0 T_e / n_e q_e^2}$ but smaller the particle mean free path. For the studies presented in this thesis contribution of particle collisions is assumed negligible in comparison with the coherent motion in the mean fields.

The Vlasov equation has be coupled with Maxwell's equations to form the relativistic Vlasov-Maxwell set of equations,

$$\begin{aligned} \nabla \times \mathbf{E} &= -\left(\partial \mathbf{B}/\partial t\right), & \nabla \cdot \mathbf{B} &= 0, \\ \nabla \times \mathbf{B} &= \mu_0 \epsilon_0 \partial \mathbf{E}/\partial t + \mu_0 \mathbf{J}, & \nabla \cdot \mathbf{E} &= \rho/\epsilon_0, \end{aligned} \tag{1.2}$$

where the second term in the Maxwell-Ampère equation (on the bottom left of these equations) is the electric current density (multiplied by the permeability constant of vacuum, $\mu_0$ )

$$\mathbf{J} = \sum_s q_s \int d\mathbf{p}\, \mathbf{v} f_s, \tag{1.3}$$

and the term on the right in the last of these equations is the electric space charge density (divided by the dielectric constant of vacuum, $\epsilon_0$ )

$$\rho = \sum_s q_s \int d\mathbf{p} f_s. \tag{1.4}$$

These equations already account for the seft-consistent coupling of the field to the particles through the definition of the electric current and particle densities as zero and first moments of the one-particle phase space distributions.

### Properties of the Vlasov-Maxwell model

Solutions of the Vlasov-Maxwell set of equations are reversible in time, the dynamic of the Vlasov system conserves the information.

Since the equations of motion define particle orbits unambiguously from the initial conditions, the points contained in a given volume in the phase space can not cross the surface (otherwise it would imply that two different particles come to be interchanged, and by reversing time one would have an equivocal evolution). Consequently, the number of particles contained in given volume is preserved during its movement. The flow in phase space is that of an incompressible fluid.

These points can be connected to the entropy conservation. In the classical statistical mechanics the entropy of a system out of equilibrium is given by the formula :

$$S = -k_B \int f(\mathbf{r}, \mathbf{v}) \ln(f(\mathbf{r}, \mathbf{v})) d\mathbf{r} d\mathbf{v}, \tag{1.5}$$

where $k_B$ is the Boltzmann constant. According to the principle of maximum entropy, any system tends to evolve in time towards the configuration that maximizes the specific entropy. Assuming that the evolution of the distribution function $f$ is described by the Vlasov equation, one obtains from (1.5), and by using (1.1) the incompressibility property:

$$\frac{dS}{dt} = 0. \tag{1.6}$$

If the boundary conditions of the system forbid any exchange with the outside world, the entropy is conserved in the Vlasov model. Many distribution functions can satisfy this maximization of entropy. The non-relativistic distribution function which has been used for different studies of this thesis is the well known Maxwell-Boltzmann distribution function.

$$f_s(\mathbf{v}) = \left(\frac{m_s}{2\pi k_\mathrm{B}\mathrm{T}_s}\right)^{\mathrm{D}/2} e^{-\frac{m_s(\mathbf{v}-\mathbf{u}_s)^2}{2k_\mathrm{B}\mathrm{T}_s}} \tag{1.7}$$

This distribution function describes a plasma equilibrium for a species with single particle mass $m_s$ and temperature $\mathrm{T}_s$, in the drifting and non-relativistic case (with $\mathbf{u}_s$ the drift velocity), where D is the dimensionality of the momentum phase-space. Here the density of particles $n_s$ is assumed to be uniform in space.

Other distribution functions have to be used to described plasmas at equilibrium with a temperature exceeding the rest mass energy of the particles, $\mathrm{T}_s >> m_s c^2$, and drifting with relativistic velocities. The Maxwell-Boltzmann distribution functions for these extreme cases, no longer gives an appropriate description, since they predict particles with velocity exceeding the speed of light. For these relativistic configurations the so-called Maxwell-Jüttner distribution function (Jüttner, 1911) or the relativistic multi-waterbag distribution function (Gremillet et al., 2007; Bret et al., 2010) are more adapted. However, the studies in this thesis are limited to non-relativistic approach, and for this reason relativistic distribution functions will not be discussed further.

### Averages and Fluctuations of the Vlasov-Maxwell set of equations

Small wave disturbances are the seeds to shocks formation, and all field and plasma quantities can be represented as a stationary part and fluctuations components

$$\{f_s, \mathbf{E}, \mathbf{B}\} = \{f_s^{(0)}, \mathbf{E}^{(0)}, \mathbf{B}^{(0)}\} + \{f_s^{(1)}, \mathbf{E}^{(1)}, \mathbf{B}^{(1)}\} \tag{1.8}$$

The stationary parts are represented as $f_s^{(0)}, \mathbf{E}^{(0)}, \mathbf{B}^{(0)}$, and the fluctuations as $f_s^{(1)}, \mathbf{E}^{(1)}, \mathbf{B}^{(1)}$. Here the average quantities are assumed to vary on much longer spatial and temporal scales than the fluctuation scales such that the condition of averaging $< f_s^{(1)}, \mathbf{E}^{(1)}, \mathbf{B}^{(1)} >= 0$ remains valid. Then, by applying the above prescription of averaging to the Vlasov equation, we obtain the kinetic equation for the average distribution functions $f_s^{(0)}(\mathbf{v}, \mathbf{x}, t)$ in the form :

$$\frac{\partial f_s^{(0)}}{\partial t} + \mathbf{v}\cdot\nabla_\mathbf{r}.f_s^{(0)} + q_s(\mathbf{E}^{(0)} + \mathbf{v}\wedge\mathbf{B}^{(0)})\cdot\nabla_\mathbf{p}.f_s^{(0)} = -q_s\langle(\mathbf{E}^{(1)} + \mathbf{v}\wedge\mathbf{B}^{(1)})\cdot\nabla_\mathbf{p}.f_s^{(1)}\rangle \tag{1.9}$$

This average Vlasov equation contains a non-vanishing pseudo-collision term on its right which accounts for the effect of the correlations between the fluctuations and particles on the average distribution. In Maxwell's equations (1.2) the full distribution functions $f_s$ appearing in the expression for the electric current density in Ampère's law and in the space charge term in Poisson's equation are to be replaced by their average counterparts $f_s^{(0)}$ , yielding

$$\begin{aligned} &\nabla\times\mathbf{E}^{(0)} = -\big(\partial\mathbf{B}^{(0)}/\partial t\big), && \nabla\cdot\mathbf{B}^{(0)} = 0,\\ &\nabla\times\mathbf{B}^{(0)} = \mu_0\epsilon_0\partial\mathbf{E}^{(0)}/\partial t + \mu_0\sum_s q_s\int d\mathbf{p}\,\mathbf{v}f_s^{(0)}, && \nabla\cdot\mathbf{E}^{(0)} = \epsilon_0^{-1}\sum_s q_s\int d\mathbf{p}f_s^{(0)}. \end{aligned} \tag{1.10}$$

The Vlasov-Maxwell set of equations for the fluctuations are obtained by the subtraction of the set of averaged equations from the full set of equations $\{f_s, \mathbf{E}, \mathbf{B}\}^{(1)} = \{f_s, \mathbf{E}, \mathbf{B}\} - \{f_s, \mathbf{E}, \mathbf{B}\}^{(0)}$.

$$\begin{aligned} \frac{\partial f_s^{(1)}}{\partial t} + \mathbf{v}\cdot\nabla_\mathbf{r}.f_s^{(1)} + q_s(\mathbf{E}^{(0)} + \mathbf{v}\wedge\mathbf{B}^{(0)})\cdot\nabla_\mathbf{p}.f_s^{(1)} &= -q_s(\mathbf{E}^{(1)} + \mathbf{v}\wedge\mathbf{B}^{(1)})\cdot\nabla_\mathbf{p}.f_s^{(0)}\\ &\quad -q_s(\mathbf{E}^{(1)} + \mathbf{v}\wedge\mathbf{B}^{(1)})\cdot\nabla_\mathbf{p}.f_s^{(1)} + q_s\langle(\mathbf{E}^{(1)} + \mathbf{v}\wedge\mathbf{B}^{(1)})\cdot\nabla_\mathbf{p}.f_s^{(1)}\rangle \end{aligned} \tag{1.11}$$

$$\begin{aligned} &\nabla\times\mathbf{E}^{(1)} = -\big(\partial\mathbf{B}^{(1)}/\partial t\big), && \nabla\cdot\mathbf{B}^{(1)} = 0,\\ &\nabla\times\mathbf{B}^{(1)} = \mu_0\epsilon_0\partial\mathbf{E}^{(1)}/\partial t + \mu_0\mathbf{J}^{(1)}, && \nabla\cdot\mathbf{E}^{(1)} = \rho^{(1)}/\epsilon_0. \end{aligned} \tag{1.12}$$

Equation (1.11) describes the evolution of fluctuations. The amplitude of the fluctuations are unknown, but their scales must be much shorter than the scales of the average field quantities. For a shock wave configuration, this means for instance that the width of the shock transition regions should be much larger than the wavelengths of the fluctuations.

There is a coupling in Eq.(1.11) to the average quantities, so that these two equations can be solved only together. The term on its right provides the greatest complications, it is the term that is responsible for anomalous dissipation and is thus the most interesting term in any theory that deals with the evolution of shock waves. For a spectrum of properly chosen fluctuations this term prevents large amplitude waves from indefinite steeping and breaking and provides the required dissipation of kinetic energy, entropy generation, and shock stabilisation. In its general version given above it should contain the whole physics of the shock including the complete collective processes which occur before the binary particle collisions come into play. These equations are too complex to be solved, and the behaviour of shocks can be described only with simplifications. The most effective simplification is to look at the macroscopic conservation laws describing changes of the plasma quantities across the shock transition layer which follows from the fundamental kinetic equations presented above. These are the magnetohydrodynamic equations which lead to the Rankine-Hugoniot jump relations across the shock transition layer.

### Average quantities and conservation Law's

The hydrodynamic approach is based on a description of plasma in terms of macroscopic quantities, such as density, temperature, mean velocity, etc. This description is accurate for distribution functions close to the equilibrium where the average quantities can be computed. This means that the hydrodynamic approach does not describe internal processes taking place inside the shock transition, the generation of dissipation and entropy production to be known, but it describes the global large scale structure of a shock.

Each microscopic physical quantity can be averaged thus, representing the correspondent macroscopic quantity in a plasma, as the density of particles

$$n_s(t,\mathbf{r}) = \int d\mathbf{p} f_s(t,\mathbf{r},\mathbf{p}), \tag{1.13}$$

the vector of mean velocity (already introduced in the Maxwellian distribution function as the drift velocity)

$$\mathbf{u}_s(t,\mathbf{r}) = \frac{1}{n_s}\int d\mathbf{p}\,\mathbf{v} f_s(t,\mathbf{r},\mathbf{p}), \tag{1.14}$$

and the mean energy

$$\mathrm{U}_s(t,\mathbf{r}) = \frac{1}{n_s}\int d\mathbf{p}\epsilon_s f_s(t,\mathbf{r},\mathbf{p}), \tag{1.15}$$

where $\mathbf{v} = \mathbf{p}/\gamma m_s$ is the speed and $\epsilon_s = \mathbf{p}^2/2m_s$ the energy of the particle . The transport processes of the momentum and of the energy in plasma can be described by the tensor of momentum flux

$$\bar{\bar{\mathrm{P}}}_s(t,\mathbf{r}) = \int d\mathbf{p}\,\mathbf{p}\otimes\mathbf{v} f_s(t,\mathbf{r},\mathbf{p}), \tag{1.16}$$

and the vector of energy flux

$$\Upsilon_s(t,\mathbf{r}) = \int d\mathbf{p}\epsilon_s\mathbf{v} f_s(t,\mathbf{r},\mathbf{p}). \tag{1.17}$$

It is often interesting to separate the mean motion of particles of the species $s$ with the mean speed $u_s$, and the chaotic (thermal) motion with the relative momentum $\mathbf{p}' = \mathbf{p} - m_s\mathbf{u}_s$. This allows to divide the energy (1.15) and the fluxes (1.16) and (1.17) of all particles into the mean and the chaotic parts. For a classical plasma the energy is

$$\mathrm{U}_s = \frac{1}{2} m_s \mathbf{u}_s^2 + \frac{3}{2} k_\mathrm{B} \mathrm{T}_s, \tag{1.18}$$

where the temperature $\mathrm{T}_s$ is a measure of thermal motion. It is defined by the following equation

$$k_\mathrm{B} \mathrm{T}_s = \frac{1}{3 m_s n_s} \int d\mathbf{p} (\mathbf{p} - m_s \mathbf{u}_s)^2 f_s(t, \mathbf{r}, \mathbf{p}). \tag{1.19}$$

In the same way, the momentum flux $\bar{\bar{\mathrm{P}}}_s(t, \mathbf{r}) = m_s n_s \mathbf{u}_s \otimes \mathbf{u}_s + \bar{\bar{\Pi}}_s$ contains a term corresponding to the plasma pressure

$$\bar{\bar{\Pi}}_s(t, \mathbf{r}) = \int d\mathbf{p} (\mathbf{p} - m_s \mathbf{u}_s) \otimes (\mathbf{v} - \mathbf{u}_s) f_s(t, \mathbf{r}, \mathbf{p}). \tag{1.20}$$

The average energy density and the local temperatures $\mathrm{T}_\parallel$, $\mathrm{T}_\perp$ parallel and perpendicular to the average magnetic field are found on the diagonal of the pressure tensor $\Pi_s$.

The average Vlasov equation (1.9) produces the well-known full set of magnetohydrodynamic equations for each particle species $s = e, i$. The two first equations are the conservation of the number of particles

$$\frac{\partial n_s}{\partial t} + \nabla_\mathbf{r} \cdot (n_s \mathbf{u}_s) = 0, \tag{1.21}$$

and the conservation of the momentum

$$\frac{\partial n_s \mathbf{u}_s}{\partial t} + \frac{1}{m_s} \nabla_\mathbf{r} \cdot \bar{\bar{\mathrm{P}}}_s = \frac{q_s \mathrm{N}_s}{m_s} (\mathbf{E}^{(0)} + \mathbf{u}_s \wedge \mathbf{B}^{(0)}) + \int d\mathbf{v} \mathbf{v} \cdot \mathbf{R}, \tag{1.22}$$

where $\mathbf{R}$ is the pseudo-collision term in the right hand side of eq. (1.9). In the first order moment equation this term produces a wave friction term (at zero order the term conserves particle number) that has the explicit form

$$\mathbf{R} = -\frac{1}{m_s} \left\{ \frac{\partial}{\partial t} \underbrace{\frac{< \mathbf{E}^{(1)} \times \mathbf{B}^{(1)} >}{\mu_0}}_{Poynting\,moment} + \nabla_\mathbf{r} \cdot \left[ \underbrace{\left( \frac{\epsilon_0}{2} \langle (\mathbf{E}^{(1)})^2 \rangle + \frac{1}{2\mu_0} \langle (\mathbf{B}^{(1)})^2 \rangle \right) \mathrm{I}}_{isotropic\,wave\,pressure} - \underbrace{\left( \epsilon_0 < \mathbf{E}^{(1)} \otimes \mathbf{E}^{(1)} > + \frac{1}{\mu_0} < \mathbf{B}^{(1)} \otimes \mathbf{B}^{(1)} > \right)}_{anisotropy\,wave\,pressure} \right] \right\}. \tag{1.23}$$

The friction term represents a ponderomotive force-density term containing the average wave pressure gradients. The main contribution of this term is due to the electron momentum density equation, since the ions are (in the non-relativistic case considered here) less sensitive to ponderomotive effects. This term affects the motion of the electrons it is responsible for the anomalous collisions, anomalous resistivity and viscosity.

### Equations of state

The third equation of the system, the next higher moment, is the equation of energy conservation. In a collisionless plasma, for the model of ideal hydrodynamics, this equation can be written as

$$\frac{3}{2} n_s k_\mathrm{B} \left( \frac{\partial \mathrm{T}_s}{\partial t} + \mathbf{u}_s \cdot \nabla_\mathbf{r} . \mathrm{T}_s \right) + n_s k_\mathrm{B} \mathrm{T}_s \nabla_\mathbf{r} \cdot \mathbf{u}_s = 0 \tag{1.24}$$

Combining (1.21) and (1.24) this equation becomes

$$\frac{3}{2} \frac{d}{dt} \ln(\mathrm{T_s}) + \frac{\mathrm{d}}{\mathrm{dt}} \ln(\mathrm{n_s}) = 0, \tag{1.25}$$

where $\frac{d}{dt} = \frac{\partial}{\partial t} + \mathbf{u}_s \cdot \nabla_\mathbf{r}$ is the total (Lagrangian) derivative. The product $\mathrm{T}_s . n_s^{-2/3}$ is a constant along the fluid stream lines, and the pressure is $p_s \propto n_s^{\Gamma_s}$ , where $\Gamma_s = 5/3$ is the adiabatic coefficient. The adiabatic constant depends of the dimension number D as

$$\Gamma_s = 1 + 2/\mathrm{D}. \tag{1.26}$$

For example, $\Gamma_s = 3$ for the flux in one dimension and $\Gamma_s = 1$ for an isothermal flux. The relation $p_s \propto n_s^{\Gamma_s}$ is the equation of state, and it describes the energy conservation in a plasma if there is no external energy source (no external magnetic field).

The equation of state has be known to investigate shock solutions. However, the equations of state are defined for systems near the equilibrium, moreover the isothermal case cannot be applied to shocks because of entropy dissipation at the shock front. The adiabatic equation can be applied to fast processes taking part in the shock environment when the flow passes across the shock front in a time so short that thermalisation becomes impossible. The momentum equations can be applied to an extended shock that represents a ramp in the real space. The shock front can be considered as a thin planar discontinuity that moves at a shock velocity $v_{sh}$ in the normal direction $\mathbf{n}$ across the plasma. In the case of a plane rigid stationary shock surface as shown in Figure 1.1, the microprocesses are confined to the interior of the shock plane.

The dissipation-free average conservation laws can be applied to the shock in order to express the downstream values in terms of the undisturbed upstream flow and field values. With this approach the "pseudo-collision" term R in (1.22) can be neglected, since this term only concerns the shock plane.

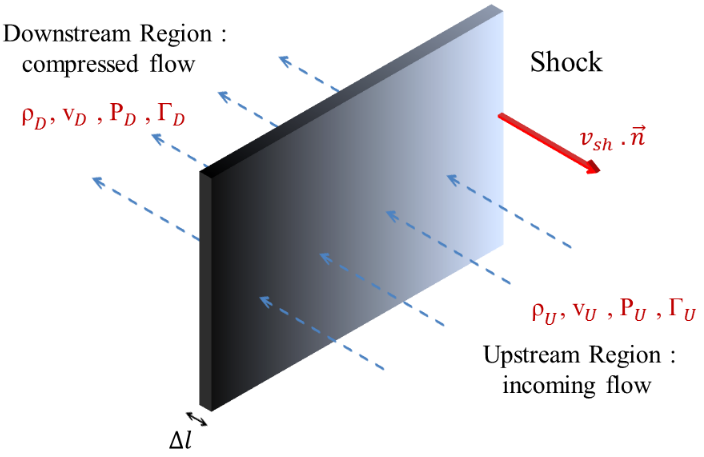

Figure 1.1 – Sketch of a planar thin shock with its front $\Delta l$ separating the upstream ($\rho_U$,$v_U$,$P_U$,$\Gamma_U$) and downstream ($\rho_D$,$v_D$,$P_D$,$\Gamma_D$) regions.

The set of separate conservation laws for electrons and ions is applicable for the problems where the characteristic velocities are high and the densities and temperatures of the components are different. However, the time to reach equilibrium between ions and electrons is $m_i/m_e$ times shorter than the time of temperature equilibration of electrons. Also the relaxation time of the electrostatic field is often shorter than the relaxation time of the magnetic field. These facts allow one to develop a more simple hydrodynamic model, assuming that the densities of both species are approximately equal.

### Single fluid magnetohydrodynamics

According to the Poisson equation, this assumption implies that the electrostatic field is zero and the charge density is almost zero $Zn_i \simeq n_e$. Then as in the theory of neutral fluids, one may introduce the center of mass, the mass density and the mass velocity as

$$m = m_e + m_i, \qquad \rho_m = m_e n_e + m_i n_i, \qquad \mathbf{V} = \frac{m_e n_e \mathbf{u}_e + m_i n_i \mathbf{u}_i}{m_e n_e + m_i n_i}. \tag{1.27}$$

This leads to the magnetohydrodynamics or MHD equations for a single-fluid plasma. The equation of continuity and the momentum conservation equation can be written down for a quasi-neutral plasma as

$$\frac{\partial \rho_m}{\partial t} + \nabla_{\mathbf{r}} \cdot (\rho_m \mathbf{V}) = 0, \tag{1.28}$$

$$\frac{\partial(\rho_m \mathbf{V})}{\partial t} + \nabla_{\mathbf{r}} \cdot (\rho_m \mathbf{V}\mathbf{V}) = -\nabla_{\mathbf{r}} \cdot \bar{\bar{\Pi}} + \mathbf{J} \wedge \mathbf{B}, \tag{1.29}$$

where $\bar{\bar{\Pi}} = \bar{\bar{\Pi}}_e + \bar{\bar{\Pi}}_i$ is the total pressure tensor, and the indices 0 have been suppressed since only the average moments are involved. The average electric field vanishes outside the shock ramp. To close these equations, relations for the current $\mathbf{J}$, magnetic field $\mathbf{B}$ and pressures must be established. For the pressures $\bar{\bar{\Pi}}_i$ , supposing that the conditions of ideal hydrodynamics are fulfilled, one can use the equations of state with the appropriate adiabatic index $\Gamma_s$. The plasma neutrality imposes $\nabla_{\mathbf{r}} \cdot \mathbf{J} = 0$, but the current can be non zero. It is defined by the Ampère equation (1.2) where the displacement current can be neglected for sufficiently slow non-relativistic movements

$$\nabla_{\mathbf{r}} \times \mathbf{B} = \mu_0 \mathbf{J}. \tag{1.30}$$

The Faraday equation for the magnetic field involves the rotation of the electric field, which can be found from the equation of electron motion. The expression for the electric field leads to the collisionless Ohm's law,

$$\mathbf{E} = -\mathbf{V} \times \mathbf{B} - \frac{1}{e\rho_m} \nabla_{\mathbf{r}} \cdot \Pi_e + \frac{1}{e\rho_m} \mathbf{J} \times \mathbf{B} + \frac{m_e}{e^2 \rho_m} \frac{\partial \mathbf{J}}{\partial t} + \eta \mathbf{J} \tag{1.31}$$

The first term on the right hand side represents the polarization due to the plasma motion in the direction perpendicular to the magnetic field. This effect originates from the drift motion of particles in crossed electric and magnetic fields. The second term is the field produced by the electron pressure, which comes from the separation of charges in an inhomogeneous plasma. The Hall effect is at the third position, representing the creation of the electric field by a current directed perpendicular to the magnetic field. The fourth term accounts for the electron inertia, which can be followed by a term of resistivity retained from the pseudo-collision term from eq (1.22) in the non-ideal case. One can introduce two characteristic lenghts: the ion inertia length

$$\frac{c}{\omega_{pi}} = \sqrt{\frac{\epsilon_0 m_i c^2}{Z^2 n_i e^2}}, \tag{1.32}$$

which is the characteristic scale length for ions to be accelerated by electromagnetic forces in a plasma and the electron inertia length

$$\frac{c}{\omega_{pe}} = \sqrt{\frac{\epsilon_0 m_e c^2}{n_e e^2}}. \tag{1.33}$$

The electron inertia lenght is usually small so one can typically assume massless electrons (since $\frac{c}{\omega_{pe}} << \frac{c}{\omega_{pi}}$). This non-collisional Ohm's law is still too complex, introducing second order spatial derivatives into Faraday's law through the pressure gradient and current expressions, to treat the conservation laws at a shock transition. However, the hypothesis of a flat shock transition allows the three latter terms in the right hand side to be neglected, and the ideal Ohm's law can be written as

$$\mathbf{E} = -\mathbf{V} \times \mathbf{B} \tag{1.34}$$

### Rankine-Hugoniot Relations

By combining of equations (1.28), (1.29) and (1.2) and considering an ideal Ohm's law, one forms the closed set of equations:

$$\partial_t \rho_m + \nabla_{\mathbf{r}} \cdot (\rho_m \mathbf{V}) = 0 \tag{1.35a}$$

$$\partial_t (\rho_m \mathbf{V}) + \nabla_{\mathbf{r}} \cdot (\rho_m \mathbf{V}\mathbf{V}) + \nabla_{\mathbf{r}} \cdot \bar{\bar{\Pi}} - \mathbf{J} \times \mathbf{B} = 0 \tag{1.35b}$$

$$\partial_t \left( \frac{\rho_m V^2}{2} + \rho_m \Xi + \frac{B^2}{2\mu_0} \right) + \nabla_{\mathbf{r}} \cdot \left( \frac{\rho_m V^2}{2} \mathbf{V} + \rho_m \Xi \mathbf{V} + \Pi \cdot \mathbf{V} + \frac{\mathbf{E} \times \mathbf{B}}{\mu_0} \right) = 0 \tag{1.35c}$$

$$\partial_t \mathbf{B} + \nabla_{\mathbf{r}} \times \mathbf{E} = 0 \tag{1.35d}$$

$$\nabla_{\mathbf{r}} \cdot \mathbf{B} = 0 \tag{1.35e}$$

where $\Xi = \frac{\Pi}{(\Gamma_i - 1)\rho_m}$ is the specific internal energy. In the rest frame of the shock the continuity equation and Maxwell's equations become,

$$\nabla_{\mathbf{r}} \cdot (\rho_m \mathbf{V}) = 0 \tag{1.37a}$$

$$\nabla_{\mathbf{r}} . (\rho_m \mathbf{V} \cdot \mathbf{V}) + \nabla_{\mathbf{r}} \cdot \Pi - \mathbf{J} \times \mathbf{B} = 0 \tag{1.37b}$$

$$\nabla_{\mathbf{r}} \cdot \left( \frac{\rho_m V^2}{2} \mathbf{V} + \rho_m \Xi \mathbf{V} + \Pi \cdot \mathbf{V} + \frac{\mathbf{E} \times \mathbf{B}}{\mu_0} \right) = 0 \tag{1.37c}$$

$$\nabla_{\mathbf{r}} \times \mathbf{E} = 0 \tag{1.37d}$$

$$\nabla_{\mathbf{r}} \cdot \mathbf{B} = 0 \tag{1.37e}$$

The magnetic force J × **B** can be decomposed into a magnetic pressure gradient force and a magnetic tension force.

$$\mathbf{J} \times \mathbf{B} = \frac{\nabla_{\mathbf{r}} \times \mathbf{B}}{\mu_0} \times \mathbf{B} = -\nabla_{\mathbf{r}} . \frac{B^2}{2\mu_0} + \frac{\mathbf{B} \cdot \nabla_{\mathbf{r}} \cdot \mathbf{B}}{\mu_0} \tag{1.39}$$

Using (1.39) one can integrate equation (1.37) across the shock front

$$\rho_m \mathbf{V} \cdot \mathbf{n} = 0 \tag{1.40a}$$

$$\rho_m \mathbf{V} . (\mathbf{V} \cdot \mathbf{n}) + \left( \Pi + \frac{B^2}{2\mu_0} \right) \mathbf{n} - \frac{(\mathbf{B} \cdot \mathbf{n}) . \mathbf{B}}{\mu_0} = 0 \tag{1.40b}$$

$$\mathbf{n} \cdot \mathbf{V} \left\{ \frac{\rho_m V^2}{2} + \rho_m \Xi + \left( \Pi + \frac{B^2}{2\mu_0} \right) \right\} - \frac{(\mathbf{B} \cdot \mathbf{n})(\mathbf{B} \cdot \mathbf{V})}{\mu_0} = 0 \tag{1.40c}$$

$$\mathbf{n} \times (\mathbf{V} \times \mathbf{B}) = 0 \tag{1.40d}$$

$$\mathbf{n} \cdot \mathbf{B} = 0 \tag{1.40e}$$

This system of equations is the implicit form of the Rankine-Hugoniot conservation equations in the ideal magnetohydrodynamics (ideal MHD). Explicit MHD shock solutions can be found (Treumann, 2009) which require finite mass flux across the shock in the normal direction. The jump conditions contain rich physics related to different wave modes in ideal MHD. They can be classified by introducing the angle $\theta$ between the magnetic field and the shock normal **n**. Three kind of shocks depending of the value of $\theta$ can exist in MHD.

- $\theta = 0$ corresponds to a parallel shock
- $\theta = \pi/2$ corresponds to a perpendicular shock

- $0 < \theta < \pi/2$ corresponds to an oblique shock

The jump conditions allow three types of discontinuities that are not shocks.

- Contact discontinuity
- Tangential discontinuity
- Rotational discontinuity

These shocks and discontinuities will be discussed in detail in Chapter 4. The ideal MHD approximation breaks down near the discontinuity where the kinetic theory becomes indispensable, which consider such effects as radiative cooling, partial ionization or thermal conduction. The ideal magnetohydrodynamic description does not take into account the high energy non-Maxwellian tail of particles accelerated by the shock which can modify the shock structure by generating instabilities while getting bounced back and forth. More complexes magnetohydrodynamic approaches as (Drury and Voelk, 1981) have included the reaction of these CRs on the shocks structures.

Collisionless shocks may give rise to various instabilities as the Weibel instability, the streaming instability or Bell's instability which will be discussed in the next section and in Chapter 2. The shock thickness $\Delta l$ depends on the dominant dissipation mechanism(s) described by the kinetic theory, this yields $\Delta l$ of the order of an ion mean free path. Laminar collisionless shocks often have a thickness of the order of an ion inertial length $\frac{c}{\omega_{pi}}$.

### 1.1.2 Waves and Instabilities

Shocks can be collisional or collisionless, but must nevertheless fulfill the Rankine-Hugoniot jump conditions. The MHD approach allows to describe the macroscopic quantities transitions as the density, the velocity, the temperature and the magnetic flux, but does not take into account the physics in the shock ramp.

Shocks evolve from waves mainly through nonlinear wave steeping and the onset of dissipation and dispersion. Various modes are responsible for the anomalous dissipation, shock ramp broadening, generation of turbulence in the shock up- and down-stream the front, as well as for the particle acceleration, and reflection from the shock. Therefore any more profound understanding of shock processes cannot avoid bothering with waves, instabilities, wave excitation and wave particle interaction. A discussion on waves and instabilities will be presented in detail in the next Chapter. Here, we introduce a general description of the plasma instabilities by using the susceptibility tensor and the dispersion relation.

Plasma in the ground state is considered as field-free (i.e. no external magnetic or electric field in a neutral plasma), homogeneous and infinite. Using the perturbative approach in eq (1.8) the linearized Vlasov equation (1.11) reads

$$\partial_t . f_s^{(1)} + \mathbf{v} \cdot \partial_{\mathbf{r}} . f_s^{(1)} + q_s(\mathbf{E}^{(1)} + \mathbf{v} \wedge \mathbf{B}^{(1)}) \cdot \partial_{\mathbf{p}} . f_s^{(0)} = 0 \tag{1.42}$$

It is possible to consider that all space-/time-dependent physical quantities can be written in the form

$$\{f_s, \mathbf{E}, \mathbf{B}\} = \{f_s^{(0)}, \mathbf{E}^{(0)}, \mathbf{B}^{(0)}\} + \{f_s^{(1)}, \mathbf{E}^{(1)}, \mathbf{B}^{(1)}\} e^{-i(\omega t - \mathbf{kr})} \tag{1.43}$$

Equation (1.42) provides then an explicit expression for the Fourier harmonic of the perturbation of the distribution function

$$f_s^{(1)} = \frac{i . q_s}{\mathbf{v}.\mathbf{k} - \omega} . (\mathbf{E}^{(1)} + \mathbf{v} \wedge \mathbf{B}^{(1)}) \cdot \partial_{\mathbf{p}} . f_s^{(0)} \tag{1.44}$$

From there one finds the density current

$$\mathbf{J}^{(1)} = \sum_s n_s q_s \int d\mathbf{p}\,\mathbf{v} f_s^{(1)} \tag{1.45}$$

Performing a Fourier transform of Vlasov-Maxwell's equations

$$\begin{aligned} i\mathbf{k}\times\mathbf{E}^{(1)} &= i\omega\mathbf{B}^{(1)}, & i\mathbf{k}\cdot\mathbf{B}^{(1)} &= 0,\\ i\mathbf{k}\times\mathbf{B}^{(1)} &= -i\frac{\omega}{c^2}\mathbf{E}^{(1)} + \mu_0\mathbf{J}^{(1)}, & i\mathbf{k}\cdot\mathbf{E}^{(1)} &= \epsilon_0^{-1}\rho^{(1)}. \end{aligned} \tag{1.46}$$

one finds an expression for the density current as

$$\mathbf{J}^{(1)} = \frac{i\omega}{\mu_0}\left(\frac{\mathbf{k}}{\omega}\wedge\left(\frac{\mathbf{k}}{\omega}\wedge\mathbf{E}^{(1)}\right) + \frac{\mathbf{E}^{(1)}}{c^2}\right) \tag{1.47}$$

Combining equations (1.45) and (1.47) for the density current, the following equation is obtained (with $c^2 = 1/\mu_0\epsilon_0$ the square of the speed of light)

$$i\sum_s \frac{n_s q_s^2}{\epsilon_0}\int d\mathbf{p}\frac{\mathbf{p}/\gamma}{\omega-\mathbf{v}.\mathbf{k}}\cdot\left(\mathbf{E}^{(1)} + \mathbf{v}\wedge\frac{\mathbf{k}}{\omega}\wedge\mathbf{E}^{(1)}\right)\cdot\partial_{\mathbf{p}}.f_s^{(0)} + i\omega\left(\frac{\mathbf{k}}{\omega}\wedge\frac{\mathbf{k}}{\omega}\wedge\mathbf{E}^{(1)} + \frac{\mathbf{E}^{(1)}}{c^2}\right) = 0 \tag{1.48}$$

The vector products can be expressed with tensor notations ⊗,

$$\mathbf{v}\wedge\frac{\mathbf{k}}{\omega}\wedge\mathbf{E}^{(1)} = \left(\frac{\mathbf{k}}{\omega}\otimes\mathbf{v} - \mathbf{v}\cdot\frac{\mathbf{k}}{\omega}\right)\cdot\mathbf{E}^{(1)}, \tag{1.49}$$

$$\frac{\mathbf{k}}{\omega}\wedge\frac{\mathbf{k}}{\omega}\wedge\mathbf{E}^{(1)} = \left(\frac{\mathbf{k}}{\omega}\otimes\frac{\mathbf{k}}{\omega} - \frac{\mathbf{k}^2}{\omega}\right)\cdot\mathbf{E}^{(1)}, \tag{1.50}$$

which allow us to write equation (1.48) as

$$\sum_s \frac{n_s q_s^2}{\epsilon_0}\int d\mathbf{p}\frac{\mathbf{p}/\gamma}{\omega-\mathbf{v}\cdot\mathbf{k}}\cdot\left(1 - \frac{\mathbf{v}\cdot\mathbf{k}}{\omega} + \frac{\mathbf{k}}{\omega}\otimes\mathbf{v}\right)\cdot\mathbf{E}^{(1)}\cdot\partial_{\mathbf{p}}.f_s^{(0)} + \omega\left(\frac{1}{c^2} + \frac{\mathbf{k}}{\omega}\otimes\frac{\mathbf{k}}{\omega} - \frac{\mathbf{k}^2}{\omega^2}\right)\cdot\mathbf{E}^{(1)} = 0 \tag{1.51}$$

$$\left\{\omega^2\left[\frac{1}{c^2} + \frac{1}{\omega^2}\sum_s \frac{n_s q_s^2}{\epsilon_0}\int d\mathbf{p}\frac{\mathbf{p}}{\gamma}\cdot\partial_{\mathbf{p}}.f_s^{(0)}\left[1 + \frac{\mathbf{k}\otimes\mathbf{v}}{\omega-\mathbf{v}\cdot\mathbf{k}}\right]\right] + \mathbf{k}\otimes\mathbf{k} - \mathbf{k}^2\right\}\cdot\mathbf{E}^{(1)} = 0 \tag{1.52}$$

Then, the general dispersion relation can be written in a compact form as the determinant of the bracketed expression

$$\mathrm{D}(\omega,\mathbf{k}) = det\left[\omega^2\epsilon + \mathbf{k}\otimes\mathbf{k} - \mathbf{k}^2\right] = 0, \tag{1.53}$$

where the dielectric tensor is introduced as

$$\epsilon = 1 + \sum_s \chi_s, \tag{1.54}$$

with the susceptibility tensor $\chi_s$ for the $s_{th}$ species as

$$\chi_s = \frac{\omega_{ps}^2}{\omega^2}m_s\int d\mathbf{p}\left(\frac{\mathbf{p}}{\gamma}\otimes\partial_{\mathbf{p}}.f_s^{(0)} + \left[\mathbf{v}\otimes\frac{\mathbf{p}}{\gamma}\right]\frac{\mathbf{k}\cdot\partial_{\mathbf{p}}.f_s^{(0)}}{\omega-\mathbf{v}\cdot\mathbf{k}}\right) \tag{1.55}$$

Solution to dispersion relation gives complex solutions, which can be written as

$$\omega(\mathbf{k}) = \omega_r(\mathbf{k}) + i\delta(\omega_r,\mathbf{k}), \tag{1.56}$$

where the index $r$ indicates the real part, and $\delta$ is the imaginary part of the frequency which itself is a function of the wave number. Each mode at given wave number evolves in time, according its frequency and damping/growth rate. The amplitude of the wave changes slowly in time, if the imaginary part of the frequency is small compared to the real part.

The solution with a complex frequency from (1.43) reads

$$\{\mathbf{E}^{(1)}, \mathbf{B}^{(1)}\} e^{\delta t} e^{-i(\omega_r t - \mathbf{k}\cdot\mathbf{r})}. \tag{1.57}$$

The sign of $\delta$ determine if the wave is exponentially damped ($\delta < 0$) or if it exponentially grows ($\delta > 0$). In the latter case, the solution is unstable with the growth rate $\delta$.

An instability is excited if an active medium like a warm plasma contains a certain amount of free energy in excess to the thermal energy. Plasma containing any form of available free energy is out of thermodynamic equilibrium. Restoration of equilibrium proceeds by excitation of waves which may grow to amplitudes large enough for either causing dissipation or transporting the energy away to a location where it can be dissipated by other processes. Depending on initial conditions one or more eigenmodes start to grow out of the thermal fluctuations and propagate across the plasma. The unstable waves that survive at nonlinear stage are those with the fastest growth. The linear dispersion theory applies to small amplitude waves. At higher amplitudes the linear theory fails and the instability needs to be described by a non-linear or quasi-linear theory.

In the context of collisionless shocks the instabilities of interest can be divided into two classes. The first class concerns low frequency waves on large scales which can grow and form a large macroscopic shock. These waves, as magnetosonic or Alfvénic modes, are discussed in Chapter 3 and 4. The other class of waves includes those formed secondarily after an initial seed shock ramp has grown in some way out of one of the wave modes from the first class, these are ion modes which have been identified to be responsible for structuring, shaping and reforming the shock. They are discussed in detail in Chapter 2. Even if these waves are not forming shocks, they contribute to the entropy generation and dissipation.

## 1.2 Numerical model

The modern age of physics is to a large degree determined by the availability of high speed and high capacity computer systems. The use of these computing facilities for performing numerical experiments on collisionless plasmas covers now almost half a century of experience. Many problems in plasmas and in particular space plasma physics with their enormous complexity could not have been solved or even tackled without computers and numerical simulations. Also, most of the discussion on shocks in this thesis will be based on such numerical simulations which must accompany observations and experiments in order to understand what is going on in the shock environment. A brief discussion about numerical methods is therefore not only unavoidable but even necessary.

### 1.2.1 Computational magnetohydrodynamics

A large quantity of problems in plasma physics can be solved using hydrodynamic models (fusion, etc). Even if in this thesis the physical phenomena studied required a kinetic description for the plasma-plasma interaction, the fluid approach was used sometimes to support the kinetic studies, especially to determine the plasma formation in laser-matter interaction (Atzeni and ter Vehn, 2004). Two approaches for hydrodynamic codes are possible. The Lagrangian description where the numerical cells move with the fluid at the fluid velocity, and the Eulerian description where the numerical grid is static and fluid is moving through it.

The Lagrangian method is in many respects the most natural form to solve complex hydrodynamic problems. In Lagrangian case the computational mesh is moving together with the simulated fluid with zero mass flux between computational cells while Eulerian method employs fixed static computational mesh with advection flux between cells. Lagrangian coordinates are superior to Eulerian coordinates for coupling to other physical processes (especially radiation) or for problems which involve changing computational domain with moving boundary conditions for which

Eulerian setup would be very difficult. However, the non-symmetric deformation of a material causes significant cell distorsions which become uncomputable (Vorticity). Many problems are therefore more easily resolved in Eulerian coordinates.

In this thesis, the hydrodynamic code CHIC (Code Hydrodynamique d'Implosion du CELIA) has been used to model laser-plasma interactions on a ns time scale where the kinetic description was not feasible due to the excessively long computational time that would have been involved. CHIC is a 2D code based on a cell-centred Lagrangian discretization scheme (Maire et al., 2007; Galera et al., 2010; Breil et al., 2011), with possibility to have an axisymmetric geometry and projection on an Eulerian grid. Plasma evolution is described in a single fluid two temperature model (ion and electron). The transport of electron energy is described by the Spitzer-Harm diffusion model with a flux limiter or with a non-local model (Schurtz et al., 2000).

Propagation of laser beams in an under-dense plasma is calculated by a three-dimensional ray tracing algorithm that takes into account refraction as well as collisional absorption. The self-generated transverse magnetic fields are evaluated using a resistive magnetohydrodynamic (MHD) model that is derived from the generalized Ohm law (1.31). Coupling to the electron energy transport performed according to the Braginskii transport theory (Braginskii, 1965). The radiative energy is described in the multi-group diffusion approximation of the radiative transfer equation. Table were used for the equations of state (SESAME, QEOS) and opacities (Atzeni and ter Vehn, 2004).

The hydrodynamic module is based on a Lagrangian description of the equations of gas dynamics. Equations describing the conservation of mass, momentum and total energy are solved by the method of finite volume on a mesh moving with the fluid velocity. The numerical scheme is conservative and fulfills the entropy inequality following the second principle of the thermodynamic. A numerical strategy based on the Arbitrary Lagrangian Eulerian (ALE) (Hirt et al., 1974) is also implemented. In this approach, the Lagrangian phase is followed by two subsequent phases: i) regularisation allowing to restore the geometrical quality of the Lagrangian mesh, and ii) conservative interpolation of the physical variables to the new Lagrangian mesh. Thanks to this procedure numerical simulations can be conducted on long time scales.

### 1.2.2 The particle-in-cell method as a kinetic approach

Almost all the physical phenomena studied in this thesis required a full kinetic description of the plasma the magnetohydrodynamic is not suitable and a numerical scheme that couples the relativistic Vlasov equation (2.1.7) with the Maxwell's equations has to be used. Thus far, two kinetic numerical approaches are commonly used in the plasma physics community to study collisionless plasma processes. The Vlasov approach (Cheng and Knorr, 1976) based on an Eulerian scheme is one of them. The code performs a direct integration of the Vlasov-Maxwell system of equations discretized on a phase-space grid. Another approach is the Particle-In-Cell method (PIC) (Birdsall and Langdon, 2004) using a Lagrangian-Eulerian approach, where the distribution function of each species is formed by a collection of computational particles (CPs) or macroparticles and Maxwell's equations are solved on an Eulerian grid. Such codes can be used to excite linear plasma modes and nonlinear plasma dynamics can be followed.

Vlasov codes are extremely efficient when a small fraction of particles is particularly important, since these codes apply equal computational effort to the part of phase space occupied by those particles and to the part of phase space occupied by the majority of particles. However, this advantage can also be a problem since they have to spend time modelling unoccupied parts of the phase space. A further disadvantage is that Vlasov codes are numerically diffusive and dispersive. It can be problematic to model a plasma/vaccum interface in the context of laser-plasma experiments, since this sharp feature can spread diffusively, and the high wavenumbers can be advected at the wrong speed. These codes have some advantages compared to PIC codes for particular 1D problems, but they are limited when studying more complex geometries where PIC codes excel.

The latters are based on numerical algorithms much simpler than the Vlasov method which tries to find the direct solution of the Vlasov partial differential equation. PIC simulations have an 'unlimited' dynamical range for the particle momenta and no boundary conditions in the phase space. However, PIC codes have a limited signal-to-noise ratio and a coarse phase space density resolution. Doing so, the PIC codes are very limited when describing the regions with a small amount of particles.

### Particle-In-Cell code: Numerical scheme

Particle-in-cell simulation codes (Eastwood, 1991; Noguchi et al., 2007) solve the Vlasov-Maxwell set of equations for collisionless warm plasmas by the method of characteristics. Real systems studied may contain an extremely number of particles. In order to make simulations efficient, each computational particle is representing many real particles the distribution function is discretized with $\mathrm{N}_c$ computational particles

$$f_c(t,\mathbf{x},\mathbf{p}) = \sum_{m=1}^{\mathrm{N}_c} \omega_m \mathrm{S}(\mathbf{x}-\mathbf{x}_m)\delta(\mathbf{p}-\mathbf{p}_m), \tag{1.58}$$

where $\mathbf{x}_m$ and $\mathbf{p}_m$ are the CP's position and momentum, $\delta$ is the Dirac distribution and S(x) is the shape function of the CP centered in its position $\mathbf{x}_m(t)$. The quantity $\omega_m$ is the numerical weight of the computational particle, defined as

$$\omega_m = \frac{n_c(\mathbf{x}_m(t=0))}{\mathrm{N}_c(\mathbf{x}_m(t=0))}, \tag{1.59}$$

where $n_c$ is the initial density of the plasma at the m-th particle position. The number of real particles corresponding to a computational particle must be chosen such that sufficient statistics can be collected on the particle motion, and a larger number of particle $\mathrm{N}_c$ provides a more accurate description of the local density variation. The mass $m_c$ and charge $q_c$ of each phase space volume element, which we refer to as a computational particle, are typically much larger than those of the physical particles, but the ratio charge/mass must be the same, $q_c/m_c = -e/m_e$ for electrons and $q_c/m_c = e/m_p$ for protons.

The continuous fields $\mathbf{B}(x,t)$, $\mathbf{E}(x,t)$ in the Maxwell's equations are replaced by their discretized counterparts. The fields are defined on a grid (Field nodes). A finite spatial resolution is introduced $x \longrightarrow g\Delta x$ as well as a finite time resolution $t \longrightarrow g\Delta t$ , with integer values g and where $\Delta x$ is the spatial resolution of the grid and $\Delta t$ the temporal resolution. The differential operators are replaced by difference operators, $\frac{d}{dx}f(x) \longrightarrow (f[(g+1)\Delta x] - f[g\Delta x])/\Delta x$. And the differential equations for the fields into algebraic equations.

Each computational particle evolution is described by the equation of motion

$$\frac{d\mathbf{p_m}}{dt} = q_c(\mathbf{E_m} + \mathbf{v_m} \times \mathbf{B_m}), \qquad \mathbf{p_m} = \gamma(\mathbf{v_m}) m_c \mathbf{v_m}, \qquad \frac{d\mathbf{x_m}}{dt} = \mathbf{v_m}, \tag{1.60}$$

where we introduced the computational particle relativistic factor $\gamma(\mathbf{v_m}) = 1/\sqrt{1-(\mathbf{v_m}/c)^2}$. $\mathbf{E_m}$ and $\mathbf{B_m}$ are the electric and magnetic field acting on the particle $m$. They are calculated at the particle position by interpolation the values of electric and magnetic fields from the neighboring grid points.

Several integration schemes exit. The Spectral approach using fast Fourier transform is used to solve the Poisson Equation on a discrete spatial grid. It has been popular in the early PIC codes (Birdsall and Langdon, 2004), when computers had very limited memory and speed. The appearance of large clusters possessing a large numbers of processors have lead the community to a new scheme more adapted to parallelization strategies, the Finite Difference Time Domain (FDTD) scheme (Taflove et al., 2005).

Two PIC codes have been used throughout this thesis, and both are using the FDTD method, the EPOCH (Arber et al., 2015) and PICLS (Sentoku and Kemp, 2008) codes. The field solver of the EPOCH code is based on the Yee leapfrog scheme (Yee, 1966) and fields and current densities are

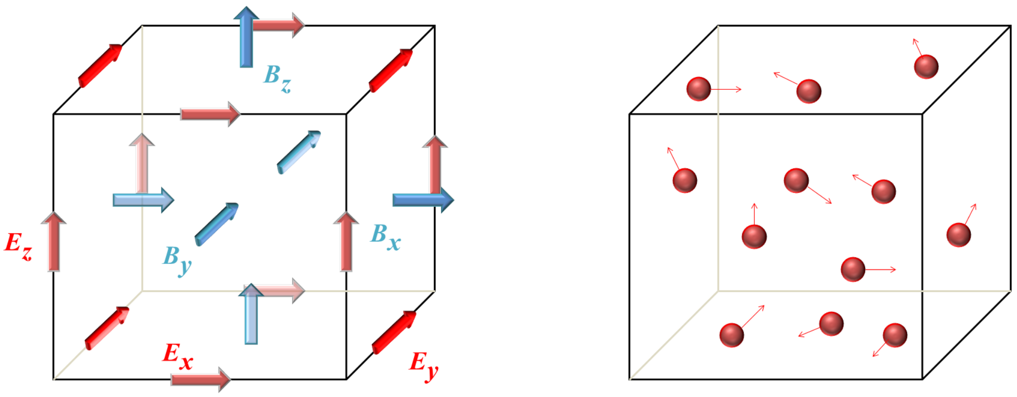

Figure 1.2 – Field mesh for the Yee scheme (left) and particles distribution into the cell (right) where their arrows represent their momentum.

discretized on a Cartesian grid (see Fig. 1.2). The Yee solver is subject to the Courant-Friedrich-Lewy (CFL) condition to ensure the algorithm stability which requires the time-step to be smaller than

$$c\Delta t_{\mathrm{CFL}} = \sum_m \frac{1}{\Delta x_m^{-2}}, \tag{1.61}$$

where the sum runs on the spatial directions resolved in the simulation.

PICLS it based in the directionnal splitting scheme. A detailed comparison between the directional splitting and the Yee scheme can be found in (Nuter et al., 2014). The directional splitting algorithm solves the electromagnetic fields on a single computational grid (Birdsall and Langdon, 2004). The computational stencil is not compatible with the Esirkepov charge conserving scheme, so that an error is performed in solving the Gauss equation at each time step. However, this error can be reduced by using the Boris correction (Birdsall and Langdon, 2004). This method imposes the computational grid to be uniform, $c\Delta t = \Delta x = \Delta y$, which makes the time step larger than for the Yee method.

Furthemore, in the code EPOCH a Yee staggered 2nd order FDTD scheme is implemented while PICLS has a fourth order current/force interpolation to suppress the numerical instability caused by under-resolving the Debye length, as explained later. This code is particularly adapted to simulate extremely dense and cold plasmas like laboratory plasmas.

### Initialisation and loop formation in PIC simulation

The PIC simulation setups are defined at $t = 0$. The user builts its simulation box with a certain number of cells $\mathrm{N}_x$, $\mathrm{N}_y$ (2D), $\mathrm{N}_z$ (3D). Then he defines a phase space profile for each species (several distribution functions can be used: Maxwellian, Maxwell-Juttner, Multi-waterbag, etc, depending of the PIC code used). The user indicates the number of macro-particles per cell to describe the distribution function of each species, which will be loaded more or less randomly in the cells.

At the first run of the simulation, the particles possessing a certain velocity and position deposit on the grid charge and current densities, $\rho(t = 0, x)$ and $\mathrm{J}(t = 0, x)$. The Poisson's equation is then solved and the initial electric fields are computed, which launch the PIC loop over N time-steps, defined by the user.

At the time $n$, electromagnetic fields are interpolated at the particle positions.

$$\mathbf{E_m}^n = \frac{1}{\Delta x^3} \int d\mathbf{x}.\mathrm{S}(\mathbf{x} - \mathbf{x}_m^{(n)})\mathbf{E_m}^n(\mathbf{x}), \tag{1.62}$$

$$\mathbf{B_m}^n = \frac{1}{\Delta x^3} \int d\mathbf{x}.\mathrm{S}(\mathbf{x} - \mathbf{x}_m^{(n)})\mathbf{B_m}^n(\mathbf{x}), \tag{1.63}$$

Then the new particle velocities and positions are computed with these fields. The particle pusher commonly used to advance particle positions in time is based on the one from the PSC code written by (Ruhl, 2005) which is based on the well-known Boris pusher (Boris, 1970). It computes the new particle momentum and position according at the half time step to

$$\mathbf{v_m}^{n+\frac{1}{2}} = \mathbf{v_m}^{n-\frac{1}{2}} + \frac{q_s}{m_s}\Delta t\left[\mathbf{E_m}^{(n)} + \frac{\mathbf{v_m}^{(n+\frac{1}{2})} + \mathbf{v_m}^{(n-\frac{1}{2})}}{2} \times \mathbf{B_m}^{(n)}\right], \tag{1.64}$$

$$\mathbf{x_m}^{n+1} = \mathbf{x_m}^{n} + \Delta t\frac{\mathbf{v_m}^{n+\frac{1}{2}}}{\gamma_\mathbf{m}} \tag{1.65}$$

The charge and current density projection onto the grid is then performed using the charge-conserving algorithm proposed by Esirkepov (Villasenor and Buneman, 1992; Esirkepov, 2001). The current densities along the dimensions of the grid are computed from the charge flux through the cell borders while the current densities along the other dimensions are performed using a simple projection. The total charge and current densities account for the contributions of all CPs of all species to the given node.

The current density is known at time-step $n+\frac{1}{2}$, the electromagnetic fields can be advanced by solving the Maxwell's equations. The Maxwell-Ampère equation is firstly solved, giving the advanced electric fields

$$\mathbf{E}^{(n+1)} = \mathbf{E}^{(n)} + \Delta t\left[(\nabla\times\mathbf{B})^{(n+\frac{1}{2})} - \mathbf{J}^{(n+\frac{1}{2})}\right], \tag{1.66}$$

followed by the Maxwell-Faraday equation leading to the advanced magnetic fields

$$\mathbf{B}^{(n+\frac{3}{2})} = \mathbf{E}^{(n+\frac{1}{2})} - \Delta t(\nabla\times\mathbf{E})^{(n+1)}. \tag{1.67}$$

The two codes use a current calculating scheme which solves the additional equation $\partial\rho/\partial t = \nabla\cdot \mathrm{J}$ to calculate the current at each timestep. Doing so the total charge is conserved on the grid. This means that the error in the solution of the Poisson's equation is conserved, so if the Poisson's equation is satisfied for $t = 0$ it remains satisfied for all times, and the two previous equations are sufficient to get a complete description of the new electromagnetic fields. This strategy have the expense of a non-perfect energy conservation. However, the error in the energy conservation for all simulations performed in this thesis was always negligible. Futhermore, other approaches which force energy conservation imply the non-exact local charge conservation. The latter can lead to the appearance of non-physical effects, due to the local deviation from the Gauss law.

The PIC loop is represented in Figure 1.3, where the simulation run with a time-step of $\Delta t$.

### Boundary conditions

After having computed the CPs positions and velocities, boundary conditions are applied to each CP that has reached the limits of the spatial grid and may be located outside of the box. Each species may have different conditions for each boundary of the simulation box. Boundary conditions in EPOCH are split into three types: The Simple field, the Laser and outflow, and the Particle boundaries. The six edge of a 3D simulation box ($z_{min}$, $z_{max}$, $y_{min}$, $y_{max}$, $x_{min}$, $x_{max}$) can have different properties. These boundaries can be combined in different ways. We only present here the boundary conditions for the fields and the particles since no laser have been used in our PIC simulations.

The EPOCH code includes four Simple field boundary conditions.

1. Open boundary: EM waves outflowing characteristics propagate through the boundary.
2. Periodic boundary: Fields reaching one edge of the domain are wrapped round to the opposite boundary.
3. Conduct boundary: This applies perfectly conducting boundary conditions to the field.
4. Reflecting boundary: The normal electric field field component is set to zero.

The EPOCH code includes four different particle boundary conditions.

1. Open boundary: Particles pass through the boundary and are destroyed (the total of CP number

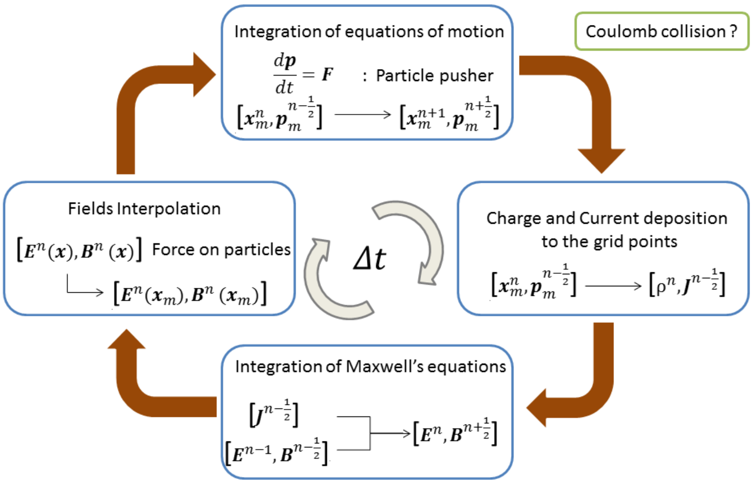

Figure 1.3 – Scheme of a Particle-In-Cell loop to advance from time-step $(n)$ to time-step $(n+1)$.

is not conserved in this mode).
2. Periodic boundary: Particles loop around the box, particles which leave one side of the box reappear on the other side.
3. Reflecting boundary: Particles reflect off the boundary as if it was a hard boundary (momentum and position follow specular reflection rules).
4. Thermal boundary: When a particle leaves the simulation it is replaced with an incoming particle sampled from a Maxwellian distribution with a temperature corresponding to that of the initial conditions. This boundary condition simulates a “thermal bath” of particles in the domain adjacent to the boundary.

The code PICLS has a more limited choice for boundary conditions, it possesses nevertheless, reflecting, periodic and thermal boundary conditions.

#### Parallelization strategies

The practicability of the PIC method for real world simulations is often limited by the huge size of some physical systems and a large number of computational particles needed for obtaining accurate simulation results. Thus, the parallelization of the PIC codes becomes necessary to permit solution of such problems in a reasonable time. Today's supercomputers often consists of clusters of Symmetric multiprocessing (SMP) nodes. Both OpenMP (Open Multi-Processing) and MPI (Message Passing Interface) are programming paradigms that can be used for parallelization of codes for such architectures. MPI is designed for distributed memory and is probably the best known paradigm in parallel computing. Communication between processes is done explicitly, and a relatively large set of functions can be used opening up for high performance and tweaking which is not available in OpenMP. And even though MPI is designed for distributed memory systems, it runs just as good on shared memory systems.

Most part of the PIC codes (specially with 2D and 3D versions) would split the spatial grid into N domains, where N is the number of cores. Each core would manage its own domain on a separate memory space, and information is communicated between cores using the MPI protocol. EPOCH and PICLS are massively parallel codes written using standard MPI and using a Cartesian domain decomposition for parallelism.

One of the major limiting factors in the scalability of PIC codes is load balancing. Due to the synchronisation of the currents required for the update of the electrodynamics fields the entire code runs at the speed of the slowest process. Since most of the time in the main EPOCH cycle is taken by the particle pusher, this equates to the process with the highest number of particles being the slowest. Since the location of particles is dependent upon the solution of the problem under consideration, in general the code can not have exactly the same number of particles on each core. The load balancer is used to move the inter-core boundaries so that the number of particles is as close on each core as possible. The code PICLS do not have any load balancing, however the latter is more needed for laser plasma interaction where the density gradient can become incredibly large. All the studies in this thesis are about plasma-plasma interaction which did not require load balancing.

### Limitations

The numerical ressources on supercomputers is the biggest limitation to take into account in PIC simulations. The time step and the grid size must be well chosen in PIC simulations, so that the time and length scales of the phenomena of interest are properly resolved.

The spatial step must satisfy the condition $\Delta x < \iota\lambda_{\mathrm{DE}}$, where $\iota$ is the numerical factor that depends on the order weighting of the fields to the grid points. If the condition is not satisfied, aliasing with the grid will lead to plasma heating. The heating will stop when the condition is fulfilled. This condition can be generalized as $v_{th}\Delta t << \Delta x$, thus the particles should not move more than one grid cell within $\Delta t$, which implies that the particle information should be accurately represented on the grid. This condition leads to the CFL criterion discussed previously, stating that the propagation of electromagnetic waves must fulfill the condition $c\Delta t < \Delta x$. These numerical heating mechanisms alter the phase space and can hide physical processes leading to incorrect interpretation of computational results.

Some other limitations need to be taken into account. The number of particles per cell should follow the Poisson statistics. For a number of $\mathrm{N}_c$ the relative fluctuations are $1/\sqrt{\mathrm{N}_c}$. These fluctuations can result in particle-wave collisions, speed up parametric instabilities, change of dispersive properties, and decrease the signal-to-noise ratio.

A last limitation of PIC codes can also be the amount of data and the memory needed on the clusters. The diagnostics are written in a very different way and can use several options, depending of which PIC code is used. For this reason we will not discuss how these diagnostics are written, nor how they are analysed.

# Chapter 2

# Instabilities competition and numerical limitations on PIC simulations of collisionless shock formation

Plasmas are usually created in a state far from thermodynamic equilibrium. Although particle collisions may lead to thermodynamic equilibrium, unstable transitions between plasma instabilities may develop at time scales that are generally shorter than typical collision times. Such instabilities can be studied by using non-collisional plasma models as it has been discussed in Chapter 1. Plasma instabilities are introduced in a cold plasma approximation in the first section of this Chapter. The second section is dedicated to our study on the numerical limitations of PIC simulation in a system where instabilities compete (Moreno et al., 2018d).

## 2.1 Description of instabilities leading to shock formation

The reserves of free energy which create instabilities are of a great diversity and depend on the mode of creation of the plasma and its confinement. In this section, electrostatic and electromagnetic instabilities are discussed in a framework of a a cold, non-magnetized ($\mathrm{B}^{(0)} = 0$) plasma.

### 2.1.1 Susceptibility in the cold plasma approximation

The cold plasma approximation assumes a negligible thermal particle motion so that the momentum distribution is a Dirac function $f_s(\mathbf{p})^{(0)} = \delta(p_x - p_{jx})\delta(p_y - p_{jy})\delta(p_z - p_{jz})$. For the stability analysis, we consider a response of the system in a form of a harmonic perturbations $\propto \exp(i\mathbf{k}.\mathbf{r} - \omega t)$ as described in Chapter 1. The susceptibility tensor $\chi_s$ using the cold distribution function can be written as (see eq. (1.55))

$$\chi_s = -\frac{\omega_{ps}^2}{\omega^2}\int d\mathbf{p}\left[\left(\partial_{\mathbf{p}} \otimes \frac{\mathbf{p}}{\gamma}\right) + \partial_{\mathbf{p}} \cdot \frac{\mathbf{k}}{\omega - \mathbf{k}\cdot\mathbf{v}}\left(\mathbf{v} \otimes \frac{\mathbf{p}}{\gamma}\right)\right].\delta(p_x - p_{jx})\delta(p_y - p_{jy})\delta(p_z - p_{jz}) \tag{2.1}$$

where we used the property of the Dirac distribution function

$$\int dx \psi(x)\delta'(x) = -\int dx \psi'(x)\delta(x) \tag{2.2}$$

The term in the bracket of equation (2.1) can be rewritten as a matrix

$$\chi_s = -\frac{\omega_{ps}^2}{\omega^2}\int d\mathbf{p}\,\frac{1}{\gamma}\begin{pmatrix} \chi_s^{xx} & \chi_s^{xy} & \chi_s^{xz} \\ \chi_s^{yx} & \chi_s^{yy} & \chi_s^{yz} \\ \chi_s^{zx} & \chi_s^{zy} & \chi_s^{zz} \end{pmatrix}\delta(p_x - p_{jx})\delta(p_y - p_{jy})\delta(p_z - p_{jz}), \tag{2.3}$$

with

$$\chi_s^{ij} = \delta_{ij} + \frac{1}{\gamma m\omega - \mathbf{k}\cdot\mathbf{p}}\left[k_i p_j + k_j p_i - \omega\frac{p_i p_j}{\gamma m c^2}\right] - \frac{1}{(\gamma m\omega - \mathbf{k}\cdot\mathbf{p})^2}\mathbf{k}\cdot\left(\frac{\mathbf{p}}{\gamma m c^2}\omega - \mathbf{k}\right) p_i p_j, \tag{2.4}$$

where $\delta_{ij}$ is the Kronecker delta, which can also be written as

$$\chi_s^{ij} = \delta_{ij} + \frac{1}{\gamma m\omega - \mathbf{k}\cdot\mathbf{p}}[k_i p_j + k_j p_i] - \frac{\omega^2 - \mathbf{k}^2 c^2}{(\gamma m\omega - \mathbf{k}\cdot\mathbf{p})^2}\frac{p_i p_j}{c^2} \tag{2.5}$$

This expression of the susceptibility will be used for all the calculations of the dispersion relations in this chapter.

### 2.1.2 Electrostatic instabilities

Free energy can be stored in a relative motion of particle species. In a uniform plasma, such a motion can be created either by injecting particles or by applying an external electric field. Instabilities can be described in one dimensional geometry assuming the waves are propagating along the direction of the particle motion, $\{k_y, k_z\} = 0$.
For the velocity directed along the x-axis, $f_s(\mathbf{p})^{(0)} = \delta(p_x - p_{s0})\delta(p_y)\delta(p_z)$, equation (2.3) can be written as,

$$\chi_s = -\frac{\omega_{ps}^2}{\omega^2}\frac{1}{\gamma}\begin{pmatrix} \frac{\omega^2}{(\gamma\omega - k_x p_x/m)^2} & 0 & 0 \\ 0 & 0 & 0 \\ 0 & 0 & 0 \end{pmatrix}. \tag{2.6}$$

#### Two-stream instability (TSI)

We consider here two groups of plasma electrons which are moving with a relative velocity v. This configuration leads to the well known Two-stream instability which has been discovered with the first observations of plasma oscillations (Bohm and Gross, 1949), and which is also related to two-beam amplifiers / oscillators (Haeff, 1948). Let one electron beam of a density $n_b$ and speed $v_b$ is coming from the left and another beam of a density $n_e$ and velocity $v_e$ is coming from the right. The density ratio between the two beams is $\alpha = \frac{n_b}{n_e}$, and we assume the current neutrality $n_e v_e + n_b v_b = 0$. We consider the case where the instability is driven by drifting electrons in the presence of motionless neutralizing ions.

The two-stream dispersion relation can be written in a compact form as

$$\mathrm{D}(\omega, k_x) = \omega^2 \epsilon_{\mathrm{TSI}} = 0, \tag{2.7}$$

where the dielectric tensor of the two-stream instability from eq. (1.54) is equal to

$$\epsilon_{\mathrm{TSI}} = 1 - \underbrace{\frac{\alpha}{\gamma_b^3(\Omega - \mathrm{Z})^2}}_{\text{beam current: 1}} - \underbrace{\frac{1}{\gamma_e^3(\Omega + \alpha\mathrm{Z})^2}}_{\text{beam current 2}} = 0, \tag{2.8}$$

where we define the normalized variables

$$\mathrm{Z} = \frac{k_x v_b}{\omega_{pe}}, \quad \alpha = \frac{n_b}{n_e}, \quad \Omega = \frac{\omega}{\omega_{pe}}. \tag{2.9}$$

This dispersion relation leads to an equation of degree 4 which can be solved analytically using the Ferrari method described in Appendix in order to find the growth rate of the instability (called $\delta$). To find the domain of the real values of $k_x$ where (2.7) gives complex solutions, we write the dispersion equation in the form

$$\mathrm{H}(\Omega) \equiv 1 = \frac{\alpha}{\gamma_b^3(\Omega - \mathrm{Z})^2} + \frac{1}{\gamma_e^3(\Omega + \alpha\mathrm{Z})^2}. \tag{2.10}$$

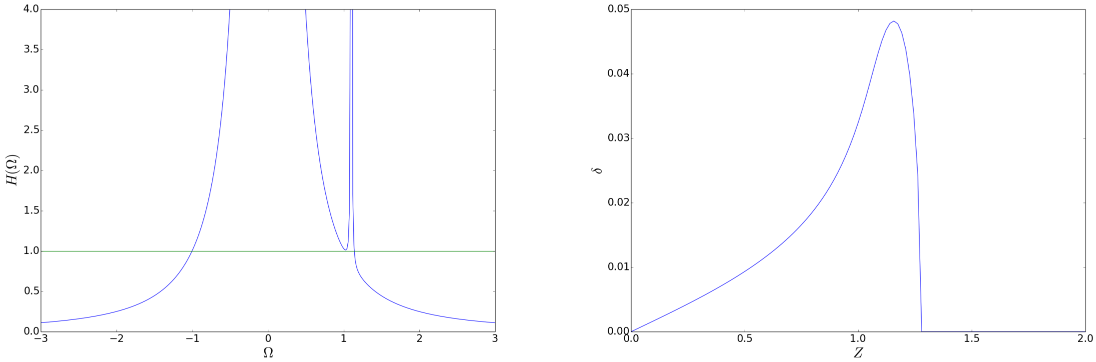

Figure 2.1 – Dispersion relation $H(\Omega_r)$ of two-stream instability for $Z = 1.1$ (left) and its $\delta(Z)$ for a Lorentz factor $\gamma_b = 2$, $\gamma_e \simeq 1$ and $\alpha = 0.003$ (right)

The dispersion relation at $Z = 1.1$ as well as the growth rate are represented in Figure 2.1 for $\gamma_b = 2$ and $\alpha = 0.003$.

Figure 2.1 left panel shows the graphic solution of equation (2.10). Two crossing points are the real high-frequency solutions of the dispersion relation. These are two of the four solutions of the dispersion relation. The remaining solutions are conjugate-complex and correspond to low-frequency imaginary crossings at frequency $\Omega < Z = 1.1$ and $\Omega > -\alpha Z = 0.0033$. One of these solutions is unstable. In the limit $\alpha << 1$ the maximum of the growth rate of the two-stream instability $\delta_{max}$ can be found for $d\delta/dZ = 0$.
At the wavenumber $Z \sim 1$,

$$\delta_{max} \sim \frac{\sqrt{3}}{2^{4/3}} \frac{\alpha^{1/3}}{\gamma_b} \omega_{pe}. \tag{2.11}$$

The nonlinear evolution of the two-stream instability was simulated on computer (Lampe and Sprangle, 1975). At the linear stage the instability is non-resonant, the energy of electric field grows exponentially taking energy from the beam kinetic energy, the beam electrons exhibit large amplitude oscillations in the phase space. After approximately 10 to 15 inverse of instability growth rates, some electrons are slowed down to zero velocity and trapped in the potential well of the growing electric field. This process is discussed at the end of this section. Trapping mixes the beam and plasma electrons towards a single peak velocity distribution function around the origin. At the same time, the energy of the electric field is saturated and a new quasi stationary state is reached.

### Buneman instability

Another physical situation where plasma becomes unstable is where the electrons are in relative motion with respect to the ions. This can occur if an electron beam neutralized by ions, or in a plasma subjected to a constant electric field. The first of these situations has been studied by (Pierce, 1948) in application to the electron beam amplifiers and by (Belyaev and Budker, 1956) for electron accelerators, while the second case has been studied in detail by Buneman (Buneman, 1958).

The equilibrium is characterized by electrons having a uniform density $n_e$ and a drift velocity $v_e$, and ions of density $n_i$ and charge $eZ_i$; the densities fulfill the condition of neutrality of charge $n_e = Z_i n_i$. The dynamics of electrons and ions have to be taken into account. The dispersion equation follows directly from eq. (2.6) (considering motionless ions)

$$D(\Omega, Z) = 1 - \underbrace{\frac{1}{R\Omega^2}}_{\text{Ion contribution}} - \underbrace{\frac{1}{\gamma_e^3(\Omega - Z)^2}}_{\text{Electron contribution}} = 0, \tag{2.12}$$

where $R = m_i/m_e$ is the mass ratio between ion and electron and in this subsection only $Z = k_x v_e/\omega_{pe}$. Because the ion plasma frequency is much smaller than the electron plasma frequency the dominating term is the electron term. The dispersion relation leads to an equation of degree 4, and so the Ferrari method can be used again to find the growth rate of the Buneman instability. We write again the dispersion equation in the following form

$$H(\Omega) \equiv 1 = \frac{1}{R\Omega^2} + \frac{1}{\gamma_e^3(\Omega - Z)^2}. \tag{2.13}$$

The dispersion relation (2.13) at $Z = 1.1$ as well as the growth rate are represented in by Figure 2.2 for $v_e = 0.0026$ ($\gamma_e \simeq 1$) and $m_i = 1836 m_e$. As the dispersion function of the two-stream instability, this function has two poles and between it has a minimum, whose position is found by calculating $dH(\Omega)/d\Omega = 0$,

$$\Omega_{Bun} = \frac{Z}{1 + R^{1/3}} \tag{2.14}$$

Inserting this value into $H(\Omega)$ and requiring that the minimum of $H(\Omega_{Bun}) > 1$, the condition for instability is found to be

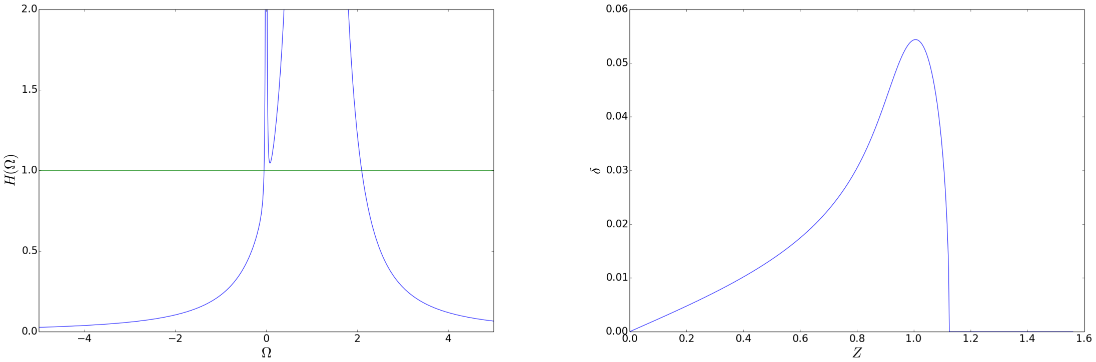

Figure 2.2 – Dispersion relation $H(\Omega_r)$ of the Buneman instability for $Z = 1.1$ (left) and its $\delta(Z)$ for a beam velocity $v_e = 0.0026$ and $m_i = 1836 m_e$ (right)

$$|Z| < (1 + R^{-1/3})^{3/2}, \tag{2.15}$$

The maximum of the Buneman instability growth rate is found at $Z \sim 1$, and is equal to

$$\delta_{max} \sim \frac{\sqrt{3}}{2^{4/3}} R^{-1/3} \omega_{pe}, \tag{2.16}$$

and for larger speeds the growth rate decreases. The Buneman-unstable long-wavelength modes have low frequencies and the corresponding low electron speeds excite low-frequency waves.

Computer simulations have shown, (Ishihara et al., 1981), that after two to three inverse of the Buneman instability growth rates, the instability is saturated due to the electron trapping as discussed in the end this section. The trapping thermalizes electrons and saturates the instability, which then establishes intense ion oscillations whose frequency is close to $\omega_{pi}$. Consequently, the electron directed kinetic energy is transferred into electron thermal motion.

Analysis of the Buneman instability with accounting for the electron thermal motion shows that the instability develops if the electron drift velocity is larger than the electron thermal velocity $v_e >> v_{Te}$. If the electron drift velocity is smaller than the thermal velocity but larger than the ion thermal velocity, the plasma is unstable against the ion-acoustic instability. This instability cannot be treated using a cold approximation, and the dirac distribution is not enough to describe it. The ion-acoustic instability origin is explained by the fact that the equilibrium distribution function of electrons with respect to the cold ions, exhibits a positive slope where resonance between waves and particles can occur. The drifting electrons have a hot shifted Maxwellian velocity distribution as eq. (1.7) while the ions are cold and motionless. In one dimension, the dielectric tensor (1.54) has been obtained by (Fried and Gould, 1961). The ion-acoustic instability occurs when the electron temperature exceeds the ion temperature, $\mathrm{T}_e >> \mathrm{T}_i$ , the wavelength is much larger than the Debye length, $k^2\lambda_{\mathrm{DE}}^2 << 1$, and the current drift velocities, $v_e > \omega/k \simeq c_s$, exceed the ion sound speed. The latter is a characteristic speed of dispersionless waves in plasmas with low frequency oscillations which we will describe later. Under these conditions the growth rate found by (Fried and Gould, 1961) takes the following form

$$\delta \sim k c_s \frac{\pi \mathrm{Z}_i m_e}{8 m_i}\left(\frac{v_e}{c_s} - 1\right) \tag{2.17}$$

The ion-acoustic instability grows until the nonlinear saturation takes place. Coupling of a growing ion acoustic wave to ions creates a wing in the high energy range in the ion distribution function. The latter giving rise to a strong ionic Landau damping which stops the growth of the wave (Baumjohann and Treumann, 1997).

### 2.1.3 Electromagnetic Weibel instability

In addition to electrostatic instabilities, electromagnetic instabilities may also develop in an unmagnetized plasma if specific conditions are satisfied. Electromagnetic modes can also become unstable in a plasma where there are fluxes of charged particles. These electromagnetic modes which contain electric and magnetic fields, cannot, be reduced to a problem with one dimension, in a direction which would be that of all the fields. One must then use the complete system of Maxwell's equations to describe the evolution of the fields. An unstable electromagnetic mode which can grow was introduced by (Weibel, 1959). A Weibel instability requires an anisotropy in the distribution function. This anisotropy can be produced by the temperature, or by the drifting particles velocities (also referred to as current-filamentation instability). We consider in this section the case where the instability is driven by drifting electrons in the presence of immobile neutralizing ions. The waves are excited in this case in the oblique direction in the plane x,y with respect to the direction of electron motion $x$. We consider here two electron streams of equal density moving with velocities $+v_0$ and $-v_0$ with respect to ions: $1/2 f_s(\mathbf{p})^{(0)} = \delta(|p_x| - p_{s0})\delta(p_y)\delta(p_z)$. Equation (2.3) can be written as

$$\chi_s = -\frac{\omega_{ps}^2}{\omega^2}\frac{1}{\gamma}\frac{1}{(\gamma m\omega - \mathbf{k}\cdot\mathbf{p})^2}\begin{pmatrix} m^2\omega^2 + k_y^2 p_{s0}^2 & (\gamma m\omega - \mathbf{k}\cdot\mathbf{p})k_y p_{s0} & 0 \\ (\gamma m\omega - \mathbf{k}\cdot\mathbf{p})k_y p_{s0} & (\gamma m\omega - \mathbf{k}\cdot\mathbf{p})^2 & 0 \\ 0 & 0 & 0 \end{pmatrix}. \tag{2.18}$$

We consider two electron populations of density $n_e/2$ and velocity $v_0$. The dispersion relation can be written in a compact form as

$$\mathrm{D}(\omega,\mathbf{k}) = det\left[\omega^2\epsilon_{wei} + \mathbf{k}\otimes\mathbf{k}c^2 - \mathbf{k}^2c^2\right] = 0, \tag{2.19}$$

where the dielectric tensor of the Weibel instability from eq. (1.54) is equal to

$$\epsilon_{wei} = 1 - \frac{\omega_{pe}^2}{2\omega^2}\frac{1}{\gamma}\begin{pmatrix} \frac{m^2\omega^2 + k_y^2 p_{s0}^2}{(\gamma m\omega - k_x p_{s0})^2} + \frac{m^2\omega^2 + k_y^2 p_{s0}^2}{(\gamma m\omega + k_x p_{s0})^2} & \frac{m k_y p_{s0}}{(\gamma m\omega - k_x p_{s0})} - \frac{m k_y p_{s0}}{(\gamma m\omega + k_x p_{s0})} \\ \frac{m k_y p_{s0}}{(\gamma m\omega - k_x p_{s0})} - \frac{m k_y p_{s0}}{(\gamma m\omega + k_x p_{s0})} & 2 \end{pmatrix} \tag{2.20}$$

The dispersion relation can be written as

$$\begin{aligned}\mathrm{D}(\omega,\mathbf{k}) = &\left[\omega^2 - \frac{\omega_{pe}^2}{2\gamma}\left(\frac{m^2\omega^2 + k_y^2 p_{s0}^2}{(\gamma m\omega - k_x p_{s0})^2} + \frac{m^2\omega^2 + k_y^2 p_{s0}^2}{(\gamma m\omega + k_x p_{s0})^2}\right) - k_y^2 c^2\right]\left(\omega^2 - \frac{\omega_{pe}^2}{\gamma} - k_x^2 c^2\right) \\ &- \left[k_x k_y c^2 - \frac{\omega_{pe}^2}{2\gamma}\left(\frac{k_y p_{s0}}{(\gamma m\omega - k_x p_{s0})} - \frac{k_y p_{s0}}{(\gamma m\omega + k_x p_{s0})}\right)\right]^2 = 0,\end{aligned} \tag{2.21}$$

which can also take the simple form

$$D(\omega,\mathbf{k}) = \left[\omega^2 - \frac{\omega_{pe}^2(\omega^2+\gamma^2 k_y^2 v_0^2)}{\gamma^3}\left(\frac{\omega^2+k_x^2 v_0^2}{(\omega^2-k_x^2 v_0^2)^2}\right) - k_y^2 c^2\right]\left(\omega^2 - \frac{\omega_{pe}^2}{\gamma} - k_x^2 c^2\right) - \left[k_x k_y c^2 - \frac{\omega_{pe}^2}{\gamma}\left(\frac{k_x k_y v_0^2}{\omega^2 - k_x^2 v_0^2}\right)\right]^2 = 0, \tag{2.22}$$

After other simplifications the distribution function can take the form of an equation of degree 6.

$$a\omega^6 + b\omega^4 + c\omega^2 + d = 0 \tag{2.23}$$

where the different coefficients are as follows

$$\begin{aligned}
a &= 1\\
b &= -\left(2k_x^2.v_0^2 + (k_x^2+k_y^2)c^2 + \left(\frac{1+\gamma^2}{\gamma^3}\right)\omega_{pe}^2\right)\\
c &= \left(\frac{\omega_{pe}^4}{\gamma^4} + (k_x^2.v_0^2)^2 + 2k_x^2.v_0^2(k_x^2+k_y^2)c^2 + \frac{\omega_{pe}^2}{\gamma}\left(\frac{k_y^2 c^2}{\gamma^2} + 2k_x^2.v_0^2 + \frac{k_x^2 c^2}{\gamma^4}\right)\right)\\
d &= -\left((k_x^2.v_0^2)^2(k_x^2+k_y^2)c^2 + \frac{\omega_{pe}^2}{\gamma}\left(-\frac{k_y^2 k_x^2.v_0^2 c^2}{\gamma^2} + (k_x^2.v_0^2)^2\left(\frac{\gamma^2-2}{\gamma^2-1}\right)\right) - \left(\frac{\omega_{pe}}{\gamma}\right)^2\left(\frac{k_x^2 v_0^2}{\gamma^2} + k_y^2.v_0^2\right)\right)
\end{aligned} \tag{2.24}$$

This equation can be solved by the Cardan method shown in Appendix.
The solution of the system can be presented in a trigonometric form

$$\omega = \sqrt{2\rho\cos\theta - \frac{b}{3}} \tag{2.25}$$

with

$$\rho = \sqrt{g^2+f^2} \qquad \theta = \frac{\arctan\left(\frac{f}{g}\right) + \pi(if \quad g<0)}{3} + k\frac{2\pi}{3} \qquad k \in [0,2] \tag{2.26}$$

and

$$p = c - \frac{b^2}{3} \qquad q = b\left(\frac{2b^2}{27} - \frac{c}{3}\right) + d \qquad f = -\frac{q}{2} \qquad g = \sqrt{\left(\frac{q}{2}\right)^2 + \left(\frac{p}{3}\right)^3} \tag{2.27}$$

The growth rate for every possible wave number is pictured in figure 2.3 for two flow velocities, $v_0 = 0.2$ and $0.99$. In the non-relativistic regime $v_0 = 0.2$, the dominant mode is oblique, with a strong influence of the two-stream instability, while in the relativistic regime (0.99) the current filamentation instability dominates.

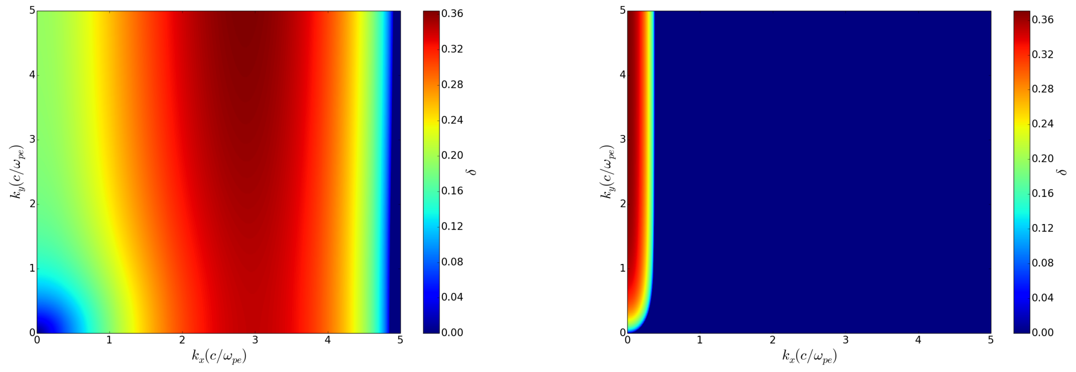

Figure 2.3 – Growth rate of the Weibel instability for a drift velocity of $v_0 = 0.2c$ (left) and $v_0 = 0.99c$ (right)

The Weibel filamentation instability has been demonstrated to be crucial for collisionless shock formation in astrophysical plasmas and will be discussed further in this thesis. The instability transfers energy from the particles to the magnetic field and tends to isotropize the particle distribution function.

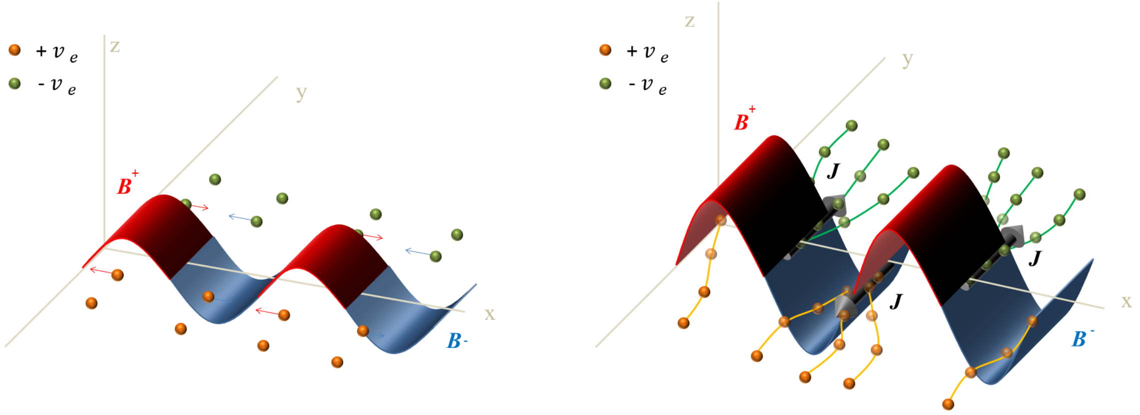

Figure 2.4 – Sketch of the center reaction mechanism in the Weibel instability. Left panel shows the magnetic field perturbation acting on the particles via the Lorentz force, and the right panel show the current formation and magnetic field pertubation amplification.

Let us now analyze the physical origin of instability and its crucial link to the Lorentz force $e\mathbf{v}_0 \times \mathbf{B}$. Consider for this purpose the two beams in equilibrium flowing in the opposite direction and suppose that there exists as indicated in figure 2.4 a magnetic disturbance $\mathbf{B}^{(1)}$ (due for example to the background noise) with magnetic field $\mathrm{B}_1$ directed perpendicularly to the plane x,y defined by the electron velocity (x) and the wave vector (y). The electrons get deflected by the Lorentz force, since the fluctuations of the magnetic field are perpendicular to their initial velocity. The electrons concentrate in spatially separed current filaments. The latter are amplifying the initial magnetic field perturbation. It is this mechanism of positive feedback that leads to instability.

The growth of instability, continues until the Lorentz force starts to decrease the average velocity of the particles. These particles are then trapped into vortices along the direction of magnetic perturbation. The magnetic field saturates and a quasi static state is reached, where approximately half of the initial kinetic energy of the beams is transferred to thermal energy along the direction of perturbation. This non-linear evolution of the electron Weibel instability has been simulated using computers by (Davidson et al., 1972).

Analytic work has also been performed for saturation of the Weibel instability. The simplest approach is based on a perturbation expansion, in the framework of quasi-linear theory (Pokhotelov and Amariutei, 2011). It describes the evolution of the average distribution function of electrons in the field of many incoherent waves, usefull to deal with the different problems of weakly turbulent wave-particle interactions in a plasma.

### 2.1.4 Particle trapping

The wave kinetic instabilities described in the previous subsections are based on the linearised Vlasov equation. Such linearisations are justified for disturbances of a small amplitude, the limitations of this linear theory can be understood only by considering, the nonlinear effects neglected so far.

In an electrostatic wave of a finite amplitude, the wave-particle resonant interaction reveals the non-linear phenomenon of trapping. This phenomenon can be understood considering the one-dimensinal motion of one electron in an electrostatic wave. The momentum equations of the particle in the wave frame of reference ($x' = x - v_{ph}t$ and $v' = v - v_{ph}$, $v_{ph}$ the phase speed) can be written as

$$\frac{dv}{dt} = \frac{e}{m_e} \mathrm{E}_0 \sin(kx) \tag{2.28}$$

considering an initial position $x_0$ and velocity $v_0$. The energy conservation can be calculated from the integration of eq. (2.28) which gives

$$\frac{1}{2} m_e v^2 + \frac{e}{k} \mathrm{E}_0 \cos(kx) = \frac{1}{2} m_e v_0^2 + \frac{e}{k} \mathrm{E}_0 \cos(kx_0) \tag{2.29}$$

It describes a particle motion in a potential well. The particle trajectory depends of the ratio between the potential energy of the wave and its kinetic energy, $2e\mathrm{E}_0/kmv_0^2$. If this ratio is smaller than 1, the particle is free, on the contrary the particle is trapped if the potential energy of the wave exceeds the particle kinetic energy as represented in figure 2.5. In the first case the velocity of the particle does not change very much and the oscillation frequency is large $\omega_b \simeq kv_0$, and in the second case, the particle has a finite trajectory and oscillates close to the minimum of the potential at the trapping frequency (or bounce frequency)

$$\omega_b \simeq \sqrt{\frac{ek\mathrm{E}_0}{m_e}}. \tag{2.30}$$

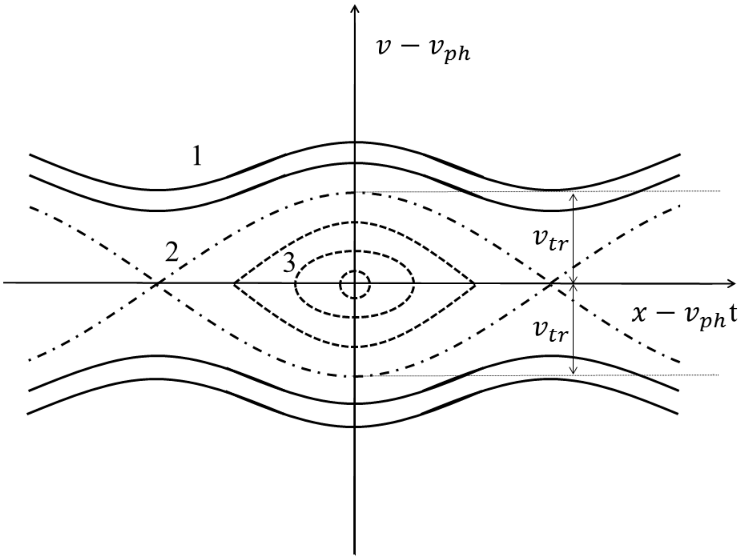

Figure 2.5 – Sketch of the phase space trajectories of particles in the wave frame of reference. 1: Untrapped Orbits ($v_0 > v_{tr}$), 2: Separatrix, 3: Trapped Orbits ($v_0 < v_{tr}$), where $v_{tr} = \sqrt{2e\mathrm{E}_0/km_e}$ defines the trapping velocity

The larger the wave field amplitude, the faster the trapped resonant electrons oscillate in the field.

Considering a non-linear resolution of the Vlasov-Poisson equations for a single wave in a maxwellian plasma, the Landau damping may be important. The latter is a phenomenon introduced by (Landau, 1946) which prevents an instability from developing, and creates a region of stability in the parameter space. It dominates for large wave numbers and prevents the existence of plasma waves with the wavelengths shorter than the Debye length. Its growth rate can be expressed as

$$\omega_{\mathrm{LD}} = \frac{\pi\omega_{pe}^2}{k(\partial\epsilon/\partial\omega)} \frac{\partial f(v)}{\partial v}. \tag{2.31}$$

For trapping to be important, $\omega_b >> \omega_{\mathrm{LD}}$, the perturbation wave number should be in the range of weak Landau damping then many particles can be trapped in the growing wave. In the opposite case, $\omega_b << \omega_{\mathrm{LD}}$, the wave is Landau damped, during a time comparable to $\tau_b = (2\pi/\omega_b)$, the number of trapped particles could be small.

The trapping mechanism can be neglected as long as the trapping frequency is much smaller than the Landau damping growth rate or the growth rate of the instability. However, in the case where an unstable wave has a growth rate exceeding the Landau damping the particle trapping is an efficient non linear saturation mechanism.

The different linear and nonlinear evolutions of the instabilities presented in this section are of crucial interest for collisionless shock formation and their analytic complexity constrains us, to support the analytic description, to perform kinetic simulations (PIC or Vlasov simulations).

## 2.2 Numerical limitations of PIC simulation in a system where instabilities compete

As shown in the previous section a charge- and current neutral collisionless plasma, which is composed of two counterstreaming electron beams and ions at rest, can be unstable. Such systems are frequently found in space- and astrophysical plasmas as well as in laboratory plasmas. They develop if a fast electron beam enters an initially unperturbed plasma at rest (Lovelace and Sudan, 1971; Thode and Sudan, 1975). The net current carried by the electron beam drives electromagnetic fields, which accelerate the electrons of the background plasma into the opposite direction. The return current of the latter eventually balances that of the beam, which restores the plasma's current-neutrality.

Several instabilities can develop after the current-neutrality has been reestablished. The two-stream instability, competes with one of two possible electrostatic instabilities if we constrain the wave vector to the direction along which the beams are drifting. It competes with the Buneman instability if the drift speed between the background electrons and the ions exceeds significantly the thermal speed of both species. The Buneman instability originally refers to the instability of one electron beam with one ion beam with the same charge density (Buneman, 1958). Here we use the term Buneman instability to denote an instability between an electron beam and an ion beam that have a similar charge density and a drift speed that fulfills the aforementioned condition. The Buneman instability does not grow if the background electrons are so hot that their thermal velocity spread exceeds by far their drift velocity relative to the ions. The two-stream instability competes in this case with the ion acoustic instability between both species of the background plasma (Baumjohann and Treumann, 1997). If the direction of the wave vector is not constrained to be parallel to the beam velocity vector then the counterstreaming electron beams can drive the magnetic filamentation instability (Califano et al., 1998) or the quasi-electric oblique mode. Instabilities driven by relativistic electron beams are reviewed in Ref. (Bret et al., 2010).

Beam instabilities have been widely examined in the past both experimentally and theoretically. Many of these studies were performed with particle-in-cell (PIC) simulations. The substantial computational cost of the PIC simulations implies that in some cases the development of instabilities has to be accelerated by choosing a reduced ion mass. The reduction of ion mass increases the exponential growth rate of instabilities where the ions are involved; it is the Buneman-type instability in the aforementioned case. The ion mass does, however, not affect the instabilities that develop by the counterstreaming electron beams.

A reduction of the mass of ions in PIC simulations not only speeds up the instability, it also alters the spectrum of the growing waves. The effects of a reduced ion mass on the exponential growth rate of beam instabilities have been studied systematically in Ref. (Bret and Dieckmann, 2010). It turns out that in some cases even a moderate reduction of the ion mass can have profound effects on the spectrum of the unstable waves. The process, by which the plasma is thermalized, depends in turn on the instability that saturates first. A reduction of the ion mass can, thus, alter the final state of the plasma with potentially far-reaching consequences. A plasma saturation by the filamentation instability results, for example, in strong magnetic fields (Kazimura et al., 1998; Honda et al., 2000; Silva et al., 2003; Sakai et al., 2004; Jaroschek et al., 2005; Nishikawa et al., 2009; Bret et al., 2013), while the other instabilities drive primarily electric fields (Thode and Sudan, 1973; Dieckmann et al., 2000a). The Buneman-type instability driven by a relative motion of ions and electrons may heat ions , while the two-stream instability driven by counterstreaming electron beams heats first the beam electrons and possibly the bulk electrons. It is unclear how the saturation of one instability affects an other. Systematic studies are needed in order to better understand the consequences of using reduced mass ratios not only during the linear growth phase of the instabilities but also after their nonlinear saturation.

Here we test some of the results obtained in Ref. (Bret and Dieckmann, 2010) with PIC simulations, which allow us to explore non-linear effects introduced by the reduced ion mass. We limit ourselves to the mildly relativistic electron speeds, which are representative for solar energetic electrons (Muschietti, 1990; Kontar, 2001; Klein et al., 2005; Reid and Kontar, 2010; Reid and Ratcliffe, 2014) and for electrons that have been heated by the ablation of a solid target by a high power laser pulse (Tabak et al., 1994). Numerical artifacts, which are caused by a reduced ion-to-electron mass ratio, become stronger with an increasing relativistic factor of the beam speed (Bret and Dieckmann, 2010). Some of our results are thus also relevant for numerical studies of interactions between plasma and energetic electron beams, which are generated by the wakefield of a laser (Esarey et al., 2009; Warwick et al., 2017). A related study involving ultrarelativistic pair beams can be found in Ref. (Sironi and Giannios, 2014). Our parametric study is conducted in one spatial dimension and we align the beam velocity vector with the simulation direction, which suppresses the oblique mode instability and the filamentation instability. The results provided by such simulations are realistic if one electron beam is dilute and the second dense and if the beam speeds are not too high (Thode and Sudan, 1973; Tzoufras et al., 2006).

### 2.2.1 Analytic representation of the system

#### Linear Theory

We consider a system composed of a relativistic electron beam with the density $n_b$, the reduced velocity $\beta_b = v_b/c$ and the Lorentz factor $\gamma_b = \frac{1}{\sqrt{1-\beta_b^2}}$. The beam crosses a spatially uniform plasma with the densities $n_i$ and $n_e$ of ions and electrons and $n_i = n_e + n_b$. The drift velocity $v_e$ of the bulk electrons is such that it cancels out the beam current with $n_b v_b + n_e v_e = 0$. The thermal speed of a species $q$ with the mass $m_q$ and temperature $\mathrm{T}_q$ is $v_{\mathrm{T}q} = (k_{\mathrm{B}}\mathrm{T}_q/m_q)^{1/2}$. Time is normalized by $\omega_{pe}^{-1}$, space by $c\omega_{pe}^{-1}$ and frequencies by $\omega_{pe}$.

For the stability analysis, we consider the response of the system to a harmonic perturbations $\propto exp(i\mathbf{k}.\mathbf{r} - i\omega t)$. We reduce the system to one spatial dimension (x direction), we align the simulation direction with the beam drift velocity and define the normalized variables introduced in the previous section

$$\mathrm{R} = \frac{m_i}{m_e}, \quad \mathrm{Z} = \frac{k_x v_b}{\omega_{pe}}, \quad \alpha = \frac{n_b}{n_e}, \quad \Omega = \frac{\omega}{\omega_{pe}}. \tag{2.32}$$

We assume that the thermal speeds of both electron species are small compared to $v_b$ and that the thermal speeds of the bulk ions and electrons are small compared to $v_e$. The dispersion equation $\mathrm{D_L}(\mathrm{Z},\Omega)$ for this cold plasma is found using the cold approximation of the susceptibility from eq. (2.5), which can also be found for example, in Ref. (Bret and Dieckmann, 2010). Its Eigenmodes fulfill the dispersion relation $\mathrm{D_L}(\mathrm{Z},\Omega) = 0$ or

$$\mathrm{D_L}(\mathrm{Z},\Omega) = 1 - \underbrace{\frac{1+\alpha}{\mathrm{R}\Omega^2}}_{\text{Ion contribution}} - \underbrace{\frac{\alpha}{\gamma_b^3(\Omega-\mathrm{Z})^2}}_{\text{beam contribution}} - \underbrace{\frac{1}{\gamma_e^3(\Omega+\alpha\mathrm{Z})^2}}_{\text{return current}} = 0. \tag{2.33}$$

This dispersion relation can be written as

$$\omega^6 + 2Z(\alpha-1)\omega^5 + \left[Z^2(1+\alpha^2-4\alpha) - \frac{1+\alpha}{R} - \frac{\alpha}{\gamma_b^3} - \frac{1}{\gamma_e^3}\right]\omega^4 + \left[2\alpha(1-\alpha)Z^4 + \frac{2Z}{R}(1-\alpha^2) - \frac{2Z\alpha^2}{\gamma_b^3} + \frac{2Z}{\gamma_e^3}\right]\omega^3$$
$$+\left[\alpha^2 Z^4 - \frac{Z^2}{R}(\alpha^3-3\alpha^2-3\alpha+1) - \frac{Z^2\alpha^3}{\gamma_b^3} - \frac{Z^2}{\gamma_e^3}\right]\omega^2 - \frac{2Z^3}{R}\alpha(1-\alpha^2)\omega - \frac{Z^4}{R}\alpha^2(1-\alpha^2) = 0, \tag{2.34}$$

this an equation of degree 6 cannot be solved by an analytic method. We used the numerical tool, “Maple“, to find the complex solutions of equation (2.34).

Figure 2.6 shows the exponential growth rate $\delta \equiv Im(\Omega)$ of the instability, which is obtained from the numerical solution of equation (2.33), as a function of R for $\gamma_b = 2$, $\gamma_e \simeq 1$ and for the values $\alpha = 0.3, 0.03$ and $0.003$.

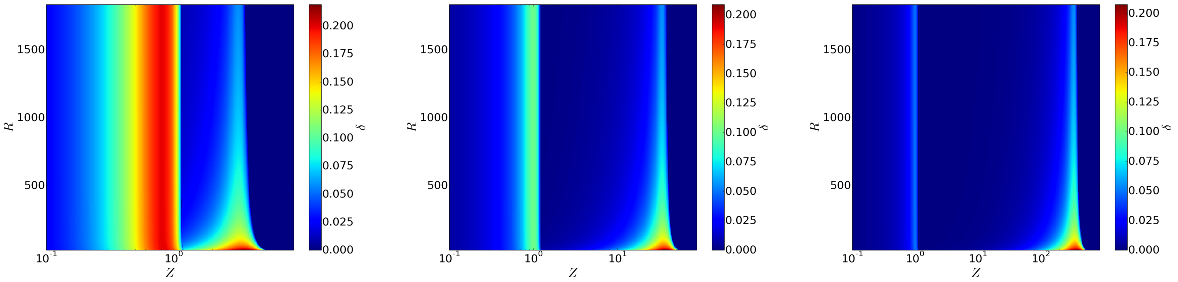

Figure 2.6 – Exponential growth rates $\delta(Z,R)$ obtained from the solution of the linear dispersion relation eq. (2.33) for $\gamma_b = 2$, $\gamma_e \simeq 1$. The growth rates for $\alpha = 0.3, 0.03$ and $0.003$ are shown in panel (a), panel (b), and panel (c) respectively.

This instability is the superposition of the electron two-stream instability and the Buneman instability introduced in the previous section. The first one at low Z is driven by the electrons of the beam and the electronic return current. The second one arises from the interaction of the electronic return current with the ions. In the limit $\alpha << 1$ the two-stream instability has its maximum growth rate $\delta$ at the wavenumber $Z \sim 1$, with $\delta \sim \frac{\sqrt{3}}{2^{4/3}}\frac{\alpha^{1/3}}{\gamma_b}$, and the unstable Buneman instability at the wavenumber $Z \sim 1/\alpha$, with $\delta \sim \frac{\sqrt{3}}{2^{4/3}} R^{-1/3}$, as shown in the previous section.

For dense beams, the growth rate of the two-stream instability is the largest regardless of R. However, when $\alpha$ and R are both small, the growth rate of the Buneman instability exceeds that of the two-stream instability. Table 2.1 lists the maximum of the growth rate $\delta$, localized at $Z \sim 330$, for $\alpha = 0.003$ and for three different values of R. Figure 2.6 demonstrates that the choice of R affects most strongly the beam with $\alpha = 0.003$ and we focus on this case.

| | ion mass R (in $m_e$) | 1836 | 400 | 25 |
|---|---|---|---|---|
| $\alpha = 0.3$ | maximum of $\delta$ | 0.20 | 0.20 | 0.22 |
| $\alpha = 0.03$ | maximum of $\delta$ | 0.10 | 0.10 | 0.21 |
| $\alpha = 0.003$ | maximum of $\delta$ | 0.058 | 0.089 | 0.207 |

Table 2.1 – The growth rate of the Buneman instability for three different values of R and for $\alpha$.

### 2.2.2 Numerical simulations

#### The initial conditions

The particle-in-cell (PIC) code used for the simulations in this chapter is EPOCH (Arber et al., 2015). We resolve one spatial dimension and the three velocity components of the CP's (1D3V).

The simulation domain is resolved with $N_x = 9 \times 10^4$ cells. The density of the dilute electron beam is $n_b = 0.003\, n_i$ and its Lorentz factor $\gamma_b = 2$. The density of the background electrons is $n_e = 0.997 n_i$ and their mean velocity $\beta_e = 0.0026$. The length of the box is $L_x = 31.4$ and its spatial resolution is $\Delta x = 3.5 \times 10^{-4}$. Periodic boundary conditions for the electromagnetic fields and for the CPs are used. The maximum resolved wave number $Z^{max}$ and its resolution $\Delta Z$ are respectively $Z^{max} = \beta_e \frac{\pi}{\Delta x} = 7800$ and $\Delta Z = \beta_e \frac{2\pi}{L_x} = 0.17$. The electrons and the ions have Maxwellian velocity distributions. We vary the ion mass and the temperatures of all species in a range where all beams are practically cold, so to respect the assumptions underlying Eq. 2.33. The temperature of the electron beam is $T_b = 10$eV, which gives the thermal speed $v_{Tb} \approx 5 \times 10^{-3} v_b$. The temperature of the bulk electrons is $T_e = 0.1$eV, which gives $v_{Te} \approx 0.2 v_e$. The Debye length $\lambda_{De} = v_{Te}\omega_{pe}^{-1}$ is $\lambda_{De} = 1.25\Delta x$. We represent the ions by 250 particles per cell (ppc), the bulk electrons by 200 ppc and the beam electrons by 50 ppc.

#### The linear wave growth and its saturation

We compare the range of unstable wave numbers obtained from the solution of equation 2.33 (see Fig.2.6) with the PIC simulations and determine the saturation time as a function of R. We analyze the electric field component $E_x(x,t)$, which grows in response to the two-stream instability and Buneman instability, by performing a Fourier transform over space

$$E_x(j\Delta Z, t) = N_x^{-1} \sum_{p=1}^{N_x} E_x(p\Delta x, t) e^{-jp\Delta x \Delta Z}. \tag{2.35}$$

Figure 2.7 shows the power spectra $P_x(Z,t) = |E_x(Z,t)|^2$ for the values R = 1836, 400 and 25. The wave numbers $Z_{Bun} \sim 333$ and $Z_{TSI} \sim 1$, where the growth rates of the Buneman instability and the two-stream instability reach their maxima according to equation 2.33, coincide with the values where the instabilities grow in Fig.2.7. The instabilities start to grow after about $t \approx 15$. This delay can be attributed to the time required by the thermal noise that seeds the instabilities to grow and to the need to establish a coherent wave along the beam direction.

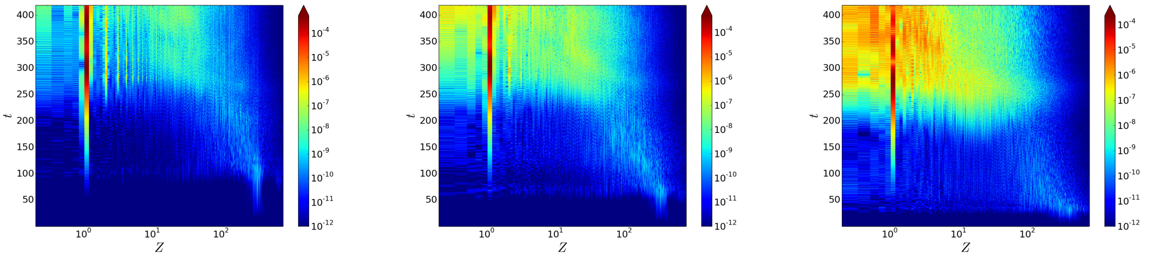

Figure 2.7 – The power spectrum $P_x(Z,t)$ of the electric field component $E_x$ normalized to $m_e^2 c^2 \omega_{pe}^2 / e^2$: panel (a) corresponds to R = 1836, panel (b) to R = 400 and (c) to R = 25. The color scale is 10-logarithmic.

Figure 2.7 shows that both instabilities grow and saturate independently. For this low value of $\alpha$ the growth rate of the Buneman instability is comparable to that of the two-stream instability if R = 1836 and larger for smaller R. Indeed the Buneman mode at $Z \approx Z_{Bun}$ reaches about the same power as the two-stream mode at $Z \approx Z_{TSI}$ at $t \approx 100$ in Fig.2.7(a) while it outgrows the two-stream modes in the cases R = 400 and R = 25.

The field power at $Z \approx Z_{TSI}$ evolves similarly in all three simulations on the displayed time interval; the evolution of this instability is unaffected by the value of R during its linear growth phase. We observe several harmonics of the wave at $Z \approx Z_{TSI}$ for R = 1836 and one for R = 400. Only a broad wave continuum is observed for R = 25. The peak power of the low-Z mode and the number of observed harmonics increases with R, which shows that the wave can sustain a sine shape for a larger amplitude and for a longer time.

The waves driven by the Buneman instability are not stable. Once the wave power at $Z_{Bun}$ has peaked the interval, in which the wave power is concentrated, it is shifted in time to lower values of Z. The waves driven by the Buneman instability are amplified after $t \approx 250$ for all R due to their coupling to the two-stream mode. This coupling is responsible for the onset of the broadband electrostatic wave activity, which is particularly strong for the cases R = 400 and R = 25.

In what follows we test if the dependence of the exponential growth rate of the Buneman instability on R is the only reason for its faster saturation with decreasing R. The exponential growth rate of the Buneman instability is $\delta \sim \frac{\sqrt{3}}{2^{4/3}} R^{-1/3}$. According to this growth rate the wave amplitude reach a given amplitude after a time $t \propto R^{1/3}$, provided that the seed electric field for the instability does not depend on R. We have performed a parametric study of the saturation time of the Buneman instability as a function of R in order to determine its scaling with the ion mass. The saturation time of the Buneman instability fulfills $t_{sat} - 15 \propto \sqrt{R}$ as shown in Figure 2.8. The subtracted time 15 corresponds approximately to the delay of the wave growth observed in Fig.2.7. The scaling of the saturation time $\propto \sqrt{R}$ does not match the scaling $t \propto R^{1/3}$ of the time it takes the Buneman wave to reach a given amplitude. The Buneman instability reaches its nonlinear regime much faster for a low value of R than for a large one.

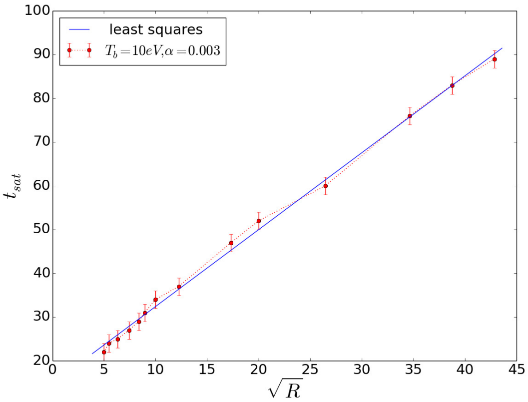

Figure 2.8 – Scaling of the saturation time with R. The temperature of the electron beam is $T_b$ = 10eV and the temperature of the bulk electrons is $T_e$ = 0.1eV.

### Non-linear saturation and energy transfer

We explore in this section how the value for R affects the energy exchange between the three plasma species and the electric field. We integrate for this purpose the energy density of the electric field's $E_x$ component and the energy densities of the individual particle species over the entire simulation box. Particle energies are measured in their own reference frame, where the total momentum is zero at $t = 0$, the simulation frame is the ion reference frame. All energies are normalized to the total energy.

Figure 2.9 shows the time evolution of energies of all species for the three mass ratios 1836, 400 and 25. The electric field energy grows exponentially at early times and saturates at $t \approx 90$ in Fig.2.9(a), at $t = 50$ in Fig.2.9(b) and at $t \approx 25$ in Fig.2.9(c). The faster rise of the field energy at low R reflects the larger growth rate of the Buneman instability. The field energies at the time the Buneman instability saturates are the same in all simulations, which suggests that the saturation is caused by the interaction between the wave and electrons. This in confirmed by Fig.2.9. The energy the ions gain when the Buneman instability saturates does increase with decreasing R

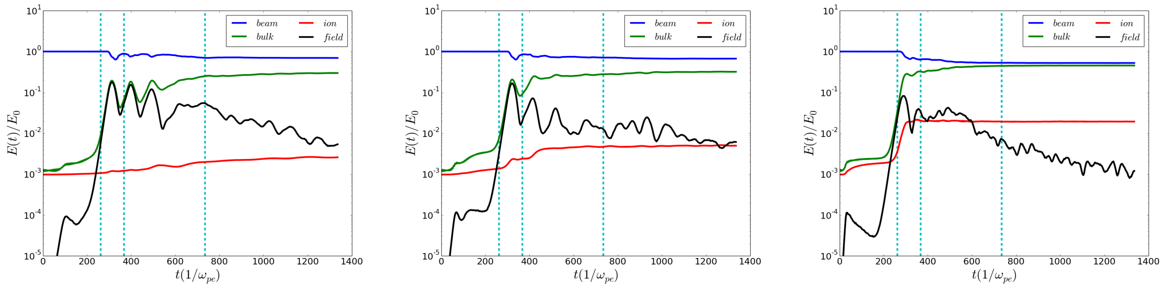

Figure 2.9 – Panel (a) shows the particle and field energies for a mass ratio R = 1836, panel (b) for a mass ratio 400 and panel (c) for the mass ratio 25. The temperature of the electron beam is $T_b = 10eV$ and the temperature of the bulk electrons is $T_e = 0.1eV$, the dashed lines correspond to the times $t = 262$, 367 and 734.

but it remains small compared to the energy gain of the bulk electrons. According to Fig.2.8 the Buneman instability saturates earlier than expected for low R, which suggests an involvement of the ions in the saturation, while Fig.2.9 demonstrates that the instability saturates due to the wave interaction with the electrons. Both observations are compatible if R affects the phase speed of the electrostatic wave relative to the electrons. A decrease of the phase speed in the rest frame of the electrons with R implies that the latter can react more easily to the wave.

The energies of the electric field, the ions and the bulk electrons all increase in Fig.2.9 when the Buneman instability saturates. Energy conservation implies that the saturation of the Buneman instability must have extracted energy from the beam electrons. The electric field energy decreases after the saturation of the Buneman instability and this energy decrease depends on R.

The electric field energy rises again after $t = 200$. Its growth rate is the same in all three simulations as expected for the two-stream instability. The electric field energy saturates at $t \approx 300$ and reaches a peak value that is about 20% of the beam electron energy for R = 1836 and 400. The two-stream instability saturates earlier and at a lower peak value for R = 25. The phase speed of the wave, which is driven by the two-stream instability, does not depend on R. This wave enforces a stronger reaction of ions for a low value of R. We have observed this stronger reaction already in Fig.2.7(c), which revealed a lower peak power of the electric field and strong broadband that set in when the wave saturated. Figure 2.9 also shows that the bulk electron energy closely follows that of the electric field until its saturation, after which the energies of electrons and ions evolve differently in all simulations.

The energies of the electric field and of the bulk electrons oscillate in phase three times for R = 1836. The beam electron energy oscillates in an opposite phase. The ion energy hardly reacts to these oscillations for R = 1836. The ions with R = 400 are accelerated by the electric field, which damps the energy oscillations of the electrons and the electric field. A reduction of the ion mass to R = 25 boosts their response to the electric field and increases damping of oscillations of energies of the electrons and the electric field. The energies of the bulk electrons and of the beam electrons converge in all simulations and they become almost equal for R = 25. However, the mean energy per electron is still much larger for the beam particles since $\alpha \ll 1$. At the end of simulations, the ion energy in the case of R = 25 exceeds that in the case of R = 1836 by an order of magnitude.

The simulations, which provided the data shown in Fig.2.8, were followed over a longer time in order to determine the efficiency of the energy transfer from the electron beam to the bulk electrons as a function of R. Figure 2.10 shows the results. The bulk electrons gain between 25% and 30% of the total energy after the two-stream instability's saturation if R > 100. The energy increases from 30% to almost 50% for decreasing values R < 100. A reduction of R thus enhances the transfer of energy from the electron beam to the bulk electrons. This effect is, however, only observed if the electron beam is cold. Increasing the temperature of the electron beam from 10 eV to 5 keV suppresses the rise of the final energy of the bulk electrons at low values of R.

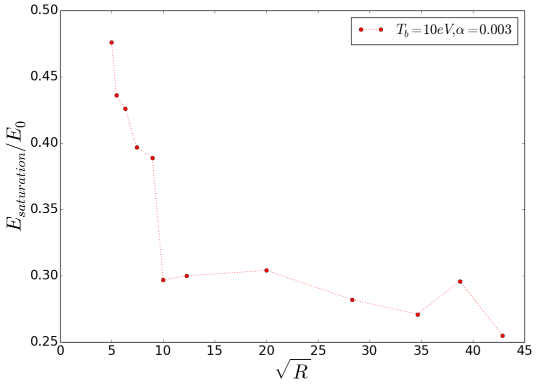

Figure 2.10 – The saturation energy of the bulk electrons at $t = 1250$ in units of the total energy for $\alpha = 0.003$ and for the temperature $T_b = 10$eV for the electron beam. The temperature of the bulk electrons is $T_e = 0.1$eV

### Phase space density distributions

We compare in this section the phase space density distributions of the particle species at the times $t = 262$, 367 and 734, which are marked by the vertical dashed lines in Fig.2.9.

**- Simulation for an electron to ion mass ratio** R = 1836

Figure 2.11 shows the distributions for the run with R = 1836. The dilute electron beam drives a Langmuir wave with a positive phase speed $\omega/k$ slightly below the beam speed. This velocity mismatch is caused by the non-zero thermal velocity of the electron beam. This wave is still growing at the time $t = 262$. Its phase is most easily determined from the phase space density distribution of the bulk electrons in Fig.2.11(d), which shows sinusoidal oscillations of the mean speed with $x$. The bulk velocity is zero at $x \approx 0.3$ and $x \approx 5.7$ and the electrostatic potential must thus have an extremum at these positions. The surrounding electrons are attracted towards these points and the potential is thus positive. The beam electrons in Fig.2.11(a) oscillate around the maxima of the positive potential and some are trapped by it. The different response of both electron species is caused by a phase speed of the wave, which is much larger in the reference frame of the bulk electrons than in that of the beam electrons.

The number density of the beam electrons at the cusps at $x = 2$ and $x = 7.4$ is large and their momentum $\beta\gamma \approx 1$ is below the initial beam momentum, which explains why the beam energy in Fig.2.9(a) has been reduced at this time. The distribution of the beam electrons is changing into the phase space vortices or phase space holes, which form when an electrostatic instability with a wave vector that is aligned with the beam velocity (Roberts and Berk, 1967; O'Neil et al., 1971) saturates. The ions oscillate in the wave's electric field at an amplitude that is small due to the large value of R.

The bulk electrons in Fig.2.11(d) show phase space structures surrounding the dense beam with the wave length $\simeq 3 \cdot 10^{-2}$. These are electron phase space holes that were driven by the Buneman instability. The time, during which such a phase space hole develops, is comparable to the bouncing frequency of a particle with the charge $q$ and mass $m$ in a wave potential $\omega_b = (qkE/m)^{1/2}$, where $k$E is the product of wavenumber and electric field amplitude (See Ref. (Dieckmann et al., 2000a) and references cited therein). Electron phase space holes form 5 times faster than ion phase space holes holes even for the lowest ion mass R = 25. Electron phase space holes are thus responsible for the initial saturation of the Buneman instability in all simulations, which explains why it always saturated at about the same electric field amplitude.

The electron phase space holes have been driven by the interaction of the charge density distribution of the ion beam with the Langmuir wave, which oscillates at the plasma frequency of the bulk electrons. Their propagation speed in the rest frame of the bulk electrons is close to that of

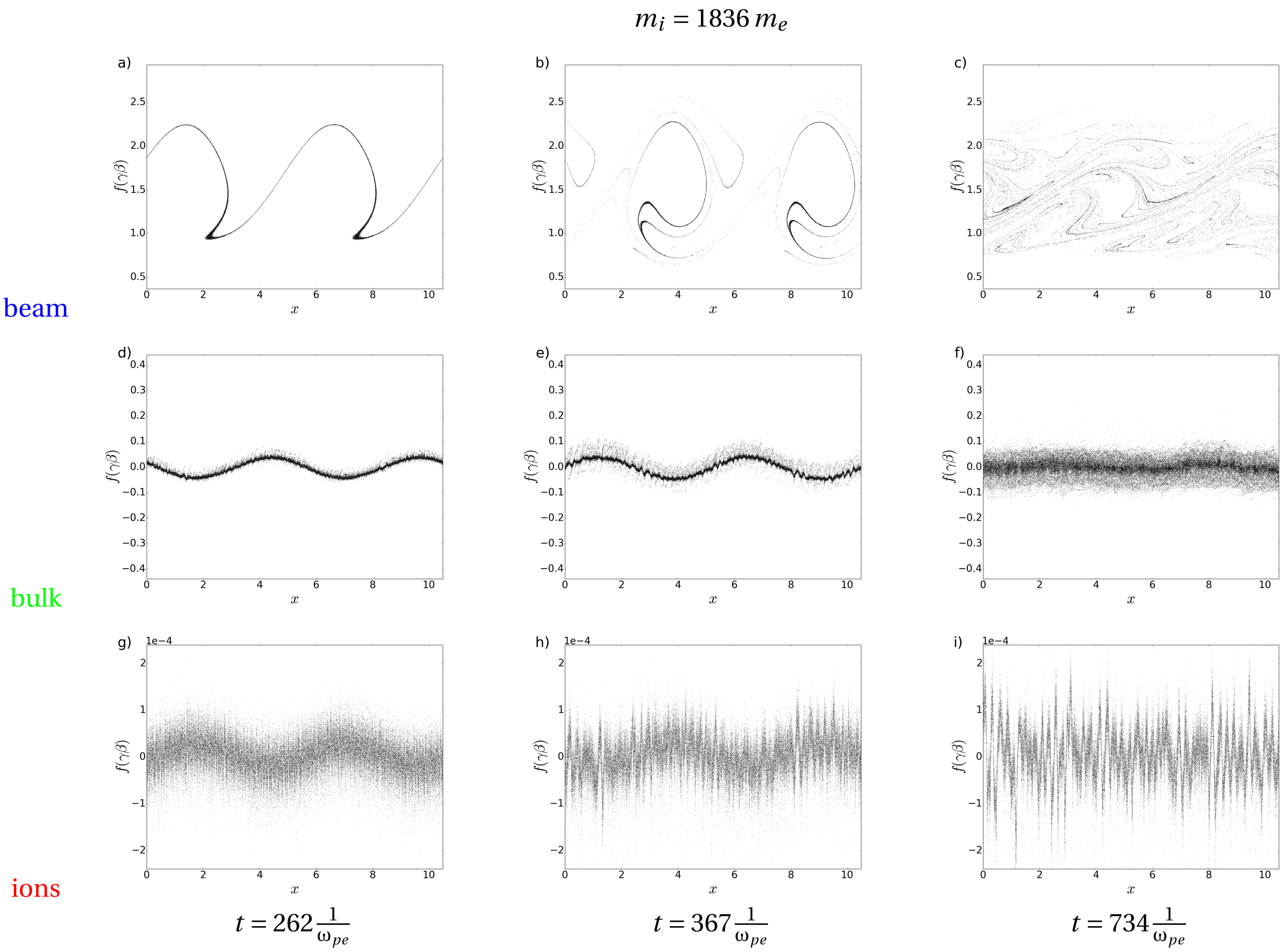

Figure 2.11 – The particle phase space density distributions. The first row shows the distribution of the beam electrons, the second row that of the bulk electrons and the bottow row that of the ions. The first column shows the distributions at the time $t = 262$, the second at the time $t = 367$ and the third one at the time $t = 734$. The ion mass is $m_i = 1836 m_e$ and the initial temperatures of the beam and bulk electrons are $\mathrm{T}_b = 10\mathrm{eV}$ and $\mathrm{T}_e = 0.1\mathrm{eV}$.

the ions at least for large R. In its rest frame, an electron phase space hole is associated with an electrostatic potential that is almost static and it can thus easily accelerate the ions. The speed gain of the ions with R = 1836 remains small due to the short acceleration time and we observe only small oscillations of the ion velocity at small wavelengths in Fig.2.11(g).

The Langmuir wave, which grew in response to the two-stream instability, has propagated towards increasing x and both cusps in the electron beam distribution have rotated further at the time $t = 367$. The mean momentum of the cusp electrons in Fig.2.11(b) has increased compared to that in Fig.2.11(a), which explains why the beam energy in Fig.2.9(a) has increased. This cusp and the current, which is associated with its motion, are causing a periodic exchange of energy between the beam electrons on one hand and the bulk electrons and the electric field on the other hand. The beam distribution in Fig.2.11(b) reveals presence of multiple beams. The bouncing in the sinusoidal potential of the electrostatic wave disperses the electrons, and results in a reduction of the amplitude of the energy oscillations.

The electron phase space holes, which were driven by the Buneman instability, coalesce to larger ones (Roberts and Berk, 1967). The larger phase space holes in the bulk electrons in Fig.2.11(e) yield now noticable oscillations with the wave length $\simeq 0.1$ in the ion distribution displayed by Fig.2.11(h); the latter are ion acoustic waves. Ion acoustic waves are linearly undamped if the ratio between the electron temperature and ion temperature is large (Baumjohann and Treumann, 1997), which is the case in our simulation after the Buneman instability has saturated. We note, however, that the presence of the electron phase space holes means that the ion velocity oscillations may not be linear since electron phase space holes and large ion acoustic waves can couple (Hosseini-Jenab and Spanier, 2017).

Coalescence of the electron phase space holes explains why the characteristic wave number of the waves, which were generated by the Buneman instability, decreases in time in Fig.2.7.

The growth of the ion acoustic waves and of the amplitude of the velocity oscillations of the phase space holes in the bulk electrons indicates that the instability driven by both electron species is still active long after the Buneman instability saturated. The velocity oscillations of the bulk electrons caused by the two-stream instability have a wavelength that is large compared to that of the ion acoustic waves in Fig.2.11(h) and an amplitude that is larger than the electron thermal speed in Fig.2.11(e). The therefrom resulting drift between the bulk electrons and ions is large enough to destabilize the ion acoustic waves and heat the bulk electrons. This mechanism is equivalent to the oscillating two-stream instability (Gupta et al., 2004) if the laser-generated electrostatic beat wave were replaced by the two-stream mode.

The ion oscillations have increased their amplitude at $t = 734$ and the density of the hot component of the bulk electrons has increased. The long-wavelength oscillation of the bulk distributions has vanished, which implies that the beam-driven Langmuir wave has been damped out. The beam electrons have been dispersed and form now a turbulent distribution with a wide velocity spread in Fig.2.11(c). The velocity spread is comparable to the velocity width of the electron phase space holes at the earlier time, which is in turn determined by the trapping velocity interval $v_{tr} = (2q\mathrm{E}/mk)^{1/2}$ around the wave's phase velocity. The beam distribution is well-separated from the bulk electron distribution along the velocity direction.

**- Simulation for an electron to ion mass ratio** R = 25

Figure 2.12 shows the phase space density distributions obtained from the run with R = 25 at the same times as the ones discussed in Fig.2.11. The electron beam distribution in Fig.2.12(a) shows that a large phase space hole is about to form. Its shape is practically identical to that in the run with R = 1836, confirming that the two-stream instability is not affected by the value of R. The earlier development of the Buneman instability and the faster onset of the ion acceleration have perturbed the bulk plasma in Figs. 2.12(d,g) more significantly than that in Figs. 2.11(d,g). A comparison of Fig.2.12(h) with Fig.2.11(h) reveals a population of energetic ions for the case R = 25 that was not present in the simulation with R = 1836.

The waves driven by the Buneman instability and the electron phase space holes they drive

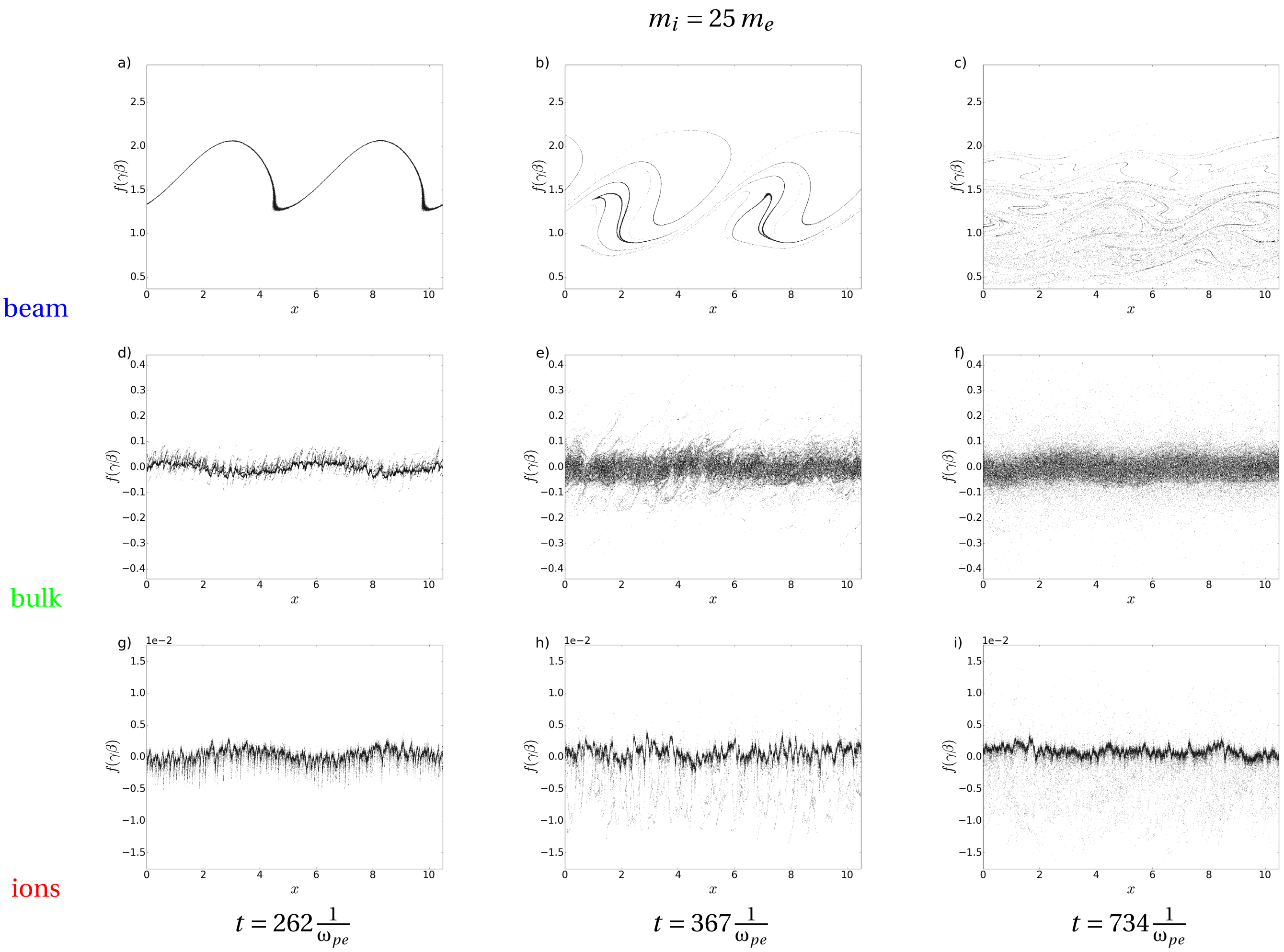

Figure 2.12 – The particle phase space density distributions. The first row shows the distribution of the beam electrons, the second row that of the bulk electrons and the bottow row that of the ions. The first column shows the distributions at the time $t = 262$, the second at the time $t = 367$ and the third one at the time $t = 734$. The ion mass is $m_i = 25m_e$ and the initial temperatures of the beam and bulk electrons are $\mathrm{T}_b = 10\mathrm{eV}$ and $\mathrm{T}_e = 0.1\mathrm{eV}$.

have a negative phase speed in the simulation frame. Ions, which are accelerated in the propagation direction of the electron phase space hole, stay in phase with its electric field for a longer time and are thus accelerated to a larger speed. The larger charge-to-mass ratio of ions with $\mathrm{R} = 25$ means that they could be accelerated to a larger speed than those with $\mathrm{R} = 1836$. The ions were accelerated at the expense of the electric field energy. The ion acceleration can explain the damping of the Buneman instability-driven waves between $t = 262$ and $t = 367$ in Fig.2.9(c).

The electric field, which is associated with the charge density oscillations of the bulk plasma, covers a broad range of wave numbers that extends even to $\mathrm{Z_{TSI}}$ (see Fig.2.7(c)). Both bulk distributions still show modulations with a long wavelength, which sustain the wave that grows in response to the two-stream instability. Figure 2.9(c) shows that the electric field energy decreases after $t = 262$, while the energies of the ions and the bulk electrons grow to values well above the ones in the simulations with $\mathrm{R} = 1836$ and 400. The growth of the energy of the bulk species slows down at $t = 367$ and the electric field energy remains high and constant until $t \approx 600$. Figure 2.12(b) shows that an electron phase space hole is still present in the electron beam distribution, but it does no longer have the quasi-circular shape as the one in Fig.2.11(b). Figures 2.12(e, h) demonstrate that the energy gain of both bulk plasma species is due to a temperature increase and not due to a spatial modulation of the mean speed as in the simulation with $\mathrm{R} = 1836$.

The temperature increase of the bulk plasma results in an increase of its thermal pressure. The increasing thermal pressure reduces the density modulation in response to the electric field of the wave. The reduced density modulation causes in turn a reduction of its electric field amplitude and of the spatial modulation of the mean velocity of the bulk electrons and ions. The electron phase space hole does no longer interact with the bulk plasma via the electrostatic wave and hence we do no longer observe oscillations due to a periodic energy exchange between the particles and the electric field.

The ion distribution in Fig.2.12(h) shows elongated tails that extend to a speed $-10^{-2}$. These tails form during the nonlinear evolution of the Buneman instability. Even though the density of these tails is low, they carry a significant momentum. The mean momentum of the ions has become negative, which is initially compensated for by a momentum increase of the bulk electrons. Electrons gain more speed when they exchange momentum with the ions and they drive a negative total current in the bulk plasma. On average, a positive electric field grows. Its effect can be seen from Fig.2.12(c). The electron beam distribution is as diffuse as that in Fig.2.11(c) and its velocity width is comparable. The mean velocity of the beam is, however, lower by a value 0.3 for all x. The lost kinetic energy is transferred to the bulk plasma. This process has been discussed previously in Ref. (Lovelace and Sudan, 1971).

### 2.2.3 Discussion

We have studied the interplay of the Buneman instability with the two-stream instability by solving the linear dispersion relation and by means of particle-in-cell simulations. The initial conditions for the instabilities were selected such that the Buneman instability would grow as fast as the two-stream instability for the ion-to-electron mass ratio of protons and faster for a reduced ion mass. This case study is a testbed for whether or not the plasma evolution is determined by the instability with the largest exponential growth rate. That criterion was used by Ref. (Bret and Dieckmann, 2010) to investigate the impact a reduced mass ratio has on the evolution of a relativistic electron beam that interacts with background electrons and ions.

Our results are as follows. Both instabilities grew independently and at the expected exponential growth rate during their initial growth phase. The wave, which was driven by the Buneman instability, saturated at an amplitude well below that of the two-stream instability. Variations of the exponential growth rate of the Buneman instability with the ion-to-electron mass R had no consequence for the plasma evolution because it always saturated first for the initial conditions we considered.

The criterion for the most important instability in a beam-plasma system used by Ref. (Bret et al., 2010) assumes that the instability saturates at a time, which is proportional to its inverse exponential growth rate. This time scales as $\propto R^{-1/3}$ for the Buneman instability. The electrostatic waves in our simulations started to grow only after a significant delay in time and the growth time, measured from the onset of the wave growth, scaled like $R^{-1/2}$. The discrepancy is large especially for low values of R.

Artifacts introduced by a reduced value for R are more pronounced during the non-linear evolution phase of the Buneman instability. The Buneman instability saturated for all R by trapping electrons from the bulk distribution. Merging of the electron phase space holes, which formed during the saturation of the instability, shifts the characteristic wave number of the electrostatic oscillations to lower wave numbers. Eventually they started to interact with the waves driven by the two-stream instability and electrostatic oscillations grew over a broad frequency band. The amplitudes of these oscillations relative to those of the two-stream mode increased with decreasing R.

The electrostatic wave, which is driven by the two-stream instability, ows to a larger amplitude when R is large and it is stable over a longer time. We observed for $R = 1836$ a periodic exchange of energy between the two-stream mode on one hand and the bulk plasma and the electric field on the other hand. These oscillations are caused by trapping of beam electrons. These oscillations are damped for $R = 400$ and asymptotically damped for $R = 25$. Decreasing R results in a faster and more pronounced energy loss of the beam electrons to the bulk electrons and ions. In particular the ion energy increased for $R = 25$.

A reduction of R below 100 results in a doubling of the energy loss of the beam electrons and in a drastic reduction of their mean speed. Simulations that address the propagation of relativistic, cold and dilute electron beams through a background plasma should thus keep a value of R close to the correct one.
We considered only wave vectors parallel to the beam velocity vector, which excluded the Weibel instability and the oblique modes as shown in Figure 2.13, that allowed us to perform the simulations at a reasonable computational cost.

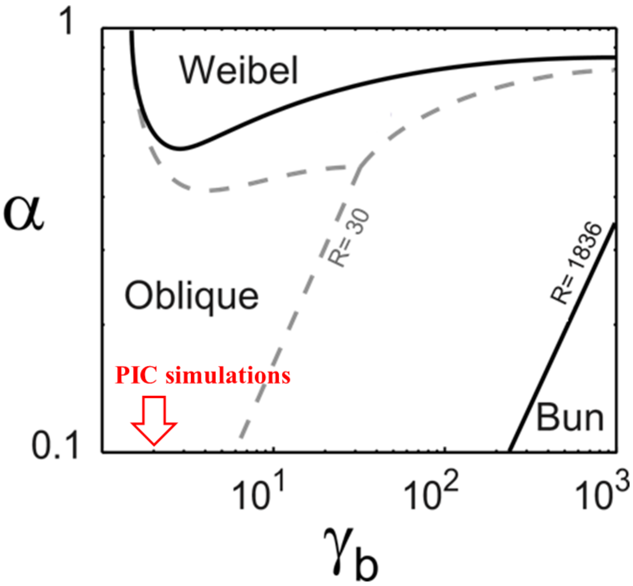

Figure 2.13 – 2D hierarchy map terms of $(\gamma_b, \alpha)$ adapted from (Bret and Dieckmann, 2010). Plain lines: $R = 1836$. Dashed lines: $R = 30$. The Weibel instability tends to govern the high density regime, the Buneman instability the ultrarelativistic one, and the oblique the rest of the phase space. The simulations presented above do not appear on this map, since they are at too low α, which confirm the non impact of the Weibel instability in 2D, but the presence of the oblique instability in the competitive game between instabilities.

We have considered the case of a mildly relativistic dilute electron beam, where the growth rates of electrostatic instabilities are comparable to or larger than those of the electromagnetic filamentation instability (Thode and Sudan, 1975). In the range of our parameters, the Weibel instability is excluded, but the oblique mode may compete with the Buneman/Two stream instability. Such beams are formed by the solar energetic electrons that propagate through the solar wind and one can also find such beams in laser-plasma experiments.

Collisionless shocks, as electrostatic or electromagnetic shocks, are mostly mediated by the instabilities discussed above. These shocks are created after the nonlinear saturation of the instabilities, as the ion acoustic instability for the case of electrostatic shocks, discussed in the next chapter. Furthermore, these instabilities can also accelerate particles, as an example, (Amano and Hoshino, 2009) showed that a fraction of electrons are reflected in the shock foot region by small-scale electrostatic waves generated by the Buneman instability. A too low numerical ion mass may overestimate the Buneman instability leading to a stronger efficiency of the acceleration process. It is thus important to consider the realistic ion mass to avoid any misrepresentation of the shock-related processes.

# Chapter 3

# Electrostatic collisionless shocks

Plasmas consist of electrically charged particles. Under normal conditions for maintaining overall charge neutrality, positively and negatively charged species are neutralizing locally.. In absence of drift velocities the plasma is free of electric currents and, in the absence of an external magnetic field $B_0$, the plasma is free of magnetic fields. In this case, an electrostatic shock can be created as a consequence of non-linear wave steepening and wave breaking of ion-acoustic modes. Such electrostatic shocks are rare in the heliosphere, because most moving plasmas there are magnetised. These shocks may, however, occur under certain very special conditions, even in strongly magnetised plasmas, in the auroral zones of magnetised planets and in the particle acceleration zones in the solar corona during particular flare events. In these cases, electrostatic shocks are strictly one-dimensional and occur on very small scales where they contribute to the generation of magnetic-field aligned electrostatic fields. These fields can promptly accelerate particles to energies of the order of the total macroscopic electrostatic potential drop.

Unmagnetized nonrelativistic shocks have been studied experimentally (Romagnani et al., 2008; Kuramitsu et al., 2011; Ahmed et al., 2013), analytically (Sagdeev, 1966; Bardotti and Segre, 1970; Raadu and Rasmussen, 1988) and numerically (Forslund and Shonk, 1970; Karimabadi et al., 1991; Kato and Takabe, 2010; Sarri et al., 2011). They are at least initially sustained by the density difference between the upstream plasma and the shock-compressed downstream plasma. Thermal diffusion lets more electrons move from the downstream plasma to the upstream one than vice versa and a space charge builds up. A dense plasma acquires a positive electric potential relative to the upstream one. The incoming upstream ions have to overcome this cross-shock potential and their kinetic energy is reduced, which has two consequences. Firstly, the density is increased downstream. Secondly, the plasma velocity is slower downstream. The shock crossing increases the ion velocity spread which heats up the ions. The electrostatic potential thus has a similar effect on the inward flowing ions as binary collisions in a hydrodynamic shock.

The ions, which could not overcome the shock potential, are reflected by the shock and propagate upstream. The shock-reflected ion beam transports energy upstream at a speed that exceeds that of the shock, which is a particularity of a collisionless medium. A shock reflected ion beam is thus a signature of a collisionless shock. Its interaction with the inflowing ions drives instabilities upstream of the shock, which ultimately destroy the narrow transition layer and replace it by a broad layer of electrostatic waves (Karimabadi et al., 1991). The lifetime of a collisionless electrostatic shock is thus limited. A sketch of the transition layer of an electrostatic shock is shown in figure 3.1.

The shock formation process is enhanced in plasmas with high mass and temperature ratios between the negatively and positively charged plasma components (Forslund and Shonk, 1970). Theoretical estimates are turbulent one-dimensional models and neglect the electromagnetic modes which are associated with the multi-dimensional features of the problem (Stockem et al., 2014).

Analytical models of electrostatic shocks rely on the electrostatic potential (cf. 3.1). This potential is described by the analytical approach proposed by Sagdeev (Sagdeev, 1966). He introduced a

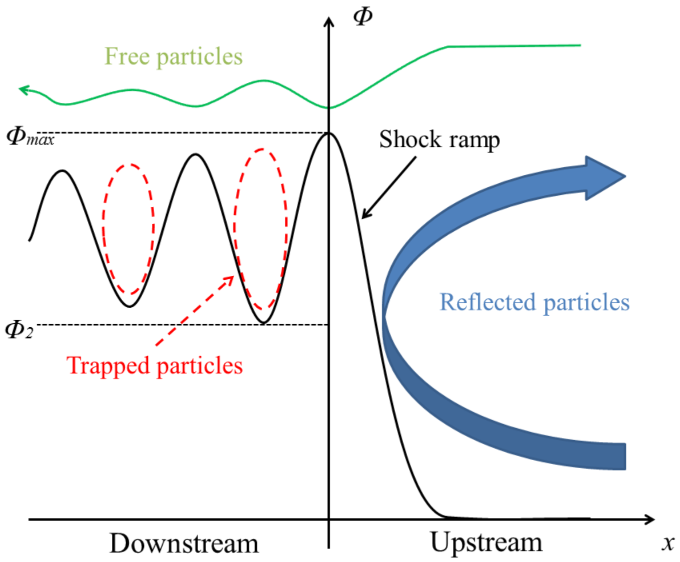

Figure 3.1 – Sketch of an electrostatic shock structure showing a monotonic increase of the potential from $\Phi = 0$ to $\Phi_{max}$ in the upstream region, and an oscillatory behavior with $\Phi_2 < \Phi \leq \Phi_{max}$ in the downstream region. Upstream particle are so reflected (blue) if their kinetic energy is lower than $\Phi_{max}$, passing in the opposite case (green). When the downstream particle's kinetic energy is smaller than $\Phi_2$, they are trapped and cannot reach the upstream (red). The value of $\Phi_2$ characterizes the dissipation of the directed kinetic energy of the upstream flow into thermal (pressure) energy in the downstream.

pseudo-potential permitting to find a certain class of nonlinear solutions of the Korteweg-de Vries equation, and to distinguish between solitary wave and shock. Different nonlinear problems in plasmas related to solitary waves can be treated using the Sagdeev pseudo-potential, but all these solutions are, dissipation free and are limited to relatively slow inward flows. Stronger shocks can be created if short wavelengths instabilities produce collisionless anomalous dissipation. Kinetic theory of microscopic interaction between waves and particles in plasmas far from thermal equilibrium are of particular importance to explain this anomalous dissipation.

A solitary wave, presents one of solutions of the Sagdeev potential in a system without dissipation. A simple treatment of the non-magnetized collisionless shock structure, taking into account finite ion temperature, is given in (Cairns et al., 2014), is briefly described in what follows.

Let us consider a collisionless shock illustrated in figure 3.1, where ions flow into a region, with an increasing potential from zero to some positive unknown value $\Phi_{max}$ . Incoming ions have a Maxwellian distribution, equation (1.7), with an average velocity $v_0$. A relation between the plasma density and the potential is $\Phi$ is given by the Boltzmann law

$$n_i(\Phi,\Phi_{max}) = \frac{1}{\sqrt{2\pi}}\int_0^{\infty} \exp\left[-\frac{(\sqrt{v^2+2\Phi}-v_0)}{2}\right]dv + \frac{1}{\sqrt{2\pi}}\int_0^{\sqrt{2(\Phi_{max}-\Phi)}} \exp\left[-\frac{(\sqrt{v^2+2\Phi}-v_0)}{2}\right]dv, \tag{3.1}$$

where the ion velocities is normalised to the thermal velocity $v_{thi} = \sqrt{k_B T_i/m_i}$, and the potential to $m_i V_i^2/Ze$. The electrons, are assumed to be in a thermal equilibrium state in the potential, and their flow produces a charge equilibrium far upstream, where the potential tends to zero

$$n_e(\Phi,\Phi_{max}) = Z n_i(\Phi,\Phi_{max}) \exp\left(\frac{\Phi T_i}{Z T_e}\right). \tag{3.2}$$

The Poisson's equation, using a scaling lengths of $v_i/\omega_{pi}$, with $\omega_{pi}$ the ion plasma fequency based on the density of the incoming flow at $\Phi = 0$, can be written as

$$\frac{d^2\Phi}{dx^2} = -\frac{\partial\Psi}{\partial\Phi}, \tag{3.3}$$

where the Sagdeev potential have been written as

$$\Psi = \int_0^{\Phi} \Big[ Zn_i(\Phi', \Phi_{max}) - n_e(\Phi', \Phi_{max}) \Big] d\Phi'. \tag{3.4}$$

The Sagdeev potential depends on the unknown quantity $\Phi_{max}$ which defines the range of parameters where a stable solution exists. In order, to verify the analytical estimates of $\Phi_{max}$, numerical simulations are needed. Simulations by (Cairns et al., 2014) demonstrated that an acceptable solution only exists if the electron temperature is sufficiently high, and the shock Mach number is sufficiently low. A choice of the electron-ion temperature ratio influences the Mach number, and that high ratios lead to larger Mach number and to a high percentage of reflected ions.

## 3.1 Parametric simulation study of the expansion of a dense plasma into an unmagnetized dilute plasma

Laser-matter interaction experiments and the associated numerical simulations are common today tools for studies of electrostatic shocks. An intense laser pulse, absorbed by a thin solid target, ionizes the target material and heats up its electrons to a temperature that is high enough for some of them to leave the target material from the front and rear side. The escaping electrons leave behind a positive net charge on the target's surface that is facing away from the laser. A double layer forms between them and the surface. Its electric field accelerates the ions of surface impurities and of the target along the surface normal. This ion acceleration process creates a rarefaction wave propagates into the target and continues to inject ions into the expanding plasma thus forming a blast shell.

The blast shell expands into vacuum and its density decreases with an increasing distance from the target's surface. Thermal diffusion of electrons in a density gradient yields an ambipolar electric field, which continues to accelerate ions far from the target's surface. However, the ions are less efficiently accelerated when the rarefaction wave reaches the center of the ablated target (Mora and Grismayer, 2009). Blast shell fronts can reach speeds of the order of $10^5 - 10^7\, m.s^{-1}$, but it is important to distinguish between two regimes of ion target acceleration via laser pulse.

The first one, concerns experiments where thick targets are irradiated with lasers with pulse durations < 1 ns and peak intensities $\mathrm{I}\lambda^2$ of the order of $10^{17}-10^{18}\mathrm{W.cm^{-2}.\mu m^2}$ (Begay and Forslund, 1982). The ions are emitted from the front surface irradiated by the laser, with a large angular divergence and an energy of a few 100 keV/nucleon (depending of the wavelengh $\lambda$ of the laser). The ions originated from the target surface, and expand into vaccum according to the theoretical models (Gurevich et al., 1968; Denavit, 1979). Simulations using parameters of these experiments showed that the plasma expansion in vacuum, could be considered isothermal (Gitomer et al., 1986), or adiabatic. The second ion acceleration regime is realized with short (picosecond) pulses (Maksimchuk et al., 2000). It was demonstrated by studying the acceleration ions from the non-irradiated rear target surface, of a thin target. The accelerating electrostatic field is generated by fast electrons produced by an ultra-intense laser pulse, and propagated through the target, as it was explained by (Wilks et al., 2001). This acceleration mechanism, called TNSA target normal sheath acceleration allows to attain higher ion energies adiabatically accelerated from the target.

In our study we consider the first configuration of target ablation by ns laser pulse, resulting to an isothermal expansion of a blast shell. Residual gas, which is present in the vacuum chamber prior to the target ablation, is ionized by secondary X-ray emissions from the ablated target. This ambient plasma resists the blast shell's expansion. Its thermal pressure is initially small compared to that of the much denser blast shell and the latter expands freely. The blast shell's front accelerates, compresses and heats up the ambient plasma. The swept-up shocked ambient plasma is separated by a shock (Forslund and Shonk, 1970; Forslund and Freidberg, 1971; Romagnani et al., 2008; Dieckmann et al., 2010; Pusztai et al., 2018) from the ambient plasma upstream of it, if the relative speed between both populations exceeds the relevant acoustic speed. This shock is collisionless and electrostatic and it is characterized by a sharp unipolar electric field pulse. Electrostatic shocks can be destabilized by an instability between the ions they reflect and those of the ambient medium (Karimabadi et al., 1991) or by a Vishniak-type instability (Ahmed et al., 2017; Dieckmann et al., 2018a).

The ram pressure, which is exerted by the upstream plasma on the shock, is balanced by the thermal pressure of the trailing medium. The latter consists of the shocked ambient medium and of the blast shell plasma. The shocked ambient medium is separated from the blast shell plasma by a contact discontinuity. A pressure balance results in a uniform density and speed of the downstream plasma behind the shock front and in a constant maximum speed of the blast shell.

Here we examine with PIC simulations, using the EPOCH code, the shock speed evolution and the formation of secondary structures and processes, such as ion phase space holes (Eliasson and Shukla, 2006) or instabilities driven by the shock-reflected ion beam, are affected by the magnitude of the initial plasma density gradient. This study is inspired from (Dieckmann et al., 2010) studied collisionless planar electrostatic shocks with a strong initial thermal pressure change. The presence of the low-pressure ambient plasma modifies the proton dynamics compared with the plasma expansion into a vacuum. In the present Chapter we investigate the case where the thermal pressure gradient is small increasing the impact of the ambient medium on the blast shell expansion.

This work can provide further insight into the dynamics of solar system shocks and the non-relativistic astrophysical shocks, such as the supernova remnant shocks (Bell et al., 1988; Woolsey et al., 2001). In particular, the case of large pressure a gradient investigated by (Dieckmann et al., 2010) corresponds to the case of forward shock, resulting from the interaction between the expanding SNR and the ISM, and, the next study will correpsond more to the reverse shock of a supernova remnant. A better understanding of such shocks is also relevant for inertial confinement fusion experiments.

### 3.1.1 Initial conditions of PIC simulations

Simulations are performed in one spatial dimension $x$ with three particle velocity components. We applied periodic boundary conditions for the fields and reflecting boundary conditions for the computational particles (CPs). The length $\mathrm{L}_0$ = 6-8 mm of the simulation box depends of the initial density ratio between the ambient plasma and the blast shell, see Tab.3.1, in order to make it large enough to separate effects introduced by the boundaries from the area of interest. The box is subdivided into evenly spaced grid cells with the length $\Delta_x = 0.2\mu m$. We consider here fully ionized hydrogen.

A dense plasma fills the domain $x < 0$ with an ion and electron density $n_0 = 10^{24} m^{-3}$. The ambient plasma fills the domain $x > 0$. Its density is defined by its ratio $\alpha$ with the denser plasma as $n_0/\alpha$, see Tab.3.1. The electron and ion temperatures of both plasmas are $\mathrm{T}_e$ = 1keV and $\mathrm{T}_i = \mathrm{T}_e/10$. The electrons from the ambient medium are 100 times hotter than in (Dieckmann et al., 2010). All species are initially at rest and we represent the electrons and ions of the ambient plasma by $10^2$ ppc and by $4 \times 10^2$ ppc for the dense plasma. The simulation setup is shown in figure 3.2.

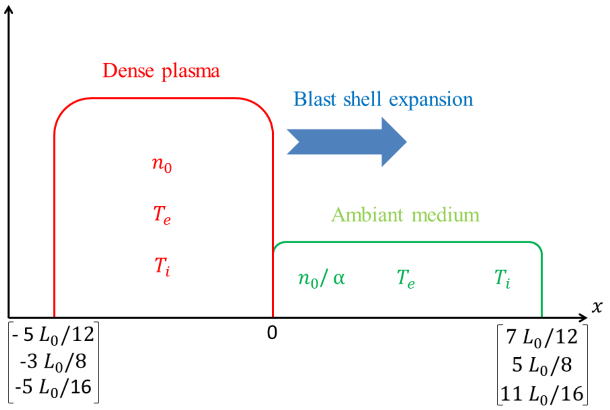

Figure 3.2 – Sketch of the plasma density distribution in the simulations. The localisation of the boundaries of the simulation box change regarding to α.

Plasma frequencies of the electrons and ions of the dense plasma are defined by $\omega_{pe} = (n_0 e^2/\epsilon_0 m_e)^{1/2} = 5.6 \times 10^{13}\mathrm{s}^{-1}$ and $\omega_{pi} = (\mathrm{Z}^2 n_0 e^2/\epsilon_0 m_i)^{1/2} = 1.3 \times 10^{12}\mathrm{s}^{-1}$ respectively. The dense plasma has an electron thermal speed of $v_{the} = (k_\mathrm{B}\mathrm{T}_e/m_e)^{1/2} = 1.3 \times 10^6\mathrm{m.s}^{-1}$ and the electron Debye length is $\lambda_{\mathrm{D}e} = (\epsilon_0 k_\mathrm{B}\mathrm{T}_e/n_0 e^2)^{1/2} = 0.235\mu\mathrm{m}$, which is larger than our spatial resolution. The ion acoustic speed in these collisionless plasmas is $c_s = ((\gamma_e \mathrm{T}_e + \gamma_i \mathrm{T}_i)/m_i)^{1/2} = 4.3 \times 10^5\mathrm{m.s}^{-1}$, where, $\gamma_e = 5/3$ and $\gamma_i = 3$ are the specific heat ratios for electrons and ions.

Debye length of the electrons of the dense plasma is used for the length normalization and the dense plasma frequency is used for time normalization. The simulation box covers $2.55 - 3.4 \times 10^4 \lambda_{\mathrm{D}e}$. We examine the data in the time interval $0 \le t\omega_{pe} \le t_{max}$ with $t_{max} = 1.5 - 1.69 \times 10^5$. $t_{max}$ is resolved by $4.0 - 4.5 \times 10^6$ time steps.

| Label | Ambient plasma density | α | Left wall | Right wall | Grid cells |
|---|---|---|---|---|---|
| Sim 1 | Very high | 2.5 | $-10^4$ | $1.5 \cdot 10^4$ | 30000 |
| Sim 2 | High | 5 | $-10^4$ | $1.5 \cdot 10^4$ | 30000 |
| Sim 3 | Medium | 10 | $-10^4$ | $1.5 \cdot 10^4$ | 30000 |
| Sim 4 | Low | 15 | $-1.21 \times 10^4$ | $2.13 \cdot 10^4$ | 40000 |
| Sim 5 | Very low | 20 | $-10^4$ | $2.34 \cdot 10^4$ | 40000 |

Table 3.1 – Characteristics of the simulations as function of the density ratio α (the left and right wall represent the localisation of the boundaries of the simulation normalized by $\lambda_{\mathrm{D}e}$).

### 3.1.2 Simulations results

A plasma density gradient, depending of the density ratio α, is created near the contact layer at $x = 0$. Due to the high electron mobility an ambipolar electrostatic field rises. The latter confines

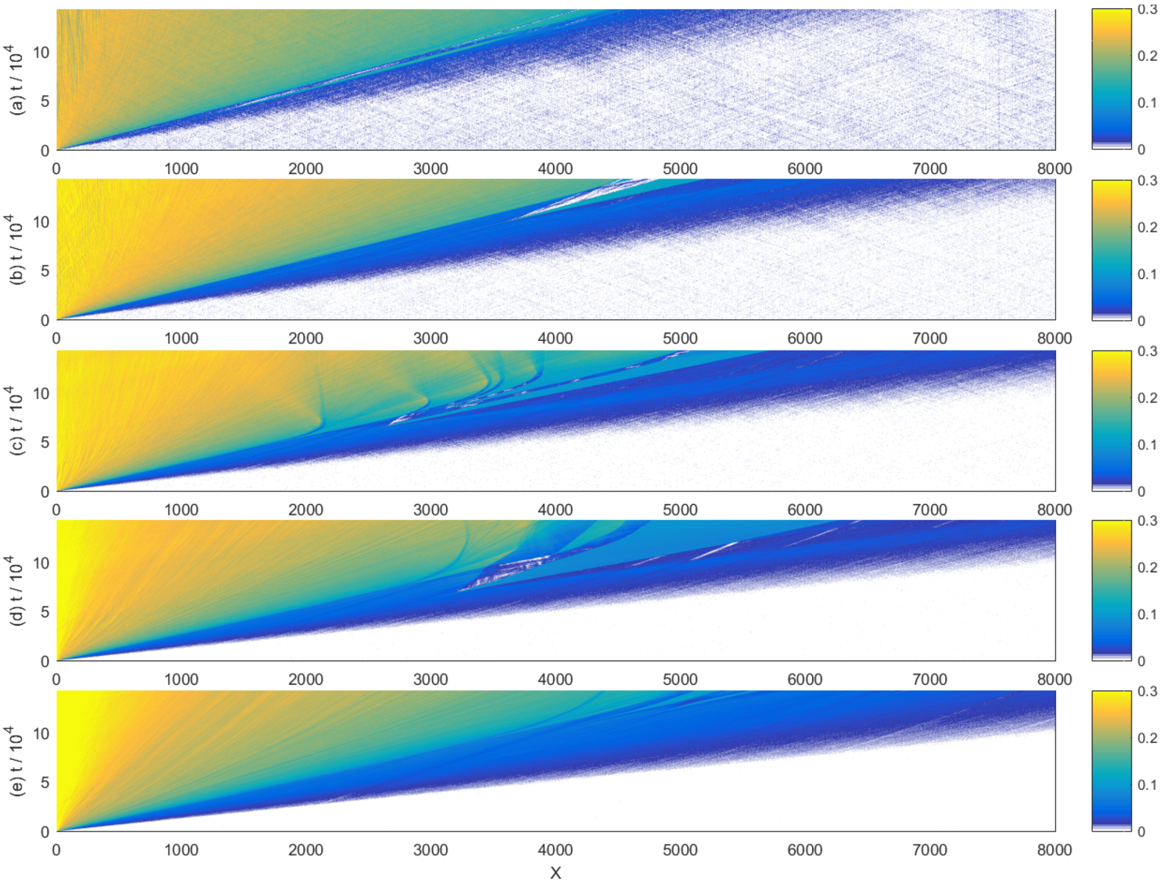

Figure 3.3 – The ion density $n_i/n_0$ time and space evolution for the density ratio $\alpha = 2.5$ (a), $\alpha = 5$ (b), $\alpha = 10$ (c), $\alpha = 15$ (d), $\alpha = 20$ (e), in the laboratory frame of reference.

the electrons and accelerates the ions. The electric field vector is antiparallel to the density gradient and the ion acceleration launches a rarefaction wave. The electron momentum along the density gradient is reduced by the electric field of the expanding wave, this way the electrons provide energy for the ion acceleration. The rarefaction front moved to the left into the dense plasma $x < 0$ and accelerates ions to the right. The accelerated ions form a blast shell that expands and launch a shock in the ambient medium.

The evolution in time, of the ion density is represented in Fig.3.3 for the different simulations in the interval $0 \leq x/\lambda_{\mathrm{D}e} \leq 8 \times 10^3$. The density ratio controls the velocity of the rarefaction wave. The shock propagates faster in a lower density ambient medium. In the cases of density ratio $\alpha =$ 5, 10 and 15 some density pulses appear after $2 \times 10^4 \omega_{pe}^{-1}$ in the interval $2 \leq x/\lambda_{\mathrm{D}e} \leq 6 \times 10^3$. The initial speed of these solitary waves is close to the shock speed and slows down after few $10^4 \omega_{pe}^{-1}$.

In order to understand these processes we consider the ion phase space at two different times, before and after the formation of these non-linear structures in front of the shock.

### Laminar hybrid structure

Figure 3.4 displays the ion phase space components at $t = 3.5 \times 10^4 \omega_{pe}^{-1}$ (0.6 ns) in the interval $-1 \times 10^3 \leq x/\lambda_{\mathrm{D}e} \leq 2,5 \times 10^3$ for the different simulations.

Electrostatic shocks are easily captured in one-dimensional simulations. They are fully described by the distribution of the electrostatic potential (Dieckmann et al., 2010). The rarefaction wave, generated by the potential across the contact discontinuity, has accelerated the blast shell ions in the interval $-10^3 \leq x/\lambda_{\mathrm{D}e} \leq 0$ and the ion density goes down when $x$ increases. Penetration of the blast shell into the ambient plasma at $x > 0$ increases the total ion density, and an electric field builds up in opposite direction to the dense plasma expansion. As a consequence, the blast

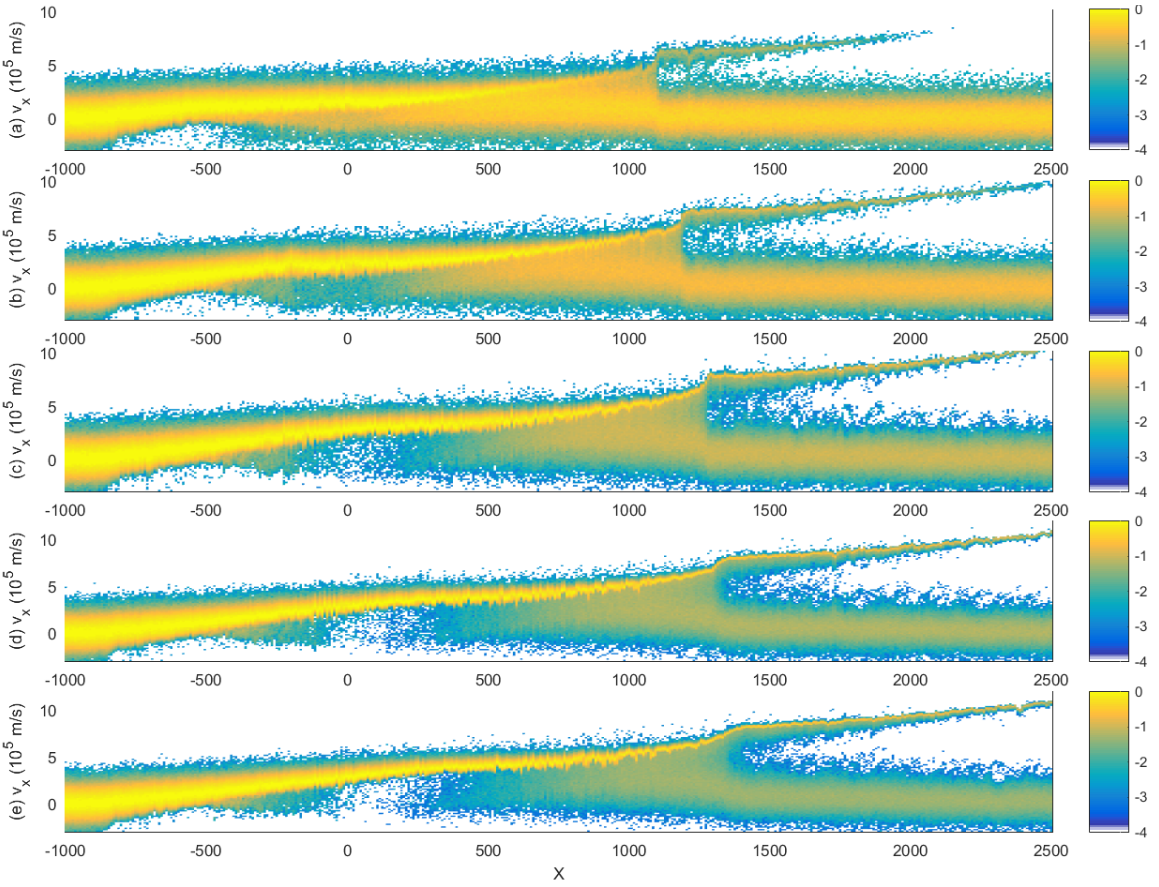

Figure 3.4 – The phase space density distribution $(x, v_x)$ of the ions on a 10-logarithmic scale at $t = 3.5 \times 10^4 \omega_{pe}^{-1}$ for $\alpha = 2.5$ (a), $\alpha = 5$ (b), $\alpha = 10$ (c), $\alpha = 15$ (d), $\alpha = 20$ (e), in the laboratory frame of reference.

shell ions are decelerated, in the laboratory frame of reference, by the ambient medium and a plateau with a constant velocity is formed for $x > 0$. A double layer structure exists in the interval $0 \le x/\lambda_{\mathrm{De}} \le x_{sh}$, where $x_{sh}$ is the position of the shock and represents the edge of the plateau. The ions from the ambient medium which have crossed the shock are decelerated by the potential in the shock frame of reference, and are mixed with the blast shell ions in the plateau region. At these time interval, the mixing region between the blast shell and ambient ions covers all the plateau region.

We define now the contact discontinuity as the interval where the two plasma species are mixed with each other. Recent works on the expansion of a blast shell into an ambient plasma immersed in an external magnetic field (Dieckmann et al., 2017a; Moreno et al., 2018c) have demonstrated that the magnetic pressure helps to form a sharp contact discontinuity between the two ion populations in the plateau region (discussed in the next Chapter). In the present purely electrostatic case, the blast shell expansion is not constrained by any magnetic field and the two populations are mixed over a larger distance. However, since the ambient medium decreases the speed of the blast shell, the latter progressively becomes less dense close to the shock front, and on large time scales the only ion species which contribute efficiently to the shock formation are those of the ambient plasma. The downstream frame of reference moves at the speed of the plateau $v_p$. The Mach number of the shock is defined as $\mathrm{M} = v_0/c_s$, where $v_0 = v_p + c_s$, and can be estimated as the density jump of the ambient plasma close to the shock boundary. The speed of the electrostatic shock and its position depend on the density ratio. This is demonstrated in Table 3.2 and in figure 3.3. The shock speed increases as the ambient plasma density decreases.

The ions from the blast shell which has passed the shock boundary, before the time response of the ambient medium, moves faster than the shock and propagates upstream as an ion beam. The electrostatic potential of the shock is able to reflect a fraction of the upstream ambient ions

| Density ratio α | 2.5 | 5 | 10 | 15 | 20 |
|---|---|---|---|---|---|
| Shock speed $v_0(10^5 m.s^{-1})$ | 4.0 | 4.35 | 4.7 | 4.9 | 5.0 |
| Mach number $(v_0/c_s)$ | 0.9 | 1.0 | 1.08 | 1.12 | 1.15 |
| Position of the shock front | 1100 | 1180 | 1250 | 1310 | 1380 |

Table 3.2 – Mach number of the shock depending of the density ratio α.

(Pusztai et al., 2018), which will move at a speed similar to the ion beam. This linear stage evolves until $2 \times 10^3 \omega_{pe}^{-1}$ where non-linear effects affect the shock propagation.

### Non-linear processes

Figure 3.5 displays the ion phase space components at $t = 14.2 \times 10^4 \omega_{pe}^{-1}$ (2.5 ns) in the interval $-1 \times 10^3 \leq x/\lambda_{De} \leq 2,5 \times 10^3$ for the different simulations.

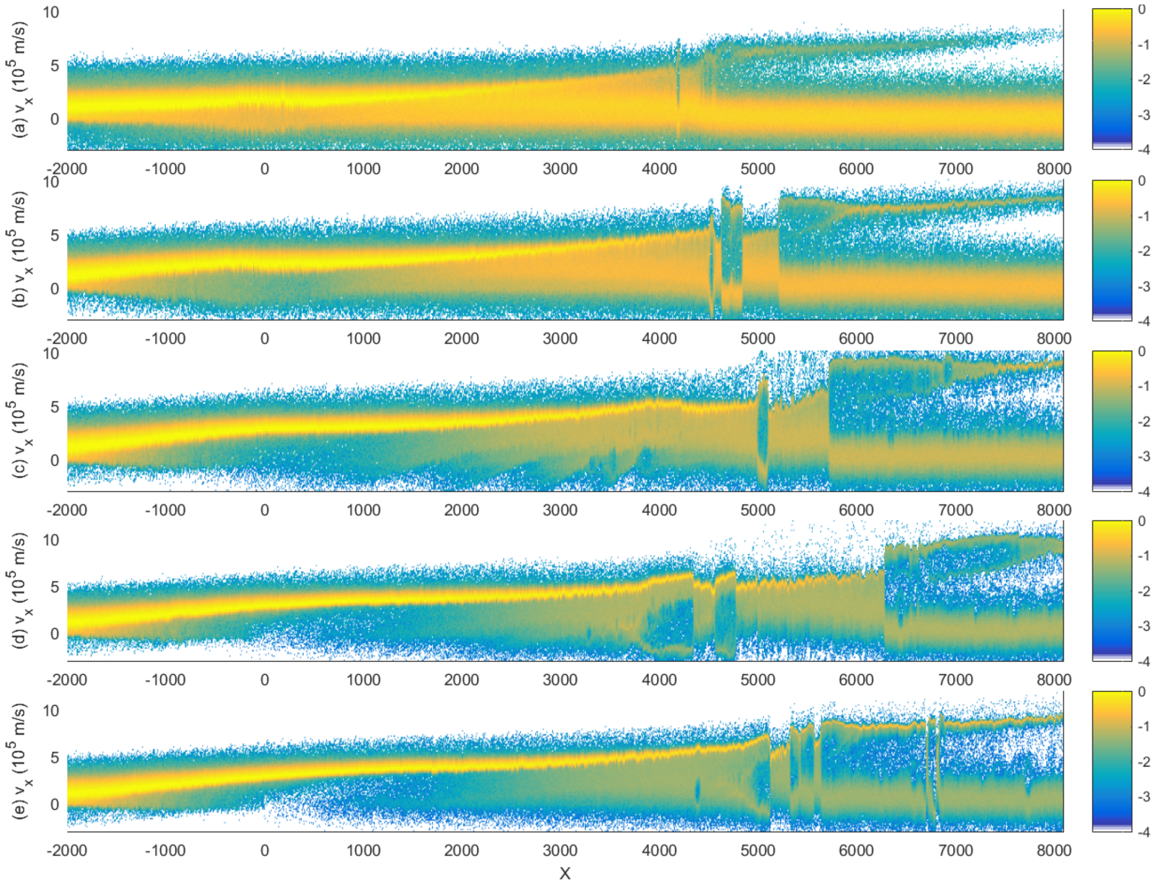

Figure 3.5 – The phase space density distribution $(x, v_x)$ of the ions on a 10-logarithmic scale at $t = 14.2 \times 10^4 \omega_{pe}^{-1}$ for $\alpha = 2.5$ (a), $\alpha = 5$ (b), $\alpha = 10$ (c), $\alpha = 15$ (d), $\alpha = 20$ (e), in the laboratory frame of reference.

Ion phase space holes appear in the downstream and upstream regions of the shock front. Holes in the particle phase space can appear when the system is time dependent and can be generated by kinetic instabilities. An ion beam propagating through an ambient medium is a possible source for excitation of several instabilities which can produce phase space holes. The one-dimensional configuration of our simulation does not allow excitation of the Vishniac-type instability, which can rise close to the shock boundaries. The Weibel instability is also forbidden in 1D geometry. Two possible electrostatic instabilities leading to shock formation can merge in these one-dimensional simulations. One of them is the Buneman instability (Buneman, 1958) which cannot grow in our present case since the electrons are so hot that their thermal velocity spread exceeds by far their drift velocity relative to the ions (speed of the ion beam). A similar reason prevents the growth of the electron two-stream instability. The electrons are initially 10 times hotter than the ions, this ratio between the electron temperature and the ion temperature is large enough to linearly undamp the ion acoustic waves (Baumjohann and Treumann, 1997). However, the shock dissipates part of the ion kinetic energy from the ambient medium which is strongly heated after crossing the shock ramp, reaching a temperature of $4T_i$. Because of their inital high temperature, $v_{te} >> v_0$ the electrons maintain the neutrality on either side of the shock without any variation of their thermal velocity.

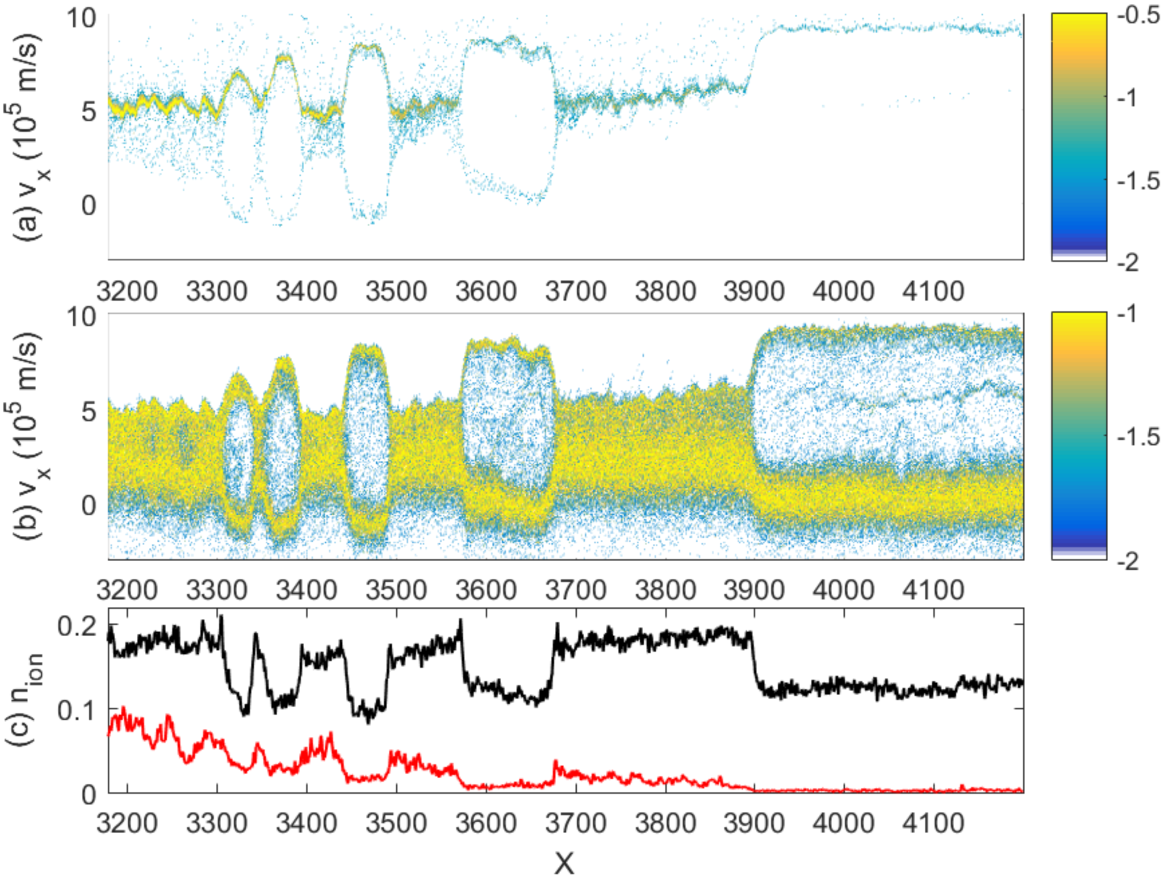

Figure 3.6 – Zoom on the phase space density distribution $(x, v_x)$ of the blast shell (a) and ambient ions (b) on a 10-logarithmic scale at $t = 10.1\ 10^4\omega_{pe}^{-1}$ for $\alpha = 10$ in the Laboratory frame of reference. Panel (c) shows the ion density of the blast shell (red) and ambient ions (black).

The increase of the ion temperature of the ambient medium therefore suppresses the growth of the ion acoustic instability downstream since the ratio $T_e/T_i$ decreases. The ion acoustic instability can however grow upstream, particularly in the case of a low density ratio. The hole formation is studied in the simulation with $\alpha = 10$.

An analysis of the evolution of the ion phase space components of the dense and ambient plasma with $\alpha = 10$, in the shock frame of reference, in the time interval $3.5 \times 10^4 < t < 14.2 \times 10^4\omega_{pe}^{-1}$, has been performed. The shock has reached the position $x/\lambda_{De} \simeq 3.9 \times 10^3$ at $t = 10.1 \times 10^4\omega_{pe}^{-1}$ (1.8 ns) at it is shown in Figure 3.6. The electrostatic shock is mostly mediated by the ambient medium as demonstrated in Fig.3.6c where the density of the inital dense blast shell is now lower than the density of the ambient medium. The reflected ion beam moves at a speed $v_{ref} = 8.5 \times 10^5$m.s$^{-1}$ which is approximatly two times higher than the ion acoustic speed. This situation is favourable for the growth of solitary waves which are formed upstream of the shock due to the ion acoustic instability. These solitary waves have already been observed by (Dieckmann et al., 2010) for cold electron beams. In this study we consider the hot plasma.

We perform now a Galilean transformation from the laboratory reference frame to the shock frame of reference $x^* = x - v_0 t$. The evolution in time, of the blast shell and ambient ion density is represented in Fig.3.7.

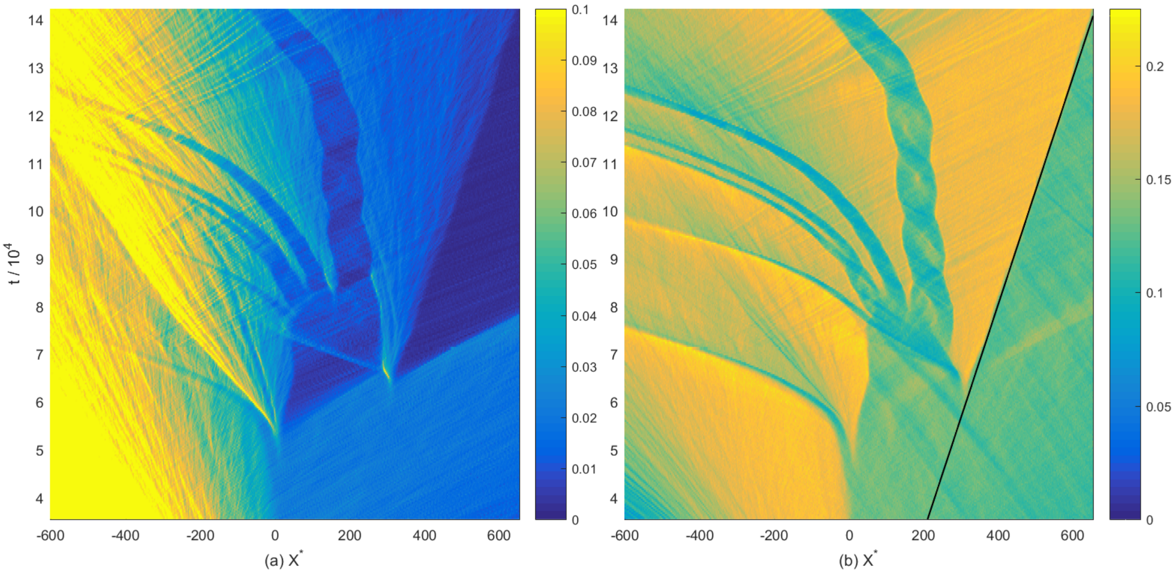

Figure 3.7 – The ion density $n_i/n_0$ component evolution for the density ratio $\alpha = 10$ of the dense plasma (left) and the ambient plasma (right), in the frame of reference $x^* = x - v_0 t$. Here $v_0 = 4.7 \times 10^5 \mathrm{m.s}^{-1}$ and the black line corresponds to the velocity of $5.7 \times 10^4 \mathrm{m.s}^{-1}$ or $1.13 v_0$.

The solitary waves excitation depends on the interaction between the shock reflect ion beam and the ambient medium, and it is difficult to estimate their localization. The first solilary wave, called SW1, appears after $4.5 \times 10^4 \omega_{pe}^{-1}$ at a distance $x^* = 22\lambda_{\mathrm{D}e} \sim c/\omega_{pe}$ from the shock ramp. A phase space hole is formed in the cavity bounded by the solitary wave potential and the shock ramp. During a short time period $\sim 0.5 \times 10^4 \omega_{pe}^{-1}$ the hole moves at the shock speed. Two conditions required for the creation of these ion holes: first, the electrons must be sufficiently hot so the ion acoustic waves are weakly damped, and second, the depth of the potential in the cavity is limited by the electron thermal energy. Ion hole is related to ion-acoustic mode (Schamel, 1986), it is more or less standing structure since it tend to self-bind as ions surrounding the hole are attracted to the hole's negative potential. Once produced, a hole located at velocity $v$, can become unstable (Dupree, 1983). The ion hole appears to be negatively charged, since it is a local phase space region deficient of ions. The electrons will be reflected by the ion hole's potential. If there are more electrons moving faster than the hole than slower, then reflecting resonant electrons will impart momentum to the hole. Consequently, the ion hole decelerates, and, therefore, it becomes deeper, because there are more particles with smaller velocities (Tetreault, 1988). The ion hole dynamics, can be seen in figure 3.7.

SW1 develops into a secondary shock, which accelerates to a speed of $0.13 v_0$ in the initial shock frame of reference $x^*$, and the hole, bounded by the SW1 potential and the initial shock ramp, accelerates identicaly in the opposite direction to the left. The hole continues to accelerate to the left reaching a steady state at a speed close to the shock speed $-1.13 v_0$ in the initial shock frame of reference $x^*$, which correspond to a speed of $-0.13 v_0$ in the laboratory frame of reference. After $6.5 \times 10^4 \omega_{pe}^{-1}$ a new solitary wave, called SW2, grows much further than the previous one at $x^* = 220\lambda_{\mathrm{D}e} \sim 10c/\omega_{pe}$, between the interval $80 \leq x^* \leq 300\lambda_{\mathrm{D}e}$. SW2 transforms to a shock at $x^* \simeq 300\lambda_{\mathrm{D}e}$. A large quantity of blast shell ions are reflected by the SW2 potential and we clearly see these ions moving through the cavity, in the direction of the ramp formed by SW1, at a speed $-0.13 v_0$, in the initial shock frame of reference $x^*$ (cf. figure 3.7). After $10^4 \omega_{pe}^{-1}$ of propagation into the cavity formed by SW1 and SW2, the reflected ions reach the shock ramp at $x^* = 80\lambda_{\mathrm{D}e}$ and start the creation of a hole. The latter is too large and unstable. A fragmentation into a train of smaller and stable holes appear after $8.6 \times 10^4 \omega_{pe}^{-1}$. Each of them will propagate downstream at the same speed, $-1.13 v_0$, as the first hole formed by SW1, reaching their steady state. The shock formed by SW2 at $x^* \simeq 300\lambda_{De}$ is only mediated by the ambient medium as shown in Fig.3.7, where the density of the ambient medium is 10 times higher compare to the blast shell. The shock then reaches a speed of $1.13 v_0$, for a Mach number of 1.6.

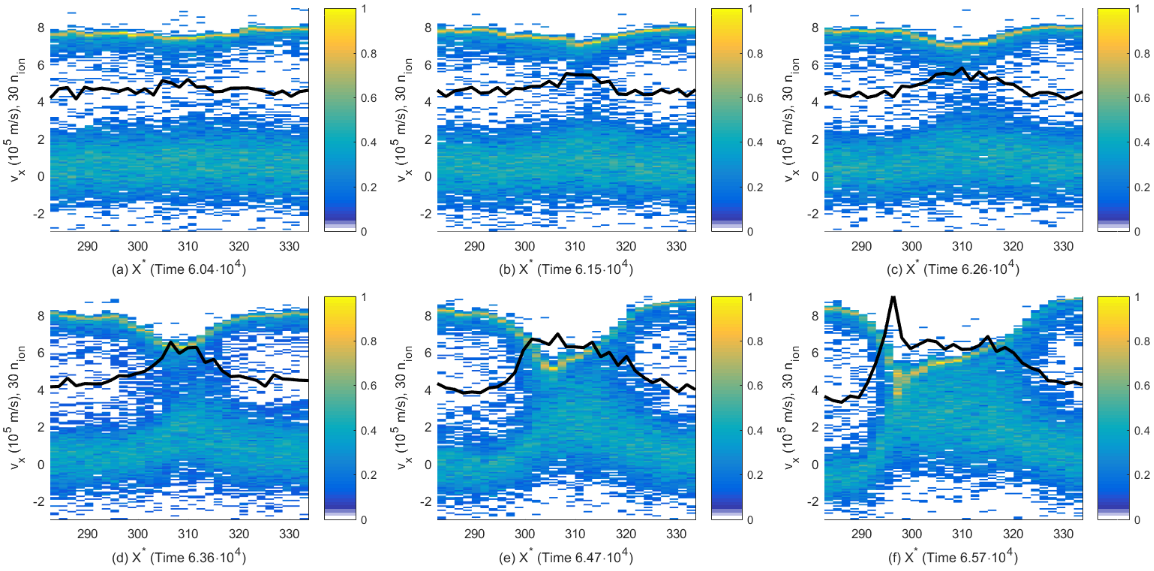

Figure 3.8 – The square root of the ion phase space density $(x, v_x)$ at differents time. The ion density is multiplied with 30 as indicated on the y axis. The overplotted line is the mean speed of the ion population.

We will now study precisely the formation process of the solilary wave near $x^* \simeq 300\lambda_{De}$, where SW2 turns to a shock. Figure 3.8 displays the ion phase space components of the upstream ions and the evolution of their average velocity, at different times in the interval $280 \leq x^* \leq 340\lambda_{De}$ where the solitary waves merge. The opposite currents create small perturbations on the beam and ambient plasma. A tail is formed by these perturbations which propagates at a lower speed than the beam. The symmetric case happens for the ambient plasma. The bipolar electric field generated by each of these tails confines the ions. Indeed, in the comoving frame of reference of the two ion populations, the electric fields have opposite polarities in the region surrounded by the tails which tends to decrease the local electric field in the interval $300 \leq x^* \leq 320\lambda_{De}$. The tail of the blast shell ions can be clearly seen in Fig.3.8f at $x^* = 295\lambda_{De}$. Since the two plasma flows are not symmetric the mean speed of the total ion population increases and reaches a speed of $1.13 v_0$.

## Discussion

In this chapter, we have introduced electrostatic shocks and investigated a thermal expansion of a dense plasma into a dilute plasma. The aim of our work has been to perform a parametric analysis of the density ratio between two clouds to see the qualitative effects of the ambient medium on the dense plasma expansion. The initial conditions and the one-dimensional geometry capture easily the electrostatic shock formation. Our results are summarized as follows. A laminar hybrid structure is formed at the first times of the expansion. It is a double layer structure composed by a rarefaction wave pushing the blast shell ions, which are slowed down by the ambient plasma forming a plateau, the latter finally forms a shock. The electrostatic shock velocity is increasing with the increase of the density ratio between the two plasma clouds. The shock evolution is time dependent; the ambient ions reflected (Malkov et al., 2016) from the shock front excite the ion acoustic instability in the upstream shock region. Other instabilities are excluded due to the chosen initial conditions and the 1D geometry. The solitary waves are excited at the nonlinear stage of the ion acoustic instability. The potential of the solitary waves is sufficiently high to reflect ions and produce phase space holes. The solitary waves form a new shock, accelerated by the phase space holes. These solitary waves gradually reflect the ions of the expanding dense plasma, and the final shock is at the end only mediated by the ambient medium. The gradient pressure between the two plasmas in (Dieckmann et al., 2010) was too large to see this separation between the initial dense and dilute plasma.

This shock acceleration by ion acoustic phase space holes can provide further insight into the dynamics of non-relativistic astrophysical shocks as Earth's bow shock or SNRs. However, particularly in the case of collisionless shocks in the heliosphere, the magnetic field plays a dominant role and the global shocks are not purely electrostatic. To properly describe such shocks, the magnetic field has to be taken into account, changing the instabilities of shock mediation. These shocks will be investigated in the next Chapter.

# Chapter 4

# Magnetosonic collisionless shock formation by the expansion of a magnetized blast shell

Since all collisionless shocks in the heliosphere are magnetised, magnetic field has to be included, and the global shocks are not purely electrostatic even though subshocks developing in them can be considered as electrostatic. We have already presented, in the previous chapters, the collisionless shocks classification in astrophysics, as well as the analytical and numerical tools needed for their analysis.

Collisionless electrostatic shocks have been studied in the previous chapter, where no external field was added. A background magnetic field modifies collisionless shocks. The particle gyromotion introduces new spatio-temporal scales and the shock behaviour becomes dependent on the orientation of its normal relative to the direction of the magnetic field. Experimental observations of the Earth's bow shock demonstrate that the shock transition layer is narrow if the shock normal and the magnetic field direction are quasi-perpendicular (Bale et al., 2005). The transition layer widens with decreasing angles between both directions and one may not even find a definitive shock front structure if both are quasi-parallel (Burgess et al., 2005).

The waves forming a shock are the lowest-frequency plasma modes that are excited under the particular conditions of the shocked plasma. In a cold and strongly magnetized plasma there are three fundamental MHD modes which we will discuss in this chapter.

## 4.1 MHD modes in cold magnetized shocks

Let us investigate the small amplitude waves which propagate through a spatially uniform magnetized plasma. Considering an ideal Ohm's law (cf. equation (1.34)), the continuity equation and Maxwell's equations can be written as:

$$\partial_t \rho_m + \nabla_{\mathbf{r}} \cdot (\rho_m \mathbf{V}) = 0 \tag{4.1a}$$

$$\partial_t (\rho_m \mathbf{V}) + \nabla_{\mathbf{r}} \cdot (\rho_m \mathbf{V}\mathbf{V}) + \nabla_{\mathbf{r}} \cdot \bar{\bar{\Pi}} - \mathbf{J} \times \mathbf{B} = 0 \tag{4.1b}$$

$$\partial_t \bar{\bar{\Pi}} + \Gamma \bar{\bar{\Pi}} \nabla_{\mathbf{r}} \cdot \mathbf{V} = 0 \tag{4.1c}$$

$$\partial_t \mathbf{B} + \nabla_{\mathbf{r}} \times \mathbf{E} = 0 \tag{4.1d}$$

$$\nabla_{\mathbf{r}} \cdot \mathbf{B} = 0 \tag{4.1e}$$

where (4.1c) corresponds to (1.35c) in its simplest form. These equations can be linearized, assuming, for the sake of simplicity, the equilibrium flow velocity and equilibrium plasma current to be zero:

$$\partial_t \rho_1 + \nabla_{\mathbf{r}} \cdot (\rho_0 \mathbf{V}) = 0 \tag{4.3a}$$

$$\partial_t (\rho_0 \mathbf{V}) + \nabla_{\mathbf{r}} \cdot \bar{\bar{\Pi}} - (\nabla_{\mathbf{r}} \times \mathbf{B}) \times \mathbf{B}_0 / \mu_0 = 0 \tag{4.3b}$$

$$\partial_t \bar{\bar{\Pi}} + \Gamma \bar{\bar{\Pi}}_0 \nabla_{\mathbf{r}} \cdot \mathbf{V} = 0 \tag{4.3c}$$

$$\partial_t \mathbf{B} - \nabla_{\mathbf{r}} \times (\mathbf{V} \times \mathbf{B}_0) = 0 \tag{4.3d}$$

The equilibrium quantities, $\rho_0$, $\bar{\bar{\Pi}}_0$, and $\mathbf{B}_0$ are constants in a spatially uniform plasma. Let us search for wave-like solutions of Eqs. (1.37) in which perturbed quantities vary like $\propto \exp(i\mathbf{k}.\mathbf{r} - \omega t)$. It follows that equation (1.37) with the coupling of eq. (4.3a) and eq. (4.3c) takes the form

$$-\omega \rho_1 + \rho_0 \mathbf{V} \cdot \mathbf{k} = 0 \tag{4.5a}$$

$$-\omega \rho_0 \mathbf{V} + \mathbf{k} \bar{\bar{\Pi}} - \frac{(\mathbf{k} \times \mathbf{B}) \times \mathbf{B}_0}{\mu_0} = 0 \tag{4.5b}$$

$$-\omega \left( \frac{\bar{\bar{\Pi}}}{\bar{\bar{\Pi}}_0} - \frac{\Gamma \rho_1}{\rho_0} \right) = 0 \tag{4.5c}$$

$$\omega \mathbf{B} + \mathbf{k} \times (\mathbf{V} \times \mathbf{B}_0) = 0 \tag{4.5d}$$

Assuming that $\omega \neq 0$, the above equations yield

$$\rho_1 = \rho_0 \frac{\mathbf{k} \cdot \mathbf{V}}{\omega} \tag{4.7a}$$

$$\bar{\bar{\Pi}} = \bar{\bar{\Pi}}_0 \Gamma \frac{\mathbf{k} \cdot \mathbf{V}}{\omega} \tag{4.7b}$$

$$\mathbf{B} = \frac{(\mathbf{k} \cdot \mathbf{V}) \mathbf{B}_0 - (\mathbf{k} \cdot \mathbf{B}_0) \mathbf{V}}{\omega}. \tag{4.7c}$$

Substitution of these expressions into the linearized equation of motion, eq. (4.5b), gives

$$\left[ \omega^2 - \frac{(\mathbf{k} \cdot \mathbf{B}_0)^2}{\mu_0 \rho_0} \right] \mathbf{V} = \left\{ \left[ \frac{\Gamma \bar{\bar{\Pi}}_0}{\rho_0} + \frac{\mathrm{B}_0^2}{\mu_0 \rho_0} \right] \mathbf{k} - \frac{(\mathbf{k} \cdot \mathbf{B}_0)}{\mu_0 \rho_0} \mathbf{B}_0 \right\} (\mathbf{k} \cdot \mathbf{V}) - \frac{(\mathbf{k} \cdot \mathbf{B}_0)\,(\mathbf{V} \cdot \mathbf{B}_0)}{\mu_0 \rho_0} \mathbf{k}. \tag{4.9}$$

Assuming the notation of the wavevector as $\mathbf{k} = k_{\parallel} \mathbf{e}_{\parallel} + k_{\perp} \mathbf{e}_{\perp}$, where $\mathbf{e}_{\parallel}$ and $\mathbf{e}_{\perp}$ are the orientation of the wavevector parallel and perpendicular to the magnetic field, respectively, the previous equation reduces to the eigenvalue equation

$$\begin{pmatrix} \omega^2 - v_{\mathrm{A}}^2 k^2 - \tilde{c}_s{}^2 k_{\perp}^2 & 0 & -\tilde{c}_s{}^2 k_{\parallel} k_{\perp} \\ 0 & \omega^2 - v_{\mathrm{A}}^2 k_{\parallel}^2 & 0 \\ -\tilde{c}_s{}^2 k_{\parallel} k_{\perp} & 0 & \omega^2 - \tilde{c}_s{}^2 k_{\parallel}^2 \end{pmatrix} \mathbf{v} = 0. \tag{4.10}$$

where we recognize the Alfvén speed

$$v_{\mathrm{A}} = \sqrt{\frac{\mathrm{B}_0^2}{\mu_0\, \rho_0}}. \tag{4.11}$$

The ion acoustic speed has the form

$$\tilde{c}_s = \sqrt{\frac{\Gamma\, \bar{\bar{\Pi}}_0}{\rho_0}}. \tag{4.12}$$

We can assume, without loss of generality, that the equilibrium magnetic field $\mathbf{B}_0$ is directed along the $z$-axis, and that the wave-vector $\mathbf{k}$ lies in the $x$-$z$ plane. Let $\theta$ be the angle subtended between $\mathbf{B}_0$ and $\mathbf{k}$. The solution requires that the determinant of the matrix (4.10) is zero, which yields the dispersion relation

$$\mathrm{D}_{\mathrm{MHD}}(\omega,\mathbf{k}) = (\omega^2 - v_{\mathrm{A}}^2 k^2 \cos^2\theta)[(\omega^2 - v_{\mathrm{A}}^2 k^2 \cos^2\theta)(\omega^2 - \tilde{c}_s{}^2 k^2) - \omega^2 v_{\mathrm{A}}^2 k^2 \sin^2\theta] = 0. \tag{4.13}$$

This dispersion equation of degree 3, in $\omega^2$, accepts three independent roots, corresponding to the three different types of wave that can propagate in a magnetized plasma. The first, and most obvious, root is

$$\frac{\omega}{k} = v_{\mathrm{A}}\cos(\theta). \tag{4.14}$$

This wave is characterized by both $\mathbf{k}\cdot\mathbf{V} = 0$ and $\mathbf{V}\cdot\mathbf{B}_0 = 0$. This solution corresponds to an incompressible mode, which means that there is no change of density or pressure. The group velocity is along $\mathbf{B}$, the wave does not transfer energy (information) across the magnetic field. So we note, that since the Alfvén wave only involves plasma motion perpendicular to the magnetic field, we can expect the dispersion relation (4.14) to hold in a collisionless, as well as a collisional plasma.

The remaining two roots of the dispersion relation (4.13) are written

$$\frac{\omega}{k} = v_{f,s}, \tag{4.15}$$

where $v_{f,s}$ correspond to the fast/ slow magnetosonic velocity respectively and take the form

$$\frac{2v_{f,s}^2}{v_{\mathrm{A}}^2} = (1+\tilde{\beta}) \pm \left((1-\tilde{\beta})^2 + 4\tilde{\beta}\sin^2\theta\right)^{1/2}, \tag{4.16}$$

where

$$\tilde{\beta} = \tilde{c}_s^2 / v_{\mathrm{A}}^2, \tag{4.17}$$

equals the ratio of the plasma's thermal to magnetic pressure. We also define here the magnetosonic velocity $\tilde{c}_{ms}$, which corresponds to the fast magnetosonic speed for $\theta = 90°$,

$$\tilde{c}_{ms}^2 = \tilde{c}_s^2 + v_{\mathrm{A}}^2. \tag{4.18}$$

Note that $v_f \geq v_s$. The wave with the upper sign in equation (4.15) is designated as the fast magnetosonic wave, whereas the wave with the negative sign is called the slow magnetosonic wave. These waves are associated with non-zero perturbations in the plasma density and pressure, and also involve plasma motion parallel, as well as perpendicular, to the magnetic field, $\mathbf{k}\cdot\mathbf{V} \neq 0$ and $\mathbf{V}\cdot\mathbf{B}_0 \neq 0$. The latter observation suggests that the dispersion relations (4.15) are likely to undergo significant modification in collisionless plasmas.

Considering the cold-plasma limit, which is obtained by letting the sound speed $c_s$ tend to zero, the slow wave has its phase velocity which tends to zero and ceases to exist, whereas the dispersion relation for the fast wave reduces to

$$\frac{\omega}{k} = v_{\mathrm{A}} \tag{4.19}$$

The fast magnetosonic wave can be identified as the compressional-Alfvén wave modified by a non-zero plasma pressure. In the limit $v_{\mathrm{A}} >> c_s$, which correspond to low-$\beta$ plasmas, the dispersion relation for the slow wave reduces to

$$\omega \simeq k\tilde{c}_s\cos\theta. \tag{4.20}$$

In low-$\beta$ plasmas the slow magnetosonic wave is a sound wave modified by the presence of the magnetic field.

A distinction between the fast and slow waves can be further understood by comparing the sign of the plasma thermal and magnetic pressure perturbations: $\bar{\bar{\Pi}}$ and $\mathbf{B}_0\cdot\mathbf{B}/\mu_0$, respectively. The fluctation of the magnetic pressure can be found from (4.7c)

$$\frac{\mathbf{B}\mathbf{B}_0}{\mu_0} = \frac{(\mathbf{k}\cdot\mathbf{V})\mathrm{B}_0^2 - (\mathbf{k}\cdot\mathbf{B}_0)(\mathbf{V}\cdot\mathbf{B}_0)}{\mu_0\omega}. \tag{4.21}$$

Now, considering the $z$- component along the magnetic field, equation (4.5b) yields

$$\omega\rho_0 v_z = k\cos\theta\bar{\bar{\Pi}}. \tag{4.22}$$

Combining equations (4.7b) with the two latter equations, we obtain

$$\frac{\mathbf{B}_0\cdot\mathbf{B}}{\mu_0} = \frac{v_{\mathrm{A}}^2}{\tilde{c}_s^2}\left(1-\frac{k^2\tilde{c}_s^2\cos^2\theta}{\omega^2}\right)\bar{\bar{\Pi}}. \tag{4.23}$$

Hence, $\bar{\bar{\Pi}}$ and $\mathbf{B}_0\cdot\mathbf{B}/\mu_0$ have the same sign if $\mathrm{V} > \tilde{c}_s\cos\theta$, and the opposite sign if $\mathrm{V} < \tilde{c}_s\cos\theta$. It is straightforward to show that $v_f > \tilde{c}_s\cos\theta$, and $v_s < \tilde{c}_s\cos\theta$. Thus, we conclude that for the fast magnetosonic wave the thermal pressure and the magnetic pressure are in phase (the fluctuations reinforce one another), whereas in the slow magnetosonic wave these pressures are in antiphase (the fluctuations oppose one another).

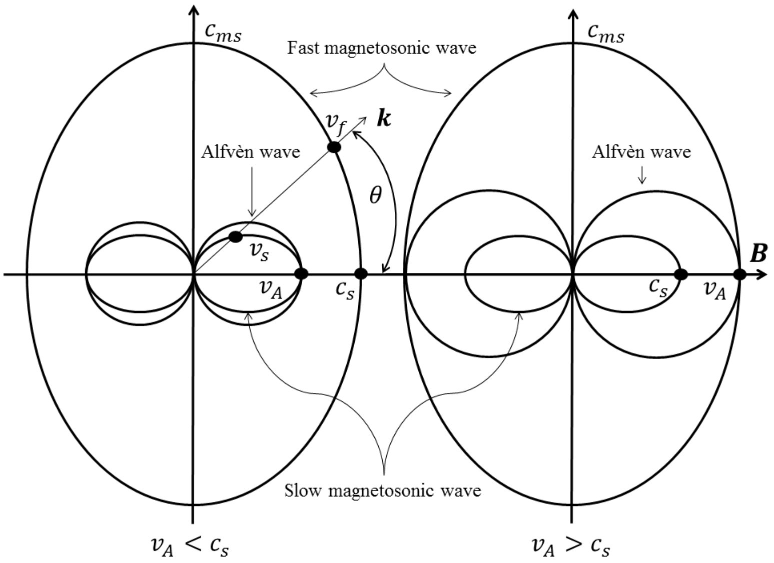

Figure 4.1 – Wave vector diagram of two cases of MHD waves in the plane of the magnetic field.

Figure 4.1 shows the angular dependence of these three phase velocities for two special cases. Clearly in the direction perpendicular to the magnetic field only the fast mode propagates and, hence, strictly perpendicular MHD shocks are fast shocks as has been noted. In the direction parallel to B all three waves can propagate. These are the lowest frequency eigenmodes of a homogeneous not necessarily isotropic plasma, a small disturbance excited in a plasma may propagate in a form of one of these modes.

These solutions are obtained in a linear approximation, where waves have been considered to be harmonic $\propto \exp(i\mathbf{k}.\mathbf{r}-\omega t)$. Shocks are formed by steepening of the leading edge of a wave, which is caused by non-linear effects. Steepening of the wave also leads to strong dispersive effects, and the competition of these two effects is responsible for the spontaneous generation of oscillations.

Let us now consider a high-pressure plasma ($\tilde{c}_s^2 >> v_{\mathrm{A}}^2$) and a very small obliquity such that $\mathrm{R}^{-1/2} << \theta << 1$ (with R the ion-to-electron mass ratio, cf. Chapter 2), then the dispersion relation for a slow mode obtained by (Sagdeev, 1966) acquires a simple form

$$\frac{\omega^2}{k^2} \approx v_{\mathrm{A}}^2\left(1+\frac{k^2\theta^2c^2}{\omega_{pi}^2}\right), \tag{4.24}$$

where the second term in the parenthesis accounts for the wave dispersion. Consequently, the dispersion effects become important at wavelengths of the order of $\theta(c/\omega_{pi})$. This particular example (Sagdeev, 1966) shows that a laminar structure of non-linear oscillations inside a shock front can be reduced to two different cases. Figure 4.2 (left) shows the two dispersion curves of low frequency waves in the $(\omega_r, \mathbf{k})$-plane from which shock waves could evolve.

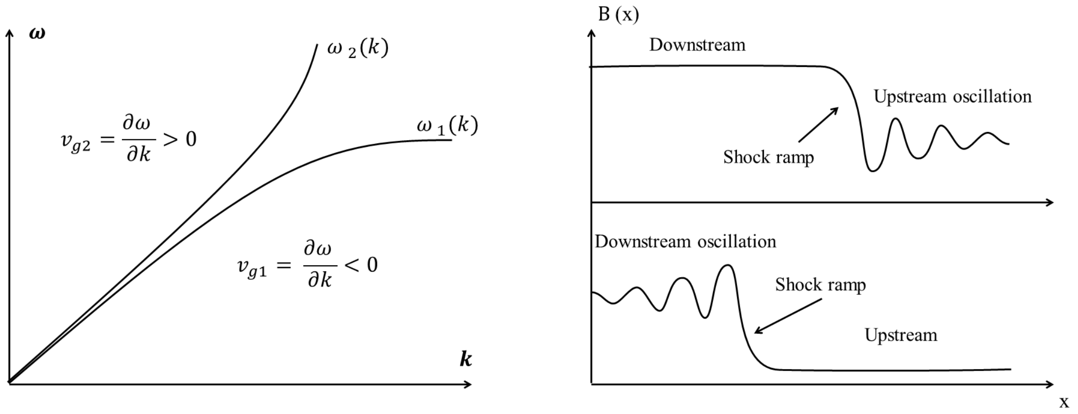

Figure 4.2 – Two different types of dispersions in the $(\omega_r, \mathbf{k})$-plane. (left) The short waves with concave dispersion relation, $\omega_1$, have a smaller group velocity than long waves and form a trail on the long wave. For a convex dispersion relation, $\omega_2$, the short waves move faster than long waves. The effect of this difference in sideband wave velocity on a laminar subcritical shock wave are shown in the right panel. The waves, spatially damped, moving-away from the shock ramp into the downstream region, are produced by a concave dispersion relation (down right). These waves occur in the upstream region for a convex dispersion relation (up right).

Both curves have in common a linear dispersion at long wavelengths, i.e. at small wave-numbers k, with slope given by the phase velocities of the waves. In this region all nonlinearly generated sidebands have same phase and group velocities causing broadening of the wave spectrum and steeping. However, at higher wave-numbers the dispersion curves start diverging from a linear slope, one of the waves turning convex, the other concave. These turnovers imply a change in the phase and group velocities. The convex dispersion implies that shorter wavelengths generated in the convex part of the dispersion curve move faster than the long waves. They thus catch up with the long wavelength wave and run away ahead thus forming upstream precursors of the shock as shown in the higher part on the right. On the other hand, for the concave dispersion shorter wavelength waves fall behind the long waves. They represent a wave trail following the large amplitude long wave as is shown in the lower part on the right. This simple analysis of the dispersion curves already demonstrates possible properties of the expected shock structure. This reasoning does not hold for all shocks it depends on the shock criticality.

The existence of a critical Mach number for high Mach-numbers collisionless shocks was predicted from consideration of the insufficiency of dissipation in the shock to provide the required, by the conservation laws, retardation of the inflow, plasma thermalisation, and entropy production. The criticality of shocks is defined as a transition from subcritical dissipative to supercritical viscous shock, accompanied by particle reflection.

To show how the critical Mach number of a shock arises from the Rankine-Hugoniot relations we consider the strictly perpendicular case where the Rankine-Hugoniot conservation equations, between the upstream (I) and downstream (II) region, in the shock frame of reference for ideal

MHD (1.40), are written as

$$\rho_{\mathrm{II}} v_{\mathrm{II}} = \rho_{\mathrm{I}} v_{\mathrm{I}} \tag{4.25a}$$

$$\rho_{\mathrm{II}} v_{\mathrm{II}}^2 + \Pi_{\mathrm{II}} + \frac{B_{\mathrm{II}}^2}{2\mu_0} = \rho_{\mathrm{I}} v_{\mathrm{I}}^2 + \Pi_{\mathrm{I}} + \frac{B_{\mathrm{I}}^2}{2\mu_0} \tag{4.25b}$$

$$\left(\frac{1}{2}\rho_{\mathrm{II}} v_{\mathrm{II}}^2 + \frac{\Gamma\Pi_{\mathrm{II}}}{\Gamma-1} + \frac{B_{\mathrm{II}}^2}{\mu_0}\right) v_{\mathrm{II}} = \left(\frac{1}{2}\rho_{\mathrm{I}} v_{\mathrm{I}}^2 + \frac{\Gamma\Pi_{\mathrm{I}}}{\Gamma-1} + \frac{B_{\mathrm{I}}^2}{\mu_0}\right) v_{\mathrm{I}} \tag{4.25c}$$

$$B_{\mathrm{II}} v_{\mathrm{II}} = B_{\mathrm{I}} v_{\mathrm{I}} \tag{4.25d}$$

An explicit solution for the different density, magnetic field and velocity jumps, $\frac{\rho_{\mathrm{II}}}{\rho_{\mathrm{I}}} = \frac{B_{\mathrm{II}}}{B_{\mathrm{I}}} = \frac{v_{\mathrm{I}}}{u_{\mathrm{II}}} = r$ respectively, can be found as

$$2(2-\Gamma)r^2 + \Gamma(2(1+\beta_{\mathrm{I}}) + (\Gamma-1)\beta_{\mathrm{I}} M_{\mathrm{I}}^2)r - \Gamma(\Gamma+1)\beta_{\mathrm{I}} M_{\mathrm{I}}^2 = 0, \tag{4.27}$$

where $\beta_{\mathrm{I}} = 2\mu_0 \Pi_{\mathrm{I}}/B_{\mathrm{I}}^2 = \tilde{c}_s^2/v_{\mathrm{A}}^2$ is the ratio of the upstream plasma pressure to the magnetic field pressure and, $M_{\mathrm{I}} = v_{\mathrm{I}}/\tilde{c}_{s\mathrm{I}}$ is the acoustic Mach number.

The only type of shock that is physically possible is a fast shock, with $v_{\mathrm{I}} > \sqrt{v_{\mathrm{AI}}^2 + \tilde{c}_{s\mathrm{I}}^2}$. The component jump produced by this shock can be written as

$$r = \frac{2(\Gamma+1)}{D + \sqrt{D^2 + 4(\Gamma+1)(2-\Gamma)M_{\mathrm{AI}}^{-2}}}, \tag{4.28}$$

where $D = (\Gamma-1) + (2M_{\mathrm{I}}^{-2} + \Gamma M_{\mathrm{AI}}^{-2})$ and $M_{\mathrm{AI}}$ the Alfvenic Mach number.

Furthermore, the ion acoustic speed in the downstream shock region can be written as

$$\frac{\tilde{c}_{s\mathrm{II}}^2}{V_1^2} = \frac{\Gamma}{r^2}\left[r\left(1 + \frac{M_{\mathrm{I}}^{-2}}{\Gamma} + \frac{M_{\mathrm{AI}}^{-2}}{2}\right) - r^3\frac{M_{\mathrm{AI}}^{-2}}{2} - 1\right]. \tag{4.29}$$

Figure 4.3 shows variation of the ion fluid and ion acoustic velocity as a function of the upstream Alfvenic Mach number, where the upstream acoustic Mach number has been taken in the limit $M_{\mathrm{I}} \longrightarrow \infty$, corresponding to vanishing upstream pressure $\Pi_{\mathrm{I}} \longrightarrow 0$.

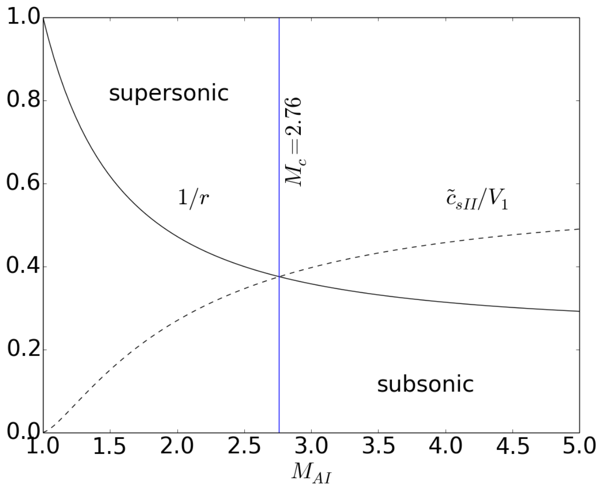

Figure 4.3 – Dependence of the downstream normalised flow $V_2/V_1$ and sound $\tilde{c}_{s\mathrm{II}}/V_1$ velocities on the upstream Alfvenic Mach number for an ideal MHD perpendicular shock with zero upstream pressure $\Pi_{\mathrm{I}} \longrightarrow 0$. The vertical line represents the critical Mach number which is $M_{\mathrm{AI}} = 2.76$.

The crossing of the two curves defines the critical Mach number which is $M_c \simeq 2.76$, found numerically for a resistive shock by (Marshall, 1955). The supercritical regime is thus, realized if the fluid velocity in the downstream shock region is subsonic ($\tilde{c}_{s\mathrm{II}} > V_2$).

Subcritical shocks are capable of generating a sufficient dissipation to account for retardation, thermalisation and entropy in the time it takes the flow to cross the shock front from upstream to downstream. The relevant processes are based on wave-particle interaction between the shocked plasma and the shock-excited turbulent wave fields.

For supercritical shocks this is, however, not the case. Supercritical shocks involve mechanisms different from wave-particle interaction permitting to dissipate the excess energy in the bulk flow that cannot be dissipated by any classical anomalous dissipation. Above the critical Mach number an efficient way of energy dissipation is rejection of the in-flowing excess energy from the shock by reflecting a substantial part of the incoming plasma back upstream. There is thus a qualitative change in the shock character above it that is not contained in the Rankine-Hugoniot conditions and the MHD model. The physical processes involved into the reflection process and their effects on the structure of the shock are discussed in the last section of this Chapter.

Thus, the description given in Fig.4.2 applies only to subcritical laminar shocks. Supercritical higher Mach number shocks behave in a more complicated way being much less dependent on dissipation and dispersion.

The approximation of a high-pressure plasma ($\tilde{c}_s^2 >> v_{\mathrm{A}}^2$) is very restricted. It is so, important to find dispersion relations for the waves the case $\tilde{c}_s^2 \simeq v_{\mathrm{A}}^2$, where equation (4.24) cannot be applied anymore. Numerical codes are inevitable to investigate this nonlinear physics.

It is also important to note that the Rankine-Hugoniot relations are based on a single-fluid MHD approach. Collisionless plasmas support energetic structures that are not captured by a single-fluid MHD theory and that can play a vital role in the thermalization of plasmas. Magnetosonic solitons are one of many examples of these structures (Stasiewicz et al., 2003; Gueroult et al., 2017) as well as the beams of shock-reflected particles ahead of the bow shock (Eastwood et al., 2005), which enforce a non-stationarity of the shock. Single-fluid MHD simulations are nevertheless used to solve problems in collisionless plasma based on the argument that they can describe the plasma dynamics on a large spatial scale. Indeed, as we demonstrate with PIC simulation studies, the MHD model is capable to reproduce large scale features of the collisionless plasma evolution.

## 4.2 Emergence of MHD structures in collisionless PIC simulation plasma

The plasma model, implemented in PIC codes neglects the binary collisions between particles compared to the collective interaction processes. Binary collisions are essential in an MHD model as they remove nonthermal plasma features and equilibrate the temperatures of all plasma species.

Many experiments have been confirmed the pertinence of the single-fluid MHD model. These are shock tube experiments investigating the thermal expansion of plasma. In a shock tube experiments (Dolder and Hide, 1960; Borisov et al., 1971), a thermal pressure gradient in a magnetized plasma accelerates a dense plasma in a dilute ambient plasma and a rarefaction wave develops. Interaction of the expanding plasma with the ambient plasma triggers shocks if the expansion speed exceeds the phase velocity of the fastest ion wave. In the rest frame of the shock, the fast-moving upstream ambient plasma is slowed down, compressed and heated as it crosses the shock and moves downstream. This net flux adds material to the downstream plasma, which lets the shock expand into the upstream direction. These shock tube experiments are describing in a one-dimensional geometry, shocks in a magnetized and collisional plasma. The equations of single-fluid MHD are well adapted to study such shocks, if collisions are frequent enough to establish a thermal equilibrium between electrons and ions on the time scales of interest. The MHD shocks emerge under such conditions (Brio and Wu, 1988; Falle et al., 1998). However, not all plasma shocks are collisional, and the experiments in shock tubes using collisionless plasmas produce different results.

In this Chapter we examine with the particle-in-cell (PIC) code EPOCH (Arber et al., 2015) relaxation of a thermal pressure gradient in a plasma in the presence of an external magnetic field. We show that these kinetic shocks are transient and that some the plasma dynamics features can be eventually described with the single-fluid MHD model (Myong and Roe, 1997). The plasma parameters are within reach for laser-plasma experiments and our results can thus be tested experimentally.

### 4.2.1 Initial conditions

We use the following inital conditions for our simulation. We resolve one spatial dimension $x$ and three particle velocity components. Periodic boundary conditions are used for the fields and for the computational particles (CPs). The simulation box is large enough to separate effects introduced by the boundaries from the area of interest. The length $L_0 = 0.75$ m of the simulation box is subdivided into evenly spaced grid cells with the length $\Delta_x = 5\mu\text{m}$. The particle dynamics is determined in PIC simulations exclusively by the charge-to-mass ratio. We consider here fully ionized nitrogen $N^{7+}$ that is frequently used in laser plasma experiments. A dilute ambient plasma fills the interval $0 < x < 2L_0/3$. Its electron and ion temperatures are $T_e = 2.32 \times 10^7$K and $T_i = T_e/12.5$. This plasma also possesses an ion density $n_i = n_0$ and an electron density $n_e = 7n_0$ with $n_e = 2.75 \times 10^{20}\text{m}^{-3}$. A denser plasma fills the interval $-L_0/3 \leq x \leq 0$. This high-pressure plasma has a density, which exceeds that of the ambient plasma by a factor 10. The electron temperature of the high-pressure plasma is 3 times higher than that of the ambient plasma, $3T_e$, while the ion temperature is the same in both plasmas, $T_i$ . All species are initially at rest. A sketch of the simulation initial conditions is provided in figure 4.27 (left). In the simulations of this section we represent the electrons and ions of the ambient plasma by $3 \times 10^4 \text{CP}s$ each, while the electrons and ions of the dense plasma are each resolved by $4.5 \times 10^4$CPs. A spatially uniform background magnetic field with the strength $B_0 = 0.85$T is applied in the simulation box its angle with respect to the flow direction is discussed below. The lengths are measured in the units of $r_{ge}$, the electron thermal Larmor radius. The simulation box covers with $\hat{x} = x/r_{ge}$ the interval $-2000 < \hat{x} < 4000$. Time and frequency units are defined by the electron cyclotron frequency $\omega_{ce}$. The ion density $n_{ion}$ is expressed in units of $n_0$. We examine the late times $T_0 \leq t \leq T_{max}$ with $T_0 = 461$(190ns). We resolve $T_{max} = 553$(227ns) by $1.4 \times 10^7$ time steps. The values for the parameters of the ambient plasma are listed in Table 4.1.

Most of these parameters have already been introduced such as the electron plasma frequency

| Parameter | Numerical value |
|---|---|
| $\omega_{pe} = (n_e e^2/\epsilon_0 m_e)^{1/2}$ | $9.35 \cdot 10^{11} \mathrm{s}^{-1}$ |
| $\omega_{ce} = e\mathrm{B}_0/m_e$ | $1.5 \cdot 10^{11} \mathrm{s}^{-1}$ |
| $v_{the} = (k_\mathrm{B} \mathrm{T}_e/m_e)^{1/2}$ | $1.87 \cdot 10^{7} \mathrm{m.s}^{-1}$ |
| $r_{ge} = v_{the}/\omega_{ce}$ | $1.25 \cdot 10^{-4} \mathrm{m}$ |
| $\omega_{pi} = (\mathrm{Z}^2 n_i e^2/\epsilon_0 m_i)^{1/2}$ | $1.54 \cdot 10^{10} \mathrm{s}^{-1}$ |
| $\omega_{ci} = \mathrm{Z}e\mathrm{B}_0/m_i$ | $4.07 \cdot 10^{7} \mathrm{s}^{-1}$ |
| $\omega_{lh} = ((\omega_{ce}\omega_{ci})^{-1} + \omega_{pi}^{-2})^{-1/2}$ | $2.46 \cdot 10^{9} \mathrm{s}^{-1}$ |
| $c_s = ((\Gamma_e \mathrm{T}_e + \Gamma_i \mathrm{T}_i)/m_i)^{1/2}$ | $4.03 \cdot 10^{5} \mathrm{m.s}^{-1}$ |
| $v_a = \mathrm{B}_0/(\mu_0 n_0 m_i)^{1/2}$ | $7.9 \cdot 10^{5} \mathrm{m.s}^{-1}$ |
| $c_{ms} = (v_a^2 + c_s^2)^{1/2}$ | $8.88 \cdot 10^{5} \mathrm{m.s}^{-1}$ |

Table 4.1 – Plasma parameters in the ambient plasma.

$\omega_{pe}$, the gyro-frequency $\omega_{ce}$ , the electron thermal speed $v_{the}$ the thermal gyroradius $r_{ge}$, the ion plasma frequency $\omega_{pi}$, the gyro-frequency $\omega_{ci}$, and the Alfvén speed $v_\mathrm{A}$.

In the case of waves travelling orthogonally to the magnetic field, the electron mobility is limited to spatial scales comparable to the electron gyroradius. The ion density gradient drives an ambipolar electric field if the electrons can still move on spatial scales below their gyroradius. The ambipolar electric field and the ion density gradient have antiparallel components, which enforces an electron drift in the direction orthogonal to the magnetic field and to the density gradient. The electron response to the ambipolar electric field is affected by their gyro- and drift motion, which modifies in turn the dispersion relation of the electric field oscillations. This effect plays an important role at frequencies above the ion gyrofrequency $\omega_{ci}$.

The single fluid MHD approximation breaks down at such high frequencies and it has to be replaced by a two-fluid approximation.
We define the ion acoustic speed $c_s$ using the so called two-fluid approximation (in difference from $\tilde{c}_s$ defined for a single fluid model). The speed $c_s$ is found by solving the system of momentum equations for the electrons and the ions, assuming the charge neutrality and without external electric or magnetic field. The resolution of this set of equation results in the dispersion equation for the ion acoustic wave $\omega = kc_s$ where

$$c_s = \sqrt{\frac{\Gamma_e \mathrm{T}_e + \Gamma_i \mathrm{T}_i}{m_i}}. \tag{4.30}$$

The values of the adiabatic indexes $\Gamma_{e,i}$ are defined by (1.26), depending of the number of degrees of freedom. The thermal speed of the electrons is much larger than the ion acoustic speed, $v_{\mathrm{T}he} >> c_s$, the electrons can travel many wavelengths during a single ion wave oscillation period. Thus the electrons are fast enough to equalise the electron temperature and therefore the electron compressions are isothermal in the ion acoustic wave, and $\Gamma_e = 1$. It is also important to note that when the collision frequency is small, the plasma may not have enough time to distribute the changes of thermal energy to all degrees of freedom, and then the situation can be reduced to lower dimensionality. In our simulation the electrons and ions are considered as adiabatic, with 3 degrees of freedom for the electrons $\Gamma_e = 5/3$, and only one degree of freedom along the box direction for the ions, $\Gamma_i = 3$. The latter is due to the fact that in a high pressure plasma, the dispersion effect becomes important at frequency above $\omega_{ci}$, where the ion trajectory is only weakly distorted by the magnetic field in one oscillation period. It is so possible to consider the ion motion as one-dimensional. The magnetosonic speed corresponding to this ion acoustic speed is $c_{ms} = \sqrt{c_s^2 + v_\mathrm{A}^2}$. Both speeds are close to their MHD counterparts, $\tilde{c}_s, \tilde{c}_{ms}$.

Furthermore, the two-fluid approximation reveals the presence of an almost electrostatic wave branch, which is known as the lower-hybrid (LH) mode. The dispersion relation of LH waves is discussed in various approximations in (Verdon et al., 2008, 2009). We define here the lower-hybrid

(LH) frequency

$$\omega_{lh} = ((\omega_{ce}\omega_{ci})^{-1} + \omega_{pi}^{-2})^{-1/2}, \tag{4.31}$$

using the approximate solution of the linear dispersion relation of LH waves, which is based on the two-fluid electrostatic cold plasma approximation. The latter takes into account the warm plasma effects and neglects electromagnetic effects. It is valid for large wavenumbers and for waves that move strictly perpendicular to the magnetic field $\mathbf{k}\cdot\mathbf{B} = 0$. This LH frequency becomes a resonance frequency at low wavenumbers, where thermal effects are negligible. Since the LH wave can have a shorter wavelength and a higher frequency than magnetosonic waves, this wave steepens into a shock faster and on a smaller spatial scale. The LH waves have received attention with respect to the instabilities close to shocks (McClements et al., 1997), and LH shocks have been observed recently in PIC simulations by (Dieckmann et al., 2016).

The ambipolar electric field, which develops at the jump of the thermal pressure between the high-pressure plasma and the ambient plasma, forms a double layer (Hershkowitz, 1981) that lets the plasma expand in the form of a rarefaction wave. Such waves have been described by (Allen and Andrews, 1970) in a low pressure plasma under conditions where ionization processes can be neglected. The rarefaction wave expands plasma (Crow et al., 1975; Mora, 2005) in the ambient gas until a shock forms. Expanding dense plasmas can be assimilated to an expanding blast shell coming from the solar wind which shocks the Earth's magnetopause (Lugaz et al., 2016; Goldstein et al., 2016).

Figure 4.4 (right) shows schematically the expansion of the blast shell in the ambient plasma, and the formation of the rarefaction wave. The expansion speed of the blast shell, for the simulations, presented here is sufficiently low so no shock reformation takes place (Gueroult et al., 2017). The latter mechanism will be discussed in the last section of this chapter.

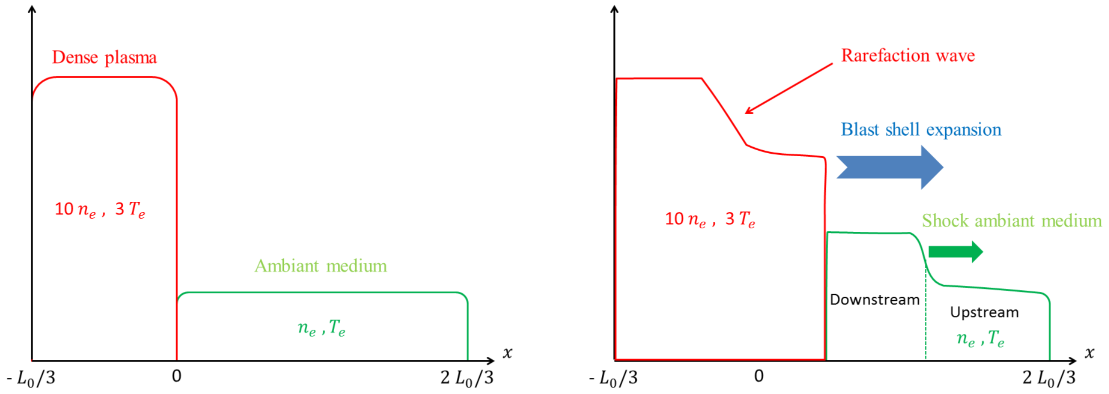

Figure 4.4 – Sketch of the initial plasma density distribution (left) and the rarefaction wave and shock formation (right) in a shock tube setup.

The setup of our simulations is the same as in (Dieckmann et al., 2016), where the external magnetic field was perpendicular to the blast shell expansion. The effect of adding this magnetic field was to replace the ion acoustic wave by the lower-hybrid (LH) wave branch, with a phase speed at large wavenumbers comparable to the ion acoustic speed $c_s$. The initial evolution of the expanding plasma formed a lower-hybrid wave shock at the front of the expanding plasma, which has no counterpart in a single-fluid theory.

In this section we discuss the collisionless shock characteristics as function of the angle between the shock normal and the magnetic field direction on much larger time scales than (Dieckmann et al., 2016) (by a factor 100). We compare aspects of the dispersion relation of a collisionless plasma with those of a single-fluid MHD model.

### 4.2.2 Fast magnetosonic shock with wave precursor in a collisionless plasma

For this simulation, the external magnetic field is aligned with the z-axis, stricly perpendicular to the direction of the simulation box. Two waves can be excited in this geometry at $\theta = 90°$; sound waves with the speed $\tilde{c}_s$ and an incompressible Alfvén wave with the speed $v_A$. The following results have been obtained in this geometry by (Dieckmann et al., 2017b), and are useful for the understanding of the next studies.

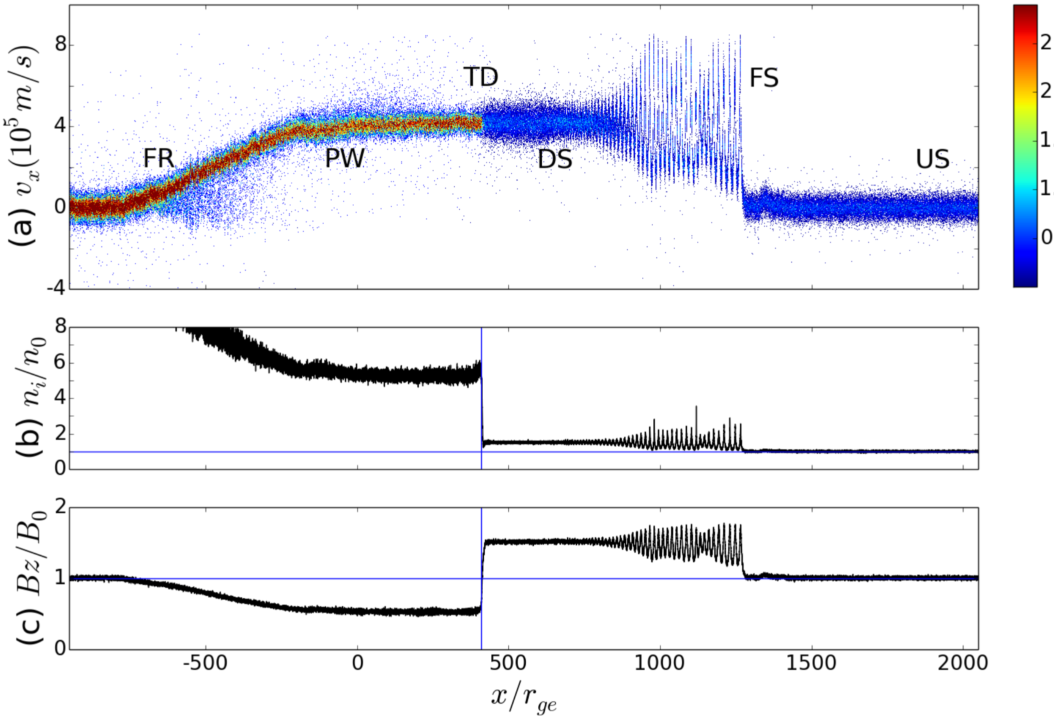

Figure 4.5 – The plasma state at the time $t\omega_{ce} = 2 \times 10^4$: panel (a) shows the phase space density distribution of the ions normalized to the maximum upstream value and clamped at 2.9 for visualization reasons. We recognize the fast rarefaction wave (FR), the precursor wave (PW), the tangential discontinuity (TD), the fast shock (FS), and the upstream/downstream (US/DS) ions. Panel (b) shows the ion density $n_i/n_0$ . The blue lines denote $n_i = n_0$ and $x/r_{ge} = 410$. The magnetic $B_z$ component is plotted in (c). The blue line denotes $B_z = B_0$ and $x/r_{ge} = 450$. The obliquity is $\theta = 90°$.

Figure 4.5 shows the ion phase space density, the ion density and the magnetic field at the time $T_0$. The ions of the dense blast shell plasma are on the left of Fig.4.5(a) where the ion phase space density has its maximum and where the mean velocity of the ions vanishes. The rarefaction wave, that propagates to the left into the dense plasma, accelerates ions to the right, in the interval $-750 \leq x \leq -200$. The ion density and the amplitude of $B_z$ decrease and the ion speed increases with increasing $\hat{x}$, a characteristic of fast rarefaction waves. The latter expands up to $\hat{x} \simeq -200$ and ends in a precursor wave that is confined to the end of the rarefaction wave. The magnetic field and the density across the precursor wave are modulated in phase which is the characteristic of a fast mode as described in the previous section. This mode is spatially damped in the direction of larger $\hat{x}$. The accelerated ions form a blast shell that expands with a constant speed, temperature and density up to $\hat{x} \approx 410$. The ion velocity remains constant but, after $\hat{x} \approx 410$, the ion density decreases, while the ion temperature and the amplitude of $B_z$ increase. This anticorrelation of both quantities in this structure is characteristic of a tangential discontinuity.

This structure is stable and long-lived. After the discontinuity, the ion distribution, density and the magnetic field remain unchanged in the interval $410 < \hat{x} < 750$. Oscillations of a fast magnetosonic shock appear further in the interval $750 < \hat{x} < 1300$. The downstream region is defined as the interval $410 < \hat{x} < 750$ that is enclosed by the tangential discontinuity and the fast magnetosonic shock. The ions close to the tangential discontinuity at $\hat{x} \simeq 410$, move at the spatially uniform mean speed $v_b \simeq 4.1 \times 10^5 \mathrm{m.s}^{-1}$ or $v_b \simeq c_{ms}/2$. The latter is the speed of the downstream plasma in the upstream frame.

The ion phase space density, ion density and magnetic field change rapidly over $5r_{ge}$ and reach their respective downstream values $\mathrm{B}_z \simeq 1.5\mathrm{B}_0$ and $n_{ion} \simeq 1.5n_0$ at $\hat{x} = 420$. The variation of magnetic field is sustained by a current of drifting electrons along the y axis.
The change in $\mathrm{B}_z$ is sustained by an electron drift along $y$ and the electron temperature to the right of the discontinuity (TD in figure 4.5) is about 100 eV below that to the left (initial dense plasma temperature is 3 keV). The variation of density yields a thermal pressure gradient force that points in the opposite direction of the magnetic pressure gradient force. The thermal pressure is controled by the electrons and takes the form $\mathrm{P}_{th}(\hat{x}) \simeq n_e(\hat{x}) k_\mathrm{B} \mathrm{T}_e(\hat{x})$. This pressure changes close to $\hat{x} = 410$ as $\Delta\mathrm{P}_{th} = \mathrm{P}_{th}(\hat{x} > 410) - \mathrm{P}_{th}(\hat{x} < 410)$. The electron density and magnetic field variation along the discontinuity is $\Delta n_e = 25n_0$ and $\Delta\mathrm{B} = \mathrm{B}_0$, which gives $|\mathrm{P}_\mathrm{B}(\hat{x} > 410) - \mathrm{P}_\mathrm{B}(\hat{x} < 410)| = \Delta\mathrm{P}_\mathrm{B} \simeq 0.6\Delta\mathrm{P}_{th}$.
The upstream medium at $\hat{x} \simeq 1300$ exerces a ram pressure $\mathrm{P}_\mathrm{R} = 0.5 n_0 m_i v_b^2$. The latter balances the difference between the thermal and magnetic pressure at $\hat{x} = 410$, $\mathrm{P}_\mathrm{R} \simeq 0.5\Delta\mathrm{P}_{th}$, which implies that the discontinuity position is stationary in the downstream frame. Since the Larmor radius of the energetic ions, which move with a few $10^5 \mathrm{m.s}^{-1}$ in the downstream frame, is only about $100r_{ge}$, consequently, they are confined and cannot cross the tangential discontinuity.

The front of the fast magnetosonic shock in figure 4.5(a) reveals ion velocity oscillations with an amplitude $\simeq v_b$. These oscillations are non-linear as confirmed by the non-sinusoidal oscillations of the ion density and the magnetic field distributions in figure 4.5(b,c). The magnetic pressure and the thermal pressure, are in phase which suggests that these waves are fast magnetosonic waves.

Figure 4.6 depicts at the front of the expanding plasma, $\mathrm{B}_z - \mathrm{B}_0$, and the ion energy density $\vartheta_i$.

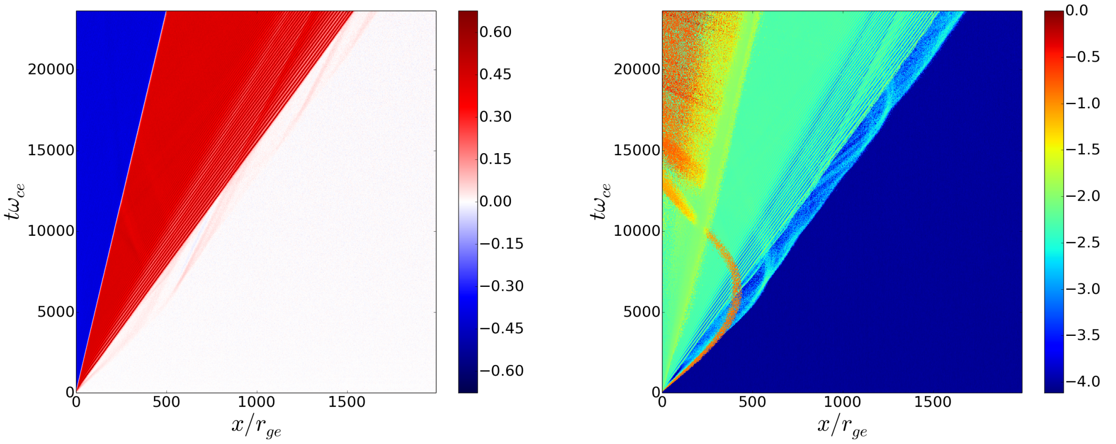

Figure 4.6 – The spatio-temporal evolution of $\mathrm{B}_z - \mathrm{B}_0$ in Tesla unit (left), and of the 10-logarithmic of $\vartheta_i$ (right) during the simulation time.

The tangential discontinuity separates the region where $\mathrm{B}_z < \mathrm{B}_0$ to $\mathrm{B}_z > \mathrm{B}_0$ (cf. Figure 4.6 left, blue and red color respectively). Due to this large gradient on $5r_{ge}$ the electrons are heated close to the discontinuity. The ions from the dense and hot blast shell which cross the tangential discontinuity at the initial time perform their gyration in the ambient medium (cf. Figure 4.6 right, red color), and return to the tangential discontinuity (these ions represent only a very low percentage of the blast shell). A population of ambient ions from the upstream medium are reflected by the shock ramp and are confined close to the ramp ($\sim 100r_{ge}$). The plasma passing the ramp is heated by the fast magnetosonic waves and oscillate in phase with the magnetic field.

The nature of oscillations in the shock transition layer can be determined from the dispersion relation of the system. Since the waves are confined to the downstream plasma, their properties must be evaluated in the downstream frame. Transformation from the laboratory frame to the downstream frame gives the following space/time components, $x^* = \hat{x} - v_b t^* - 1300$ and $t^* = (t - \mathrm{T}_0)$, since the shock is localized at $\hat{x} = 1300$ at time $\mathrm{T}_0$. The ion density and magnetic field are $\sim 1.5 n_0$ and $\sim 1.5 \mathrm{B}_0$ in the downstream region, which gives a lower-hybrid frequency $\omega_{lh}^* = 1.5\omega_{lh}$ .

Figure 4.7 depicts $\mathrm{B}_z(x^*, t^*)$ at the front of the expanding plasma. The wave front moves at the speed $v_{wf} \simeq 8.5 \times 10^5 \mathrm{m.s}^{-1}$, which corresponds to the shock speed measured in the downstream frame $x^*$ and it is thus well below the fast magnetosonic speed $c_{ms}^* = (v_a^{*2} + c_s^{*2})^{1/2} \simeq 1.3 \times 10^6 \mathrm{m.s}^{-1}$ in the downstream plasma.

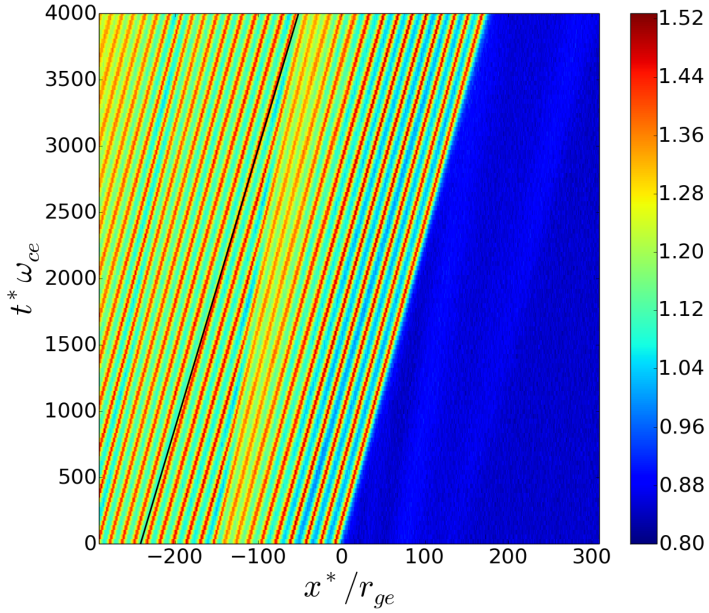

Figure 4.7 – The evolution in time of $\mathrm{B}_z(x^*, t^*)$ in the downstream reference frame that moves with $v_b$ sampled in the downstream frame of reference. The black line correspond to the speed $v_{wf}$.

The speed of the wave front in the upstream medium is supersonic with $v_{wf} + v_b \simeq 1.5 c_{ms}$. The power spectrum $\mathrm{S_B}(k, \omega)$ of $\mathrm{B}_z(x, t)$ is shown in Fig.4.8. The latter was measured in a separate PIC simulation which modelled a spatially uniform plasma in a thermal equilibrium with the plasma parameters of the downstream region in Fig.4.5(a). The plasma was initialized with the parameters given in Table 4.1 in a box of 1 m length with periodic boundary conditions and the field evolution was studied over the time interval $0 \leq t\omega_{ce} \leq 1.7 \times 10^4$. The wave spectrum was obtained by sampling the magnetic field $\mathrm{B}_z(x, t)$, taking its Fourier transform over space and time and squaring the modulus, $\mathrm{S_B}(k, \omega) = |\mathrm{B}_z(k, \omega)|^2$. The spectrum in PIC simulations peaks at values $(\omega, k)$, which correspond to eigenmodes of the system (Dieckmann et al., 2004). The maxima of $\mathrm{S}(k, \omega)$ regions in $k, \omega$-space where waves are weakly damped. The noise vertical blue lines with periodic wavenumbers are electrostatic periodic modes induced by the periodic boundary conditions of our simulation.

This power spectrum is compared to the dispersion relation of the fast magnetosonic mode $\omega / k = c_{ms}^*$ in the longwavelength limit $k \longrightarrow 0$. The dispersion relation $\omega_f$ follows the frequency interval with strong fluctuations for $kr_{ge} < 0.15$. The dispersion relation of plasma normal modes takes into account also the electrostatic component of the fast magnetosonic mode, which becomes important close to $\omega_{lh}$. The frequency of the mode increases beyond $\omega_f$ for $kr_{ge} > 0.15$.

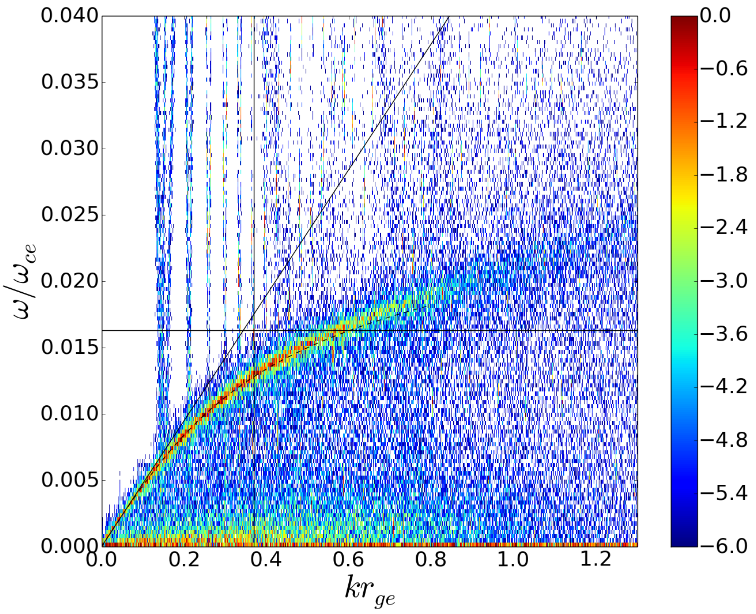

Figure 4.8 – The 10-logarithmic power spectrum $S_B(k,\omega)$ of $B_z(x,t)$. The dispersion relation $\omega_f = v_f v_{the}^{-1} k$ is overplotted and the horizontal line is $\omega = \omega_{lh}\omega_{ce}^{-1}$. The vertical line represents the wavelength of the fast magnetosonic mode in figure 4.5. Strong fluctuations indicates weakly damped waves and the dash line represents a fit of location of strong fluctuations.

The dispersion relation is concave at such large $k$ (Sagdeev, 1966). The band with the strong fluctuations cannot cross $\omega_{lh}$, which is a resonance for perpendicular magnetic field in a cold plasma (Verdon et al., 2008), and the high wavenumbers are blocked at the lower-hybrid frequency. The phase speed of modes with $kr_{ge} > 0.15$ decreases. The dispersion relation thus explains why the wave front in Fig.4.5(a) moves at the speed $v_{wf} \simeq 0.65c^*_{ms}$. The steepening of the fast magnetosonic shock results in waves with a larger k that fall behind the shock due to their lower phase speed.

### 4.2.3 Quasi-perpendicular fast magnetosonic shock with wave precursor in a collisionless plasma

The previous one-dimensional PIC simulation described propagation of MHD shocks across a perpendicular magnetic field. Shocks reach a steady state (Forslund and Freidberg, 1971; Dieckmann et al., 2016, 2017b) if they move slow enough to avoid a self-reformation, as discussed in (Gueroult et al., 2017) and in the last section of this Chapter. If the shock propagates perpendicularly to the magnetic field then the dispersion relation of fast magnetosonic waves is concave for high frequency waves, which implies that their phase velocity decreases with increasing wave numbers; shock steepening drives slower waves that fall behind the shock as seen in Ref. (Dieckmann et al., 2017b) and in figure 4.5.

Waves, which propagate obliquely to the magnetic field, can be subdivided into fast modes with the phase speed $v_f$ and slow modes with the phase speed $v_s$ as explained in section 4.1. The fast mode (addition of both terms on the right hand side in equation (4.16)) is characterized by a magnetic pressure and a thermal pressure that are in phase, while both pressures are in antiphase in the case of the slow mode (Balogh and Treumann, 2011). The phase speed of the slow mode goes to zero as $\theta \rightarrow 90^\circ$ (see eq. (4.22) and (4.23) in section 4.1) and it becomes a tangential discontinuity. Magnetohydrodynamic shocks can be sustained by the slow and fast modes as well as by acoustic waves (Verscharen et al., 2017).

Here we demonstrate with a one-dimensional PIC simulation how turning the concave dispersion relation into a convex one removes the trailing wave and gives rise to a shock precursor. The precursor is formed by fast magnetosonic modes that outrun the shock. The initial conditions match those in the previous subsection except for the magnetic field direction, which makes an angle $\theta = 85^\circ$ with respect to the shock normal. The plasma parameters that determine the properties of the magnetized plasma are defined in Table 4.1. Equation (4.16) gives the speeds $v_f \approx v_{fms}$ and $v_s \approx v_{fms}/25$ for $\theta = 85^\circ$ and the dispersion relations of the slow and fast modes are $\omega_{s,f} = v_{s,f} k$.

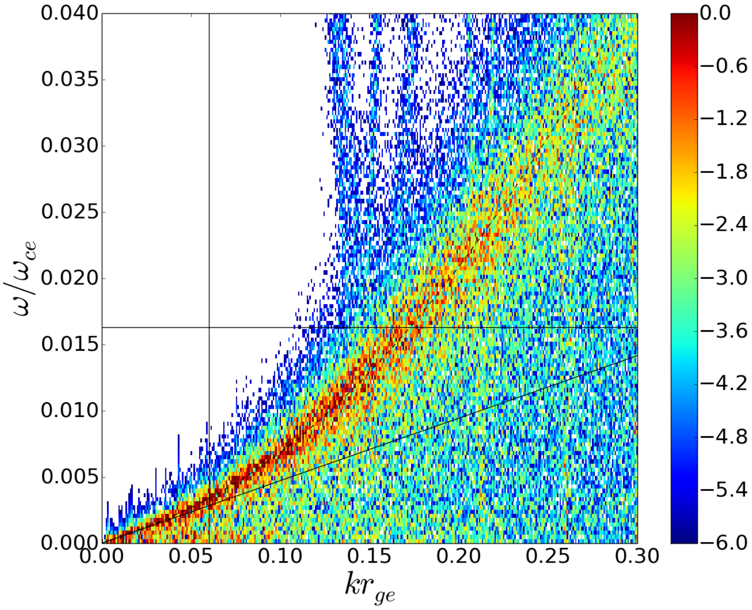

Figure 4.9 – The 10-logarithmic power spectrum $P_B(k,\omega)$ of $B_z(x,t)$ for $\theta = 85^\circ$. The dispersion relation $\omega_f = v_f k$ is overplotted and the horizontal line is $\omega = \omega_{lh}$. The vertical line represents the wavelength of the fast magnetosonic mode in figure 4.10. Strong noise indicates weakly damped waves and the dashed line represents the fit of the strong noise.

The dispersion relations of the fast/slow modes $\omega_{f,s} = v_{f,s} k$ are estimated with a separate PIC simulation. The simulation conditions are the same than those used in the previous subsection, except the magnetic field orientation. Figure 4.9 shows the power spectrum $S_B(k,\omega)$ of $B_z(x,t)$. Strong fluctuations indicate regions in $k,\omega$-space where waves are weakly damped. The dispersion relation $\omega_f$ follows the frequency interval with strong fluctuations for $kr_{ge} < 0.05$. The frequency of this mode increases beyond $\omega_f$ for $kr_{ge} > 0.05$. The dispersion relation is convex at such large $k$ (Sagdeev, 1966). The band with the strong fluctuations crosses $\omega_{lh}$, which is not a resonance frequency for $\theta = 85^\circ$, since $\cos^2\theta \not\lesssim m_e/m_i$ (Verdon et al., 2008), and it gradually damps out with increasing $\omega$. Modes with $kr_{ge} \approx 0.15$ reach a frequency $\omega \approx 0.015\omega_{ce}$. Their phase speed is $v_{the}/10 \approx 2v_f$.

Figure 4.10 shows the ion phase space density, ion density and magnetic field at the time $T_0$. The ion phase space density has maximum at the left of Fig.4.10(a) where the mean velocity is zero. These are the ions of the dense plasma. The ions gain speed with increasing $x$ in the interval $-500 \leq x/r_{ge} \leq -50$ and their density decreases in Fig.4.10(b). The ion acceleration is accomplished by the rarefaction wave that propagates to the left into the dense plasma and accelerates its ions to the right. The accelerated ions form a blast shell that expands with a constant speed and density up to $x/r_{ge} \approx 400$. The ion velocity remains constant but the density decreases from its value in the blast shell to the density $n_i \approx 1.5n_0$. In the region $400 < x/r_{ge} < 700$, the magnetic field amplitude and, hence, the magnetic pressure increase as the ion density decreases and the anticorrelation of both is characteristic of a slow magnetosonic wave (see SW region in Fig.4.10). A

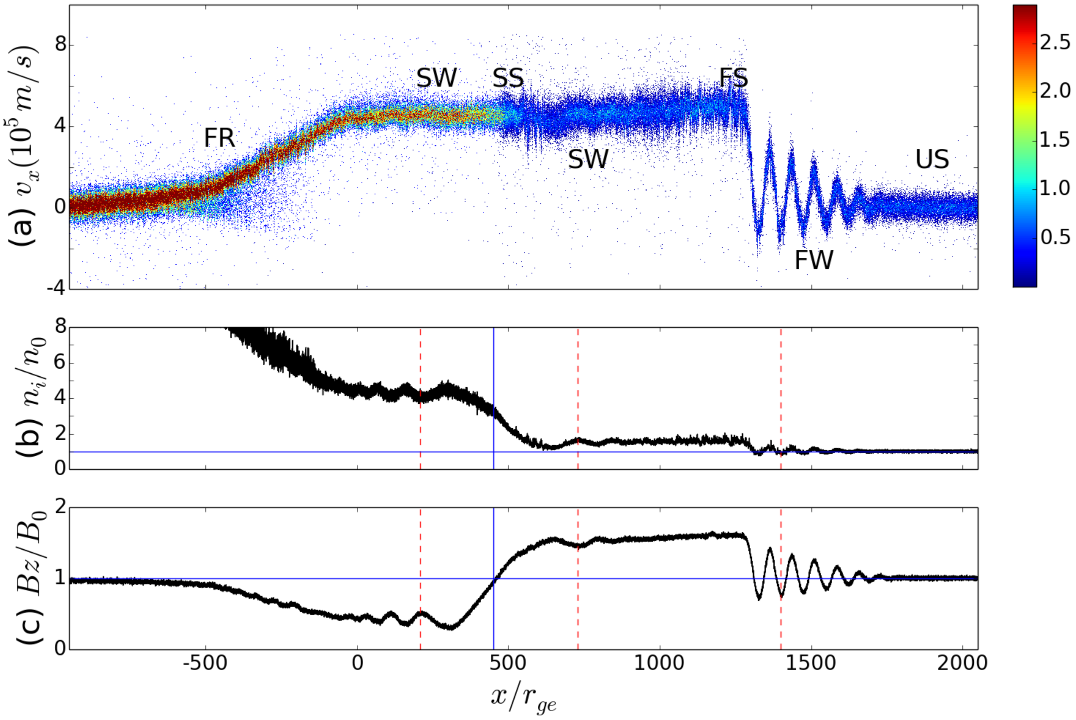

Figure 4.10 – The plasma state at the time $t\omega_{ce} = 2 \times 10^4$: panel (a) shows the phase space density distribution of the ions normalized to the maximum upstream value and clamped at 2.9 for visualization reasons. We recognize the fast rarefaction wave (FR), the slow shock (SS), the fast shock (FS), the fast wave (FW) precursor and the upstream (US) ions. We observe a slow wave (SW) precursor close to the slow shock. Panel (b) shows the ion density $n_i/n_0$ . The blue lines denote $n_i = n_0$ and $x/r_{ge} = 450$. The magnetic $B_z$ component is plotted in (c). The blue line denotes $B_z = B_0$ and $x/r_{ge} = 450$. The dashed red lines in (b,c) emphasize the phase relation between $n_i$ and $B_z$ and, thus, the wave mode. The obliquity is $\theta = 85°$.

tangential discontinuity has been shown to form at this location in Ref. (Dieckmann et al., 2017b), which considered a magnetic field direction $\theta = 90°$. The oblique magnetic field facilitates particle transport across the discontinuity, which changes the tangential discontinuity into a slow magnetosonic shock. A slow shock, which separates the blast shell ions from those of the shocked ambient medium, has also been observed in Ref. (Dieckmann et al., 2018b) and it changed into a tangential discontinuity for an increasing propagation angle.

The source of ions in the interval $600 \leq x/r_{ge} \leq 1350$ is the ambient plasma. They have been accelerated and compressed by the forward shock, which is located in Fig.4.10(a) at $x/r_{ge} \approx 1350$. The ion density and the magnetic field amplitude both decrease with increasing $x$ across the shock and it is thus mediated by the fast magnetosonic mode. Strong waves, for which the ion density oscillates in phase with the magnetic amplitude, are observed between the shock and the upstream. The amplitude of oscillations of the ion velocity and magnetic field of this shock precursor decreases with increasing $x$ and the phase relation between the thermal and magnetic pressure shows that it is formed by the fast magnetosonic mode.

The precursor is a consequence of the convex dispersion relation observed in Fig.4.9. Shock steepening drives waves with a large wave number, which outrun the shock and propagate upstream. The wavelength of the precursor wave is $\approx 80r_{ge}$, which gives the wave number $kr_{ge} \approx 0.08$ and a phase speed $\approx 1.3v_f$ (See Fig.4.9). The precursor wave is damped with increasing $x > 1350r_{ge}$.

Waves are also observed on both sides of the slow shock which is centered at $x/r_{ge} = 500$. The vertical dashed red lines demonstrate that the oscillations of the magnetic and thermal pressures have an opposite phase, which suggests that they are slow magnetosonic waves. We gain additional information about these waves and the precursor by examining their evolution in time in their rest frame. Figure 4.10(a) shows that the ions move at the spatially uniform mean speed $v_b \sim 4.5 \times 10^5$ m/s. The simulation frame equals the upstream frame and $v_b$ is thus the speed of the rest frame of the waves in the upstream frame. We transform the distribution of $\mathrm{B}_z(x,t)$ from the upstream frame into the rest frame of the waves for the times $0 \leq t^*\omega_{ce} \leq 4000$ (where $t^*\omega_{ce} = t\omega_{ce} - 2\times10^4$) and for the coordinates $x^* = x - v_b t^*$. The moving frame matches that of Fig.4.10 at $t^* = 0$.

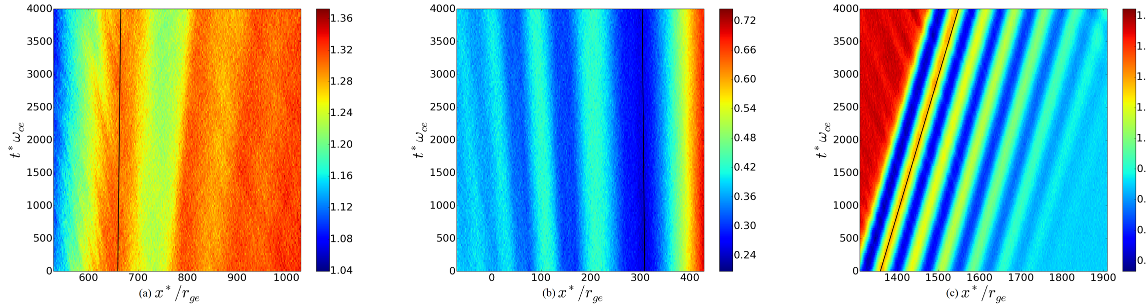

Figure 4.11 – The evolution in time of $\mathrm{B}_z$ in the reference frame that moves with $v_b$: panel (a) shows the field distribution of the magnetosonic waves to the left of the slow shock, panel (b) that of the waves to the right and panel (c) shows the magnetic field distribution of the fast shock and the precursor. The black lines in (a, b) have a slope that corresponds to the speed $v_s$, while that in panel (c) corresponds to the speed $v_f$.

Figure 4.11 shows the wave fields in three intervals of the box. The wave fields close to the slow magnetosonic shock (location $x/r_{ge} \approx 400$) in Figs. 4.11(a, b) reveal waves that propagate away from the shock. Their phase speed $\sim v_s$ together with the phase relation between the magnetic pressure and the thermal pressure in Fig.4.10 demonstrates that these are slow magnetosonic waves. The shock in Fig.4.11(c) propagates at the speed $v_f$ in the downstream frame of reference and at $v_f + v_b \simeq 1.5v_{fms}$ in the upstream frame. The precursor waves outrun the shock but their phase speed $\sim 1.3v_f$ does not much the phase velocity of the fast normal mode.

### 4.2.4 Oblique fast magnetosonic shock with wave precursor in a collisionless plasma

The obliquity of the shock is too small and the ratio between the fast and slow magnetosonic speed is large (25 times). We consider here a setup with a smaller magnetic field angle and determine a dispersion relation for the nonlinear fast magnetosonic wave as a function of the obliquity. The initial conditions match those in the previous subsection except for the magnetic field angle $\theta = 70-80^\circ$. The plasma parameters are defined in Table 4.1.

Figure 4.12 and 4.13 shows the ion phase space density, the ion density and the magnetic field at the time $T_0$ for an obliquity $\theta = 80^\circ$ and $\theta = 70^\circ$ respectively.

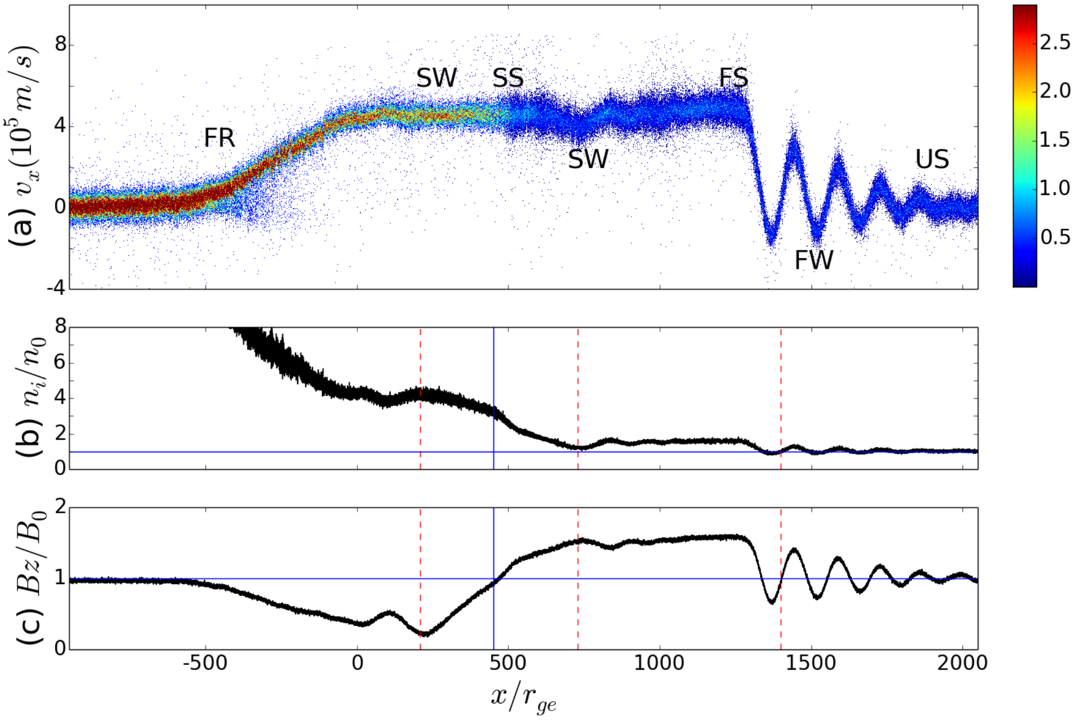

Figure 4.12 – The plasma state at the time $t\omega_{ce} = 2 \times 10^4$: panel (a) shows the phase space density distribution of the ions normalized to the maximum upstream value and clamped at 2.9 for visualization reasons. We recognize the fast rarefaction wave (FR), the slow shock (SS), the fast shock (FS), the fast wave (FW) precursor and the upstream (US) ions. We observe a slow wave (SW) precursor close to the slow shock. Panel (b) shows the ion density $n_i/n_0$ . The blue lines denote $n_i = n_0$ and $x/r_{ge} = 450$. The magnetic $B_z$ component is plotted in (c). The blue line denotes $B_z = B_0$ and $x/r_{ge} = 450$. The dashed red lines in (b,c) emphasize the phase relation between $n_i$ and $B_z$ and, thus, the wave mode. The obliquity is $\theta = 80^\circ$.

The shock characteristics are similar to the obliquity $\theta = 85^\circ$ (See Fig.4.10). The thermal pressure jump between the dense and dilute plasma drive a fast rarefaction wave, which propagats into the dense plasma and launchs a blast shell into the ambient plasma. A slow mode shock formed at the boundary between the blast shell plasma and the shocked ambient plasma. The shocked ambient plasma is separated from the pristine ambient plasma by a fast magnetosonic shock. The dominant wavelengths of the fast and the slow magnetosonic waves are larger.The increase of the wavelength with decreasing angle presents inconvenience for numerical analysis quasi-parallel shocks can only be described in simulations with a larger spatial resolution. The width of the slow shock at $x/r_{ge} = 450$ also increases with the decreasing angle theta, since the mobility of the electrons in the x-direction increases.

Dispersion relations are found by using numerical approach similar to the previous subsections. They are shown in figure 4.14. Convex dispersion relations of the fast magnetosonic modes are observed, which give rise to shock precursors as in the previous subsections.

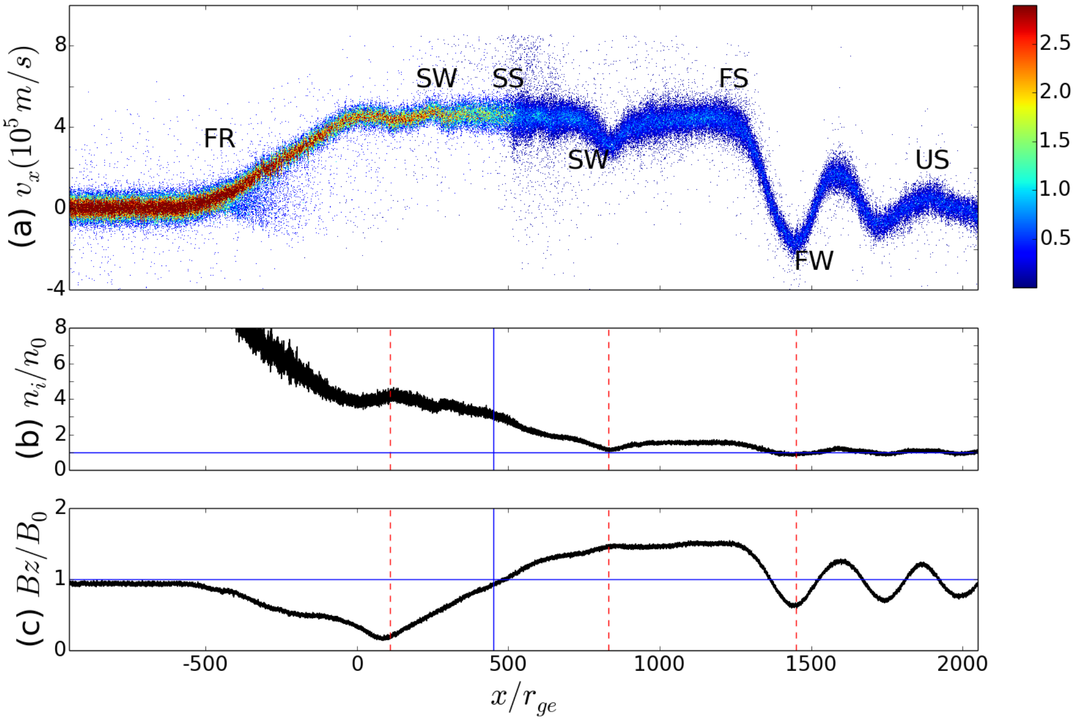

Figure 4.13 – The plasma state at the time $t\omega_{ce} = 2 \times 10^4$: panel (a) shows the phase space density distribution of the ions normalized to the maximum upstream value and clamped at 2.9 for visualization reasons. We recognize the fast rarefaction wave (FR), the slow shock (SS), the fast shock (FS), the fast wave (FW) precursor and the upstream (US) ions. We observe a slow wave (SW) precursor close to the slow shock. Panel (b) shows the ion density $n_i/n_0$ . The blue lines denote $n_i = n_0$ and $x/r_{ge} = 450$. The magnetic $B_z$ component is plotted in (c). The blue line denotes $B_z = B_0$ and $x/r_{ge} = 450$. The dashed red lines in (b,c) emphasize the phase relation between $n_i$ and $B_z$ and, thus, the wave mode. The obliquity is $\theta = 70°$.

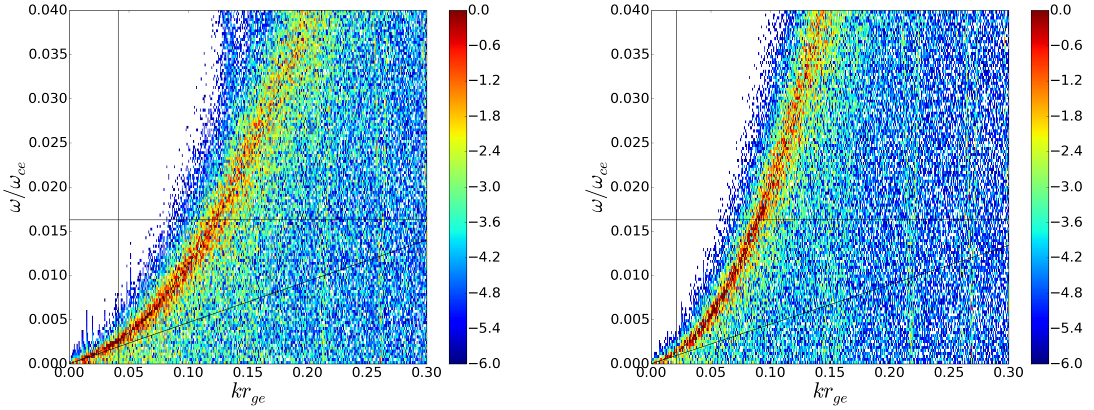

Figure 4.14 – The 10-logarithmic power spectrum $P_B(k,\omega)$ of $B_z(x,t)$ for $\theta = 80°$ (left) and $\theta = 70°$ (right). The dispersion relation $\omega_f = v_f k$ is overplotted and the horizontal line is $\omega = \omega_{lh}$. The vertical line represents the wavelength of the fast magnetosonic mode in figures 4.12 and 4.13. Strong noise indicates weakly damped waves and the dashed line represents the fit of the strong noise.

Dependence on θ of the nonlinear fast magnetosonic wave can be estimated using some numerical fit of the strong fluctuations observed in simulations. Using an equation of the form

$$\omega = k\frac{v_f}{v_{\mathrm{T}he}}\left(1 + a(\theta) * k^2\right)^b, \tag{4.32}$$

where $a(\theta)$ defines the deviation from the linearity depending of the obliquity, and $b$ is equal to $-1/2$ in the stricly perpendicular case and $+1/2$ in the other cases. Integrating different simulations and obliquity we obtained the following (fit shown with dashed line in Figs.4.8,4.9,4.14)

$$\omega = k\frac{v_f}{v_{\mathrm{T}he}}\left(1 + (\mathrm{C} + \mathrm{D}(\theta - 90)^2) * k^2\right)^{\pm 1/2}, \tag{4.33}$$

where the numerical values C and D, equal 4.33 and 3 respectively for our plasma parameters. They depend of the characteristic frequencies of the system. This dispersion relation is comparable to equation (4.24) proposed by (Sagdeev, 1966) for a high pressure plasma. Further simulations using different values of external magnetic field and plasma temperatures may reveal the dependence of C and D.

In summary we have modeled the expansion of a dense plasma into a dilute ambient plasma in presence of an initially spatially uniform magnetic field. A blast shell is launched by the propagation into the dense plasma of a fast mode rarefaction wave due to the initial thermal pressure gradient between the dense and the dilute plasmas. The discontinuity between the blast shell and the shocked ambient plasma is a tangential discontinuity in the stricly perpendicular case, the obliquity releasing the slow mode that replaces the tangential discontinuity. The nature of the shock in the ambient plasma is controlled by the dispersion relation which is concave or convex depending of the obliquity. In the stricly perpendicular case, the concave dispersion relation confines the fast magnetosonic mode in the downstream region, and in the oblique case, the convex dispersion relation gives rise to a shock precursor which softens the transition from the ambient plasma to the shocked ambient one. Because of this we could not observe a strong acceleration of ions by the shock passage. An absent shock-reflected ion beam implies that the shock did not reform by driving solitons upstream (Gueroult et al., 2017).

## 4.3 Expansion of a radially symmetric blast shell into a uniformly magnetized plasma

Magnetized collisionless shocks can be driven by a magnetic pressure gradient (Forslund and Freidberg, 1971) or by a drifting plasma (Lembege and Simonet, 2001). Another way to create a shock is to launch a rarefaction wave (Sack and Schamel, 1987; Grismayer and Mora, 2006; Grismayer et al., 2008; Thaury et al., 2010; Dieckmann et al., 2012), at the contact between a high density shell and a dilute ambient plasma. The latter case was studied in the previous section and in Refs. (Dieckmann et al., 2016, 2017b; Moreno et al., 2018c) with one-dimensional PIC simulations and in the presence of an initially spatially uniform magnetic field.

The shock speed reported in Ref. (Dieckmann et al., 2017b) exceeded 1.5 times the fast magnetosonic speed. Shocks with such a low Mach number reflect only a small fraction of the inflowing upstream ions. The beam of reflected ions is not energetic enough to enforce cyclic shock reformations observed for collisionless magnetized shocks with higher Mach numbers (Lembege and Savoini, 1992; Scholer and Burgess, 1992; Shimada and Hoshino, 2000; Hoshino and Shimada, 2002; Scholer et al., 2003; Lee et al., 2005; Chapman et al., 2005; Burgess and Scholer, 2007; Marcowith et al., 2016; Gueroult et al., 2017; Schaeffer et al., 2017a).

Structuring of the plasma flow into a rarefaction wave, a tangential discontinuity that separates the blast shell plasma from the shocked ambient plasma, and a laminar forward shock, observed in Ref. (Dieckmann et al., 2017b), closely follows the expectations following from a MHD model. In this case the shock forms on time scales much shorter than an inverse ion gyro-frequency because it involves the high-frequency part of the fast magnetosonic mode. In Ref. (Moreno et al., 2018c) we explored the changes of the shock structure as function of the angle between the shock normal and the magnetic field direction. This study is motivated by forthcoming experiments similar to that in Ref. (Schaeffer et al., 2017a). Such experiments, in which a blast shell of collisionless plasma is created by the ablation of a solid target by an intense laser pulse and interacts with a second plasma, allow one to study in the laboratory processes that take place in energetic astrophysical or solar system plasma (Remington et al., 1999; Zakharov, 2003). A similar experiment in the natural environment was conducted by the AMPTE satellite mission (Bernhardt et al., 1987), it consisted in a release in the ionosphere a cloud of barium vapors which were swiftly ionized and led to formation of shock-like structures (Chapman, 1989).

In this section, we study with PIC simulations, a similar problem of expansion of an initially radially symmetric blast shell of a collisionless plasma into a magnetized ambient medium. The simulation is conducted in 2 spatial and 3 velocity dimensions, the magnetic field is aligned with one of the directions the simulation plane. Such a setup allows us to study formation of shocks for a wide range of angles between the shock normal and the magnetic field direction. We also consider the case of a magnetic field, which is aligned with the normal of the simulation plane. We test with this simulation if instabilities like the Weibel instability in an unmagnetized rarefaction wave (Weibel, 1959; Quinn et al., 2012).

### 4.3.1 Initial conditions

We model fully ionized nitrogen ions and electrons with the correct mass ratio $m_n/m_e \approx 2.6 \times 10^4$ and with the electron charge-to-mass ratio $e/m_e$. The plasma position in the two-dimensional simulation plane is shown in Fig.4.15. Simulation 1 resolves the interval $L_1 = 16$ mm by 2000 grid cells and $L_2 = 32$ mm by 4000 grid cells. Simulation 2 resolves the side length of the quadratic box $L_1$ by 2000 grid cells. The origin of the coordinate system is placed in the center of the simulation box and the radius is $r = \sqrt{x^2 + y^2}$. A circular boundary with radius $r_0 = 2$ mm separates a dense plasma in the interval $r \leq r_0$ from the ambient plasma with $r > r_0$. The azimuthal angle relative to the positive y-axis in the counter-clockwise direction is $\rho$ (only in this section, in the other sections, $\rho$ is defined as the density).

The ambient plasma consists of ions with the number density $n_0 = 1.42 \times 10^{14}\text{cm}^{-3}$. The ions are 15 times denser in the interval $r \leq r_0$. The electrons are 7 times denser than the ions. The

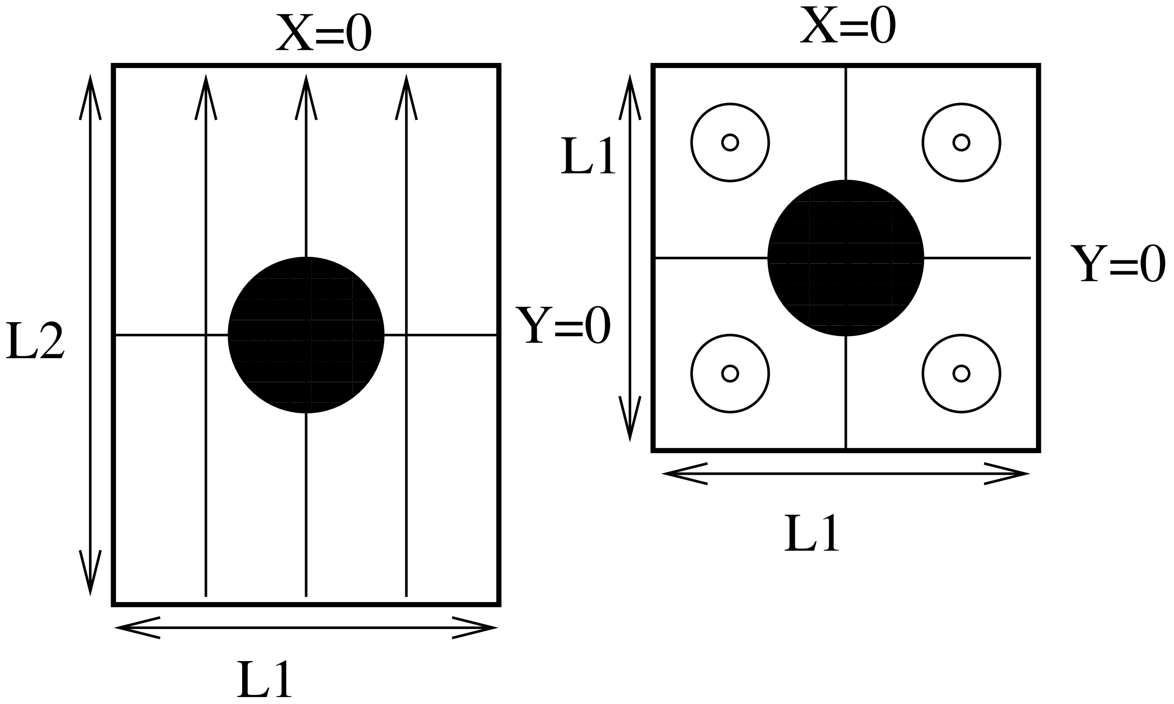

Figure 4.15 – Initial plasma distributions. The black circle shows the location of the dense ions with the density $15n_0$ in the circle with a radius $r \leq r_0$, which is surrounded by the ambient plasma with a density $n_0$. Left panel sketches the box of simulation 1 with the side length $L_1 = 4r_0$ along x and with the side length $L_2 = 2L_1$ along the y-axis. The magnetic field is aligned along the y-axis. Right panel shows the simulation box geometry of simulation 2. The size of the simulation box is $L_1$ along both the x- and y-directions and the magnetic field is aligned with the z-axis. The boundary conditions are periodic in all directions.

electron temperature of the ambient medium is $T_0 = 2$ keV giving an electron thermal speed $v_{The} = (k_B T_0/m_e)^{1/2} \approx 1.9 \times 10^7 \text{m.s}^{-1}$. The electron plasma frequency $\omega_{pe} = (7e^2 n_0/m_e\epsilon_0)^{1/2}$ is $\approx 1.8 \times 10^{12}\,\text{s}^{-1}$ in the ambient plasma and the ion plasma frequency $\omega_{pi} = (7m_e/m_n)^{1/2}\omega_{pe} \approx 3 \times 10^{10}\,\text{s}^{-1}$.

Dimensional units are used in the last two sections of this Chapter for a direct comparaison with laboratory scales. However, our simulations are meant to identify phenomena that may be observed on very different scales. The dimensionless normalized quantities can be found from the plasma parameters.

On average, thermal diffusion lets electrons stream from the dense plasma into the dilute plasma. Consequently, the dense plasma will go onto a positive potential relative to the dilute one. Electrons, which enter the dense plasma, are accelerated by this potential jump and form a cloud of energetic electrons. We set the electron temperature within the dense cloud to $2T_0$, which suppresses two-stream instabilities between this cloud and the thermal electrons. The ion temperature is $T_0/12.5$ everywhere.

Simulation 1 resolves electrons with $6.4 \times 10^8$ computational particles (CPs) and the ions with $9.6 \times 10^8$ CP's. Simulation 2 employs a half of the total number of CPs. Initially the net charge and current are zero everywhere in the simulation box. The electric and magnetic field components are set to zero at the time $t = 0$ except the background magnetic field $B_0 = 0.85$ T. The ratio of the thermal to magnetic field pressures $\beta \equiv (7n_0 k_B T_0)/(B_0^2/2\mu_0) = 1.1$ in the ambient plasma, the pressure contribution of the cold ions is neglected. The ambient electron thermal gyro-radius is $r_{ge} = 0.125$ mm.

The ion acoustic speed in the ambient plasma is $c_s \approx 4 \times 10^5$ m/s with $c_s = ((\gamma_e k_B T_0 + \gamma_N k_B T)/m_N)^{1/2}$. We assumed that the adiabatic constants of electrons and ion are $\gamma_e = 5/3$ and $\gamma_N = 3$, respectively. The Alfvén speed $v_A = B_0/(\mu_0 n_0 m_N)^{1/2}$ is $v_A \approx 4.1 \times 10^5$ m/s for our plasma parameters. The speed of the fast magnetosonic wave $v_{fms} = (c_s^2 + v_A^2)^{1/2}$ for perpendicular propagation is $v_{fms} \approx 5.8 \times 10^5$ m/s.

We can estimate the speeds of normal modes for intermediate angles of propagation with respect to the magnetic field direction by using a single fluid MHD model presented in section 4.1 that is valid for the frequencies below the ion gyrofrequency, which is in our case that of fully ionized nitrogen $\omega_{ci} = 7eB_0/m_N$. The sound speed $\tilde{c}_s$ in the collisional MHD plasma is close to the ion acoustic speed $c_s$ in collisionless plasma and the same holds for the fast magnetosonic speed. Linear Alfvén waves, which propagate along the magnetic field, do not affect the palsma density and $\tilde{c}_s$ is the only relevant phase speed of density waves that propagate along this direction. The fast magnetosonic speed is the only relevant one in the MHD plasma if the density waves propagate perpendicularly to the magnetic field. Acoustic waves, which propagate obliquely to the magnetic field, can change into slow magnetosonic modes. Slow- and fast magnetosonic modes coexist for a wide range of oblique propagation angles and the phase speeds $v_f$ ($v_s$) of the fast (slow) obliquely propagating magnetosonic mode are described by equation (4.16).

### 4.3.2 Simulation results

We consider the plasma distribution at the time $t_{sim} = 3.57$ ns or $t_{sim}\omega_{ci}/2\pi \approx 2.3 \times 10^{-2}$. The observed shocks are mediated by gradients in the thermal and magnetic pressures. The role of the external magnetic field is negligible on that time scale. All densities are normalized to the ion density $n_0$ of the ambient medium and the magnetic pressure is normalized to the external magnetic field $P_B(x, y) = (B_x^2(x, y) + B_y^2(x, y) + B_z^2(x, y))/B_0^2$.

#### Simulation 1: magnetic field in the simulation plane

Figure 4.16(a) shows the ion density in the quadrant $x > 0$ and $y > 0$. The ion density along the x-axis decreases below 4.5, which is the maximum value displayed on the color scale, at $y \approx 2$ mm, it reaches its minimum value $\approx 2$ at $y \approx 2.8$ mm and increases to over 3 just behind the shock, which is located at $y \approx 4$ mm. This density profile resembles that of a circular blast shell in an unmagnetized plasma (Dieckmann et al., 2017a). The ion density distribution maintains a radially symmetric profile up to $x \approx 2$ mm. A striped high density band is located in the interval 2.7 mm $\leq x \leq 3.2$ mm and $y \leq 2$ mm.

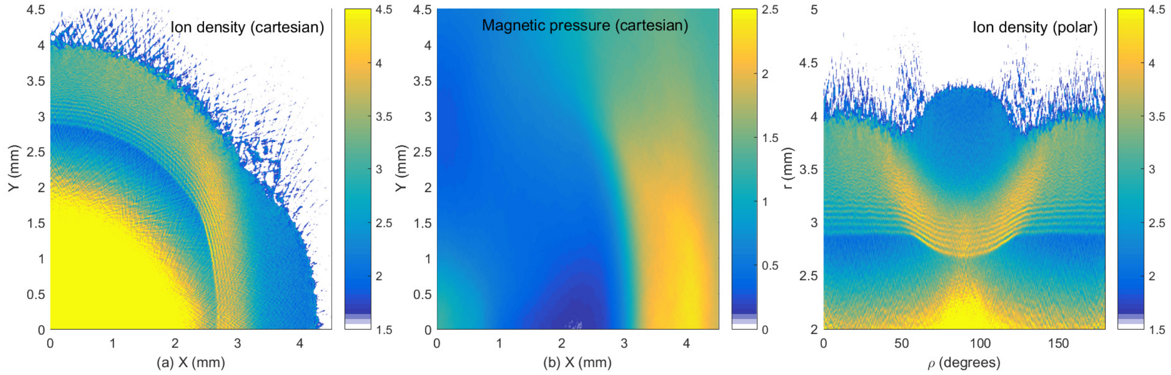

Figure 4.16 – The distribution of the ion density $n_i$ and of the normalized magnetic pressure $P_B = (B_x^2 + B_y^2 + B_z^2)/B_0^2$. The ion density is shown in cartesian coordinates in (a). Panel (b) shows the magnetic pressure in cartesian coordinates. The ion density distribution in polar coordinates is shown in panel (c). The linear color scale is clamped to the value 1.5 in (a, c) in order to emphasize the location of the shock. The time is $t_{sim} = 3.57$ ns.

Figure 4.16(b) shows that the front of this high-density band coincides with an interval with a steep gradient of $P_B$ up to $y \approx 3$ mm. The front of the perpendicular shock in Fig.4.16(a) is located at $x \approx 4.3$ mm for $y \approx 0$ and the magnetic pressure in the interval between the shock and the high-density band is higher than that upstream. A shock, which compresses the plasma density and the magnetic pressure like the one moving along $\rho \approx 90°$, is mediated by the fast magnetosonic mode.

Figure 4.16(c) shows the ion density distribution in polar coordinates. The shock front is fastest and its separation from the trailing high-density band is largest for $\rho \approx 90^\circ$. The radius of the latter increases as we move away from $\rho = 90^\circ$ until $\rho \approx 60^\circ$ or $\rho \approx 120^\circ$, which is what we expect from Fig.4.16(a) since there the high-density structure is field-aligned. A second high-density structure extends in the direction $\rho = 90^\circ$ up to $r \approx 2.5$ mm. The gradients of the magnetic pressure and of the thermal pressure are parallel along this direction, as we can see from Fig.4.16, which causes a stronger acceleration of the blast shell ions in this direction. Figure 4.16(c) reveals that the density stripes, which are also seen in the ion high-density band in Fig.4.16(a), extend to angles that range from $\rho = 0$ to $\rho = 90^\circ$.

According to Fig.4.16(c) these stripes are located in the intervals 2.9 mm $\le r \le$ 3.2 mm for $\rho = 0$ and 2.6 mm $\le r \le$ 3.1 mm for $\rho = 90^\circ$. Figure 4.17 explains their origin by looking at the shocks propagating along and perpendicular to the magnetic field. The density stripes correspond to ion density waves, which cause velocity oscillations of the blast shell ions. They are ion acoustic waves for $\rho = 0$ and lower-hybrid waves for $\rho = 90^\circ$. The oscillations start at the locations, where the blast shell ions are no longer accelerated by the electric field of the rarefaction wave. These positions are $y = 2.9$ mm and $v_y \approx 6 \times 10^5$ m/s for the unmagnetized shock and $x = 2.7$ mm and $v_x \approx 4.5 \times 10^5$ m/s for the magnetized shock. The oscillation amplitudes of the mean velocity and of the density decrease with an increasing positive distance from these positions. These oscillations resemble those found at the boundary between a hydrodynamic rarefaction wave and the velocity plateau (Gurevich and Meshcherkin, 1984). Their cause is the discontinuous first derivative of the mean velocity.

The mean speed of the blast shell ions is lower for $\rho = 90^\circ$ than for $\rho = 0$, which explains why the density stripes in Fig.4.16(c) are located at lower radii. The amplitude of the density modulations changes with $\rho$ because they are tied to different wave modes. Comparing the location of the shocks and the distributions of the downstream ions in Fig.4.17 one concludes that, even though the blast shell ions and the ions of the ambient medium behind the shock with $\rho = 90^\circ$ are propagating at a lower speed, the actual shock is faster (See also Fig.4.16(c)). Figure 4.16(c) reveals the reason for the different shock speeds: the post-shock density of the plasma along $\rho = 90^\circ$ is $\approx 2.2 n_0$ while it is $\approx 3.3 n_0$ for an angle $\rho = 0$. The lower compression along $\rho = 90^\circ$ leads to a shock speed that is larger in the rest frame of the downstream ions.

The mean velocity of the dense shell ions decreases behind the end of the rarefaction wave until it reaches a minimum at $y = 3.4$ mm in Fig.4.17(a) and at $x = 3.2$ mm in Fig.4.17(b). Such a velocity decrease is explained by an electric field. Figure 4.16(a) shows that the rapid initial decrease of the mean speed in Fig.4.17(a) coincides with an increase of the density for $x = 0$. The density increase at $x = 2.7$ and $y = 0$ in Fig.4.16(a), which is a consequence of the slowdown of the blast shell ions, and that of the magnetic pressure in Fig.4.16(b) results in an electric field which is tied to the different mobility of electrons and ions in gradients of the density and magnetic pressure. This electric field decreases the ion velocity at this value of $x$ in Fig.4.17(b).

Figure 4.18 shows the amplitudes of the three magnetic field components and the mean kinetic energy of the electrons. The magnetic $B_y$ component is the main contributor to the magnetic pressure $P_B$. The large amplitudes of $B_x$ are caused by the bending of the field lines by the plasma expansion along the x-axis. This can be seen from a comparison of Fig.4.18(a,b), for example at the location $(x, y) \approx$ (3 mm, -2 mm). The positive value for $B_x$ implies that the magnetic field line bends at this location towards increasing $x$, which is consistent with Fig.4.18(b). The same is true for the four magnetic field patches at small $r$ in Fig.4.18(a). Their polarity is opposite to those at larger radii. This is explained by the magnetic field depletion due to the plasma expansion (see also Fig.4.16(b)) which shifts the magnetic field lines towards smaller $r$. The magnetic $B_z$ component in Fig.4.18(c) also shows structures that follow the deformation of the field lines in the x-y plane. The magnetic field deformation is correlated with an electron current. The electrons flow along the magnetic field lines to large $|y|$, which can be seen in Fig.4.18(d).

Figure 4.19 shows the phase space density distribution of ions over the azimuthal interval $0 \le \rho \le 100^\circ$. It shows the distribution as a function of the radial velocity $v_r$ and the azimuthal velocity

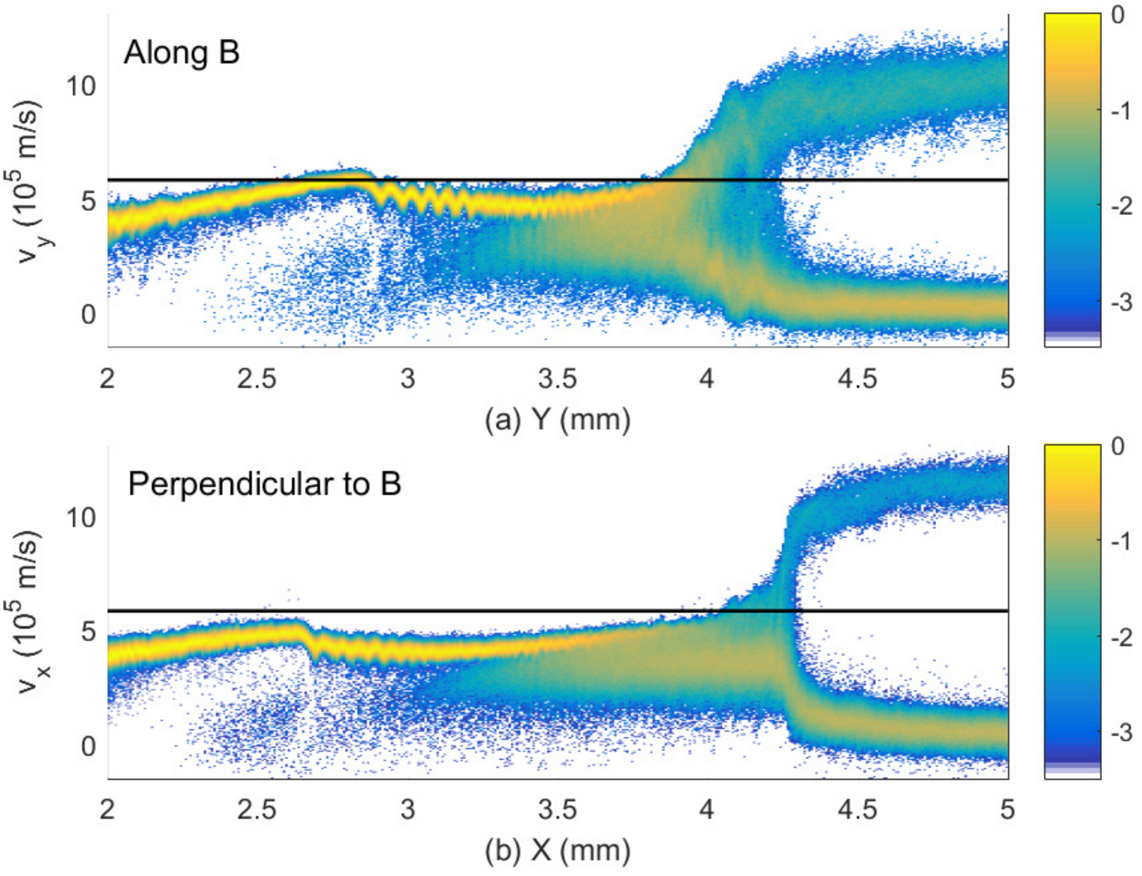

Figure 4.17 – Ion phase space density distribution at $t_{sim} = 3.57$ ns: panel (a) shows the distribution $f_n(y, v_y)$ along y, which has been averaged over the interval -0.2 mm ≤ $x$ ≤ 0.2 mm. It depicts an ion acoustic shock that propagates along the background magnetic field. Panel (b) shows the distribution $f_n(x, v_x)$ along x, which has been averaged over the interval -0.2 mm ≤ $y$ ≤ 0.2 mm. It is a fast magnetosonic shock that propagates perpendicularly to the background magnetic field. The color scale is 10-logarithmic. Horizontal line: fast magnetosonic speed $5.8 \times 10^5$ m/s.

$v_\rho$. The blast shell has driven a shock, which heats up the ambient ions, in all directions. The blast shell ions form the dense core part in both distributions at $r < 4$ mm. The thermal spread of the blast shell ions is larger in the azimuthal direction than in the radial direction; the reason being that the ions are cooled in the radial direction where the ambipolar electric field of the rarefaction wave accelerates them and faster ions outrun the slower ones. The ambient ions, which have not yet encountered the shock, form the cool dense population at $r > 4$ mm. The diffuse population for all radial distances is formed by ambient ions, which have crossed the shock ($r < 4$ mm), and by shock-reflected ions ($r > 4$ mm).

A velocity modulation of the upstream ions is observed at $\rho \approx 45°$ and $r \approx 5.4$ mm. Prior to the arrival of the shock the ions are accelerated radially to several times their thermal speed $v_{tn} = (k_B T_0/(12.5 m_n))^{1/2} \approx 3.3 \times 10^4 \mathrm{m.s}^{-1}$. This velocity increase along the radial direction persists up to a propagation direction $\rho = 100°$ albeit with a lower magnitude. The shocks propagating along the angles $45° \leq \rho \leq 135°$ thus have a foot, which does not exist for $\rho \leq 45°$.

Figure 4.16(c) showed that the high-density band reached the shock front at $\rho = 45°$ and we assess its connection to the shock foot. Figure 4.20 compares slices of the ion density and of the magnetic pressure for the propagation angles $\rho = 45°$ and $\rho = 90°$ with those of the ion acoustic shock at $\rho = 0$. The density distribution in Fig.4.20(a) has a maximum between $r \approx 2.8$ mm and $r \approx 3.8$ mm. The peak density $3.6 n_0$ downstream of the shock at $r \approx 3.5$ mm exceeds the post-shock peak density $2.2 n_0$ at $r \approx 4$ mm in Fig.4.20(b) and the maximum downstream density $3 n_0$ of the shock in Fig.4.20(c) at $r \approx 3.5$ mm. The magnetic pressure has been depleted at small radii in all considered cases. Figures 4.20(a,b) demonstrate that the shocks pile up magnetic field ahead

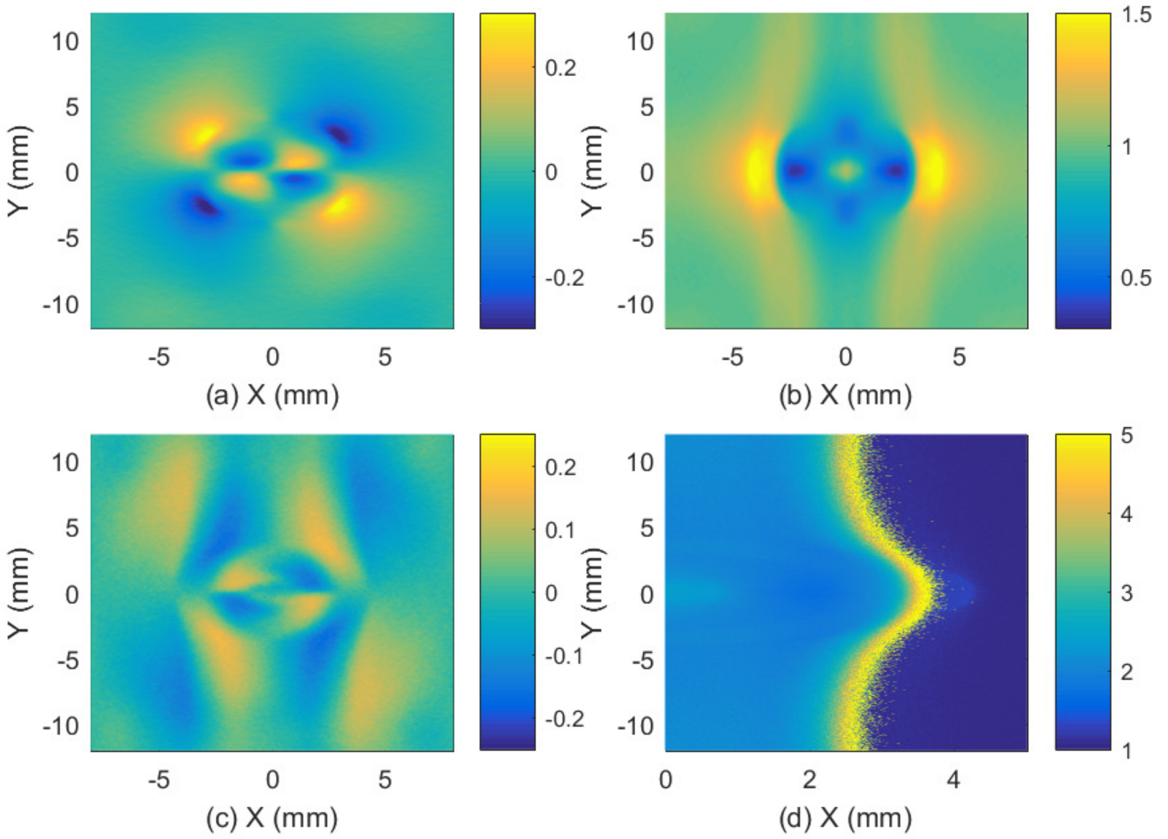

Figure 4.18 – Spatial distribution of magnetic field components: $B_x$ (a), $B_y$ (b) and $B_z$ (c) in units of $B_0$. Panel (d) shows the mean kinetic energy of electrons in units of the temperature $T_0$. The time is $t_{sim} = 3.57$ ns.

of them. The magnetic pressure in Fig.4.20(b) has started to increase even at the boundary at $r = 8$ mm.

A fast magnetosonic pulse emitted at $t = 0$ at the boundary at $r = 2$ mm would have reached the position $2\,\text{mm} + v_{fms}t_{sim} \approx 4.1$ mm in Fig.4.20(b). The magnetic field is increased beyond this radius, which suggests together with the exponentially decreasing $P_B$ for $r > 4.1$ mm that this pulse is a damped precursor.

The magnetic pressure and the plasma density both increase in Fig.4.16(b) across the shock at $r \approx 4.3$ mm from the upstream into the downstream region. Based on this observation we have already concluded that it is a fast magnetosonic shock. The magnetic pressure decreases and the plasma density increases across the shock at $r \approx 3.9$ mm in Fig.4.20(a); this is a slow magnetosonic shock. The gradient of $P_B$ at the shock accelerates ions to lower radii, which enhances the plasma compression and yields a large post-shock density.

The magnetic pressure gradient ahead of the slow- and fast magnetosonic shocks depicted in Fig.4.20(a,b) points to increasing radii and the associated force accelerates ions in the same direction. The upstream ions in Fig.4.19 obtain a mean radial speed, which is larger than zero, that lets them move away from the shock. In contrast, the magnetic field is depleted ahead of the shock in Fig.4.20(c) and its pressure gradient accelerates upstream ions towards the shock, which amplifies the mean velocity change at $\rho \approx 45°$ in Fig.4.19(a).

Depletion of $P_B$ in Fig.4.20(c) extends far ahead of the shock and it can thus not be explained in terms of an Alfvén wave that is launched by the expanding blast shell at $r = 2$ mm at $t = 0$. The Alfvén speed is simply too low. Effects due to Alfvén waves and a modification of shocks by a shear Alfvén wave would also not emerge on the short time scales $t \ll \omega_{ci}^{-1}$ we consider here due to their low frequencies (Gekelman et al., 2011). The magnetic field depletion can only be caused by the current of hot electrons, which is carried into the plasma at the electron's thermal speed $v_{The} \gg v_A$

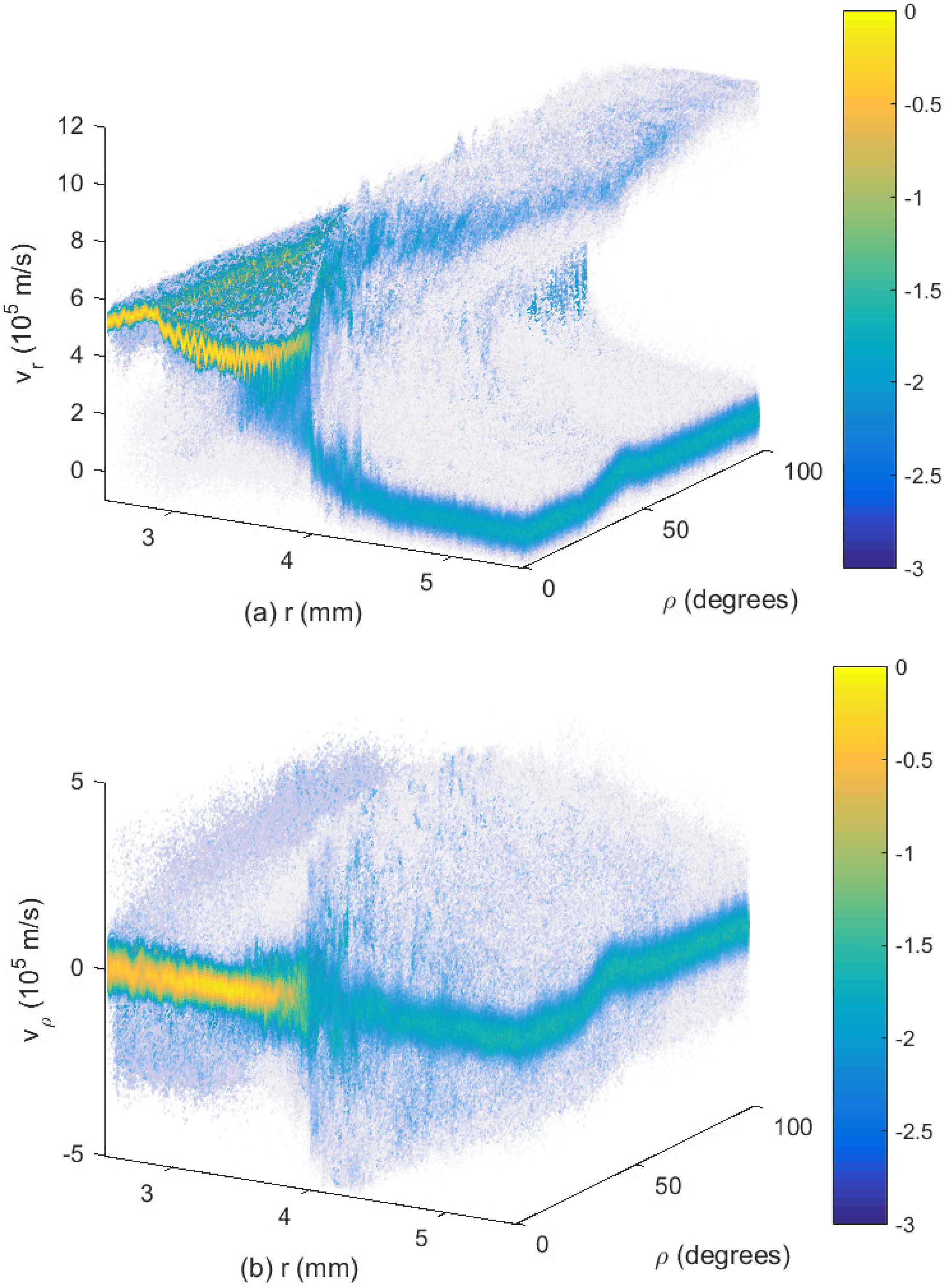

Figure 4.19 – The 10-logarithmic ion phase space density distribution. The time is $t_{sim} = 3.57$ ns. Panel (a) shows the velocity in the radial direction $v_r$ while panel (b) shows the azimuthal velocity component $v_\rho$.

(See Fig.4.18(d)).

We have estimated the speed of the shocks shown in Fig.4.20 by measuring the distance the density jump associated with the forward shock propagated from $t = 0.9t_{sim}$ until $t = t_{sim}$. The

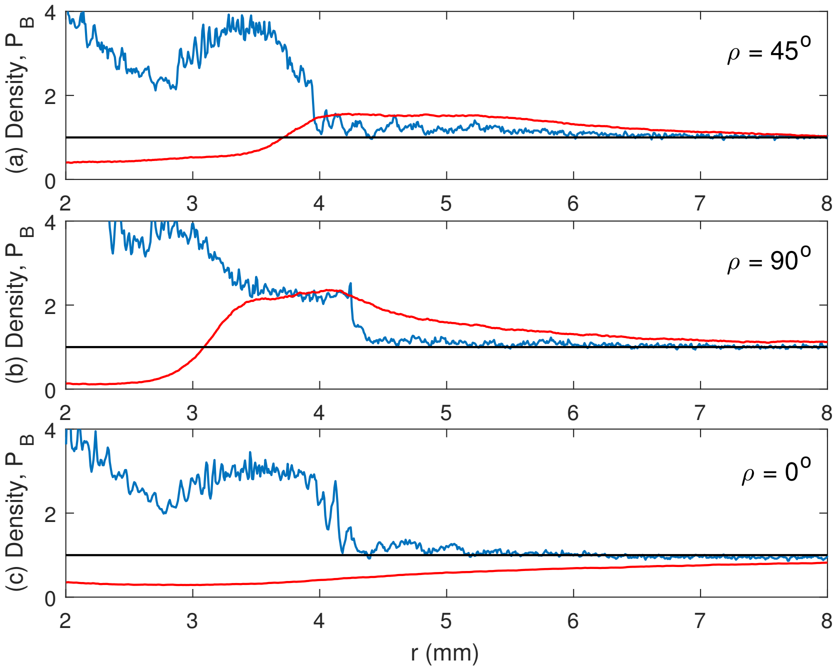

Figure 4.20 – Radial profiles of the ion density (blue) and the magnetic pressure $P_B$ (red): (a) along the direction 45°, (b) along the direction 90° and (c) along $\rho = 0$. Both distributions have been averaged over an angular interval with the width 0.5°. The time is $t_{sim} = 3.57$ ns.

speed of the slow magnetosonic shock in Fig.4.20(a) is about $4.5 \times 10^5$ m/s, that of the fast magnetosonic one in Fig.4.20(b) is about $6.7 \times 10^5$ m/s or $\approx 1.15 v_{fms}$ and that of the unmagnetized shock in Fig.4.20(c) is about $5.4 \times 10^5$ m/s or $1.3 c_s$.

**Simulation 2: magnetic field transverse to the simulation plane.**

Figure 4.21(a) shows the ion density for $x > 0$ and $y > 0$. This distribution is radially symmetric for all radii with the exception of the density stripes found for $2.75\,\text{mm} < r < 4\,\text{mm}$. The magnetic pressure is radially symmetric only for $r \leq 1.2$ mm and $r \geq 3.7$ mm as seen from Fig.4.21(b). The magnetic pressure waves in the interval $1.3\,\text{mm} \leq r \leq 3.7\,\text{mm}$ rotate in time in the counterclockwise direction (Fig.4.21). Figure 4.21(c) shows that the plasma expansion is no longer a func-

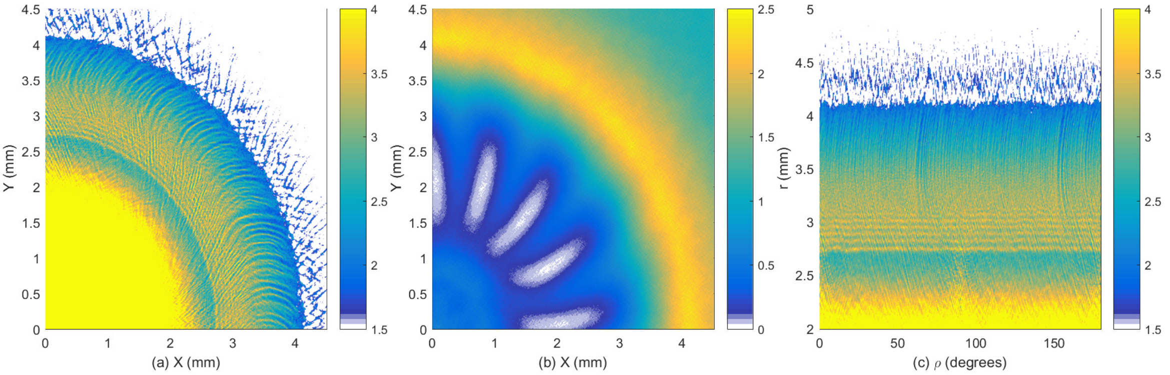

Figure 4.21 – The distribution of the ion density $n_i$ and of the normalized magnetic pressure $P_B = (B_x^2 + B_y^2 + B_z^2)/B_0^2$. The ion density is shown in cartesian coordinates in (a). Panel (b) shows the magnetic pressure in cartesian coordinates. The ion density distribution in polar coordinates is shown in panel (c). The linear color scale is clamped to the value 1.5 in (a, c) in order to emphasize the location of the shock. The time is $t_{sim} = 3.57$ ns.

tion of $\rho$. We observe the density stripes, which form at the end of the rarefaction wave at the same location $2.7\text{mm} \leq r \leq 3.2\text{mm}$ (see Fig.4.21(a)), with the same amplitude and wavelength as their counterparts in Fig.4.16(c) for $\rho = 90^\circ$. Their amplitude and wavelength do not depend on $\rho$ because these are lower-hybrid waves propagating transverse to the background magnetic field.

The front of the shock in Fig.4.21(a,b) is located at $r \approx 4$ mm and it compresses the plasma density and the magnetic pressure. It is a fast magnetosonic shock, which is underlined by the phase space density distribution of the ions in Fig.4.22. The distribution does not depend on $\rho$ and it resembles that in Fig.4.19 at $\rho = 90^\circ$. Figure 4.22 furthermore reveals that the ion distribution has not been visibly affected by the azimuthal oscillations of the magnetic pressure in Fig.4.21(b).

Figure 4.23 shows the distribution of the magnetic field components and the mean electron energy at $t = t_{sim}$. We observe modulations of the magnetic field components in the simulation plane and of the mean kinetic energy of the electrons. The wave vector of these oscillations is aligned with the azimuthal direction.

The Weibel instability can lead to the growth of magnetic fields in a density gradient (Quinn et al., 2012). However, it would affect the out-of-plane magnetic field, which is not what Fig.4.23 shows. The background magnetic field maintains an electron temperature in the simulation plane on the considered time scales $\omega_{ce} t_{sim} \approx 500$, which suppresses this instability.

Instabilities can also be driven by a drift between electrons and ions. The guiding center approximation is valid for the electrons since they perform about 100 gyroperiods during $t_{sim}$. The radial variation of $\mathrm{B}_z$ in Fig.4.23(c) leads to a grad-B drift. The drift velocity $\mathbf{v}_\mathrm{D}$ of an electron with the charge $q = -e$ can be estimated by assuming that $\mathrm{B}_x, \mathrm{B}_y \ll \mathrm{B}_z$ and that $\mathbf{B} = (0, 0, \mathrm{B}_z)$ changes slowly relative to the value of $\mathrm{B}_z$ on spatial scales comparable to an electron thermal gyroradius. According to Fig.4.23(c) this is the case for the electrons with $r_{ge} = 1.25 \times 10^{-4}$m. The drift speed is (Baumjohann and Treumann, 1997)

$$\mathbf{v}_\mathrm{D} \approx \frac{m_e v_{\mathrm{T}he}^2}{2q\mathrm{B}_z} \frac{\mathbf{B} \times \nabla \mathrm{B}_z}{\mathrm{B}_z^2}. \tag{4.34}$$

Changes along $z$ are excluded by our simulation geometry. We define $c_\mathrm{D} = (m_e v_{\mathrm{T}he}^2)/(2q\mathrm{B}_z^3)$ and obtain the two drift components $v_{\mathrm{D}x} \approx -c_\mathrm{D}\mathrm{B}_z \partial_y \mathrm{B}_z$ and $v_{\mathrm{D}y} \approx c_\mathrm{D}\mathrm{B}_z\partial_x\mathrm{B}_z$. Electrons drift in the clockwise direction.

We compute $\mathbf{v}_\mathrm{D}$ with Eq. (4.34) from the magnetic field data in Fig.4.23(c). The azimuthal average of its modulus is shown in Fig.4.24. The drift speed exceeds $v_{\mathrm{T}he}$ in the radial interval, where magnetowaves are excited in Figs. 4.23(a,b). Equation (4.34) accurately estimates $\mathbf{v}_\mathrm{D}$ only if $|\mathbf{v}_\mathrm{D}| \ll v_{\mathrm{T}he}$ and beam instabilities grow once $|\mathbf{v}_\mathrm{D}| \sim v_{\mathrm{T}he}$. It is thus unlikely that electrons can reach a drift speed $7v_{\mathrm{T}he}$. This is confirmed by Fig.4.23(d) that shows that the mean electron kinetic energy is only 3 times larger than the temperature $\mathrm{T}_0$.

Drift speeds below $v_{\mathrm{T}he}$ can drive the lower-hybrid drift instability (Brackbill et al., 1984; Winske; Ripin et al., 1993; Daughton et al., 2004), corresponding to excitation of the ion density waves. The linear growth rate of this instability is smaller than the lower-hybrid frequency. Figure 4.23 shows that the magnetowaves grow on time scales $\sim \omega_{ce}^{-1}$ while $\omega_{ce}/\omega_{lh} \approx 60$ in the ambient plasma. The slow growth of lower-hybrid waves and the absence of ion density modulations Fig.4.21(a) on spatial scales that are similar to those of the magnetic pressure in Fig.4.21(b) rule out this instability.

A faster-growing instability that involves electron-cyclotron waves (Forslund et al., 1972; Dieckmann et al., 2000b) sets in if the drift speed is comparable to the electron's thermal speed. Such waves hardly modulate the ion density. They are sustained by the interplay of the magnetic pressure with the electron thermal pressure when they are saturated nonlinearly. The time evolution of Fig.4.23(d) (not shown) evidences modulations of the mean thermal energy of the electrons, which suggests that such an instability may be excited.

We can quantify a correlation between the magnetic pressure, which oscillates twice as fast as the magnetic amplitude in Fig.4.23(a,b), and the mean electron energy by transforming both from the Cartesian into a polar coordinate system followed by a Fourier transform over the azimuth angle. We define $n$ as the number of oscillations along the azimuthal direction; one oscillation

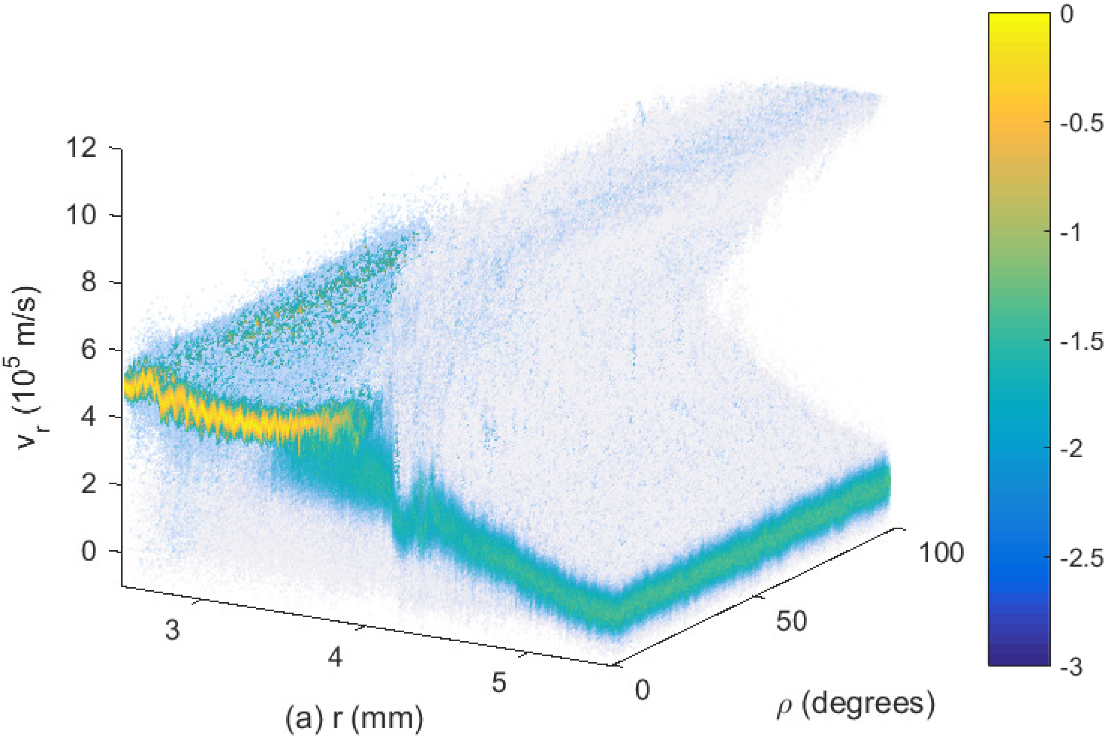

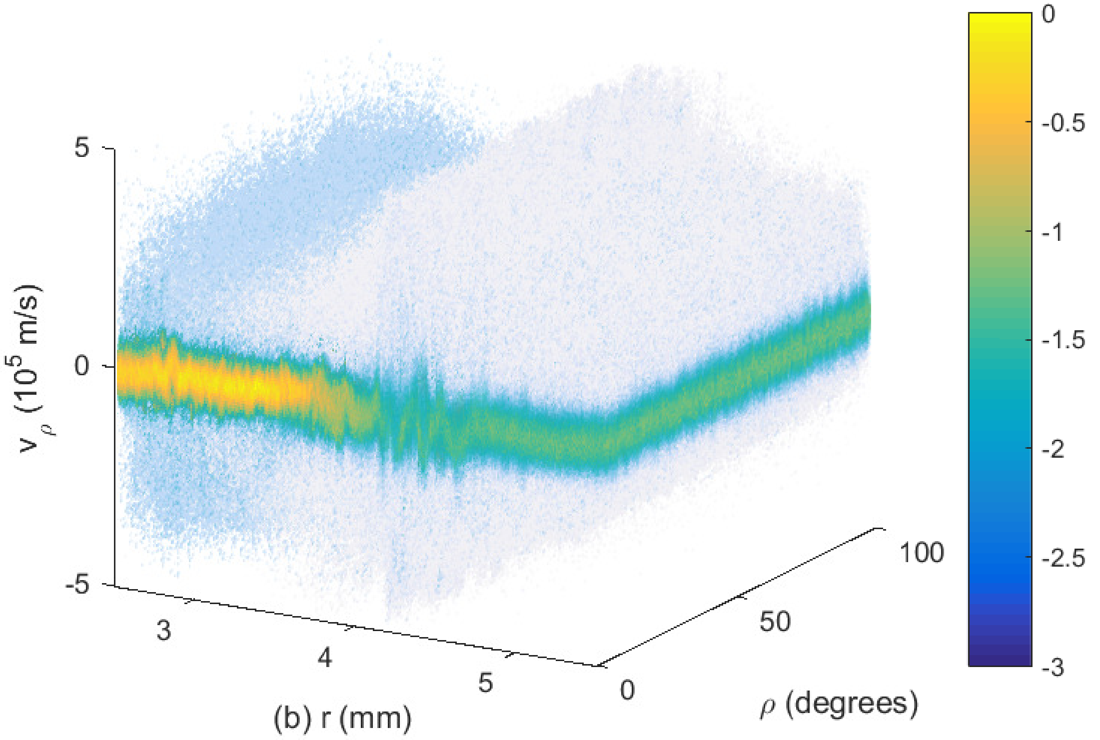

Figure 4.22 – The 10-logarithmic ion phase space density distribution. The time is $t_{sim} = 3.57$ ns. Panel (a) shows the velocity in the radial direction $v_r$ while panel (b) shows the azimuthal velocity component $v_\rho$.

per 360° corresponds to $n = 1$. The result in Fig.4.25(a, b) shows the dominant mode $n = 16$. The signal in Fig.4.25(a) peaks at a smaller radius than that in Figure 4.25(b). The density decreases with increasing $r$ and the magnetic pressure must thus be balanced by a larger electron kinetic

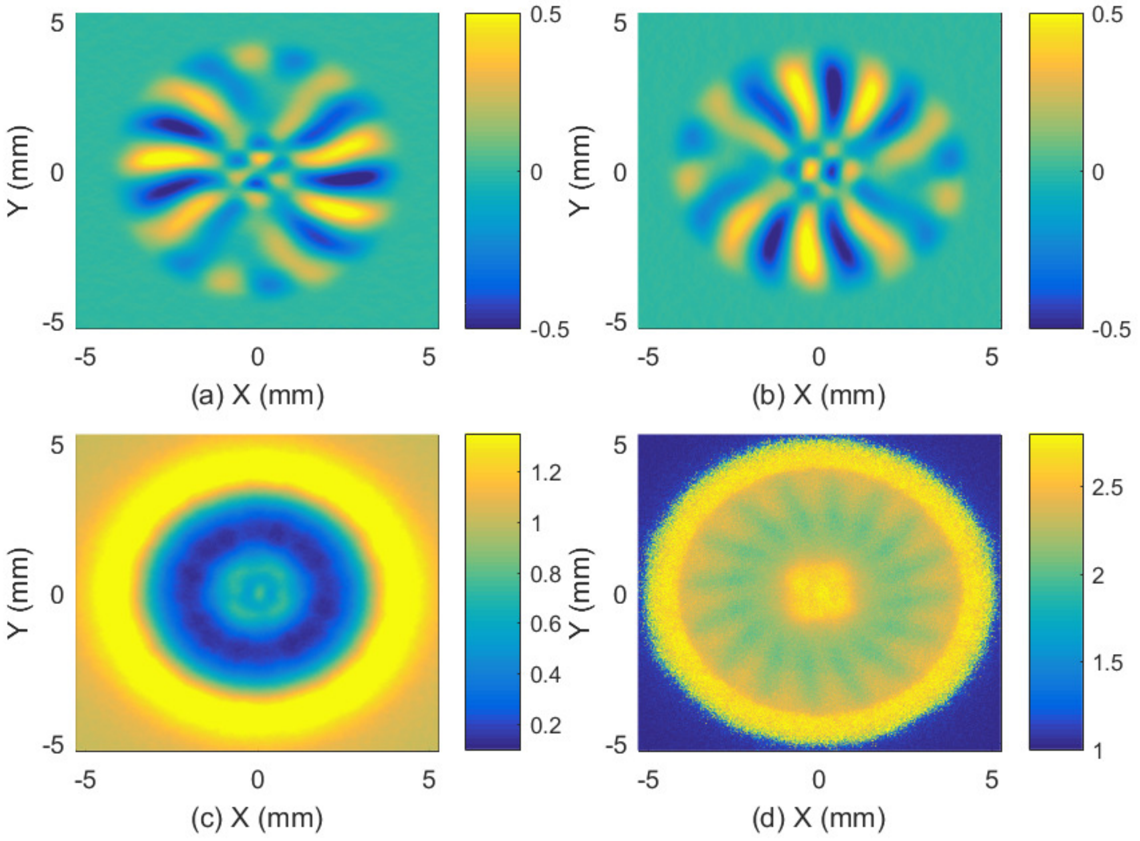

Figure 4.23 – Spatial distribution of the magnetic field components: $B_x$ (a), $B_y$ (b) and $B_z$ (c) in units of $B_0$. Panel (d) shows the mean electron kinetic energy in units of the temperature $T_0$. The time is $t_{sim} = 3.57$ ns.

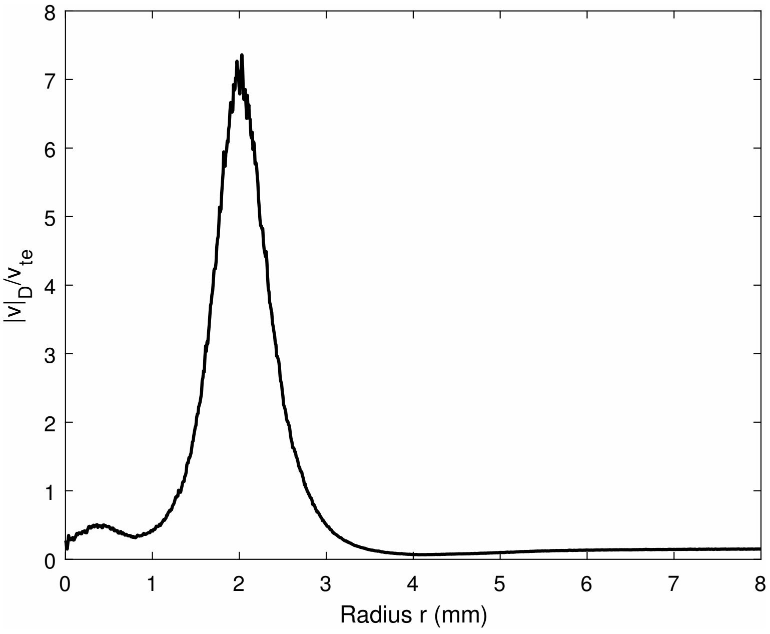

Figure 4.24 – The magnitude of the azimuthally averaged drift speed $|\mathbf{v}_D|/v_{The}$ at the time $t_{sim} = 3.57$ ns.

energy.

We have extracted the phase angle $\alpha_1(r)$ of the Fourier transformed signal at $n = 16$ in Fig.4.25(a) and that of its counterpart $\alpha_2(r)$ at $t = t_{sim} - 54$ ps. A phase difference $\Delta_\alpha = \alpha_1(r) - \alpha_2(r) = 2\pi$ im-

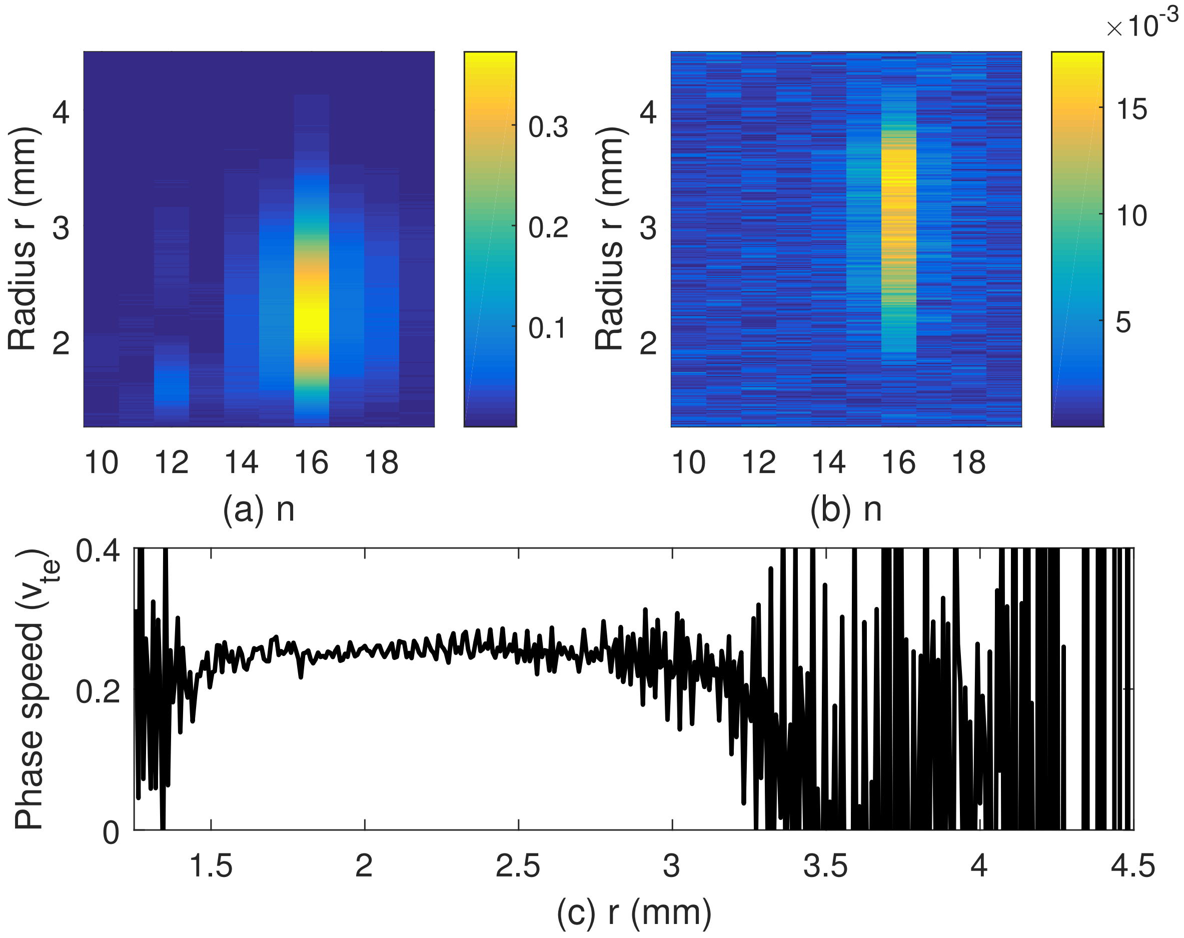

Figure 4.25 – Amplitude modulus and phase speed of the drift wave: panel (a) shows the amplitude modulus of the magnetic pressure and panel (b) that of the mean electron kinetic energy. A value $n = 1$ implies one oscillation per full cycle. Both spectra are normalized for each value of $r$ to the power at $n = 0$ at that $r$. Panel (c) shows the propagation speed of the magnetic-structure as a function of the radius.

plies that the structure has completed one full rotation around the z-axis. The azimuthal phase speed of the structure $r\Delta_\alpha/54$ ps is shown in Fig.4.25(c). A positive phase speed corresponds to a counter-clockwise rotation. The phase velocity equals $v_{The}/4$ over the radial interval $1.5\,\mathrm{mm} \leq r \leq 3.3\,\mathrm{mm}$, which is typical for electron Bernstein waves (Ram et al., 2002). The magnetowave rotates in the opposite direction as the electrons, which is characteristic for waves driven by the resonant electron-cyclotron drift instability. The opposite rotation direction is caused by the oppositely directed phase and group velocities of electron Bernstein waves. Energy is transported with the group velocity in the same direction as the electrons move and the phase velocity thus has the opposite sense of rotation. This effect has been observed experimentally (Ripin and Stenzel, 1973).

### 4.3.3 Summary

We have examined the expansion of an initially radially symmetric blast shell into an ambient plasma followed by formation of a magnetic cavity (Bernhardt et al., 1987) by means of two-dimensional particle-in-cell simulations. The blast shell was driven by a jump in the thermal pressure between a dense azimuthally symmetric plasma cloud and a spatially uniform dilute ambient medium in a spatially uniform magnetic field.

One simulation considered the case of a magnetic field that was aligned with one of the axes of the simulation box. This simulation demonstrated that collisionless forward shocks form for all orientations of the shock normal with respect to the ambient magnetic field. The forward shocks are located between the pristine and the shocked ambient medium. The forward shock that propagates perpendicularly to the magnetic field ($\rho = 90^\circ$) is mediated by the fast magnetosonic mode. It was trailed by a tangential discontinuity, which separates the blast shell plasma from the shocked ambient medium. The tangential discontinuity changes into a slow magnetosonic shock for propagation angles $45^\circ \leq \rho < 90^\circ$ (Eliasson, 2014). The slow magnetosonic shock replaces the fast magnetosonic shock for the propagation angle $\rho \approx 45^\circ$. The forward shocks are mediated by the ion acoustic wave for propagation angles $\rho < 45^\circ$.

Our simulation time is short compared to the inverse ion gyro-frequency. In spite of this short time, the shocks developed features that are typical for magnetosonic shocks such as the phase relation between the plasma density and the magnetic field amplitude and a shock speed that depends on the propagation direction. We attribute this fast shock formation time to the fact that the magnetosonic shocks are mediated by the magnetic pressure gradient. The magnetic pressure acts on the electrons and ions. A higher electron mobility results in a charge separation and, hence, in an electrostatic field. The characteristic time scale, during which the force develops, is much shorter than the time it takes an ion to complete one gyration in the magnetic field. Indeed it has been shown in the one-dimensional simulation in Ref. (Dieckmann et al., 2017b) that the shock, which propagates orthogonally to the magnetic field, becomes a fast magnetosonic one.

The second simulation considers a background magnetic field that pointed out of the simulation plane. This geometry implies that the forward shock is mediated by the fast magnetosonic mode. No difference between this shock and the perpendicular one in the first simulation is observed. The expanding blast shell depletes the magnetic field and piles it up ahead of it in the shocked ambient medium. The spatially non-uniform magnetic field results in the grad-B drift of electrons in the simulation plane at a speed comparable to the electron thermal speed. This drift speed is large enough to trigger the growth of an electron-cyclotron drift instability.

Evolution of the ion phase space density, observed in a collisionless shock, matches the MHD model with exception of the shock-reflected ion beam. The latter is absent in collisional plasmas. It can drive instabilities upstream of the shock or force it into a cyclic reformation, as discussed in the next section. These kinetic effects were negligible in our simulation because the shock-reflected ion beam was dilute. We have not examined here the electrons; their high temperature implied that they were not in a thermal equilibrium with the ions. Their thermal pressure drives expansion of the blast shell and creates a current that modifies the magnetic field and induces the kinetic drift instability.

Further simulations examine evolution of the shock for a wider range of values of electron pressure and for the blast shell's expansion speeds in order to determine cases where the shock evolution deviates from that predicted by the MHD model.

## 4.4 Failed self-reformation of a sub-critical fast magnetosonic shock in collisionless plasma

A gas is accelerated by rapid changes of its pressure in space or time. Binary collisions mediate this acceleration and give rise to density waves. Density waves move at the speed of sound, which depends on the gas temperature. A shock wave forms if the bulk velocity of accelerated material relative to that at rest is faster than the sound speed. It separates the accelerated gas from the one upstream of the shock.

In the rest frame of the shock, the gas in the upstream region flows towards the shock. It is slowed down and heated as it crosses the shock and enters the downstream region behind it. The heating is accomplished by binary collisions between the particles of the gas and it implies that the sound speed in the downstream gas is higher than that upstream of the shock. The downstream region expands due to the transport of material across the shock and, hence, the shock can not be stationary in the downstream frame of reference. Its speed in this reference frame can, however, not exceed the sound speed of the downstream material.

The shock boundary is sharp and well-defined only as long as binary collisions between the particles of the gas occur frequently on the characteristic time scale of the gas flow. If this is not the case then the width of its transition layer widens. This scenario is frequently encountered in outer space where the particle density is low.

The probably best understood shock in a dilute medium is the Earth's bow shock. The Earth's magnetic field is an obstacle for the solar wind (Goldstein et al., 2016), which is fed by particles that escape the solar corona. The solar wind is fully ionized and composed of electrons, protons and a minor fraction of heavier ions. It is a good conductor and, hence, it carries with it a magnetic field from the Sun. The relative speed between the Earth's magnetosphere and the magnetized solar wind exceeds that of the charge density waves in the solar wind plasma. A shock forms, which separates the solar wind from the Earth's magnetosheath (Lucek et al., 2005). The latter is the downstream region. The shock is approximately stationary in the rest frame of the Earth while the magnetosheath plasma flows around the Earth's magnetic field and escapes in the anti-sunward direction.

The average shape of the Earth's bow shock is drawn in Figure 4.26 in an ecliptic cross section. Its shape is defined by interaction of the solar wind with the dipolar geomagnetic field.

The bow shock thickness is about 100 kilometres (Bale et al., 2003). The mean free path of solar wind particles is orders of magnitude larger than that and binary collisions are unlikely to occur in the plasma while it crosses the bow shock. The shock dynamics is regulated instead by the interactions of the charge- and current densities carried by the ensemble of the plasma particles with the electromagnetic field.

The Earth bow shock is the paragon of a collisionless shock. In-situ studies of the Earth's bow shock by satellites can thus further our understanding of them. However, the dependence of shocks on plasma bulk parameters like the direction and relative strength of the upstream magnetic field and on the plasma temperature and flow speed (Bale et al., 2005; Burgess et al., 2005) implies that we may not be able to generalize the insight gained from studies of the Earth's bow shock to other collisionless shocks.

Collisionless shocks are thus also being studied in the laboratory, for example by letting a laser-driven blast shell collide with an ambient plasma (Dean et al., 1971) or an obstacle (Bell et al., 1988), and numerically with kinetic simulation codes (Winske and Omidi, 1996; Arber et al., 2015). Both approaches allow one to study systematically a wider range of collisionless shocks than those in the solar system that can be reached by satellites. However, the limited laser energy or computer time restrain the size and complexity of the shocks that can be created by these two approaches.

Nonrelativistic collisionless perpendicular shocks have been widely studied in the past theoretically (Woods, 1969; Shimada and Hoshino, 2000; Schmitz et al., 2002; Scholer et al., 2003) and with laser-plasma experiments (Schaeffer et al., 2015, 2017a). Those studies revealed three important parameters that determine the dynamics of the shock: the magnetization of the upstream medium, the shock speed relative to the speed of the density wave upstream and the ratio between the electron and ion temperatures upstream. Most previous research considered parameters, which are representative for the Earth's bow shock. Close to Earth, the solar wind's thermal pressure is comparable to the magnetic pressure. The electron temperature is similar to that of the protons and the shock speed usually exceeds that of the density waves by a factor 2-10 although it can drop below 2 and even become subsonic (Lugaz et al., 2016).

Although detectable (Balikhin et al., 2002), the cross-shock potential is not large enough on its own to dissipate the energy of the incoming solar wind protons if the shock exceeds about 2.5 times the speed of the density wave. In the case of the Earth's bow shock the consequence is reflection of upstream protons due to the Larmor rotation in the shock's magnetic field. Such supercritical shocks are non-stationary.

Non-stationarity of collisionless shocks has been evidenced in laboratory experiments (Morse et al., 1972) and for the terrestrial bow shock (Walker et al., 1999) it has also been measured by a cluster of four spacecrafts (Horbury et al., 2002). Non-stationary processes can be separated in two groups, including and excluding micro-instabilities . The first category of non-stationary processes based on micro-instabilities triggered within the shock front. They are responsible for the

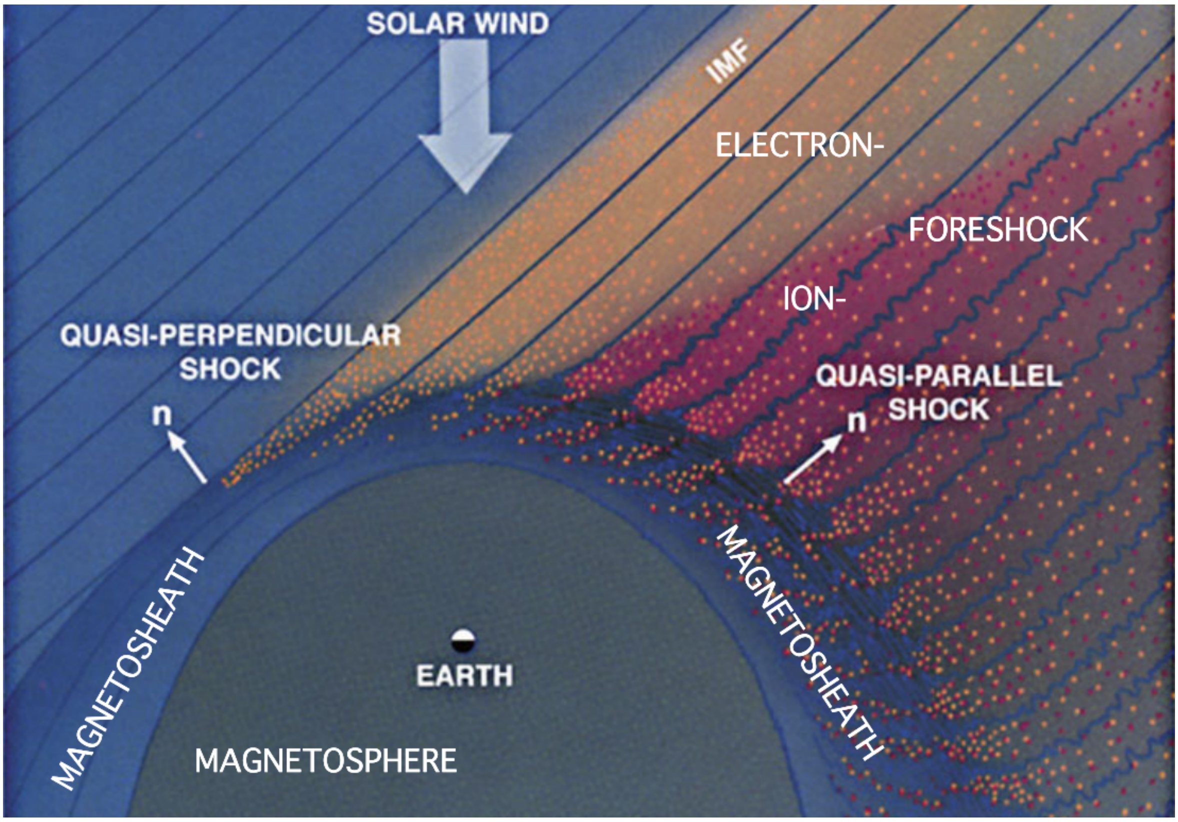

Figure 4.26 – A two-dimensional schematic view on Earth's steady-state bow shock in front of the blunt magnetosphere by (Stone and Tsurutani, 1985), which forms when the supersonic solar wind streams against the dipolar geomagnetic field. The bow shock is the diffuse hyperbolically shaped region standing at a distance in front of the magnetopause. The inclined blue lines simulate the solar wind magnetic field (interplanetary magnetic field IMF). In this figure the magnetic field lines lie in the plane. The direction of the shock normal is indicated at two positions. Where it points perpendicular to the solar wind magnetic field the character of the bow shock is perpendicular. In the vicinity of this point where the solar wind magnetic field is tangent to the bow shock the shock behaves quasi-perpendicularly. When the shock is aligned with or against the solar wind magnetic field the bow shock behaves quasi-parallel. Quasi-perpendicular shocks are magnetically quiet compared to quasi-parallel shocks. This is indicated here by the gradually increasing oscillatory behaviour of the magnetic field when passing along the shock from the quasi-perpendicular part into the quasi-parallel part. Correspondingly, the behaviour of the plasma downstream of the shock is strongly disturbed behind the quasi-perpendicular shock. Finally, when the shock is super-critical, as is the case for the bow shock, electrons and ions are reflected from it. Reflection is strongest at the quasi-perpendicular shock but particles can escape upstream only along the magnetic field. Hence the upstream region is divided into an electron (yellow) and an ion foreshock accounting for the faster escape speeds of electrons than ions.(Treumann, 2009)

turbulence which develops at the shock front and in the downstream region in electron, hybrid and ion ranges. These instabilities are discussed in detail by (Marcowith et al., 2016). Two main mechanisms explaining the shock front non-stationarity, excluding micro-instability processes, have been recovered in numerical simulations. The first one is related to non-linear Whistler waves emitted from the shock front at a very large amplitude comparable to that at the ramp, propagating at an angle oblique to both the normal to the shock front and the static upstream magnetic field (Walker et al., 1999). The second process is the already well mentioned, shock self-reformation.

This mechanism is due to the accumulation of reflected ions by the shock ramp. Because of the gyromotion, these reflected ions pile up upstream of the foot at a distance slightly smaller than an ion gyroradius ahead of the shock ramp, and create local magnetic field and density maxima there. Through a feedback mechanism, this foot then grows until it becomes as large as the initial shock ramp, effectively creating a new ramp. This new ramp reflects incoming ions thus with the shock is advancing to a new position. The process repeats cyclically: the shock is advancing stepwise with a period less than one upstream ion gyroperiod. During the cyclic self-reformation, the shock front fluctuates in time. The variations of the overshoot (behind the shock ramp) versus the foot amplitude are anti-correlated (the overshoot decreases while that of the foot increases), the ramp thickness strongly varies from a large value (a fraction of $c/\omega_{pi}$) to a very small value (only a few $c/\omega_{pe}$). These modifications of the shock profile have a strong impact on the particles' dynamics which depends on the front amplitude/ramp thickness. Numerical simulations suggest that the onset of this non-stationary reformation process is conditioned by a large-enough Mach number a fraction of incoming ions reflected by the shock (Hada et al., 2003), a sufficiently low ratio of plasma to magnetic pressure (Hada et al., 2003; Scholer et al., 2003; Burgess and Scholer, 2007; Yuan et al., 2009) and a ratio of the ion thermal velocity to the shock velocity (Scholer et al., 2003). Thus, supercritical shocks under certain conditions may reform themselves periodically (or quasi-periodically), this process does not destroy the shock but, on the contrary, keeps it intact while changing it with time.

Slower subcritical quasi-perpendicular shocks can dissipate most of the directed flow energy of the upstream medium via their cross-shock potential (Dieckmann et al., 2017b, 2018b; Moreno et al., 2018d). Their cross-shock potential is sustained by changes in the thermal and magnetic pressures. Such shocks reflect only a few ions and they can thus not carry significant amounts of energy upstream. Their modification of the upstream plasma remains weak, which stabilizes the shock.

Recent works by (Gueroult and Fisch, 2016; Gueroult et al., 2017) explored behaviour of shocks with parameters between sub-critical and supercritical shocks and demonstrated onset of shock reformation. We focus here on an instability that can cause the self-reformation of a perpendicular shock with a normal that is orthogonal to the magnetic field direction (Lembege and Savoini, 1992; Shimada and Hoshino, 2000; Schmitz et al., 2002; Scholer et al., 2003).

Perpendicular shocks are mediated by a wave, which has the fast magnetosonic speed $v_{fms}$ as its phase- and group velocity in the limit of large wavelengths. The current of the ion beam, which is reflected by a supercritical shock, can interact with fast magnetosonic solitons. Such solitons are nonlinear pulses, which are characterized by increased magnetic and thermal pressures and propagate faster than $v_{fms}$. The passage of the soliton does not modify the plasma in the sense that the plasma conditions far upstream of the soliton equal those in its distant downstream region. A soliton suffers no loss of energy and momentum to the plasma and hence it is undamped. It maintains its shape and strength as long as the surrounding plasma conditions do not change.

A fast magnetosonic soliton can grow if it is driven by an external current, in which case it ceases to be a soliton. We will refer to it in this case as a fast magnetosonic solitary (FMS) wave. It can grow to an amplitude that turns it into a shock (Gueroult et al., 2017) that replaces the original one. This process is the self-reformation of a perpendicular shock discussed previously. Satellite measurements suggest that the Earth's bow shock is affected by it (Lobzin et al., 2007).

We examine here with a particle-in-cell (PIC) simulation a shock that moves through an electron-proton plasma at the speed 1.5 $v_{fms}$. Such a speed is well below the threshold speed 2.76 $v_{fms}$ above which shocks become supercritical (Marshall, 1955; Gosling and Robson, 1985). Indeed our shock does not reflect upstream protons via their Larmor rotation in the shock's magnetic field as in Ref. (Gueroult et al., 2017). However, the thermal velocity spread of the inflowing protons implies that some cannot overcome the shock potential and are reflected back upstream. Studying self-reformation using a subcritical shock turns out to have two main advantages. Firstly the shock-reflected proton beam carries little energy. Self-reformation is less violent and complex than that of super-critical shocks. Secondly, we remove the time scale related to the Larmor-rotation of protons.

Our results are the following. The shock-reflected proton beam drives a FMS wave upstream of the original shock that grows into a fast magnetosonic shock with a partially developed downstream region. We call this structure a proto-shock. It reflects the protons of the shock-reflected proton beam back to the trailing original shock. This momentum transfer pushes the proto-shock, which maintains the high speed of its downstream region. Since the forward shock of the proto-shock is propagating faster than the downstream material this momentum transfer lets the proto-shock grow.

The interplay of the proto-shock with the protons that were reflected by the original shock increase in time the density and the magnetic field amplitude of the plasma behind it. Both reach values that are higher than those upstream of the proto-shock. Unequal plasmas on either side of the proto-shock imply that it is not a soliton. It changes the mean speed of the protons that cross it. The original shock runs into a plasma that moves in the same direction, which leads to its acceleration. A reduction of the pressure difference across the rear end of the proto-shock reduces the potential difference between both plasmas and its ability to decelerate the shock-reflected proton beam that arrives from the original shock. The rear end of the proto-shock accelerates in order to reduce its speed relative to the incoming proton beam through which it can continue to reflect them back to the original shock and extract their momentum. The rear end of the proto-shock reaches a speed that exceeds that of its front. The downstream region of the proto-shock shrinks and it collapses before the trailing original shock catches up with it; the shock reformation fails.

### 4.4.1 Initial conditions

Numerical shock tube simulation (Fig.4.27 left) is based on the setup already explored in section 4.2 a,d in Refs. (Dieckmann et al., 2017b; Moreno et al., 2018d). The kinetic shocks and plasma dynamics in these conditions are regulated by structures that exist also in the single-fluid MHD model (Myong and Roe, 1997). An electrostatic lower-hybrid shock is formed initially accompanied with a current that modifies the magnetic field, and excites the magnetosonic mode. These shocks are producing a weak shock-reflected ion beam which does not lead to self-reformation. In the present simulation, we modifed plasma parameters in order increase the shock speed and to generate a self-reformation. We use here ionized hydrogen instead of nitrogen in section 4.2, which increases the ion thermal spread, and allows a larger range of reflected ions.

Table 4.27 defines plasma parameters that used in the simulation with $\gamma_e = 5/3$ and $\gamma_i = 3$.

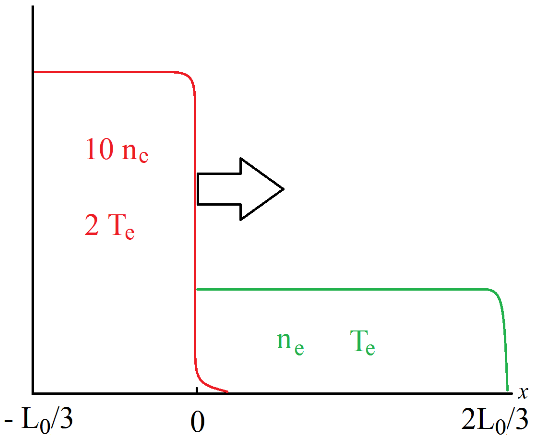

| Parameter | Numerical value |
|---|---|
| $\omega_{pe} = (n_e e^2/\epsilon_0 m_e)^{1/2}$ | $1.78 \cdot 10^{12}\mathrm{s}^{-1}$ |
| $\omega_{ce} = eB_0/m_e$ | $1.58 \cdot 10^{11}\mathrm{s}^{-1}$ |
| $v_{the} = (k_B T_e/m_e)^{1/2}$ | $1.87 \cdot 10^{7}\mathrm{m.s}^{-1}$ |
| $r_{ge} = v_{the}/\omega_{ce}$ | $1.67 \cdot 10^{-1}\mathrm{mm}$ |
| $\omega_{pi} = (Z^2 n_i e^2/\epsilon_0 m_i)^{1/2}$ | $4.16 \cdot 10^{10}\mathrm{s}^{-1}$ |
| $\omega_{ci} = ZeB_0/m_i$ | $8.61 \cdot 10^{7}\mathrm{s}^{-1}$ |
| $v_{thi} = (k_B T_i/m_i)^{1/2}$ | $1.24 \cdot 10^{5}\mathrm{m.s}^{-1}$ |
| $r_{gi} = v_{thi}/\omega_{ci}$ | $1.43\mathrm{mm}$ |
| $c_s = ((\gamma_e T_e + \gamma_i T_i)/m_i)^{1/2}$ | $6.04 \cdot 10^{5}\mathrm{m.s}^{-1}$ |
| $v_a = B_0/(\mu_0 n_0 m_i)^{1/2}$ | $6.20 \cdot 10^{5}\mathrm{m.s}^{-1}$ |
| $\beta = (c_s/v_a)^2$ | $\sim 1$ |
| $v_{fms} = (v_a^2 + c_s^2)^{1/2}$ | $8.66 \cdot 10^{5}\mathrm{m.s}^{-1}$ |

Figure 4.27 – Sketch of the plasma density distribution (left) and the ambient plasma parameters in our simulation (right).

We resolve one spatial dimension $x$ and three particle velocity components. Periodic boundary conditions are used for the fields and open boundary conditions for the computational particles (CPs). The simulation box is large enough to separate effects introduced by the boundaries from the area of interest. The length $L_0 = 0.5$ m of the simulation box is subdivided into evenly spaced grid cells with the length $\Delta_x = 5\mu$m. We consider here fully ionized hydrogen.

The ambient plasma fills the interval $0 < x < 2L_0/3$. Its electron and ion temperatures are $T_e = 2.32 \times 10^7$K and $T_i = T_e/12.5$. Table 4.27 lists all relevant parameters of the ambient plasma with the ion and electron density $n_i = n_e = n_0$ with $n_e = 10^{21}\mathrm{m}^{-3}$. A denser plasma fills the interval $-\mathrm{L}_0/3 \leq x \leq 0$. It consists of ions and electrons with the density $10n_0$ and with the temperature $\mathrm{T}_i$ for ions and $2\mathrm{T}_e$ for electrons. All species are initially at rest. A spatially uniform background magnetic field with the strength $\mathrm{B}_0 = 0.9$ T and orientation $\theta = 90°$ fills the entire simulation box. We represent the electrons and ions of the ambient and dense plasma by $2 \times 10^3$ ppc each. The simulation box covers the interval $-990 < x/r_{ge} < 1980$ ($r_{ge}$ : electron thermal gyroradius). We examine the data during the time interval $0 \leq t\omega_{ce} \leq t_{max}$ with $t_{max} = 1.2 \times 10^4$ (~ 80 ns). $t_{max}$ is resolved by $4.8 \times 10^6$ time steps.

### 4.4.2 Simulations results

**Early expansion phase at 9.5 ns** ($t\omega_{ci} = 0.82$)

Figure 4.28 displays the proton density, the magnetic field amplitude and the projections of the proton phase space density distributions on the $x, v_x$ plane and on the $x, v_y$ plane at 9.5 ns in the interval $-10\,\mathrm{mm} \leq x \leq 25$ mm.

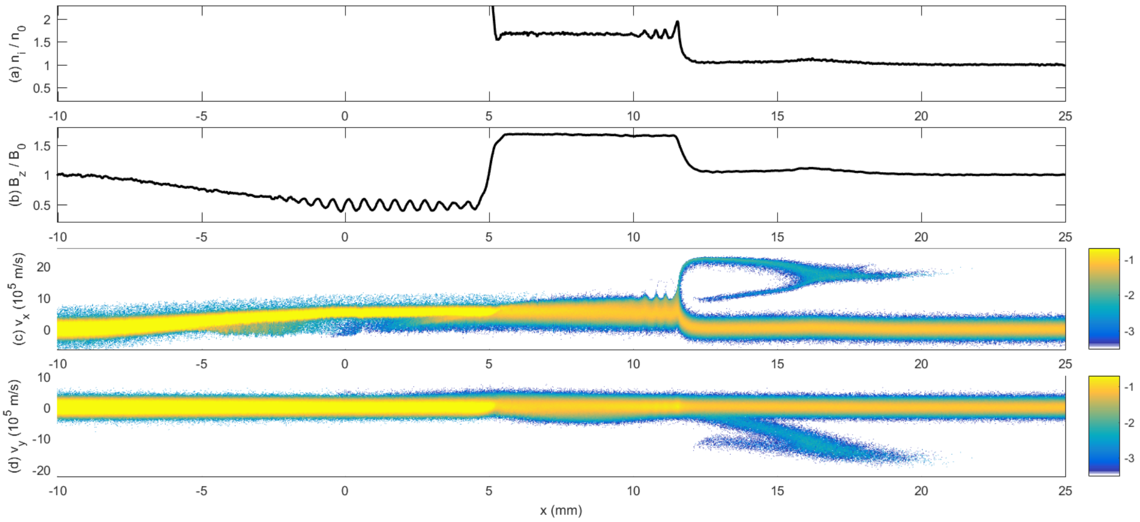

Figure 4.28 – The plasma state at the time $t\omega_{ci} = 0.82$: Panel (a) shows the ion density $n_i/n_0$. The magnetic $\mathrm{B}_z/\mathrm{B}_0$ component is plotted in panel (b). Panels (c,d) shows the phase space density distribution $(x, p_x)$ and $(x, p_y)$ respectively of the ions on a 10-logarithmic scale.

Figure 4.28(a) reveals a density plateau with $n_i \approx 1.7n_0$ in the interval 5 mm $\leq x \leq$ 10 mm and a density distribution that oscillates around this value in the interval 10 mm $\leq x \leq$ 12 mm. The density decreases to a value just above $n_0$ for $x >$ 12 mm. A small density hump is located in the interval 15 mm $\leq x \leq$ 17 mm. The density jumps to $5n_0$ in the interval 0 mm $\leq x \leq$ 5 mm and grows for decreasing -10 mm $\leq x \leq$ 0 mm at an almost constant slope to $10n_0$ (not shown). We observe a reduced magnetic field amplitude in the interval -10 mm $\leq x \leq$ 5 mm and oscillations in the interval 0 mm $\leq x \leq$ 5 mm. These magnetic field oscillations are in phase with the density oscillations and they are thus fast magnetosonic modes. The magnetic amplitude jumps to $1.7\mathrm{B}_0$ at $x = 5$ mm where the proton density decreases. The magnetic field amplitude remains constant up to $x \approx 12$ mm where it decreases to the initial value $\mathrm{B}_0$ with the exception of a hump that coincides with that in the density.

The proton beam in Fig.4.28(c) shrinks along the velocity direction and its mean speed increases for increasing values -10 mm $\leq x \leq$ 0 mm in Fig.4.28(c). The proton's mean speed reaches $v_b \approx 5.2 \times 10^5$ m/s at $x \approx 0$. Figure 4.28(d) shows no changes of the proton distribution in this spatial interval. An acceleration of protons along $x$ and a proton density and magnetic amplitude that decrease with increasing $x$ imply that this structure is a fast rarefaction wave. It propagates to the left into the dense plasma and accelerates its protons to the right. The proton acceleration is accomplished by the electric field driven by the changing thermal and magnetic pressures.

The proton's mean speed does not change in the interval 0 mm $\leq x \leq$ 10 mm in Fig.4.28(c). The decrease of the proton density at $x \approx 5$ mm coincides with an increase of the magnetic field amplitude and of the velocity spread (temperature) of the protons. We recognize this structure as a tangential discontinuity, which separates the protons of the dense plasma from those of the ambient one. Velocity oscillations are observed in the interval 10 mm $\leq x \leq$ 12 mm and they are responsible for the density oscillations in the same interval in Fig.4.28(a). The shock at $x \approx 12$ mm reflects a minor fraction of the ambient protons in Fig.4.28(c), which propagate at the speed $v_x \approx 2 \times 10^6$ m/s to increasing $x$. We do not observe a change of the proton distribution at $x = 12$ mm in Fig.4.28(d) and the reflection is thus not accomplished by a rotation of ambient protons in the shock's magnetic field. They are reflected by the shock potential, which is mediated by fast magnetosonic waves and their changing thermal and magnetic pressures. The density of these reflected ions can be estimated considering the electrostatic potential of the ramp $\Delta\Phi$. The particle able to cross the ramp are those with velocities higher than $v_{cross} = \sqrt{2e\Delta\Phi/m_i}$. Considering a 2D bi-Maxwellian distribution for the ions, the density of the reflected ions is

$$\alpha = \frac{1}{2}\left[1 - \frac{2}{\sqrt{\pi}}\int_0^{\sqrt{\frac{e\Delta\Phi}{\mathrm{T}_x}} - v_{sh}\sqrt{\frac{m_i}{2\mathrm{T}_x}}} e^{-t^2}\,dt\right], \tag{4.35}$$

which corresponds in the simulation to $\alpha = 0.036\,n_i$. We can so make a first estimation of the ramp potential in the simulation, which is

$$\Delta\Phi \simeq \left[(1-2\alpha)\frac{\sqrt{\pi}}{2} + v_{sh}\sqrt{\frac{m_i}{2\mathrm{T}_x}}\right]\frac{\mathrm{T}_x}{e} \simeq 1.5\,10^3\mathrm{V}. \tag{4.36}$$

The shock-reflected protons gain speed in the negative $v_y$ direction with increasing $x > 12$ mm in Fig.4.28(d) and they are slowed down along $v_x$ in Fig.4.28(c). These protons gyrate in the magnetic field of the stationary upstream plasma. A slowdown of the shock-reflected protons along the simulation direction increases their density, which accounts for the density hump at $x \approx 17$ mm that is in phase with a magnetic field hump. We observe in Fig.4.28(c) two separate proton beams in the interval 13 mm $\leq x \leq$ 15.5 mm, which merge at $x \approx 16$ mm and $v_x \approx 1.7 \times 10^6$ m/s or $v_x \approx 2v_{fms}$. Some protons are reflected by an electrostatic potential that moves at $2v_{fms}$ to increasing $x$.

### Solitary wave growth at 19 ns ($t\omega_{ci} = 1.64$)

Figure 4.29 displays the distributions of the proton density, the magnetic field and the proton phase space density at 19 ns in the interval -20 mm $\leq x \leq$ 40 mm.

All distributions resemble qualitatively those at the earlier time up to $x \approx 20$ mm. The blast shell, which was set in motion by the thermal pressure jump between the dense and the dilute plasma, has expanded farther. The tangential discontinuity, which separates the dense plasma from the shocked ambient plasma, is now located at $x = 10$ mm. It propagated 5 mm during 9.5 ns and is thus stationary in the rest frame of the protons between 0 mm $\leq x \leq$ 24 mm that move with the mean speed $v_b$. The shock, which forms the front of the shocked ambient medium, has propagated from $x = 12$ mm to 24 mm. Its speed is $\approx 1.3 \times 10^6$ m/s (1.5 $v_{fms}$).

Significant differences can be observed in the interval $x > 20$ mm in Fig.4.29 compared to that with $x > 12$ mm in Fig.4.28. The humps in the proton density and magnetic field have grown in amplitude and they are now centred at $x \approx 29$ mm. A velocity modulation is observed at this position in Fig.4.29(c) but not in Fig.4.29(d), which implies that the velocity oscillation is sustained by an electric field in the x-direction. This phase space distribution and oscillations of the density and of the magnetic field, which are in phase, are characteristic for a FMS wave. The approximate symmetry of the distribution of the shock-reflected proton beam around the shock speed $1.3 \times 10^6$ m/s and in the interval 24 mm $\leq x \leq$ 28 mm suggests that the FMS wave moves at about the same speed as the trailing shock.

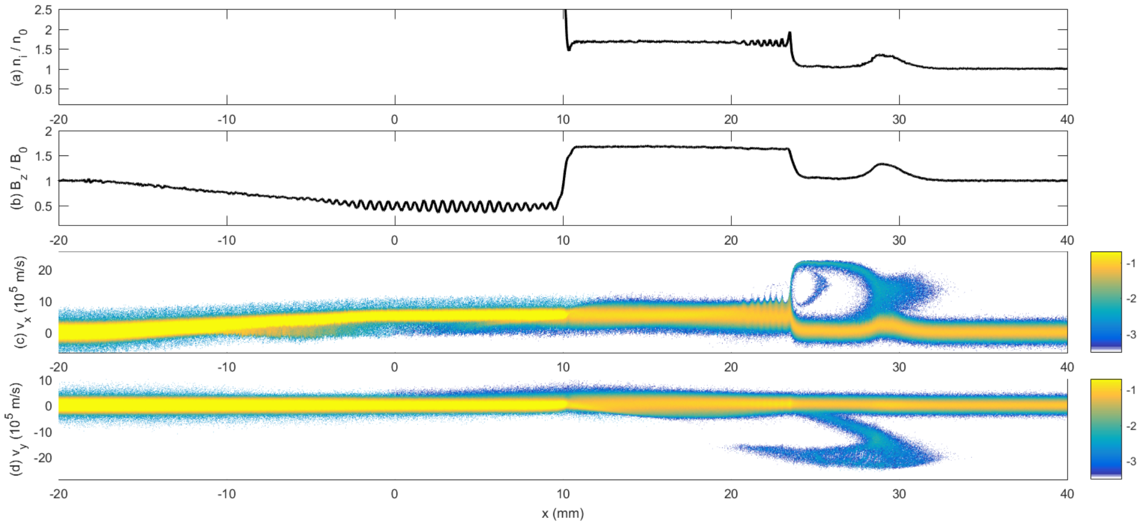

Figure 4.29 – The plasma state at the time $t\omega_{ci} = 1.64$: Panel (a) shows the ion density $n_i/n_0$. The magnetic $\mathrm{B}_z/\mathrm{B}_0$ component is plotted in panel (b). Panels (c,d) shows the phase space density distribution $(x, p_x)$ and $(x, p_y)$ respectively of the ions on a 10-logarithmic scale.

### Emergence and time-evolution of the proto-shock

Figure 4.30 shows the density of the protons of the ambient plasma and the magnetic field amplitude as a function of space and time. We do not consider the protons of the dense plasma since they are separated from the shock and the FMS wave by the tangential discontinuity. The data is transformed into a moving frame $\hat{x} = x - v_0 t$ with $v_0 = 1.25 \times 10^6$ m/s.

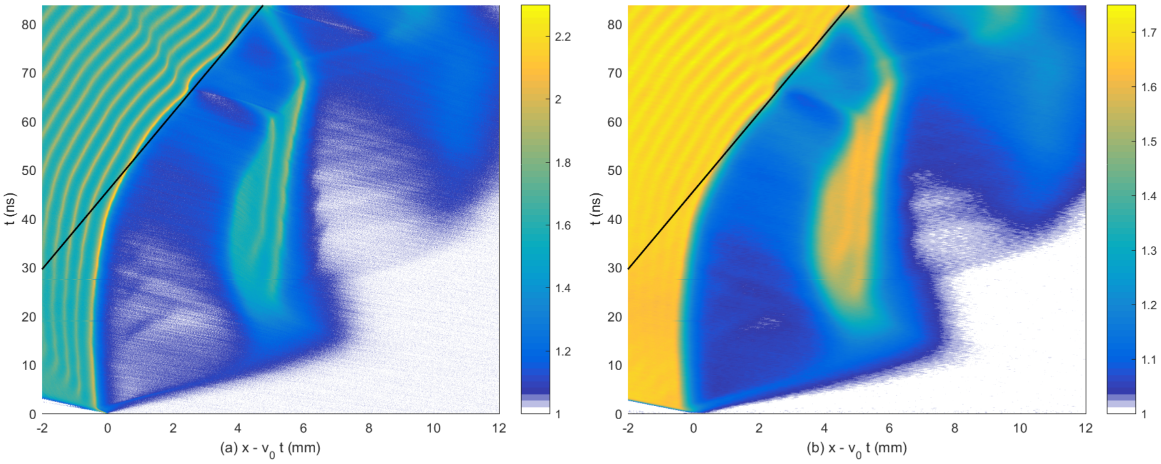

Figure 4.30 – The proton density distribution $n_i(\hat{x}, t)/n_0$ is shown as a function of space and time in panel (a) and that of the magnetic $\mathrm{B}_z(\hat{x}, t)/\mathrm{B}_0$ component in panel (b). Both distributions are sampled in the reference frame $\hat{x} = x - v_0 t$ with $v_0 = 1.25 \times 10^6$ m/s. The overplotted line has the slope $v_0/10$.

Figure 4.30(a) shows how the shock is launched at $\hat{x} = 0$ and $t = 0$. We call it the original shock. A contour with a density $\approx 2.3n_0$ that starts at $\hat{x} \approx -0.2$ and $t = 0$ marks its front. It is followed by additional density contours in Fig.4.30(a) which are separated by the distance $\approx 0.5$ mm ($3r_{ge}$) along the horizontal direction. Figures 4.29(a, c) show that these density contours correspond to the crests of the fast magnetosonic modes that mediate the original shock. They are not correlated with magnetic field modulations prior to $t \approx 25$ ns in Fig.4.30(b).

Initially the shock is stationary in the moving frame and its speed is thus $v_0 - v_b \approx 7.3 \times 10^5$ m/s or $0.84 v_{fms}$ in the downstream frame. The Alfvén speed $v_a$ is proportional to $\mathrm{B}_z(\hat{x}, t)$ and the ion acoustic speed $c_s$ is higher in the hotter downstream plasma. Faster Alfvén and ion acoustic speeds give a larger fast magnetosonic speed downstream of the original shock, which reduces further the shock speed relative to this speed. Our shock involves high-frequency waves, which follow a dispersion relation that is concave as a function of the wave number for a perpendicular propagation. Shock steepening transfers wave energy to larger wave numbers, which fall behind the shock due to their lower group velocity (Sagdeev, 1966) and cause the observed density oscillations.

The original shock launches a proton beam at $t \approx 2$ ns which reaches the position 7 mm at $t \approx 10$ ns giving the speed $\approx 7 \times 10^5$ m/s. Specular reflection of protons at rest by the original shock should give a speed $\sim v_0$ in this frame. However, the thermal velocity spread of the ambient protons implies that the original shock reflects protons from the Maxwellian tail with a positive value of $v_x$, which have a lower speed relative to the shock (See Fig.4.28). The density peaks at the front of the beam, which carries the protons that were accelerated during the growth of the original shock. Once the original shock has fully developed it reflects a lower number of protons. The original shock accelerates at $t \approx 40$ ns and reaches the speed $v_0/10$ shortly after that.

The original shock amplifies $B_z$ to $1.65B_0$ and the proton beam it reflects amplifies it to $\sim 1.1B_0$. The magnetic field amplitude at the front of the shock-reflected proton beam rises immediately after its launch. This rules out an amplification of $B_z$ by the current along y of this proton beam, which gives rise to magnetic field amplification on ion gyro-scales in the foot of a perpendicular shock (Treumann, 2009). We interpret the magnetic field amplification by the shock-reflected beam as follows. The proton beam constitutes a positive current $j_x > 0$ along x that must be balanced by a net flow of electrons $v_e$ in the positive direction. The magnetic field is frozen in the plasma. The magnetic field in the interval, which is occupied by the shock-reflected proton beam, moves to increasing x. It thus carries a convective electric field $E_y > 0$ with $v_e = E_y B_z$ giving $E_y = v_e/B_z$. This electric field component vanishes far upstream and we obtain at the front of the shock-reflected proton beam $dE_y/dx < 0$, which gives via Faraday's law in one dimension $dE_y/dx = -\partial B_z/\partial t$ a magnetic field jump.

A FMS wave grows in Figure 4.30 at $\hat{x} \approx 5$ mm during 10 ns $\leq t \leq$ 25 ns. Its length reaches 2 mm (12 $r_{ge}$) at $t \approx 35$ ns, which can accommodate three wavelengths of the periodic fast magnetosonic wave that mediates the original shock. At this time the FMS wave has become a proto-shock with a forward shock and a partially developed downstream region. The front of the proto-shock expands at a constant speed while its downstream region expands to the left in this moving frame. The proton beam, which is reflected by the original shock, is slowed down by the electric field driven by the thermal- and magnetic pressure gradient at the rear end of the proto-shock. This momentum transfer pushes the proto-shock's downstream region and maintains its speed in the box frame. The shock at the front of the proto-shock moves at a high speed in the rest frame of the downstream medium and the length of the proto-shock increases. The density and magnetic field amplitude behind the proto-shock and ahead of the original one start to increase at around $t = 30$ ns.

The front of the proto-shock moves at the speed $\approx 2 \times 10^4$ m/s in the moving frame between $t =$ 20 ns and 65 ns. A density depletion propagates from its trailing end to increasing $\hat{x}$ after $t \approx 50$ ns. Figure 4.30(a) shows that another density structure propagates at the same time from the trailing end of the proto-shock into the interval between it and the proto-shock. It crosses about -3 mm during 4 ns, which gives it the speed $-7.5 \times 10^5$ m/s in the moving frame or $5 \times 10^5$ m/s ($4v_{thi}$) in the box frame.

Waves are launched towards the original shock when the density depletion crosses one of the density peaks in the proto-shock's downstream region. A weak wave is launched at $\hat{x} = 5$ mm and $t = 60$ ns and a stronger one at $\hat{x} \approx 6$ mm and $t = 65$ ns. The weak wave moves in the direction of the downstream region at a speed of $\sim v_0/3$ in the $\hat{x}$ frame of reference. It crosses the original shock at $t \approx 65$ ns and is responsible for the distortion of the wave fronts behind it along the line that starts at $\hat{x} \approx 2.2$ mm and $t = 65$ ns and ends at $\hat{x} \approx 0.2$ mm at $t = 86$ ns. After crossing the potential of the shock ramp, the weak wave has decreased its speed to $\sim v_0/10$. The velocity of the weak wave behind the shock ramp, in the shock frame of reference moving at the speed $1.1v_0$, is estimated from the energy conservation

$$v_{ww} = \frac{2v_0}{10} = \sqrt{\left(\frac{v_0}{3} + \frac{v_0}{10}\right)^2 - \frac{2e\Delta\Phi}{m_i}}. \tag{4.37}$$

This simple model allows us to estimate the potential of the shock ramp at $\Delta\Phi = 1.2\,10^3$ V, which is comparable to our first estimation. After that the weak wave continues its propagation downstream without any perturbation or attenuation. The original shock outruns the stronger wave and crosses it at $t = 86$ ns. The stronger wave crosses the distance -1.5 mm during 20 ns before it is swept up by the original shock. Its speed in the moving frame is thus $\approx -7.5 \times 10^4$ ms or $1.2 \times 10^6$ m/s in the box frame. Both waves are unipolar density and magnetic field pulses and the stronger one propagates faster than the weaker one in the rest frame of the simulation box, which is typical for fast magnetosonic solitons.

We do not observe here a self-reformation of the original shock. That would require that a FMS wave forms in its upstream region and is transformed into a new shock while the original shock collapses. In what follows we examine the cause of the proto-shock's collapse and determine why and how faster fast magnetosonic shocks self-reform.

### The proto-shock at 38 ns ($t\omega_{ci} = 3.27$)

Figure 4.31 displays the proton density, the magnetic field amplitude and the phase space density distribution of the protons in a spatial interval close to the original shock at the time 38 ns when the proto-shock has reached its maximum size. This shock is located at $x \approx 48$ mm. It separates the modified upstream plasma with the density $\approx 1.1n_0$ and the magnetic field amplitude $\approx 1.1\text{B}_0$ from its downstream region with the density $\approx 1.7n_0$ and magnetic amplitude $\approx 1.7\text{B}_0$. Its transition layer 44 mm $\leq x \leq$ 48 mm is characterized by strong proton density oscillations. The amplitude of the density oscillations and of the associated electrostatic field is large enough to trap protons downstream of the shock; we observe closed circular structures known as ion phase space holes Eliasson and Shukla (2006) at $v_x \approx 1.5 \times 10^6$ m/s and 42 mm $\leq x \leq$ 48 mm in Fig.4.31(c).

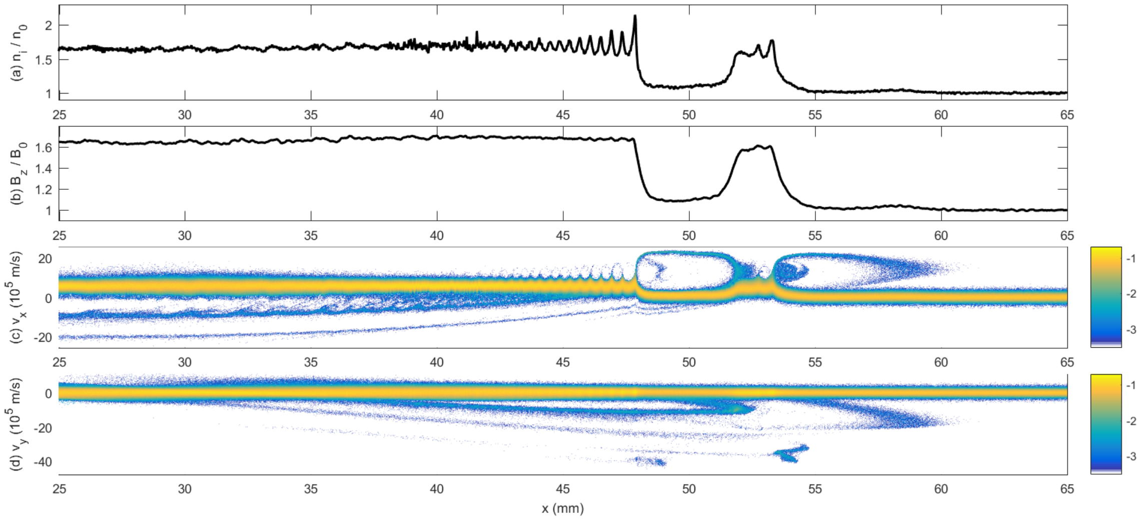

Figure 4.31 – The plasma state at 38 ns: panel (a) shows the proton density $n_i/n_0$. The magnetic $\text{B}_z/\text{B}_0$ component is plotted in panel (b). Panels (c, d) show the phase space density distributions $(x, v_x)$ and $(x, v_y)$ of the protons. The latter are normalized to their maximum values and displayed on a 10-logarithmic scale.

The proto-shock is located in the interval 51 mm $\leq x \leq$ 54 mm. Its downstream region has values of the proton density and magnetic field amplitude that are marginally below those behind the original shock. Proton density oscillations caused by the dispersive fast magnetosonic modes trail the front of the proto-shock. Small humps have developed ahead of the proto-shock at $x \approx$ 58 mm in Figs. 4.31(a, b). Figures 4.31(c) shows that these humps consist of plasma that was piled up by the beam of protons that have been reflected by the proto-shock. Similar fronts of the proto-shock and of the original shock in Fig.4.28 witness the onset of a shock self-reformation.

Upstream protons, which were reflected by the original shock, propagate towards the proto-shock. They start to slow down at $x \approx 49$ mm under the influence of the electric field, which is driven by the slowly changing thermal and magnetic pressures in the interval 49 mm $\leq x \leq$ 52 mm. The protons can not overcome the positive potential of the proto-shock and are reflected at its rear end in Fig.4.31(c) forming the large circular phase space structure in the interval 48 mm $\leq x \leq$ 52 mm.

Figures 4.31(c, d) demonstrate that protons, which were reflected by the proto-shock and return to the original shock, are not reflected by it even though their velocity along $v_x$ at $x = 48$ mm is comparable to that of the inflowing upstream protons. This large vortex is thus not an ion phase space hole where trapped ions gyrate in an electrostatic potential and follow closed orbits. Figure 4.31(d) shows that the returning protons have the speed $v_y \approx -10^6$ m/s at $x \approx 48$ mm. The $\mathbf{v} \times \mathbf{B}$-force accelerates the protons in the negative x-direction and helps them overcoming the shock potential (Treumann, 2009). A second energetic proton beam is created by the reflection of upstream protons at the front of the proto-shock. These protons rotate in the upstream magnetic field and reach the speed $v_y \approx 2 \times 10^6$ m/s in the downstream region of the original shock.

The proton beam in the interval 25 mm $\leq x \leq$ 40 mm with the speed $v_x \approx -10^6$ m/s in Fig.4.31(c) maintains this speed over more than 10 mm. A proton, which moves at the speed modulus $1.5 \times 10^6$ m/s in the downstream reference frame (relative speed $v_b$) and rotates in the downstream magnetic field 1.6B$_0$, has the Larmor radius 10 mm. We would expect a faster change of $v_x$ with $x$ for this beam. This energetic proton beam is injected at the shock, which moves at the speed $\approx v_0$ to increasing $x$. The structure of the beam of energetic protons downstream of the original shock is thus determined by the shock motion and by the Larmor rotation of the protons.

Small proton clouds with speeds halfway between the mean speed of the upstream protons and that of the shock-reflected protons are located close to $x \approx 49$ mm and 54 mm in Fig.4.31(c). These protons are trapped in the shock potential; their low speed in the shock frame implies that they can neither escape upstream nor overcome the shock potential and move downstream. They are located upstream of the shock and they are thus transported across a magnetic field, which is practically at rest in the simulation frame. This transport accelerates the trapped protons in the negative y-direction and they have reached the speed $v_y \approx -4 \times 10^6$ m/s in Fig.4.31(d). They detrap once the $\mathbf{v} \times \mathbf{B}$-force exceeds that the shock imposes on them and they move downstream (Lee et al., 1996).

### The proto-shock at 57 ns ($t\omega_{ci} = 4.91$)

Figure 4.32 shows the relevant plasma distributions at the time 57 ns when the size of the proto-shock has halved compared to that in Fig.4.31. The original shock is located at $x \approx 73.5$ mm and its average speed between $t = 38$ ns and 57 ns amounts to $1.34 \times 10^6$ m/s. Its transition layer is otherwise similar to that in Fig.4.31. The proton distribution at the proto-shock's front at $x \approx 78$ mm is also qualitatively unchanged. A strong FMS wave has formed in its upstream region. We find no protons trapped in the potential of the original shock; they have detrapped at this time. A circular structure at $x \approx 78$ mm and $v_x \approx 1.5 \times 10^6$ m/s evidences that shock surfing acceleration is still at work at the proto-shock and the trapped protons have reached the speed $v_y \approx -6 \times 10^6$ m/s; their kinetic energy is close to 200 keV.

Clear differences between Figs. 4.31 and 4.32 are observed in the downstream region of the proto-shock. We observed fast magnetosonic waves in this region at $t = 38$ ns and the proton beam, which was reflected by the original shock, could not cross the downstream region of the proto-shock. Figure 4.32(c) reveals a solitary ion phase space hole at $x = 77.5$ mm and $v_x \approx 1.5 \times 10^6$ m/s. Protons from the incoming shock-reflected proton beam are not stopped by such a structure, which is sustained by a localized negative excess charge. Some of the protons of the incoming beam are accelerated when they approach the ion phase space hole and decelerated when they leave it on the other end. These protons can thus cross the proto-shock without transfering their

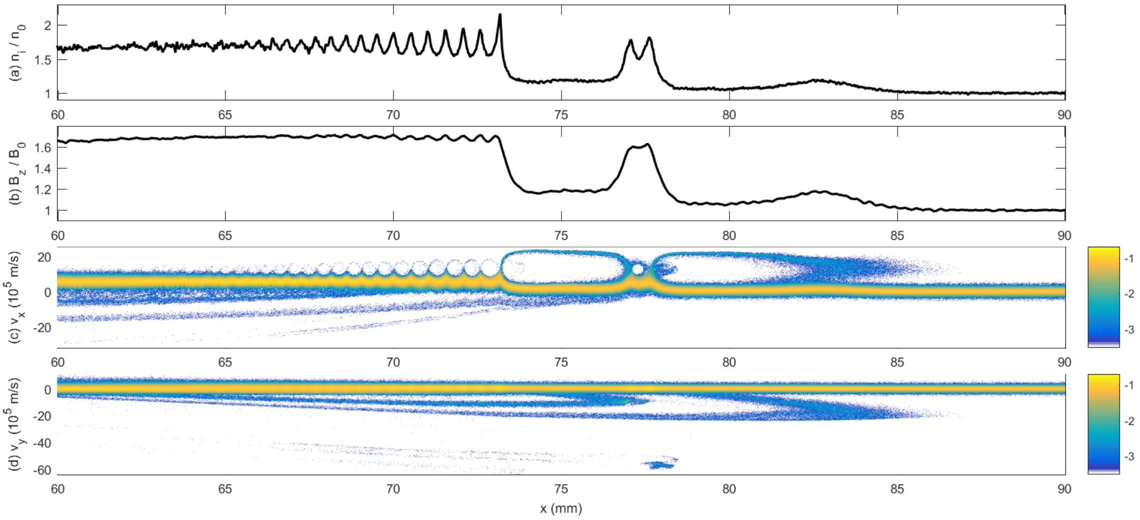

Figure 4.32 – The plasma state at 57 ns: panel (a) shows the proton density $n_i/n_0$. The magnetic $B_z/B_0$ component is plotted in panel (b). Panels (c, d) show the phase space density distributions $(x, v_x)$ and $(x, v_y)$ of the protons. The latter are normalized to their maximum values and displayed on a 10-logarithmic scale.

momentum to it and the proto-shock is no longer pushed by the beam; it will collapse.

### The mechanism for the collapse of the proto-shock

Figure 4.33 compares the intervals between the original shock and the proto-shock at the times 38 ns and 57 ns. Figures 4.33(a, b) depict the proton phase space density distributions in the $x, v_x$ plane. One oscillation of the proton distribution is visible at low $x$, which is tied to the electrostatic potential of the fast magnetosonic wave. We observe a faint beam of trapped protons. The overplotted horizontal bar shows that the wavelength of the mode is 5.35 mm ($3.2r_{ge}$) at 38 ns and about 10% larger at 57 ns. Such a marginal change of the wave length hardly affects the phase- and group velocities of a fast magnetosonic waves and it can thus not be responsible for the shock acceleration between 38 and 57 ns in Fig.4.30.

Figures 4.33(c, d) show the density and magnetic field distributions that sustain the proton phase space density distributions. The waves at the front of the original shock at low $x$ have a similar density- and magnetic field amplitude at both times and it is thus unlikely that the shock acceleration is tied to nonlinear modifications of their dispersion relation. Both distributions differ at the rear end of the proto-shocks at large $x$. A smooth change of both densities from values $B_z \approx 1.1B_0$ and $n_i = 1.1n_0$ to values $1.6B_0$ and $1.6n_0$ is observed at the time 38 ns while we observe an overshoot at the time 57 ns that is followed by a density depletion. The latter is tied to the ion phase space hole visible in Fig.4.33(b). Ion phase space holes are electrostatic structures and hence we do not see a modification of $B_z$ at its location.

The most important difference between the plasma state at both times shown in Fig.4.33 are the different values for the density and magnetic field amplitude in the intervals between the original- and the proto-shock. Both values are 1.1 times their initial one in Fig.4.33(c) and 1.2 times that in Fig.4.33(d). Figure 4.30(a) reveals that this difference is tied to the density structure that is launched at $\hat{x} \approx 3.5$ mm and $t \approx 32$ ns and reaches $\hat{x} \approx 0.5$ mm at $t \approx 36$ ns. This speed corresponds to $5 \times 10^5$ m/s in the box frame. We are thus looking for a proton density structure with a speed just above the peak speed of the bulk protons in Figs. 4.33(a, b). The latter suggest that this structure is tied to the proton beam that was reflected first at the original shock and then again at the rear end of the proto-shock. This beam is returning back to the original shock at a velocity just above the cutoff velocity $v_x \approx 4 \times 10^5$ m/s of the proton distributions in Fig.4.33(c). Its protons yield the suprathermal proton tail at $x \approx 51.5$ mm and $v_x \approx 5 \times 10^5$ m/s in Fig.4.33(a). This beam

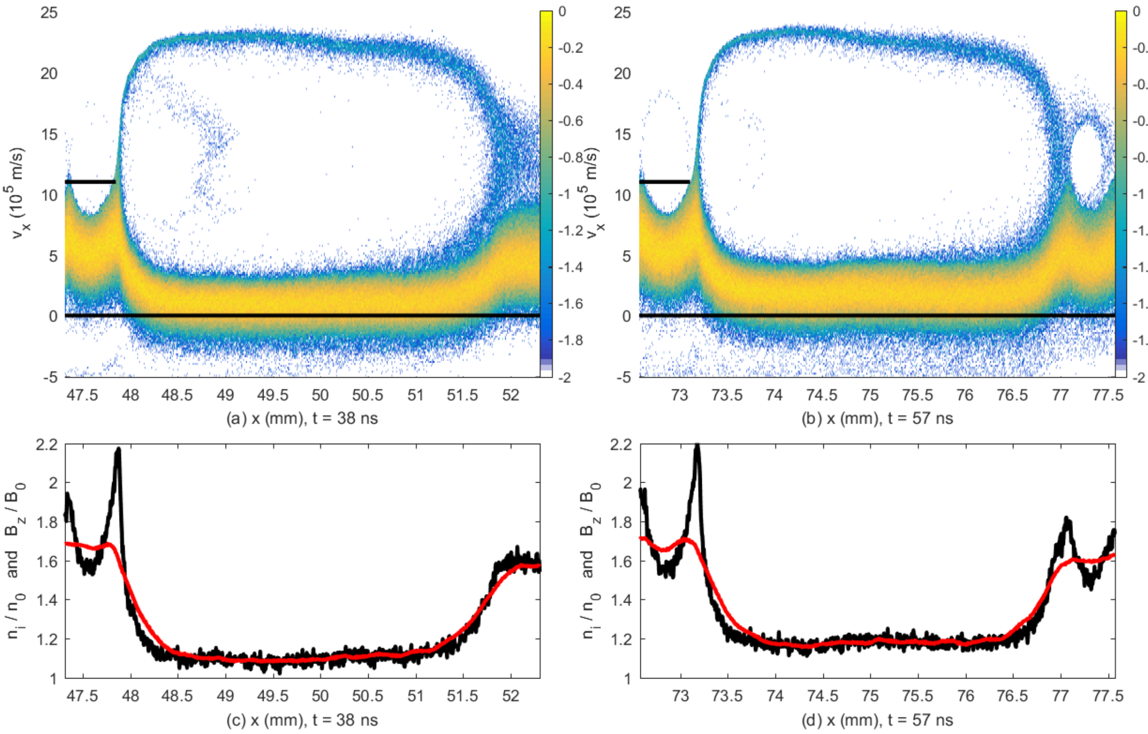

Figure 4.33 – A comparison of the plasma distributions at 38 ns and 57 ns: panels (a) and (b) show the phase space density distributions along $x, v_x$ at the times 38 ns and 57 ns, respectively. Each distribution is normalized to its peak value and displayed on a 10-logarithmic color scale. Horizontal lines show the initial mean speed $v_x = 0$ of the ambient protons. Horizontal lines at $v_x = 11 \times 10^5$ m/s indicate the reference length 5.35 mm. Panel (c) shows the proton density $n_i(x)/n_0$ (black) and $\mathrm{B}_z(x)/\mathrm{B}_0$ (red) corresponding to (a). Panel (d) shows them in the interval resolved by (b).

mixes eventually with the bulk of the protons and both populations can not be distinguished any more in Figs. 4.33(b).

Can the shock-reflected proton beam by itself be responsible for the density increase between the original shock and the proto-shock? We integrated the distributions in Figs. 4.33(a, b) over $1.5 \times 10^6$ m/s $\leq v_x \leq 2.5 \times 10^6$ m/s and obtained a density $n_0/50$ for the proton beam in the interval 49 mm $\leq x \leq$ 51 mm. Its density accounts for the elevated values in the interval 0.5 mm $\leq \hat{x} \leq$ 3.5 mm and 10 ns $\leq t \leq$ 25 ns in Fig.4.30(a). This proton beam is reflected at the rear end of the proto-shock and its speed decreases from $2.3 \times 10^6$ m/s to $5 \times 10^5$ m/s, which results in its compression by the factor 4.6. Adding up the densities of the fast incoming beam and the slow reflected beam and neglecting the loss of protons that enter the downstream region of the proto-shock in Fig.4.33(a) at $x > 52$ mm yields $0.11n_0$, which can account for the density enhancement in Fig.4.33(c). This density remains unchanged between 38 ns and 57 ns and we require another source of proton density to explain the density plateau with $1.2n_0$ in Fig.4.33(d).

Most protons between the original shock and the proto-shock are upstream protons that crossed the proto-shock. Its forward shock is maintained by a balance between the thermal and magnetic pressure of its downstream region and the ram pressure of the inflowing upstream plasma. This pressure difference is high because $\mathrm{B}_z$ and $n_i$ increase by the factor 1.6 at this forward shock, which changes the proton's mean velocity from the value of zero upstream of the shock to a value $v_b$ in its downstream region. An electric potential, which is set by the difference between the thermal and magnetic pressures in the proto-shock and behind it, accelerates the protons that leave the proto-shock at its rear end. Figure 4.33(c) shows that the values for $n_i$ and $\mathrm{B}_z$ behind the proto-shock are 1.1 times higher than those upstream of the proto-shock. In the rest frame of the proto-shock's downstream region the protons that leave the proto-shock are accelerated less than they were decelerated at its front. This implies also that they are decompressed less than they were compressed at the forward shock. The plasma between the proto-shock and the original shock must thus be denser than that upstream of the proto-shock, which provides the additional density in Fig.4.33(d).

Figure 4.33(a) reveals a weak change of the proton's mean velocity with increasing 49 mm $\leq x \leq$ 51 mm. Their mean speed is $6.3 \times 10^4$ m/s at 49.25 mm and increases to $9.3 \times 10^4$ m/s at 50.75 mm. A velocity change leads to a density change. The latter is responsible for the density structure that is emitted at the rear end of the proto-shock in Fig.4.30(a). The mean velocity of the bulk protons in Fig.4.33(b) reaches $1.65 \times 10^5$ m/s ($0.32 v_b$) between 74.75 mm $\leq x \leq$ 75.5 mm surrounded by minimum values $1.5 \times 10^5$ m/s ($0.29 v_b$) at 74 mm and 75.5 mm. This substantial decrease of the proton acceleration and decompression at the rear end of the proto-shock can account for the density increase beyond $1.1 n_0$ in Fig.4.33(d). The original shock in Fig.4.33(c) is no longer propagating into a plasma at rest but into one that moves at the speed $\approx v_0/10$ into the shock's propagation direction. The increase of the speed of the original shock Fig.4.30 is probably a consequence of the changed mean speed of its upstream plasma.

Figure 4.33(b) demonstrates that the shock-reflected proton beam maintains its speed $2.3 \times 10^6$ m/s even after the original shock has accelerated. This proton beam is slowed down at the rear end of the proto-shock. A momentum transfer from this beam to the proto-shock is most efficient if the proto-shock can reflect them back to the original shock. Figure 4.33(a) shows that this is true for most protons at the time 38 ns. The potential difference across the rear end of the proto-shock and its ability to reflect the incoming proton beam has decreased at the time 57 ns. Figure 4.30 shows that the rear end of the proto-shock accelerates at this time, which reduces the velocity gap between it and the incoming protons that were reflected by the original shock. It can thus continue to reflect them until the rear end reaches the front of the proto-shock.

### The remainder of the proto-shock at 76 ns ($t\omega_{ci} = 6.55$)

Figure 4.34 displays the distributions of the magnetic field and of the protons density as well as that of the phase space density at the time 76 ns. The original shock has reached $x \approx 100$ mm, which yields an average propagation speed $\sim 1.4 \times 10^6$ m/s between $t = 57$ ns and 76 ns. Its structure and that of its downstream region remain qualitatively unchanged compared to those at earlier times. Such a stability is typical for subcritical shocks. It is no longer preceded by a fully developed proto-shock. Humps in the density and magnetic field distributions are found at $x \approx 101.5$ mm in Figs. 4.34(a, b). Figure 4.30 shows that these humps are what remains from the proto-shock. Figure 4.34(c) reveals a velocity modulation at the position of the hump, which is responsible for the local increase of the proton density and of the magnetic field amplitude. This structure is thus

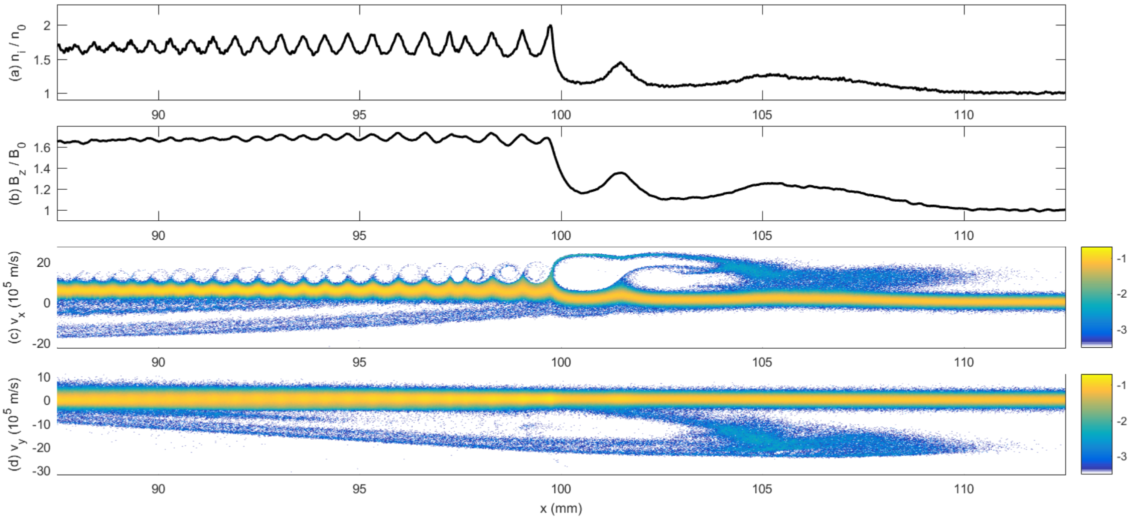

Figure 4.34 – The plasma state at 76 ns: panel (a) shows the proton density $n_i/n_0$. The magnetic $B_z/B_0$ component is plotted in panel (b). Panels (c, d) show the phase space density distributions $(x, v_x)$ and $(x, v_y)$ of the protons. The latter are normalized to their maximum values and displayed on a 10-logarithmic scale.

still a FMS wave. It propagates to increasing x at the speed $1.2 \times 10^6$ m/s in the box frame (See Fig.4.30). Some of its upstream protons are reflected by the wave potential and give rise to a beam with $v_x \approx 1.5 \times 10^6$ m/s in the interval 102 mm $\leq x \leq$ 104 mm. We computed the mean speed $v_x \approx 0$ of the protons ahead of the FMS wave. Their mean speed reaches $3.5 \times 10^5$ m/s at the crest of the FMS wave and decreases to $1.3 \times 10^5$ m/s behind it. Its peak speed exceeds $v_{thi}$ by a factor ~ 3. The more energetic proton beam, which is reflected by the original shock at $x \approx 100$ mm, is slowed down and then reaccelerated by the potential of the FMS wave. This beam does not thus transfer any net momentum to the solitary wave.

### The end of the proto-shock at 86.5 ns ($t\omega_{ci} = 7.45$)

Figure 4.35 displays the distributions of the density and magnetic field and that of the proton phase space density distributions at the time 86.5 ns. The FMS wave was significantly slower than the original shock and it has just been swept up by it at this time. Both structures are located in the interval 110 mm $\leq x \leq$ 112 mm. We can distinguish both with the help of the proton beams they reflect. Previously the proton beam, which was reflected by the original shock, reached a higher speed than the one that was reflected by the FMS wave and we assume that this is still the case. We identify the original shock as the one that accelerates protons at $x \approx 110.5$ mm while the FMS wave gives rise to the less energetic proton beam at $x \approx 111$ mm.

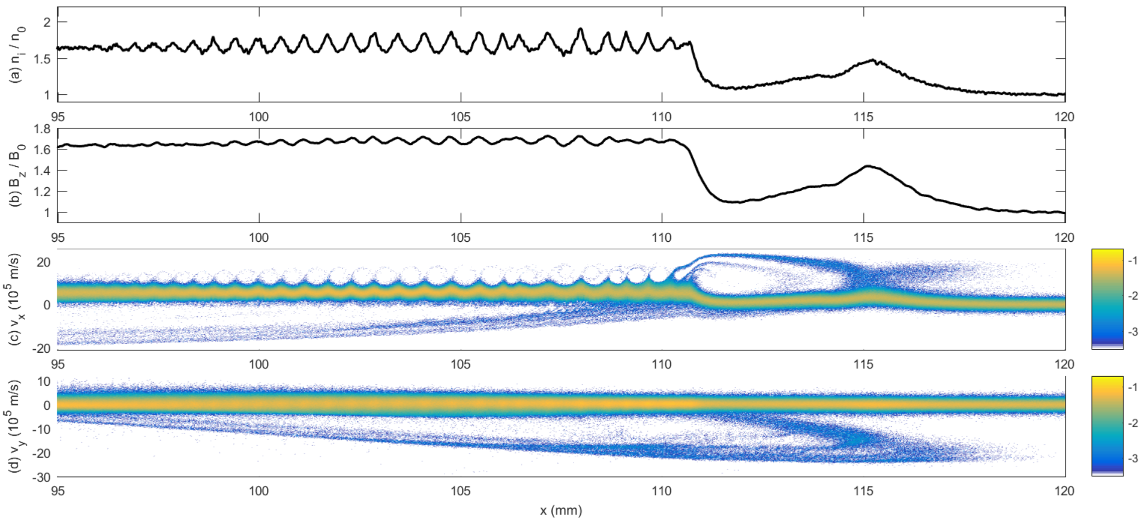

Figure 4.35 – The plasma state at 86.5 ns: panel (a) shows the proton density $n_i/n_0$. The magnetic $B_z/B_0$ component is plotted in panel (b). Panels (c, d) show the phase space density distributions $(x, v_x)$ and $(x, v_y)$ of the protons. The latter are normalized to their maximum values and displayed on a 10-logarithmic scale.

We anticipate from looking at Fig.4.35(c) how the FMS wave could interact with the original shock. As long as the FMS wave was located in the plasma ahead of the original shock its speed was limited by the fast magnetosonic speed and the low speed of the upstream plasma. The original shock could catch up with it. However, the FMS wave has now entered the downstream region that moves at the speed $v_b$ to increasing $x$ and its hotter plasma and stronger magnetic field let the FMS wave move faster. If this nonlinear wave is fast enough to stay ahead of the original shock it will grow by its interaction with the inflowing upstream plasma. Figure 4.35(c) shows that the proton beam, which is reflected by the original shock, slows down while it approaches the FMS wave. Its protons can still cross its potential at this time and are reaccelerated at the other side. Let us assume that the FMS wave continues to grow. The proton beam, which is reflected by the original shock at $x = 110$ mm, will not be able to cross its potential any more. It will be reflected back and form a beam of protons trapped in the potential of an ion phase space hole. The FMS wave will become the new original shock. We note that the FMS wave will only become the new original shock if its amplitude and, hence, its speed are high enough to let it stay at the front of the shocked ambient plasma. The weaker and slower FMS wave, which was launched at the earlier time in Fig.4.30, crossed the original shock and propagated into the downstream region.

A new FMS wave grows at $x \approx 115$ mm, as well as potential build up, and a new ion reflection starts, suggesting a cyclic process. However, this process is beyond the scope of the present part of the thesis and will be considered separately.

### 4.4.3 Discussion

We have studied with a particle-in-cell (PIC) simulation the evolution of a subcritical perpendicular fast magnetosonic shock through a plasma, which consisted of electrons and protons with the correct mass ratio. The shock was launched by a thermal pressure jump and it propagated at 1.5 times the fast magnetosonic speed into the ambient plasma. This speed was similar to that in section 4.2 and several of the plasma structures we observed here have already been discussed in this earlier section. These were the fast rarefaction wave, the tangential discontinuity and the fast magnetosonic shock. Here we have replaced the fully ionized nitrogen by protons and we increased the plasma density, which changed the evolution of the fast magnetosonic shock.

Supercritical shocks reflect inflowing ions by their rotation in the magnetic field in the shock transition layer. This beam develops and evolves on a time scale that is comparable to an inverse ion gyrofrequency. Such beams consist of a significant fraction of the inflowing upstream ions and their speed is high. This energetic ion beam drives violent processes upstream of the shock, which are difficult to analyse and interpret. Subcritical shocks like the one we consider here do not have to reflect inflowing ions; the shock transition layer can be sustained by the electrostatic potential of the shock. We selected protons with a large thermal velocity spread, which implied that protons on the Maxwellian tail with the lowest speed relative to the shock could not overcome its potential. They were reflected upstream forming a dilute beam. This beam disappears when the magnetic field is tilted just by a few degrees (Moreno et al., 2018d).

This beam triggered the growth of a fast magnetosonic solitary wave upstream of the shock, which propagated into the same direction as the shock. Its moving potential reflected the incoming beam of shock-reflected protons back to the shock. This reflection transfered the momentum and energy of the protons to the solitary wave. The wave grew into a structure with a forward shock and a short downstream region. We called this structure a proto-shock. No such structure was observed in section 4.2 and Ref. (Dieckmann et al., 2017b). The proto-shock was separated spatially from the original shock and this interval was filled with a plasma that formed the upstream region of the original shock.

Protons from the shock-reflected proton beam increased the density of this plasma and the amplitude of its magnetic field which reduced its potential difference relative to the original shock and relative to the proto-shock. Our simulation demonstrated that the protons, which crossed the proto-shock and entered the plasma that separated the original shock from the proto-shock, reacted to the decreased potential jump. This plasma and the original shock accelerated. The potential drop across the original shock was still large enough to sustain it and it did not collapse. A reduction of the potential difference between this plasma and the proto-shock implied that the trailing end of the proto-shock had to speeds up in order to continue reflecting the incoming proton beam. It reached a speed that exceeded that of the forward shock at the front of the proto-shock and the trailing end caught up with it. The proto-shock collapsed and was swept up by the original shock and the self-reformation of the latter failed. The FMS wave disappears in a time scale of $\sim 4\omega_{ci}^{-1}$, leading to a new FMS wave which will possibly repeat the cycle performed by the first one downstream the shock. Even if our simulation is stopped at the beginning of the new FMS wave merging, it is reasonable to suppose that the process can repeat itself and will allow the shock to reach much higher velocities leading to a cyclic shock acceleration by FMS wave formation upstream in a subcritical regime.

We expect a different evolution if the shock-reflected ion beam is either denser or faster. In either case it will increase further the density between the original shock and the proto-shock. The potential jump between it and the original shock will decrease and it will become too weak to sustain this shock. Decreasing the potential jump between this plasma and the proto-shock will reduce the velocity change at its trailing end, which will extend the downstream region of the proto-shock to the original one.

The simulations presented in this chapter are experimentally relevant. The blast shell of collisionless plasma can be created in laboratory by the ablation of a solid target by an intense laser pulse and made to interact with a second plasma population. These magnetized shocks have been investigated with high-energy laser systems, and Chapter 6 will discuss of an experimental proposal to recreate such shocks in laboratory. Furthermore, an overview of the different laboratory experiments on collisionless shocks will be discussed in the next chapter, which will also present an experiment on collisionless shock formation, where the non-stationarity of the shock is based on micro-instabilities, as the Weibel instability responsible for the turbulence which develops at the shock front and in the downstream region in electron, hybrid and ion ranges.

# Chapter 5

# Collisionless shocks in the context of laboratory experiments

High power laser facilities are a tools of choice to study the properties of astrophysical objects, the overview of the different facilities and their usefulness has already been presented in the Introduction.

Along with rapid theoretical progress enabled by large-scale numerical simulations, intensive efforts are underway to generate collisionless shocks using powerful lasers. These scaled experiments provide unprecedented test-beds for scenarios of shock formation and evolution. The astrophysical community is particularly interested to better understand the origin of cosmic rays from supernova remnants (Park et al., 2015, 2016), and one goal of these experiments is to observe nonthermal particles and radiation generation, processes related to these shocks.

Two classes of collisionless shocks, magnetized (MHD) and electrostatic shocks have been discussed in two previous chapters.

Collisionless magnetized shocks are ubiquitous in Space, they are mediated by MHD modes. These shocks have been investigated with high-energy laser systems (Podgorny, 1979; Bell et al., 1988; Courtois et al., 2004). The first observation of collisionless perpendicular shocks have been reported, using the Large Plasma Device (Gekelman et al., 1991) and a high energy laser system (Niemann et al., 2012). More recently (Schaeffer et al., 2017b,a) performed an experiment on the OMEGA laser facility (cf. figure 7) and showed the first laboratory generation of high-Mach-number magnetized collisionless shocks created through the interaction of a laser-driven magnetic piston and a magnetized ambient plasma. These shocks can reflect particles and heat them via the magnetosonic wave modes. However, no clear particle acceleration has been measured experimentally for the magnetized shocks yet. PIC simulations showed that these shocks are very inefficient at particle accelerations, but are efficient particle heater.

Collisionless electrostatic shocks can originate from the temperature or/and density jumps of plasmas free of magnetic fields. Various schemes of generation of collisionless electrostatic shocks have been realized on high energy laser facilities. The first one is an interaction between a laser produced high-density ablating plasma and a low-density ambient plasma. Using this scheme, on the LULI2000 laser facility, (Romagnani et al., 2008) have observed a very thin structure of the shock and the formation of ion acoustic solitons by using the proton radiography. Similar shocks have been observed in the experiment conducted by (Ahmed et al., 2013) on the VULCAN laser facility (cf. figure 6). Later in time they transformed in a double layer structure. The second scheme involves laser-ablated counter-streaming plasmas created from two plane targets. These experiments have been motivated by the numerical simulation by (Kato and Takabe, 2008) who demonstrated that an electrostatic shock can be produced at early stages of the Weibel-instability mediated electromagnetic shock. Electrostatic shocks are generally easy to produce in experiments and do not require large facilities, since their width is on the microscopic scale. Electrostatic shocks can promptly accelerate particles to energies of the order of the macroscopic electrostatic potential drop $Z_i e\Phi_{max}$. Numerical simulations have revealed ion acceleration in a relativistic electrostatic shock generated in an overdense plasma due to reflection of ions in the upstream region by the shock front (Stockem et al., 2013), quasi-monoenergetic proton acceleration by such shocks has been shown experimentally (Haberberger et al., 2011).

These two classes of shocks are not able to accelerate particles above the electrostatic potential jump and cannot explain high energy cosmic ray emission which require multipass acceleration mechanisms such as the first order Fermi acceleration process.

The third class of collisionless shocks presented in the introduction, are Weibel-mediated shocks. These shocks of electromagnetic nature, results from the long-time non-linear evolution of the Weibel-filamentation instability. This class of shock covers the relativistic domain for low magnetization, but also a part of the nonrelativistic domain. A transition between the two regimes of non-magnetized shocks, the electromagnetic shocks lead by a cold electron distributions, and the electrostatic shocks driven by slow flows, have been investigated by (Stockem et al., 2014, 2016). An electrostatic shock (ES) can be transformed into an electromagnetic shock (EM) when the Weibel modes time scale $t_{\mathrm{W}}$ is equal to the ES formation time scale $t_{sf}$ as demonstrated in figure 5.1.

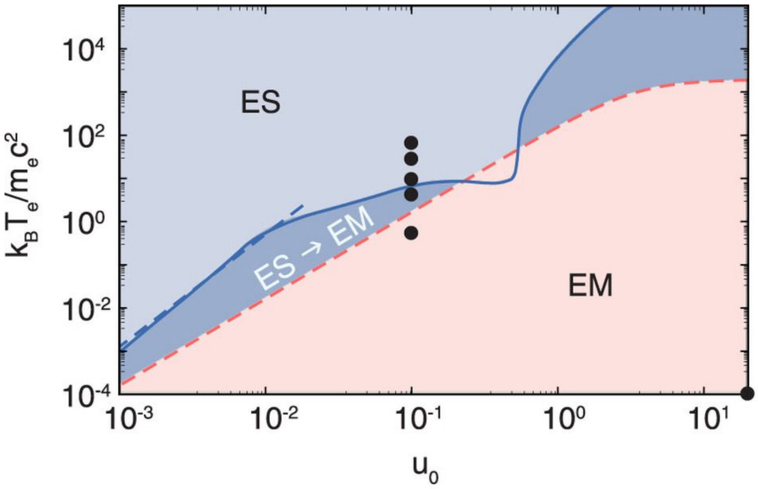

Figure 5.1 – Definition of electrostatic, electromagnetic and transition regimes depending on input parameters $v_{\mathrm{Te}}^2/c^2 = k_{\mathrm{B}}\mathrm{T}_e/m_e c^2$ and proper flow velocity $u_0 = \beta_0\gamma_0$ . The electrostatic shock formation condition (Forslund and Shonk, 1970) (red dashed line) limits the parameter space of electromagnetic shocks (EM). The blue line represents the condition $t_{sf} = t_{\mathrm{W}}$, with the nonrelativistic approximation in dashed, separating the region of purely electrostatic shocks (ES) and the transition region (ES ⟶ EM). The black dots represent the sub-set of simulation parameters discussed by (Stockem et al., 2014).

These shocks are mediated by the ion Weibel instability. The Weibel instability presented in the second chapter only affects the electrons and appears, on electron time scales. The two-stream and Weibel electron-electron instabilities are important for the isotropization (mutualization) and heating of electrons. But the dissipation mechanism essential for the shock formation appears at the second stage of interaction and involves ions.. The electrons are thermalized relatively rapidly, and the ion Weibel instability develops when an ion beam propagates through a hot isotropic electron gas. Small transverse magnetic field perturbations can drive the oppositely moving ions into current layers of opposite sign, which reinforce the initial field (Medvedev and Loeb, 1999), this scheme is similar to the one presented in Chapter 2 for the electron Weibel instability but involves ion currents. This instability is saturated by ion trapping in magnetic wells followed by magnetic micro turbulence. According to recent ab initio particle-in-cell (PIC) simulations (Spitkovsky, 2008a; Martins et al., 2009; Sironi and Spitkovsky, 2011a), this instability both triggers formation of the shock, and sustains its long-time propagation through continuous interaction between upstream and reflected particles. Furthermore, the turbulence from the nonlinear evolution of the Weibel instability is a way to accelerate particles by the Fermi acceleration process which is discussed in this Chapter.

Laboratory experiments on electromagnetic collisionless shocks are formidably difficult to conduct, since they have to meet critical shock properties in astrophysical regimes as magnetization, low collisionality, and they have to be super Alfvénic (Alfvénic Mach number $M_A > 2-3$) (Drake, 2000; Treumann, 2009). They require matter under extreme conditions and must satisfy the strict condition

$$\lambda_{mfp} >> l_{sys} >> l_{\mathrm{EM}}, \tag{5.1}$$

where $\lambda_{mfp}$ is the ion mean free path (discussed in the next section), $l_{sys}$ the system size, and $l_{\mathrm{EM}}$ is the scale for instability growth $\propto c/\omega_{pi}$ (Kato and Takabe, 2008; Park et al., 2012). The latter equation means that these shocks require that the flows are highly collisionless and also that the Weibel instability reaches the non-linear regime within the bounds of the experiment.

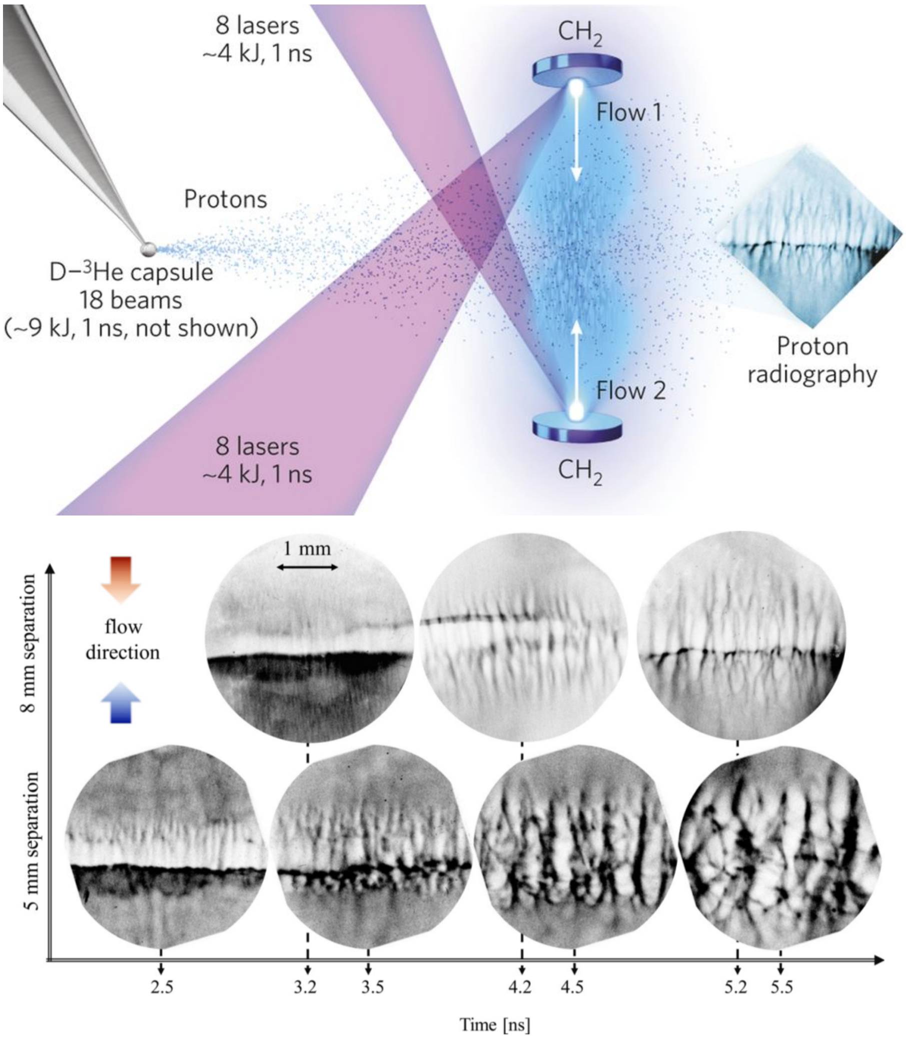

Figure 5.2 – Top panel: Experimental setup by (Fox et al., 2013), two counter-streaming plasmas are generated by two flat plastic (CH) targets irradiated by laser beams of 500 J and 1 ns of duration focused to a spot approximately 300 $\mu m$ in diameter. Bottom panel: Proton radiography diagnostic by (Huntington et al., 2013, 2017), observation of magnetic filaments and their merging up to longer wavelengths.

The most explored experimental route, to create electromagnetic collisionless shocks, consists in colliding two ablative flows driven by high-energy nanosecond lasers. This setup has recently yielded promising results at the Omega Laser Facility (Fox et al., 2013; Huntington et al., 2013, 2017). The setup used in these experiments is shown in Figure 5.2. Filamentary electromagnetic structures of typical wavelength of a few 100s μm have been observed through proton radiography in the overlap region of ablative plasmas of drift velocity $v$ limited to 1000 km.s$^{-1}$ and density $10^{18} - 10^{19}$cm$^{-3}$ (cf. Fig 5.2).

Synthetic proton radiographs of the observed patterns suggest peak amplitudes of ~ 10T, corresponding to a few percents of the equipartition field. The space-time dynamics of these filaments is consistent with the Weibel instability, as further supported by large-scale PIC simulations.

However, the experiment on the OMEGA laser facility failled to fully form the electromagnetic shock even after 6 ns of interaction. The region where the filaments were detected, have not revealed increase of the ion temperature expected for shock formation: the ion temperature increased only to ~1.5 keV, whereas the Hugoniot value would be ~10 keV; the density also corresponded to a simple overlap of the streams (i.e., a sum of densities of two interpenetrating streams). The Weibel instability at non-linear stage creates magnetic turbulence (cf. figure 5.2 at 5.5 ns), but the interpenetration distances ($< 50\mathrm{c}.\omega_{\mathrm{pi}}^{-1}$) and time duration of the flows were not sufficient for shock formation and ion heating, which was consistent with PIC simulations (Huntington et al., 2013). The difficulty to fullfil condition (5.1) can be solved by increasing the flow velocity and density in the interaction region. Doing so, the mean free path will strongly increase ($\lambda_{mfp} \propto v^4/n$) while the ion skin depth will decrease ($c.\omega_{pi}^{-1} \propto n^{-1/2}$). The National Ignition Facility (NIF), possesses much greater energy (30 times higher than the OMEGA laser facility), able to form much hotter and faster plasma flows on larger lengths, and timescales as compared to OMEGA, which will allow this combination of parameters. Indeed, NIF experiments have already demonstrated increased density ($n_e = 1.5\,10^{20}$cm$^{-3}$) and 1000 km.s$^{-1}$ flows for foil separations in the range 6-10 mm. However, due to the shorter distance between the foils in the NIF experiment, the collision characteristic times are shorter than the duration of the experiment, meaning that collisional effects may play as significant role (Ross et al., 2017), leading to a situation where collisionless and collisional effects are tightly intertwined and both have to be accounted for. From these measurements, generation of sub-relativistic collisionless shocks seems within the reach of larger-scale, NIF-class systems, but yet remains to be demonstrated.

The difficulty to access these very large resources and the limitations in the repeatability of such experiments force us to image other possible experiments to form such shocks on smaller scale facilities. In this chapter, we report the formation of collisionless shocks mediated by the Weibel instability using a different experimental route than (Fox et al., 2013) on the OMEGA laser facility.

## 5.1 Experiment on electromagnetic collisionless shocks on the OMEGA laser facility

A novel experiment has been conducted recently by (Li et al., 2019) on the OMEGA laser facility to reveal the critical role of nonlinear collective interactions between plasma particles and instability-generated magnetic turbulence. The following study presents a theoretical interpretation of this experiment, supported by numerical simulations.

The configuration of the experiment is schematically illustrated in Figure 5.3. A highly collimated plasma jet was generated by six laser beams, of 500J and 1ns of duration each (total energy ~ 3kJ), illuminating the interior of a plastic (CH), hemispherical target. This plasma jet propagated into a gasbag filled with 0.1 atmosphere hydrogen gas ($H_2$), surroundind by a plastic shell (CH) of 0.8 μm thickness.

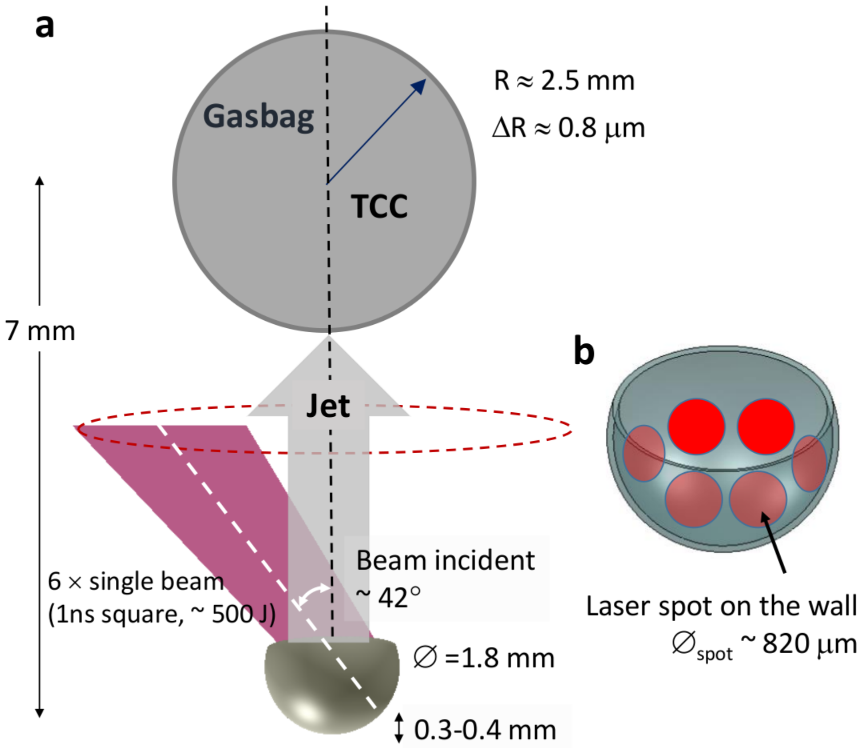

Figure 5.3 – Schematic of the experimental setup and targets. a. The subject target is a gasbag (Type 1), made with 0.8 μm-thick polyimide and filled with hydrogen gas at the pressure of 0.1 atmosphere. An aluminum washer is used for holding the gasbag (not shown on the figure), which is 7 mm in diameter and 0.5 mm thick. b. The 60% hemisphere has a diameter 1.8 mm and is made with 100 μm thick plastic. Six laser beams uniformly distribute in the inner wall with an incident angle 42 degrees. The laser spots on the hemisphere wall are about 820 μm with full spatial and temporal smoothing. Each individual laser spot is determined by phase plate SG5 (Super Gaussian, defined as 95% energy deposition), resulting of a laser intensity in an order of $\sim 2 \times 10^{14}$W.cm$^{-2}$. (Li et al., 2019)

The laser-ablation process can be considered as adiabatic for this very intense nanosecond laser pulse (Amoruso et al., 1999), and can so be separed in two phases. The first one is the laser absorption coupled with the target heating, and the second corresponds to the expansion of the ablated plume where the initial thermal energy of the ablated plasma is converted into the kinetic energy of the expanding flow. Using this description, one can model the plasma formation and expansion using two relatively simple analytical and numerical models. The laser interaction as well as the plasma plume propagation have been simulated in a 2D axisymmetric geometry using the three-dimensional (3D) radiation-hydrodynamic code FLASH (Tzeferacos et al., 2015). Figure 5.4 shows the plasma jet formation, propagation (in vacuum), and interaction (with the gasbag shell), indicating the structure and dynamics of the jet density, temperature and self-generated magnetic fields.

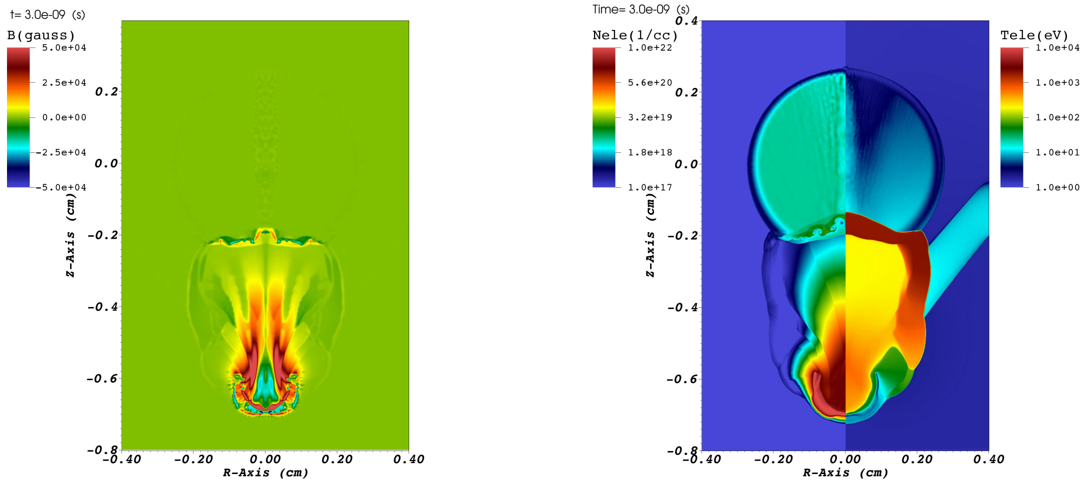

Figure 5.4 – Hydrodynamic simulations of the 2D maps for plasma density, electron temperature, (right) and magnetic fields (left) at the time 3 ns when the plasma jet interacts with the gasbag shell. (Li et al., 2019)

During the expansion process, the electrons and ions cool down and a very high-Mach number flow is formed. The plasma jet expansion is non-uniform and density and temperature gradients appear. Magnetic fields develop spontaneously in the presence of non-parallel density and temperature gradients

$$\frac{\partial \mathbf{B}}{\partial t} = \frac{1}{e n_e} \nabla \mathrm{T}_e \times \nabla n_e. \tag{5.2}$$

This phenomenon introduced by (Biermann, 1950) is known as the Biermann battery effect. This large-scale self-generation of magnetic field features has also been observed in (Huntington et al., 2013). The Biermann fields, created at the target surface during the laser ablation, are carried by the expanding plasma flow and form a loop around it. The frozen fields in Figure 5.4 at the border of the expanding plume has a typical amplitude ~ 2T. The simulation also indicates that the gasbag shell and fill-gas were nearly fully ionized by radiation from the laser-illuminated hemisphere before the jet reached the gasbag, forming an unmagnetized electron-proton plasma inside the gasbag with a density $\sim 5 \times 10^{18} \mathrm{cm}^{-3}$ and an electron temperature ~ 10eV . The parameters of the edge of the plasma jet just before its interaction with the shell are compiled in Table 5.1.

| Parameter | $n_e = n_i (\mathrm{cm}^{-3})$ | $\mathrm{T}_{e,i}(\mathrm{eV})$ | $v_0(\mathrm{m.s}^{-1})$ | $\mathrm{B}_0(\mathrm{T})$ |
|---|---|---|---|---|
| Numerical value | $10^{18}$ | 100 | $2 \times 10^6$ | 2 |
| Parameter | $\omega_{pe}(\mathrm{s}^{-1})$ | $v_{the}(\mathrm{m.s}^{-1})$ | $\omega_{ce}(\mathrm{s}^{-1})$ | $r_{ge}(\mathrm{m})$ |
| Numerical value | $5.63 \cdot 10^{13}$ | $4.19 \cdot 10^6$ | $3.5 \cdot 10^{11}$ | $1.2 \cdot 10^{-5}$ |
| Parameter | $\omega_{pi}(\mathrm{s}^{-1})$ | $v_{thi}(\mathrm{m.s}^{-1})$ | $\omega_{ci}(\mathrm{s}^{-1})$ | $r_i(\mathrm{m})$ |
| Numerical value | $1.31 \cdot 10^{12}$ | $9.78 \cdot 10^4$ | $1.91 \cdot 10^8$ | $1.0 \cdot 10^{-2}$ |
| Parameter | $c_s(\mathrm{m.s}^{-1})$ | $v_\mathrm{A}(\mathrm{m.s}^{-1})$ | $c_{ms}(\mathrm{m.s}^{-1})$ | $\sigma$ |
| Numerical value | $2.11 \cdot 10^5$ | $4.3 \cdot 10^4$ | $2.15 \cdot 10^5$ | |

Table 5.1 – Plasma parameters of the edge of the plume before its interaction with the gasbag shell, where σ is the magnetization described by (2) in the Introduction.

These numerical predictions, found by the hydrodynamic model, for the plasma jet properties have been confronted to Thomson scattering measurements.

This diagnostic tool excels at measuring the fundamental parameters in laser-produced plasmas (Sheffield et al., 2010). This technique has been applied to diagnose high-temperature and high-density plasmas such as those found in inertial confinement fusion experiments and other high-energy density plasma experiments (Froula et al., 2006; Ross et al., 2012; Morita et al., 2013). In our experiment, the Thomson scattering measurements have been performed in shots without the gasbag when the jet propagates freely in vaccum. The speed, temperature and density of the jet obtained from these measurements are presented in Figure 5.5.

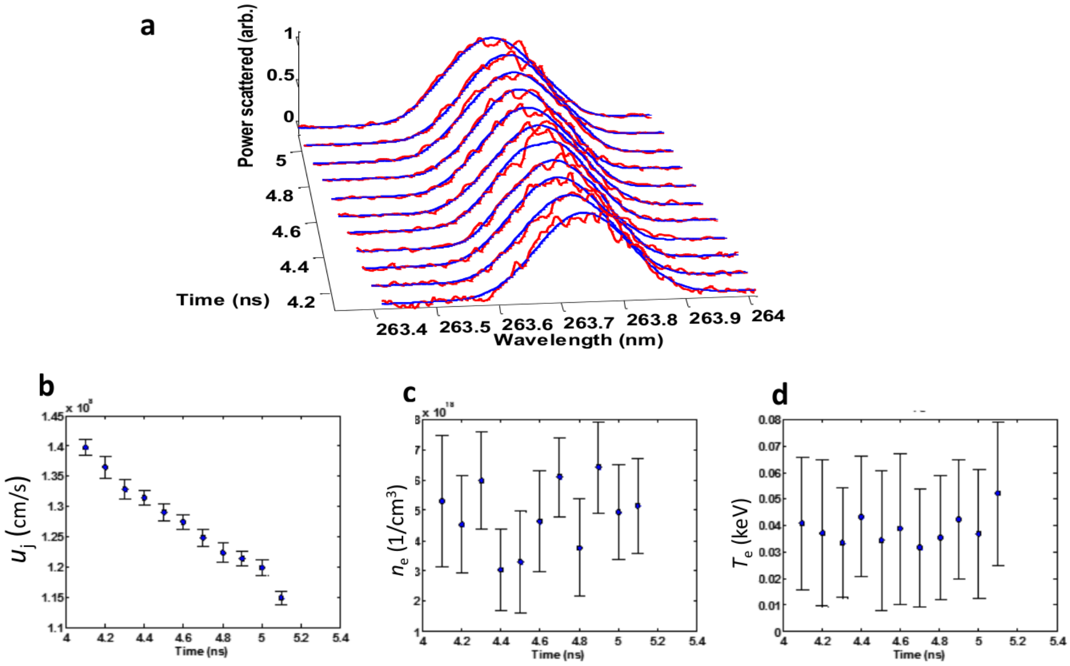

Figure 5.5 – 4ω Thomson scattering measurements (in vacuum). a. Lineouts taken at different times from 4ω Thomson-scattering spectra of ion-acoustic wave plotted against wavelength (Froula, 2011). The measurements were conducted at target chamber center (TCC) without a gasbag, which is 7 mm from the hemisphere tip, and are fitted with a multi-parameter model to provide a number of physical properties, including jet velocity, plasma density and plasma temperature. In these experiments, the plasma density was too low for a direct T$_e$ measurement, and the equality T$_e$ ∼ T$_i$ is assumed, due to the collisionality of the jet discussed later. A number of physical properties for the jet at position z=7 mm are plotted as a function of Thomson probing time (uncertainty $\Delta t = \pm 50$ps): b, jet flow velocity (uncertainty $\Delta v_0 = \pm 14$km.s$^{-1}$); c, jet plasma density ($\Delta n_e = \pm 2 \times 10^{18}$cm$^{-3}$ ); and d, jet plasma temperature (T$_e$ ∼ T$_i$, ΔT = ±50eV). (Li et al., 2019)

From the simulation we can conclude that, the jet reaches the shell of the gasbag after 3 ns of propagation with a speed of $\sim 2 \times 10^8$cm.s$^{-1}$. The Thomson-scattering measurements (cf. Fig.5.5) show that after 4 ns of propagation in vaccum, the jet speed has decreased to $1.4 \times 10^8$cm.s$^{-1}$ and even below $1.15 \times 10^8$cm.s$^{-1}$ after 5 ns. Thomson-scattering measurements have not been performed in the experiment before 4 ns, but the decrease of the jet speed seems to be linear in time and the speed of the jet at 3 ns must probably be around $1.6 \times 10^8$cm.s$^{-1}$ which is lower than the $2 \times 10^8$cm.s$^{-1}$ predicted by the simulations. However, this experimental jet speed is faster than the jet obtained by (Huntington et al., 2013), by at least a factor 1.5. The hemispherical geometry of our target, compared to the plane targets used by (Huntington et al., 2013), confines the plasma jet and allows it to reach higher propagation speed. At the same time the jet is found to have a density of $\sim 5 \times 10^{18}$cm$^{-3}$ and a temperature of ∼ 40eV, these values remain unchanged during the propagation. These experimental values agree with numerical counterparts within ±50%. The jet is supersonic $M_s = v_0 / c_s \simeq 10$ and superAlfvénic $M_A = v_0 / v_A \simeq 50$ when reaching the gasbag (using numerical values).

### 5.1.1 Collision aspects in the plasma jets and interaction with the gasbag

The collisionless nature of the plasma interaction is an important prerequisite to develop collisionless shocks, as well as other collisionless phenomena such as magnetic reconnection (Daughton et al., 2009). In the case of collisionless shocks, the mean free path of particles, has to be much larger than the shock width, considered as the typical length of the interaction. The binary collisions depend dramatically of the plasmas parameters (density, temperature, energy), and the collisionality is thus one of the biggest limitation of scaling experiments in laser facilities (Ross et al., 2017). Indeed, most of the plasmas formed in experiments are weakly collisional (2-3 collisions during the timescale of the experiment), and the effect of these collisions can impact the development of instabilities (Ryutov et al., 2014) and so change the shock behavior.

In order to determine if the plasma jet and gasbag interaction are collisionnal or collisionless we used a binary collision model by (Huba, 2009). For a test particle (labeled $\alpha$) streaming with velocity $v_\alpha$ through a background of field particles (labeled $\beta$), a collision frequency is defined by four relaxation processes:

$$\begin{array}{ll}\text{Slowing down} & \dfrac{d\mathbf{v}_\alpha}{dt} = -\nu_s^{\alpha/\beta}\mathbf{v}_\alpha, \\ \text{Transverse diffusion} & \dfrac{d}{dt}(\mathbf{v}_\alpha - \widehat{\mathbf{v}_\alpha})_\perp^2 = \nu_\perp^{\alpha/\beta} v_\alpha^2, \\ \text{Parallel diffusion} & \dfrac{d}{dt}(\mathbf{v}_\alpha - \widehat{\mathbf{v}_\alpha})_\parallel^2 = \nu_\parallel^{\alpha/\beta} v_\alpha^2, \\ \text{Energy loss} & \dfrac{dv_\alpha^2}{dt} = -\nu_\epsilon^{\alpha/\beta} v_\alpha^2 \end{array} \tag{5.3}$$

where $v_\alpha = |\mathbf{v}_\alpha|$ and the averages are performed over an ensemble of test particles and a Maxwellian field particle distribution. Exact formulas have been found by (Trubnikov, 1965) and written as

$$\begin{aligned} \nu_s^{\alpha/\beta} &= (1 + m_\alpha/m_\beta)\psi(x^{\alpha/\beta})\nu_0^{\alpha/\beta}; \\ \nu_\perp^{\alpha/\beta} &= 2\left[(1 - 1/2x^{\alpha/\beta})\psi(x^{\alpha/\beta}) + \psi'(x^{\alpha/\beta})\right]\nu_0^{\alpha/\beta}; \\ \nu_\parallel^{\alpha/\beta} &= \left[\psi(x^{\alpha/\beta})/x^{\alpha/\beta}\right]\nu_0^{\alpha/\beta}; \\ \nu_\epsilon^{\alpha/\beta} &= 2\left[(m_\alpha/m_\beta)\psi(x^{\alpha/\beta}) - \psi'(x^{\alpha/\beta})\right]\nu_0^{\alpha/\beta}, \end{aligned} \tag{5.4}$$

where

$$\begin{aligned} \nu_0^{\alpha/\beta} &= 4\pi e_\alpha^2 e_\beta^2 \Lambda_{\alpha\beta} n_\beta / m_\alpha^2 v_\alpha^3, \qquad & x^{\alpha/\beta} &= m_\beta v_\alpha^2 / 2k\mathrm{T}_\beta, \\ \psi(x) &= \frac{2}{\sqrt{\pi}}\int dt\, t^{1/2} e^{-t}, \qquad & \psi'(x) &= \frac{d\psi}{dx}. \end{aligned} \tag{5.5}$$

The Coulomb logarithm $\Lambda_{\alpha\beta}$ is typically $\Lambda_{\alpha\beta} \sim 10 - 20$ and depends of the plasma parameters (mass, density and temperature) and a detailed expression is given in Ref. (Huba, 2009). Approximate solutions can be found for $\nu_s$, $\nu_\perp$ and $\nu_\parallel$ depending of the drift motion of the test particles $x^{\alpha/\beta}$, very slow ($x^{\alpha\ \beta} << 1$) and very fast ($x^{\alpha\ \beta} >> 1$) respectively.

$$\begin{array}{lll} & \text{Very slow} & \text{Very fast} \\ \nu_s^{\alpha/\beta}/n_\beta Z^2 \Lambda_{\alpha\beta} \propto & \mathrm{T}^{-3/2} & \epsilon^{-3/2}, \\ \nu_\perp^{\alpha/\beta}/n_\beta Z^2 \Lambda_{\alpha\beta} \propto & \mathrm{T}^{-1/2}\epsilon^{-1} & \epsilon^{-3/2}, \\ \nu_\parallel^{\alpha/\beta}/n_\beta Z^2 \Lambda_{\alpha\beta} \propto & \mathrm{T}^{-1/2}\epsilon^{-1} & \mathrm{T}\epsilon^{-5/2} \end{array} \tag{5.6}$$

In these expressions, $\epsilon$ represents the energy of the test particle, and T the temperature of the background plasma. A test particle collides more often with the background particles if the plasma kinetic energy and the background temperature are low and if its density is large.

Considering the experiment, the test particles $\alpha$ are represented by the edge of the plasma jet and the background of field particles by the ionized gasbag. The external mean free path $l^{ex}_{\alpha\beta}$ (which corresponds to collisions with particles from different plasmas) of all jet particles (electron, proton, ionized carbon) can be written as

$$l^{ex}_{\alpha\beta} = \frac{v_p}{\nu_s^{\alpha/\beta}}, \tag{5.7}$$

where $v_p$ corresponds to the typical speed of the particle. This speed can be the drift speed of the particle or the thermal speed of the particle, depending on which one is higher. In the case of hot electrons $v_{T\alpha} > v_\alpha$, the typical speed will be $v_p = v_{T\alpha}$, while for ions which have a thermal speed much lower (a factor $\sqrt{m_i}$) this speed will be $v_p = v_\alpha$.

The mean free pathes of the jet test particles in the background ionized gasbag are presented in Table 5.2.

| $l_{e\mathrm{C}}$ | $l_{ee}$ | $l_{e\mathrm{H}}$ | $l_{\mathrm{C}e}$ | $l_{\mathrm{H}e}$ |
|---|---|---|---|---|
| 0.5 | 0.8 | 1.1 | $1.6\,10^3$ | $3.0\,10^3$ |

| $l_{\mathrm{HC}}$ | $l_{\mathrm{HH}}$ | $l_{\mathrm{CH}}$ | $l_{\mathrm{CC}}$ | $l_{\alpha\beta}$ |
|---|---|---|---|---|
| $1.9\,10^5$ | $1.7\,10^7$ | $2.7\,10^7$ | $1.2\,10^9$ | ext |

Table 5.2 – External mean free path $l^{ex}_{\alpha\beta} = \max(\mathrm{v}_{T\alpha}, \mathrm{v}_\alpha)/\nu_s^{\alpha/\beta}$ of all different Coulomb collisions in µm.

Collisions between ions are unlikely since the lowest value of the ion-ion collision mean free path is $l_{\mathrm{HC}} > 10$cm which is much larger than the interaction region length and even larger than the size of the experiment. This condition ensures the collisionless nature of the future shock formation between the plasma jet and the ionized gasbag. The electrons from the plasma jet are highly collisional with the particles coming from the gasbag, since $l_{e\beta}$ is on the µm scale, which is much smaller than $c/\omega_{pi} \simeq 220$µm the typical length of an EM shock width (Kato and Takabe, 2008; Park et al., 2012; Huntington et al., 2013). This means that the electrons are thermalized during the interaction and the shock formation. This thermalization is also a natural process of collisionless shocks driven by the inital electron instability (cf. Chapter 2). However, the electron-ion collisionality has an impact on the growth rate of the Weibel instability. Due to the suppression of free electron streaming in the transverse direction, (Ryutov et al., 2014) found that the growth rate is significantly reduced at small wave numbers ($k < 3\omega_{pi}/c$) compared to what predicted by the collisionless model. However, L. Gremillet (private communication) in 1D simulations performed with the PIC code CALDER has not observed a growth rate reduction, and further demonstrated a positive impact of the electron collisionality on the Weibel instability, helping to maintain the linear regime of the instability on longer timescale allowing the field to reach much higher amplitudes (~ factor 3). The electron-ion collisionality can therefore facilitate the Weibel-mediated shock formation.

These Coulombian mean free paths have been evaluated for the plasma jet particles moving through the ionized gasbag. It is important to distinguish these collisions (jet and gasbag) from those taking place inside the plasma jet itself. The collisions between the plasma jet particles ($\alpha$) and the gasbag ($\beta$) are called external collisions (when particles have a drift motion relative to each other), and the collisions inside the jet, are called internal collisions. If particle species of a plasma have different temperatures, but no relative drift, the equilibration is described by

$$\frac{dT_\alpha}{dt} = \sum_\beta \nu_\epsilon^{\alpha/\beta}(T_\beta - T_\alpha), \tag{5.8}$$

where

$$\nu_\epsilon^{\alpha/\beta} = 1.8\times10^{-19}\frac{(m_\beta m_\alpha)^{1/2} Z_\alpha^2 Z_\beta^2 n_\beta \lambda_{\alpha\beta}}{(m_\alpha T_\beta + m_\beta T_\alpha)^{3/2}} s^{-1}. \tag{5.9}$$

The internal mean free path $l_{\alpha\beta}^{in}$ of all particles can thus be written as

$$l_{\alpha\beta}^{in} = \frac{v_{T\alpha}}{\nu_s^{\alpha/\beta}}, \tag{5.10}$$

and its value for internal Coulomb collisions are presented in Table 5.3.

| $l_{eC}$ | $l_{ee}$ | $l_{eH}$ | $l_{Ce}$ | $l_{He}$ |
|---|---|---|---|---|
| $2.1\,10^3$ | $1.2\,10^0$ | $5.9\,10^3$ | $2.0\,10^0$ | $2.0\,10^1$ |

| $l_{HC}$ | $l_{HH}$ | $l_{CH}$ | $l_{CC}$ | $l_{\alpha\beta}$ |
|---|---|---|---|---|
| $4.3\,10^{-1}$ | $7.0\,10^0$ | $1.4\,10^0$ | $1.4\,10^{-2}$ | int |

Table 5.3 – Internal mean free path $l_{\alpha\beta}^{in} = v_{T\alpha}/\nu_\epsilon^{\alpha/\beta}$ of all different Coulomb collisions in μm.

The ions and electrons in the plasma jet are highly collisional. The electron mean-free-path is much smaller than the jet radius, $l_{ie} << r_{jet} \sim 500\mu$m. The ions are even more collisional than the electrons due to their higher charge (for the carbon only) and mass, the latter decreasing their thermal velocity and thus their mean-free-path. However, the Weibel instability, supposed to mediate the shock in the experiment, grows from an initial velocity anisotropy (i.e. from the particles interaction with relative drift), which means that only the external collisions are relevant for the instability. Internal collisions insure the plasma equilibrium. As indicated by the hydrodynamic simulation, while $T_i$ is higher than $T_e$ close to the jet-launching region because of heating from the collision of plasma plumes, the electron-ion equilibrium time is shorter than the time preceding the measurements ($\tau_{ie} \sim$ 500ps << t ~ 5ns), leading to thermalization and electron-ion equilibrium of the jet plasma. The assumption of equality of $T_i$ and $T_e$ used in Thomson scattering measurements (cf. Figure 5.5) therefore justified for the plasma jet.

We conclude, from these calculations, that interaction between the thermalized plasma jet and the ionized gasbag are of a collisionless nature.

### 5.1.2 Plasma jet and gasbag shell interaction

Before interacting with the ionized gas, the plasma jet has to penetrate the shell which surrounds it. Thomson scattering measurements (cf. Figure 5.5) show that the velocity of the jet front in vacuum is 1400km.s$^{-1}$. Ions having such velocity deposit in the shell a significant part of their energy (Gericke and Schlanges, 1999).

A simplified model of such interactions is schematically displayed below.

First let us consider the photon energy deposition from the laser. We first assume that about 10% of the total laser energy (3kJ) is radiated with the effective radiation temperature ~ 1keV. Then the energy flux at the distance 5mm from the source (assuming isotropic emission in 2π) is 300J/3cm$^2$ = 100J.cm$^{-2}$. The shell areal mass is 10$^{-4}$g.cm$^{-2}$ and the Planck opacity of the plastic (according to (Drake, 2006) p.255) is about 100cm$^{-1}$, that is, the 1keV photon stopping length is 100μm and 1% of its energy is absorbed in a shell of a thickness of 1 mm. Therefore, the absorbed energy is 10$^4$J.g$^{-1}$. The plastic heat capacity is about 1J.K$^{-1}$.g$^{-1}$, therefore the expected plastic temperature is 10$^4$K = 0.9$e$V. While it is not destroyed by radiation from the laser-target interaction, the plastic shell is heated to a temperature of a few eV.

Let us consider now the energy deposition from the protons in the plasma jet. Let us assume again that 10% of the total laser energy is transferred to the jet propagating with an average velocity of $2\times10^6$m.s$^{-1}$. This corresponds to an average proton energy of 25keV. The plasma jet is weakly divergent, its radius at the shell position is comparable with the shell radius of 2.5mm. For the jet radius of 0.3cm, the jet cross section is $0.3\text{cm}^2$ and the energy flux is $300\text{J}/0.3\text{cm}^2 = 1000\text{J.cm}^{-2}$.

The stopping power of fast ions by free electrons for in a plasma can be expressed (Gericke and Schlanges, 1999) with the formula

$$\frac{d\mathrm{E}_i}{dx} = -\frac{\mathrm{Z}_i^x \omega_{fe}^2 e^2}{v_i^2} \ln\left(\frac{2m_e v_i^2}{\hbar\omega_{fe}}\right) \tag{5.11}$$

where the parameter $x = 1.3 - 2$ accounts for a deviation from the $\mathrm{Z}_i^2$ which decreases with increasing plasma density and beam charge number. Here $v_i$ and $\mathrm{E}_i$ are, respectively, the velocity and the kinetic energy of ions in the plasma jet, $n_{fe}$ is the number density of free electrons in a shell, $\omega_{fe} = \sqrt{4\pi n_{fe} e^2/m_e}$ is the plasma frequency. The stopping power of a proton with such a velocity in an electron plasma with the temperature 5eV and the density $10^{21}\text{cm}^{-3}$ is $20\text{MeV.cm}^{-1}$ (Gericke and Schlanges, 1999). As the stopping power is proportional to the density, the proton stopping power in the solid plastic heated to 5 eV will be about $10000\text{M}e\text{V.cm}^{-1}$ or $1\text{M}e\text{V.}\mu\text{m}^{-1}$. Even if this is a very crude estimate, we conclude that protons are depositing an essential part of their energy in the shell. Therefore, the proton energy deposition in the shell is about $10^7\text{J.g}^{-1}$, which corresponds to an average shell temperature of a few keV.

The 2D hydrodynamic simulation presented above (cf. fig.5.4) does not account for mixing of the jet plasma and the shell, which means that collisional jet energy deposition in the shell is not accounted for. The jet fluid, may only push the shell according to the conservation laws. For this reason, other 2D hydrodynamic simulations have been performed with the code CHIC to characterize the isothermal explosion of the shell into the ambient low-density plasma, considering an intial energy deposition into the shell according to equation (5.11). The intial conditions of the simulation is an energy deposition of 200J localized on 100μm along the y-axis into a planar shell of density $1.05\text{g.cm}^{-3}$ and thickness 0.8μm (for the sake of simplicity no curvature of the shell is assumed). The simulation results are shown in figure 5.6.

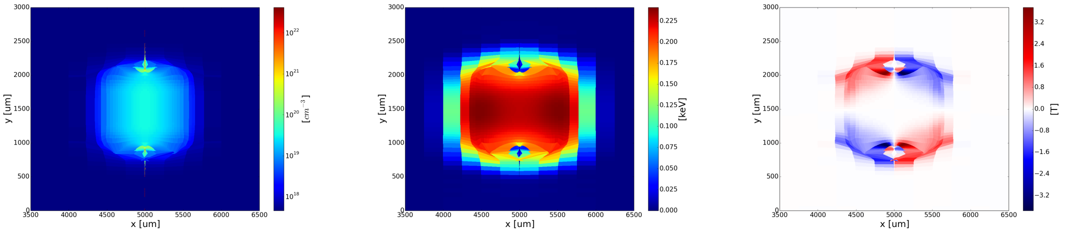

Figure 5.6 – Hydrodynamic simulations of an expanding planar shell, electron density (left), temperature (middle) and magnetic fields (right), are shown 2 ns after of the energy deposition (200 J). The jet and the gasbag are not represented in the simulation. We only simulate the shell expansion, localized at $5000\mu m$ on the x-axis, in vaccum (semi-vaccum). One can consider the gasbag fills the interval $> 5000\mu m$ and the jet the interval $< 5000\mu m$.

Inhomogeneous shell heating by the jet ions, is represented in the simulation as the local energy deposition. It results in the shell explosion. The density and temperature gradients of the expanding shell generate at a magnetic field of $\sim 2-3$T due to the Biermann battery effect. These magnetic fields have a structure of two rings with the axes common with the jet axis and with the radius comparable but smaller than the shell radius. The shell expands to a speed of $\sim 400\text{km.s}^{-1}$, with a density of $\sim 10^{18}\text{cm}^{-3}$ and a temperature $\sim 100e\text{V}$. The density and temperature values of the expanding shell are comparable to those of the plasma jet. However, the shell is 5 times slower than the jet.

Shell expansion in the ambient gas is an adiabatic process the expanding plasma is accelerated to a velocity three times more than the acoustic velocity. Interaction of the jet with the gasbag shell is illustrated in the cartoon figure 5.7.

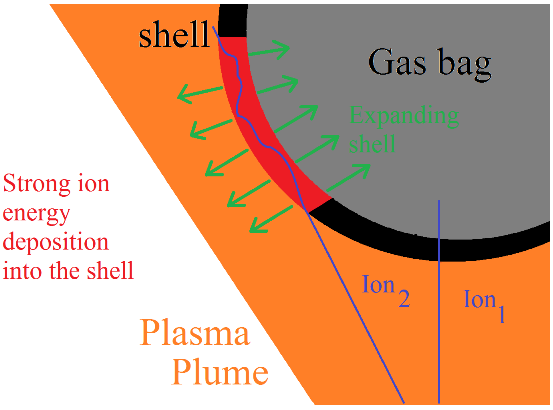

Figure 5.7 – Sketch of the ion jet stopping into the gasbag shell. $Ion_2$ interacts on a longer time scale than $Ion_1$ and deposit much more energy into the shell. From this, a non uniform expansion of the shell is launched. The red part corresponds to the region simulated with the code hydrodynamic CHIC presented in figure 5.6.

The plasma jet propagates with a certain dispersion angle and for illustration we consider here that it covers all the gasbag surface. The ions at the edges of the jet because of their oblique propagation into the shell (Ion 2 in fig. 5.7) deposite more energy than the ions propagating along the shell surface normal. This energy deposition anisotropy will launch a non uniform explosion of the shell, which will collide with the upcoming plasma jet on one side and with the ionized gas bas on the otherside.

The shell expands radially according to the shell normal surface (cf. figure 5.7). The shell isothermal expansion produces fast ions with the velocity at least 3 times faster than the average expansion velocity. These fast ions from the shell are collisionless and their interaction with the gas inside the shell and with the jet outside the shell produces the Weibel instability, which is enhanced by the magnetic field generated with the Biermann battery mechanism. These numerical estimations are obviously undersestimating the complexity of the interaction, but can nevertheless give us a good idea of the range of parameters of the expanding shell.

### 5.1.3 Plasma shell expansion and shock formation

Figure 5.8 shows a series of time-gated, side-on proton radiographs (Li et al., 2006) of the plasma jet interaction with the gasbag.

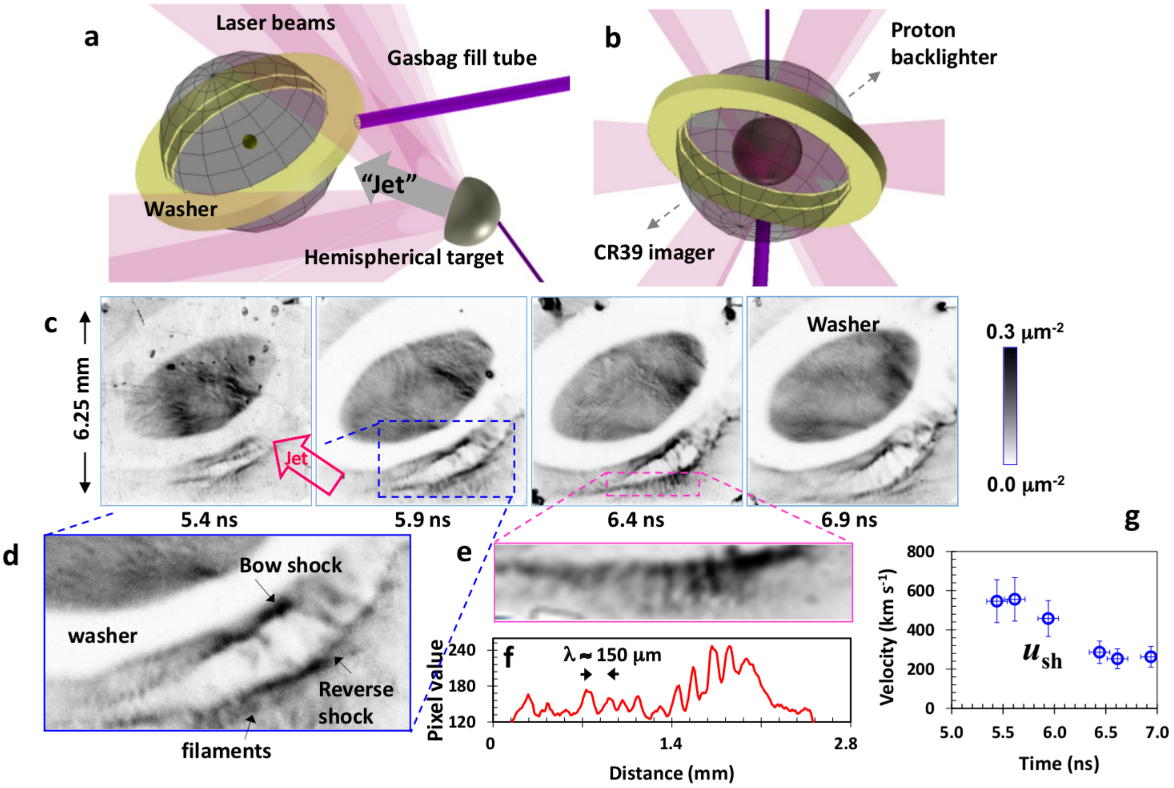

Figure 5.8 – Experimental setup and proton radiographs. a. Side-on view of the experiments [from the positon of the CR39 imager, which is 15 cm from the Target Chamber Center (TCC)]. A supersonic plasma jet, driven by 6 laser beams, is formed with a hemisphere target and propagates toward the gasbag. The proton backlighter is at 1 cm from TCC opposing the CR39 imager (The proton flux is out of the paper). b. End-on view from the gasbag towards the hemisphere target (against the direction of plasma jet propagation). c.Side-on radiographs (in target plane) sampled at different times with 3.3 MeV protons [generated from deuterium-deuterium (D-D) nuclear fusion reactions: $\mathrm{D}+\mathrm{D}\longrightarrow p(3\mathrm{MeV})+\mathrm{T}$]. The arrow at right-lower corner (the image at t = 5.4 ns) points in the direction of plasma jet propagation. Images ahead of the gasbag washers clearly indicate the formation of crescent-shaped, quasi-perpendicular shocks and their evolution. d. The enlarged part of an image (at 5.9 ns) displays the detailed structure (The accurate shock positions and shock width are determined in Fig.5.9 where the small imaging effects due to the backlighting proton Coulomb scattering are removed). Current filaments appear in the upstream plasma. e. The enlarged part of an image (at 6.4 ns) indicates strong filament structure in front of the moving shock. f. Circular lineout indicates that the wavelength of these filaments is ~ 150µm. g. The measured shock velocity at the different times. (Li et al., 2019)

The Weibel instability develops in a zone where the expanding shell plasma overlaps with the jet. Figures 5.8c,d show filaments aligned with the flow (radial to the shell expansion) and crescent-shaped magnetic fields at the shock fronts generated in the interaction zone. Figure 5.8 d shows details of two shock structures, enlarged from part of a proton radiograph of the shock at t = 5.9 ns. Both shocks have a typical width of ~ 1mm perpendicular to the flow direction and carry a magnetic field. The orientation of the magnetic field with respect to the shock front is difficult to estimate, because of a 3D geometry of experiment the magnetic field may have a component perpendicular to the observation plane which is not detected by the proton radiography. However, assuming that the shock behavior is 2-dimensional, the orientation of the magnetic field carried by the shock front will be in the plane of the shock front. A bow shock accelerates the ambient hydrogen plasma and a reverse shock decelerates the CH jet plasma. The filaments are more pronounced at later timed, as shown in Figure 5.8 e, enlarged from the shock front image at t = 6.4 ns. Fourier transform analysis indicates that the filaments are distributed with a wavelength ≃ 150µm (Fig.5.8 f). The shock if fully formed at 6 ns and its velocity $u_{sh}$ reduces from ~ 600 to ~ 300km.s$^{-1}$ (Fig.5.8 g) corresponding to $u_{sh} \approx v_0/3$.

To quantify the experimental measurements, the structure of path-integrated magnetic fields was reconstructed from experimental data (Bott et al., 2017). Shown in Fig.5.9 a is a simulated proton radiograph of a measured shock based on the field reconstruction.

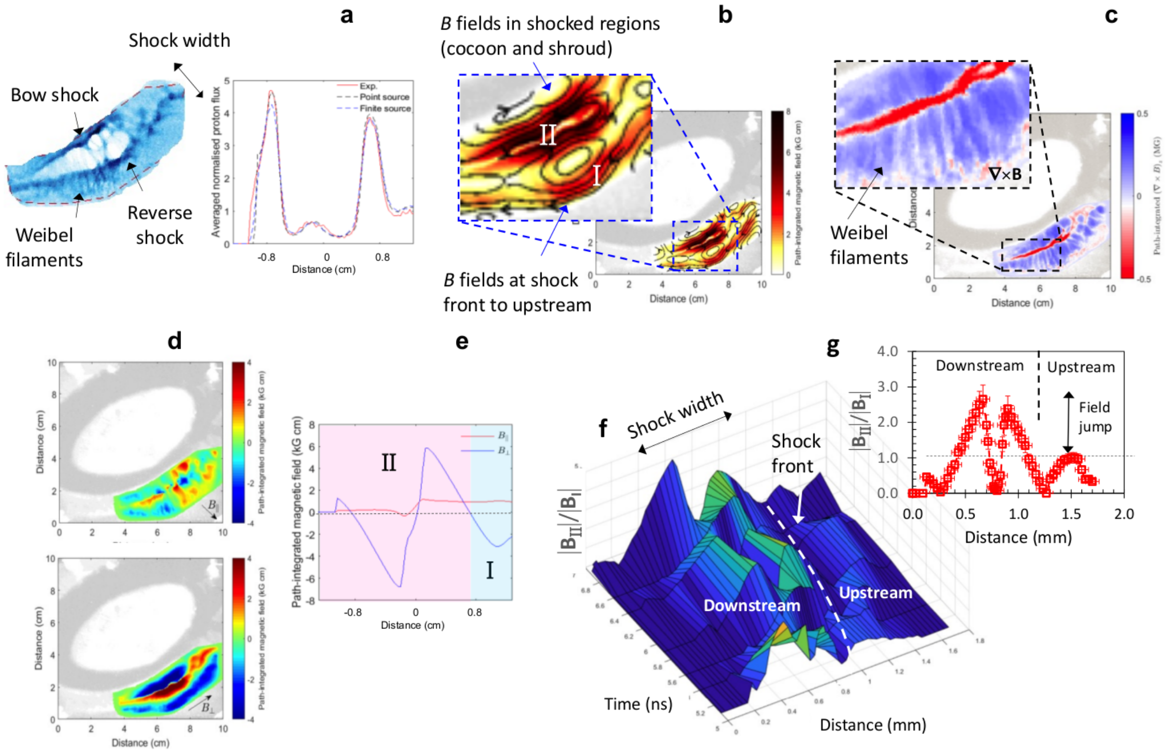

Figure 5.9 – 2D reconstruction of path-integrated magnetic fields (on detector plane, the magnification factor is 16). a. Reconstruction of proton radiograph based on the measurement (Fig. 1c, at t = 6.4 ns) resolves the detailed structure of the bow shock, reverse shock, filaments and the shock width. Diagonal lineouts across the shock transition (transversely averaged over 1 cm width) give the shock width (≃ 1mm). b. Spatially resolved magnetic fields in two different regions: I- shock front (ramp) to upstream, and II- shocked jet (cocoon) and ambient plasma (shroud). c. The reconstructed MHD current, $\mathbf{J} = (c/4\pi)\nabla\times\mathbf{B}$ , clearly shows the Weibel-generated ion current filaments. d. The path-integrated parallel and perpendicular component of the magnetic fields de-convoluted from (b). e. Transversely averaged lineouts across the shocks in (d) indicate the strength of the parallel (red) and perpendicular (blue) components of magnetic field in kG.cm. f. The profiles of path-integrated, perpendicular magnetic field (absolute values) plotted as a function of time and space from upstream to downstream. The dashed line indicates the shock position. g. The magnetic field jump between the regions I (upstream) and II (downstream) at time t = 6.4 ns. (Li et al., 2019)

It is remarkably consistent with the experimental image, providing a critical validation of the reconstruction algorithm. A lineout across the shock transition gives a width, $l_{\mathrm{EM}} = \mathrm{K}c/\omega_{pi} =$ 1mm, suggesting that K ≥ 10, is required for shock formation after instability saturation. Shown in Fig.5.9 b, the spatial topology resolves the magnetic fields in two different regions: Region I from the reverse shock front to the upstream region, and Region II which is the shocked region consisting of the shocked jet (cocoon) and a compressed ambient plasma (shroud).

The filaments from upstream penetrate into the magnetized interaction region and support magnetic turbulence resulting in electron heating and ion slowing down. A fine structure of filaments is found by applying the Ampère law to the measured magnetic field.

Figure 5.9 c shows a distribution of path-integrated electric current, $\mathbf{J} = 1/mu_0\nabla\times\mathbf{B}$ in the direction perpendicular to the observation plane, assuming the observed structure as 2D. The reconstructions generate clear images of current filaments and small scale transverse magnetic fields compatible with the ones expected from the Weibel instability.

Figures 5.9 d shows the components of large scale magnetic fields that are parallel and perpendicular to the shock normal, and their lineouts (Fig.5.9 e). Their small ratio ~ 0.1 confirms that the observed shocks are quasi-perpendicular. Interestingly, both shocks carry magnetic fields of the same polarity (down left, see Fig.5.9b), while the compressed zone contains a magnetic field of the opposite polarity separated by two magnetic islands from the shocks. Such a structure provides experimental evidence of two sources of Biermann magnetic fields generated when the shell explodes inside and outside. A bipolar structure of magnetic field in the shocked region implies a possibility of magnetic line reconnection that has to be further studied.

Figure 5.9 f shows the ratio of measured magnetic fields in regions I and II, up and down the shock fronts at different times (absolute value of path-integrated perpendicular fields, $|\int \mathrm{B}_\perp \times dl|$ given in Fig.5.9 e). The magnetic field values are determined assuming the proton path length $l \sim 1$mm in the field region, which is tangential to the crescent-shaped shock transition. The measured path-integrated field of 5 kG·cm corresponds thus to a 50 kG field strength, which is 3 times the initial field. Thus, a significant jump in magnetic field, $\mathrm{B}_{\mathrm{II}}/\mathrm{B}_{\mathrm{I}} = 3$ (Fig.5.9 g), occurs within a millimeter wide shocked region.

Assuming the shock as perpendicular, the implicit Rankine-Hugoniot conservation equations, in the shock frame of reference for ideal MHD (1.40), are written as

$$\rho_{\mathrm{II}} v_{\mathrm{II}} = \rho_{\mathrm{I}} v_{\mathrm{I}} \tag{5.12a}$$

$$\rho_{\mathrm{II}} v_{\mathrm{II}}^2 + \Pi_{\mathrm{II}} + \frac{\mathrm{B}_{\mathrm{II}}^2}{2\mu_0} = \rho_{\mathrm{I}} v_{\mathrm{I}}^2 + \Pi_{\mathrm{I}} + \frac{\mathrm{B}_{\mathrm{I}}^2}{2\mu_0} \tag{5.12b}$$

$$\left(\frac{1}{2}\rho_{\mathrm{II}} v_{\mathrm{II}}^2 + \frac{\Gamma\Pi_{\mathrm{II}}}{\Gamma-1} + \frac{\mathrm{B}_{\mathrm{II}}^2}{\mu_0}\right) v_{\mathrm{II}} = \left(\frac{1}{2}\rho_{\mathrm{I}} v_{\mathrm{I}}^2 + \frac{\Gamma\Pi_{\mathrm{I}}}{\Gamma-1} + \frac{\mathrm{B}_{\mathrm{I}}^2}{\mu_0}\right) v_{\mathrm{I}} \tag{5.12c}$$

$$\mathrm{B}_{\mathrm{II}} v_{\mathrm{II}} = \mathrm{B}_{\mathrm{I}} v_{\mathrm{I}} \tag{5.12d}$$

An explicit solution for the different density, magnetic field and velocity jumps, $\frac{\rho_{\mathrm{II}}}{\rho_{\mathrm{I}}} = \frac{\mathrm{B}_{\mathrm{II}}}{\mathrm{B}_{\mathrm{I}}} = \frac{v_{\mathrm{I}}}{u_{\mathrm{II}}} = r$ respectively, can be found as

$$2(2-\Gamma)r^2 + \Gamma(2(1+\beta_{\mathrm{I}}) + (\Gamma-1)\beta_{\mathrm{I}}\mathrm{M}_{\mathrm{I}}^2)r - \Gamma(\Gamma+1)\beta_{\mathrm{I}}\mathrm{M}_{\mathrm{I}}^2 = 0, \tag{5.14}$$

where $\beta_{\mathrm{I}} = 2\mu_0\Pi_{\mathrm{I}}/\mathrm{B}_{\mathrm{I}}^2 = c_s^2/v_{\mathrm{A}}^2$ is the ratio of the upstream plasma pressure to the magnetic field pressure and, $\mathrm{M}_{\mathrm{I}} = v_{\mathrm{I}}/c_{s\mathrm{I}}$ is the acoustic Mach number.

The only type of shock that is physically possible is a fast shock, with $v_{\mathrm{I}} > \sqrt{v_{\mathrm{AI}}^2 + c_{s\mathrm{I}}^2}$. The component jump produced by this shock can be written as

$$r = \frac{2(\Gamma+1)}{\mathrm{D} + \sqrt{\mathrm{D}^2 + 4(\Gamma+1)(2-\Gamma)\mathrm{M}_{\mathrm{AI}}^{-2}}}, \tag{5.15}$$

where $\mathrm{D} = (\Gamma-1) + (2\mathrm{M}_{\mathrm{I}}^{-2} + \Gamma\mathrm{M}_{\mathrm{AI}}^{-2})$ and $\mathrm{M}_{\mathrm{AI}}$ is the Alfvénic Mach number.

We consider a plasma jet density of $10^{18}\mathrm{cm}^{-3}$ at a temperature of 100eV which carries a magnetic field of 2T. The measured shock speed, $u_{sh} \sim 600\mathrm{km.s}^{-1}$, can be considered as the upstream velocity in the shock frame of reference $v_{\mathrm{I}}$, assuming that the velocity of the upstream plasma jet is zero in the laboratory frame of reference. It is not however true in our geometry since, the shell expansion occurs obliquely to the jet propagation direction.

The upstream velocity in the laboratory frame of reference can be estimated as $v_0 \cos\theta$, where $\theta = 50°$ is the angle of the jet propagation to the shock normal (estimated from figure 5.8). Then the upstream velocity in the shock frame of reference can be estimated as $v_0 \cos\theta + u_{sh} \approx v_0$. The particles behind the shock can be considered at rest (0 velocity) in the laboratory frame of reference, the downstream velocity is thus in the shock frame of reference at the shock velocity $\approx u_{sh}$.

The jump in velocity can thus be written as $v_{\mathrm{I}}/v_{\mathrm{II}} \approx v_0/u_{sh} \approx 3$. Regarding all these estimations, the density jump in equation (5.15) can be evaluated as $r \approx 3$ which is in good agreement with the magnetic field jump and the velocity jump. (assuming the plasma adiabatic index $\Gamma \approx 5/3$, in 3D.)

However, these measurements, present no direct experimental evidence of the shock formation. The latter is provided by the x-ray imaging, which provides access to the plasma density in the shock. Bremsstrahlung emission shown in Fig.5.10 allows to evaluate the plasma density jump across the shock front.

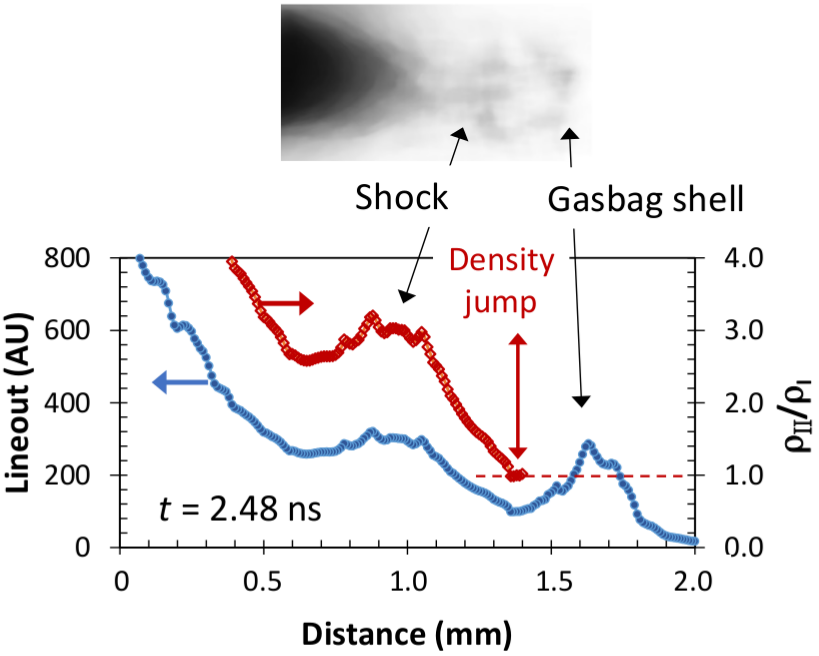

Figure 5.10 – Image of Bremsstrahlung x-ray emissions. Side-on x-ray self-emissions depict the plasma jet, gasbag (Type 2, Extended Data Fig. 1) shell and forward moving plasma shock (opposing the moving direction of the shocks shown in Fig. 1c). The lineout along jet propagation (blue line, left axis) shows the emissions from the shock and the gasbag shell (The error bars are ±20%). The density jump in the shocked region, $\rho_{\mathrm{II}}/\rho_{\mathrm{I}} \simeq 3$, is inferred (red line, right axis). The emission from the gasbag shell is a direct experimental evidence of the electron heating in the upstream plasma. (Li et al., 2019)

The plasma density jump inferred from Bremsstrahlung x-ray emission is $\rho_{\mathrm{II}}/\rho_{\mathrm{I}} = 3$, and it is in good agreement with the jumps of the magnetic field and shock velocity inferred from the proton radiography. Finally all the experimental jump components, measured velocity jump (given by $u_{sh} \approx v_{shell}/3$, Fig.5.8 g), field jump (Fig.5.9 g), and density jump (Fig.5.10), are in good agreement with equation (5.15), and written as

$$\frac{v_{\mathrm{I}}}{v_{\mathrm{II}}} = \frac{\mathrm{B}_{\mathrm{II}}}{\mathrm{B}_{\mathrm{I}}} = \frac{\rho_{\mathrm{II}}}{\rho_{\mathrm{I}}} \simeq \frac{\Gamma + 1}{(\Gamma - 1) + 2\mathrm{M}_{\mathrm{I}}^{-2}} = r \approx 3, \tag{5.16}$$

where the Alfvénic Mach number has been considered much higher than the acoustic Mach number, $\mathrm{M}_{\mathrm{AI}} >> \mathrm{M}_{\mathrm{I}}$. The shock is magnetosonic $\mathrm{M}_{ms\mathrm{I}} = 1/\sqrt{\mathrm{M}_{\mathrm{I}}^{-2} + \mathrm{M}_{\mathrm{AI}}^{-2}} \approx \mathrm{M}_{\mathrm{I}} \approx 3$, and super Alfvénic $\mathrm{M}_{\mathrm{AI}} \simeq 45$.

These experiments have demonstrated the presence of a shock which has been confirmed by the Rankine-Hugoniot jump conditions (considering some approximations). However, these observation do not reveal the physics in the shock formation and which instabilities are responsible for dissipation processes developing in the shock front. In order, to understand which are the dissipative mechanisms responsible for the entropy generation downstream of the shock, additional kinetic modeling is required.

## 5.2 Formation of electromagnetic collisionless shocks in the interpenetration of magnetized and unmagnetized plasma flows

The filamentary magnetic field structures in Fig.5.8 grow from kinetic interaction with particles. Hydrodynamic codes cannot describe interpenetration of plasmas and formation of collisionless shocks. In order to represent the interactions between all species we performed kinetic studies with kinetic codes like Particle-in-cell codes. Due to the large computational time of PIC codes, we consider a small fraction of the interaction region, large enough to study the shock formation process. We have modeled with PIC simulations using the fully relativistic code PICLS (Sentoku and Kemp, 2008), the interaction zone of Fig.5.7, between the plasma jet and the expanding shell, that is, only one magnetic compression structure. The considered computation setup presents a simplified version of the experiment and accounts only for the main processes of the shock formation. Particularly, we consider a higher collision speed of the two plasmas in order to increase the growth of the Weibel instability and reduce the size of filaments (reducing as well the size of the simulation box).

### 5.2.1 Initial conditions

The following inital conditions are used in our simulations. We resolve two spatial directions $x-y$ and three particle velocity components (2D3V). Absorbing boundary conditions for the computational particles and fields are used in the transverse direction ($y$). The simulation box is large enough to separate effects introduced by the boundaries from the area of interest, its size in 2D is $3\times 3$mm with a spatial resolution 2.5μm in both directions.

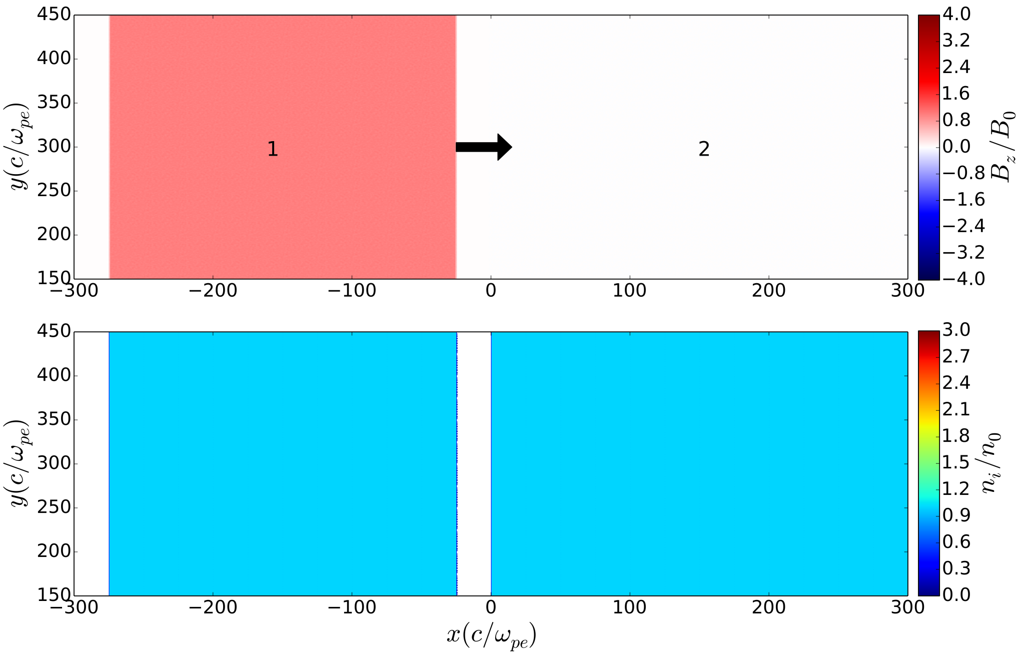

Figure 5.11 – Magnetic field (top line) and ion density (bottom line) at the initial time, the numbers in the top left panel indicate the numeration of zones used in the text. Plasma 1 moves from the left to right, carries a magnetic field.

Two counterstreaming cold plasma flows contain electrons and protons.(The carbon ions from the shell and jet are heavier compared to protons and are less affected by the magnetic perturbations at the considered time scales).
Plasma 1, fills the interval $-1.5 < x < 0$mm, and is moving at a velocity $v_0 = 2\times 10^8$ cm/s from the

left to the right along the $x$-axis. The electron and ion temperatures are $T_{e1} = T_{i1} = 100$ eV, and the electron and ion densities are $n_{e1} = n_{i1} = n_0 = 10^{18}\text{cm}^{-3}$. It represents the expanding shell and carries a magnetic field $B_0 = 2$T.
Plasma 2 represents the jet, it fills the interval $0 > x > 1.5$mm, with cold electrons, motionless ions and without magnetic field. Its electron and ion temperatures are $T_{e2} = T_{i2} = 10$ eV, and its electron and ion densities are $n_{e2} = n_{i2} = n_0 R = 10^{18}\text{cm}^{-3}$, where $R = n_{i2}/n_{i1}$ is the density ratio between Plasma 1 and Plasma 2.

The simulation is initialized with Maxwellian velocity distributions for electrons and protons with 50 particles per cell and per species.

A magnetic field of strengh $B_1 = 2$ T, in plasma 1 is sufficient to magnetized electrons. The magnetic field inside is maintained by the integral currents on the surface, which are created by electrons, confined by ions with the electrostatic tension. Without collisions, the magnetic flux in plasma, is conserved.

The values for the parameters of the moving plasma 1 are listed in Table 5.4, considering a real proton/electron mass ratio $m_i/m_e = 1836$, and the inital time of the simulation is shown in figure 5.11

| Parameter | Numerical value |
|---|---|
| $\omega_{pe1} = (n_{e1}e^2/\epsilon_0 m_e)^{1/2}$ | $5.63 \cdot 10^{13}\text{s}^{-1}$ |
| $\omega_{ce1} = eB_0/m_e$ | $3.5 \cdot 10^{11}\text{s}^{-1}$ |
| $v_{the1} = (k_B T_{e1}/m_e)^{1/2}$ | $4.19 \cdot 10^{6}\text{m.s}^{-1}$ |
| $r_{ge1} = v_{the1}/\omega_{ce1}$ | $1.2 \cdot 10^{-5}\text{m}$ |
| $\omega_{pi1} = (Z^2 n_{i1}e^2/\epsilon_0 m_i)^{1/2}$ | $1.31 \cdot 10^{12}\text{s}^{-1}$ |
| $\omega_{ci1} = ZeB_0/m_i$ | $1.91 \cdot 10^{8}\text{s}^{-1}$ |
| $c_{s1} = ((\Gamma_e T_{e1} + \Gamma_i T_{i1})/m_i)^{1/2}$ | $2.11 \cdot 10^{5}\text{m.s}^{-1}$ |
| $v_{a1} = B_0/(\mu_0 n_{i1} m_i)^{1/2}$ | $4.3 \cdot 10^{4}\text{m.s}^{-1}$ |
| $c_{ms1} = (v_{a1}^2 + c_{s1}^2)^{1/2}$ | $2.15 \cdot 10^{5}\text{m.s}^{-1}$ |

Table 5.4 – Parameters of Plasma 1 in our simulations, considering a real proton/electron mass ratio $m_i/m_e = 1836$.

These parameters define the interaction mode which is typical for astrophysical electromagnetic shocks. The flow is supersonic with the acoustic Mach number $M_s = 9.5$ and super Alfvénic with the Alfvén Mach number $M_A = 45$. The thermal to magnetic pressure ratio $\beta = 20$ in plasma 1. The electrons are magnetized, their Larmor radius $r_{ge1} = v_{Te1}/\omega_{ce1}$ is $\sim 10\,\mu$m, which is comparable to the electron inertia length $c/\omega_{pe1} \simeq 5\,\mu$m. The fluid velocity is chosen large enough, so that the external ion mean free path from Plasma 1 with respect to Plasma 2 ions is much larger than the considered dimensions of the system in order to assure the collisionless nature of the shock. The external mean free path of the ions from Plasma 1 with respect to collision with electrons from Plasma 2, for the chosen parameters, is $l_{p-e} \simeq 3$ mm, which is comparable to the length of the simulation box, making possible an important contribution of the electron-ion collisions on the development of the instabilities as discussed before.

The characteristic length of our simulations is the electron inertia length $c/\omega_{pe1}$ of Plasma 1. The simulation box covers with $\hat{x} = x/(c/\omega_{pe1})$ the interval $-300 < \hat{x} < 300$, with a spatial resolution $0.5c/\omega_{pe1}$ in both directions. Wave numbers are multiplied by $c/\omega_{pe1}$. Time and frequency units are $\omega_{pe1}^{-1}$ and $\omega_{pe1}$ respectively. The ion density $n_i$ is expressed in units of $n_0$.

Large scale 2D simulations were run, for different density ratios R, resolving $T_{max} = 3 \times 10^4 \omega_{pe1}^{-1} \simeq 600$ ps by $0.5\omega_{pe1}^{-1} = 9$ fs time steps. These simulations were sufficient to reach the saturation of the ion filamentation instability.

### 5.2.2 Numerical limitation

Before the presentation of our results, it is important discuss a numerical limitation. The colder is the plasma, the more difficult to resolve of the Debye length. Furthermore, the denser is the plasma, the more difficult to resolve a large plasma size (as an example the plasma in section 3 of Chapter 4 was $10^4$ less dense and 20 times hotter, allowing a correct resolution of the Debye length even in 2D). The simulation box has been taken large enough to represent the development of the Weibel instability, and due to the large density of the plasma it leads to a large simulation box and a large number of cells.

The Debye length in our simulations is $\lambda_{\mathrm{DE}} \sim 0.014c/\omega_{pe1}$, which leads to an unresolution of the Debye length by a factor $\Delta x/\lambda_{\mathrm{DE}} \simeq 35$. The non-resolution of the Debye length can lead to numerical heating discussed in Chapter 1. This heating can alter the phase space of the plasma by the apparition of unphysical processes leading to incorrect interpretation of computational results.

The PIC simulations for the range of parameters presented above are already very costly in computational time. A typical simulation runs over 1024 processors during 4 days, which represents $\sim 10^6$ computational hours. The correct resolution of the Debye length will lead to increase the number of cell by a factor $35 \times 35 = 1225$, and the number of time steps by a factor 35. If we consider the computational time as linear with the box size and the number of time steps (which is true as long as MPI communications do not degrade too much the scaling), the typical computational time of one simulation with a correct resolution of the Debye length will be $> 4 \times 10^{10}$ hours. Using 10 times more processors (10240) the time required will be higher than 450 years, which is out of the time range of this thesis.

The non-resolution of the Debye length is so inevitable, but the undesirable numerical heating can be limited by using a high number of computational particles per cell. The numerical heating has been tracked in time for all the simulations to be sure this it does not affect the physical convergence of the simulations.

### 5.2.3 Simulation results

The overall dynamics of the plasma flows explaining the initial condition and the evolution towards the formation of a shock is presented in figure 5.12.

The unperturbed plasmas 1 and 2 penetrate each other. At the time $2.25 \times 10^4 \omega_{pe1}^{-1}$, the interpenetration length of these two plasmas is $> 100c.\omega_{pe1}^{-1}$ and forms two distinct zones. A region of magnetic field compression, referenced as zone 3, is visible in the interval $0 < x < 60c.\omega_{pe1}^{-1}$. And zone 4 correspond to the interval $60 > x > 120c.\omega_{pe1}^{-1}$, where the initial magnetic fied carried by Plasma 1 is no more present, and interaction of plasmas 1 and 2 results in generat ion of magnetic filaments.

The initial distance between the plasmas is $25c.\omega_{pe1}^{-1}$ and they are entering in contact at $t = 4 \times 10^3 \omega_{pe1}^{-1}$, corresponding to the formation time of zones 3 and 4. The boundary between them propagates with a constant velocity, two times smaller than the ion velocity in this particular case. The magnetic field, initially carried by Plasma 1, propagates 2 times slower than the ions of Plasma 1. This is illustrated in figure 5.13 showing the time evolution of the magnetic field strength and of the ion density averaged over the transverse coordinate.

The structure in figure 5.13 is not, strictly speaking, a shock. Indeed, according to equation (5.15), for the acoustic and Alfvénic Mach numbers of Plasma 1 ($\mathrm{M}_s = 9.5$, $\mathrm{M}_{\mathrm{A}} = 45$, and $\Gamma = 2$ in two dimensions), the jump parameter should be $r \sim 2.9$. The magnetic field and density jumps between zones 1 and 3 is only of a factor 2 resulting of the interpenetration of Plasma 1 and Plasma 2. These two ion populations are so interpenetrating freely and compress the magnetic field. Furthermore, even after $2.25 \times 10^4 \omega_{pe1}^{-1} = 600\mathrm{ps}$ of interpenetration, no nonlinear evolution of the Weibel instability to magnetic turbulence, essential for the shock formation, is observed.

However, this initial configuration of magnetic structure in the interpenetration region presents a seed for shock formation, and it is so, important to understand the underlying physical processes

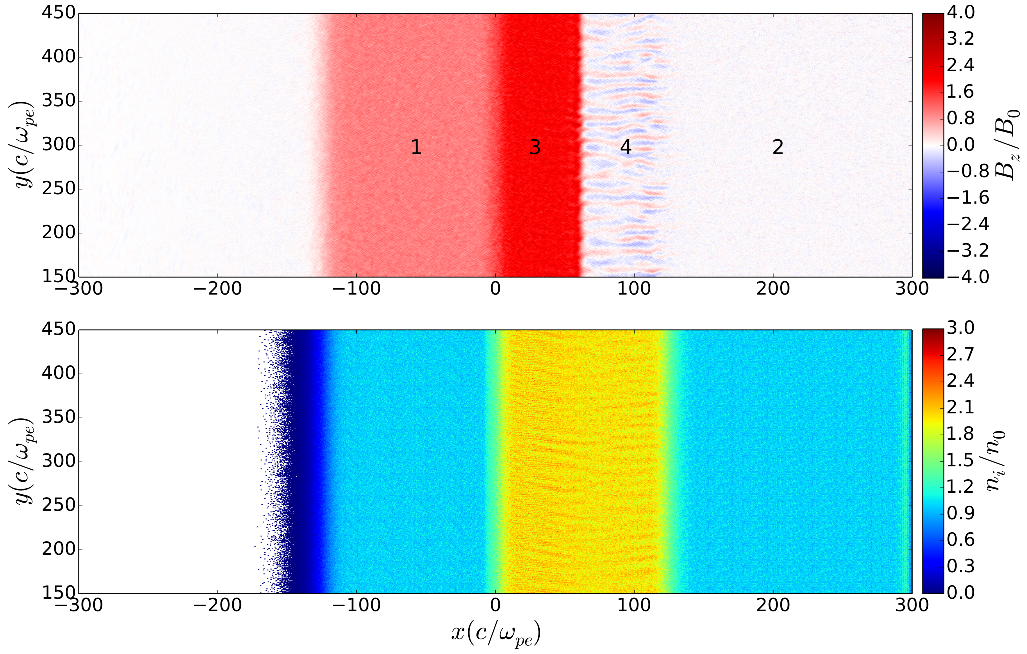

Figure 5.12 – Magnetic field (top line) and ion density (bottom line) at the time $2.25\times10^4\omega_{pe1}^{-1}$, the numbers in the top left panel indicate the numeration of zones used in the text.

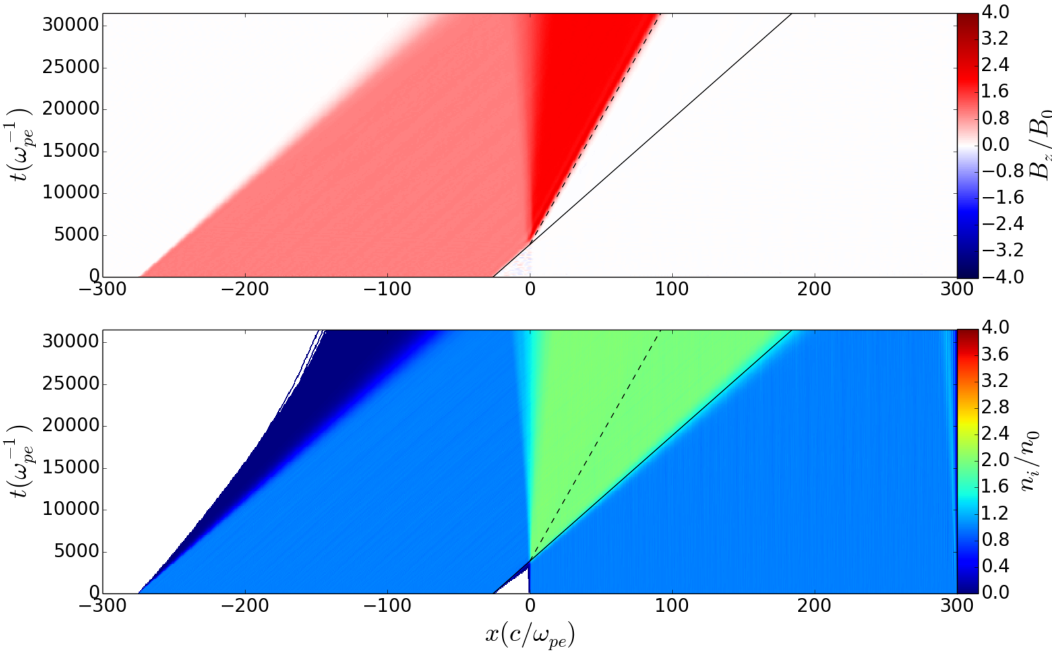

Figure 5.13 – Magnetic field (top line) and ion density (bottom line) evolution with time. The deep blue in the density panel shows the thermal diffusion of the ion in the simulation. Furthermore, the discontinuity between zone 1 and 3 shows also thermal and magnetic diffusion. The black line represents the intial Plasma 1 velocity $v_i$, and the dashed black line the velocity of the magnetic field $v_b$.

leading to the magnetic field configuration of figure 5.12.

### 5.2.4 Adiabatic compression

The ions of Plasma 1 are penetrating freely in Plasma 2 because there are no collisions that could slow them down. The kinetic pressure of these ions is $\mathrm{P}_{i1} = 3.3 \times 10^4$ bars, which is 2000 times higher than the thermal pressure of the electrons of Plasma 2 (16 bars). The electrons of Plasma 1 are pulled with their ions by the electrostatic field of charge separation (Bochkarev et al., 2015), but their motion is constrained by the magnetic field. So initially, electrons can penetrate only over a depth of the order of the Larmor radius. However, it is sufficient to activate the magnetic field propagation into the unmagnetized zone. Gradual accumulation of electrons in the magnetized plasma, charge neutralization and the magnetic field compression lead eventually to the displacement of the magnetic field edge in the direction of the ion flow but with a velocity $v_b$ which is smaller than $v_i$.

The collisionless structure is changing in the kinetic scales of the electron skin depth, of the Larmor radius and of the inertia length. On larger hydrodynamical scales, the jump conditions between zones 1,2,3,4 and the magnetic front velocity are defined by the conservation laws. First, the charge conservation implies that the electron density in the plasma overlapping zones 3 and 4 is equal to the ion density, that is,

$$n_{e3} = n_{e4} = n_{i1} + n_{i2} = (1+\mathrm{R})n_{e1}, \tag{5.17}$$

where R represents here the density ratio between Plasma 1 and Plasma 2. Second, as the electrons are magnetized, the magnetic field in a continuous flow is proportional to the electron density, $\mathrm{B}/n_e = \mathrm{const}$ (Baumjohann and Treumann, 1997). That is, compression of the electrons by a factor $1+\mathrm{R}$ implies the same magnetic field compression,

$$\mathrm{B}_3 = \mathrm{B}_1 n_{e3}/n_{e1} = (1+\mathrm{R})\mathrm{B}_1. \tag{5.18}$$

A third point is that the magnetic flux is conserved, that is, the product of the magnetic field and the electron flow velocity is also conserved, then the velocity of the magnetic front propagation reads

$$v_b = v_i \mathrm{B}_1/\mathrm{B}_3 = v_i/(1+\mathrm{R}). \tag{5.19}$$

Fourth, the electron adiabatic compression results in an increase of electron temperature. In magnetized plasmas this effect corresponds to the conservation of the electron magnetic invariant, $\mu_e = m_e v_\perp^2/2\mathrm{B}$, where $v_\perp^2 = \tilde{v}_y^2 + \tilde{v}_y^2$ is the electron rotational velocity in the plane perpendicular to the magnetic field direction, with $\tilde{v}_{x,y} = v_{x,y} - < v_{x,y} >_t$ the latter corresponding to an average in time (Sagdeev et al., 1988).

Consequently, compression of the magnetic field by a factor $1+\mathrm{R}$ implies an increase of the electron fast transverse velocity, which corresponds to the transverse temperature $\mathrm{T}_\perp = m_e v_\perp^2/2$, by the same factor:

$$\mathrm{T}_{e3\perp} = \mathrm{T}_{e1\perp}\mathrm{B}_3/\mathrm{B}_1 = (1+\mathrm{R})\mathrm{T}_{e1\perp}. \tag{5.20}$$

As the electron average energy in the magnetic field direction remains unchanged, the effective temperature in zone 3 increases by a factor of $1+2\mathrm{R}/3$:

$$\mathrm{T}_{e3} = \mathrm{T}_{e1\parallel}/3 + 2\mathrm{T}_{e3\perp}/3 = (1+2\mathrm{R}/3)\mathrm{T}_{e1}. \tag{5.21}$$

These estimates for the parameters upstream and downstream of the magnetic field discontinuity are in good agreement with 2D3V numerical simulations shown in Fig.5.12. Two times magnetic field and electron density compression are shown in Fig.5.12. A stationary propagation of the magnetic field front with a velocity two times smaller than the ion flow velocity can be seen in Fig.5.13. (a delay of shock formation of $\sim 4 \times 10^3 \omega_{pe1}^{-1}$ is explained by the initial distance between the colliding plasmas of $25c.\omega_{pe1}^{-1}$, see Fig.5.13.)

A dependence of the magnetic field compression on the plasma density ratio is studied in more detail with 1D PIC simulations performed with the code EPOCH (Arber et al., 2015) (the choice of this code for these simulations is explained by an efficient 1D3V parallelization of EPOCH). These simulations of a smaller scale but with a much higher resolution were performed in one spatial dimension in a box of $120c.\omega_{pe1}^{-1} \simeq 0.6$ mm with spatial and temporal resolutions of 30 nm and 0.1 fs, and were run for a total time of $6 \times 10^3 \omega_{pe1}^{-1} \simeq 120$ ps to support the physical interpretation of the processes responsible for the adiabatic magnetic compression.

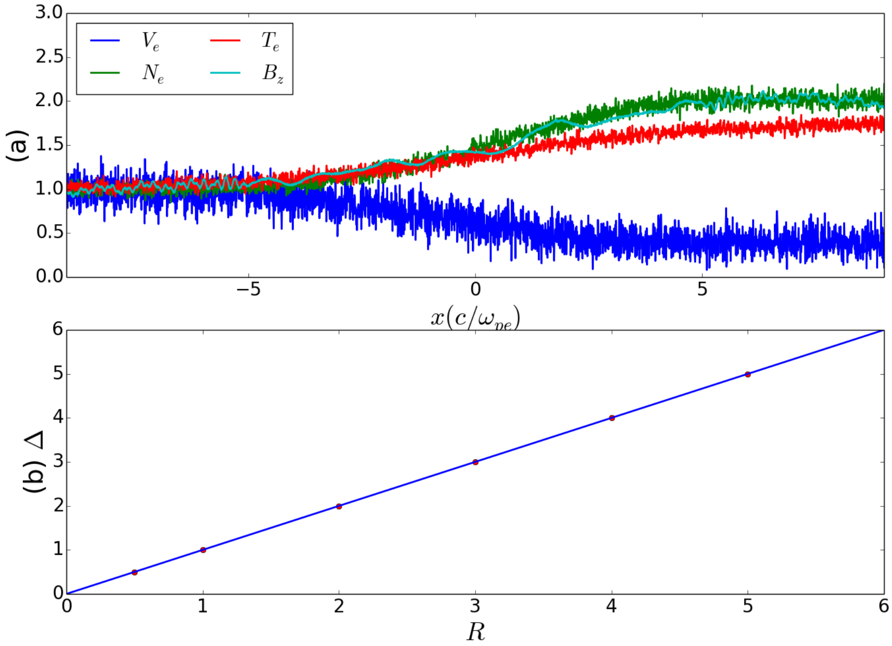

Figure 5.14 – a) Detailed view of the shock discontinuity between zones 1 and 3, at the time $5633\omega_{pe1}^{-1}$ for the density ratio R = 1. Dependence of the magnetic field jump $\Delta_b = B_3/B_1$ on the density ratio $R = n_{i2}/n_{i1}$.

Figure 5.14a shows details of the shock front at the edge of the motionless plasma, Plasma 2, at $x = 0$. The formal discontinuity is in reality a smooth transition on the electron spatial scale. It begins with a width of a few electron Larmor radii then gradually widens because of the magnetic field diffusion. This process can also be considered as a propagation of finite amplitude magnetosonic waves to the right in Plasma 2 and to the left in Plasma 1. A linear dependence of the magnetic field compression on the plasma density ratio is shown in Fig.5.14b.

The work made for the magnetic field compression and electron heating is performed by ions and this energy is subtracted from the ion flow. This ion energy loss represents less than 1% of the total ion kinetic energy, for a configuration of R = 1. The magnetic field profiles and the particle phase spaces at the end of the simulation are shown in Fig.5.15. At the initial time moment the moving plasma, Plasma 1 has a length of $250c.\omega_{pe1}^{-1}$ with the front edge at a distance of $25c.\omega_{pe1}^{-1}$ from Plasma 2, which has a length of $300c.\omega_{pe1}^{-1}$. At the end of the simulation one can recognize two magnetic field fronts: a broader one at the position $x = 0$ between zones 1 and 3 and a narrower one between zones 3 and 4 at $x \approx 100c.\omega_{pe1}^{-1}$. The ion phase spaces are not strongly modified.

The electron distribution shows two particular features: a strong heating in zone 3 due to the adiabatic compression and a weaker heating in zone 4 due to the two-stream instability followed by the Weibel instability as discussed below.

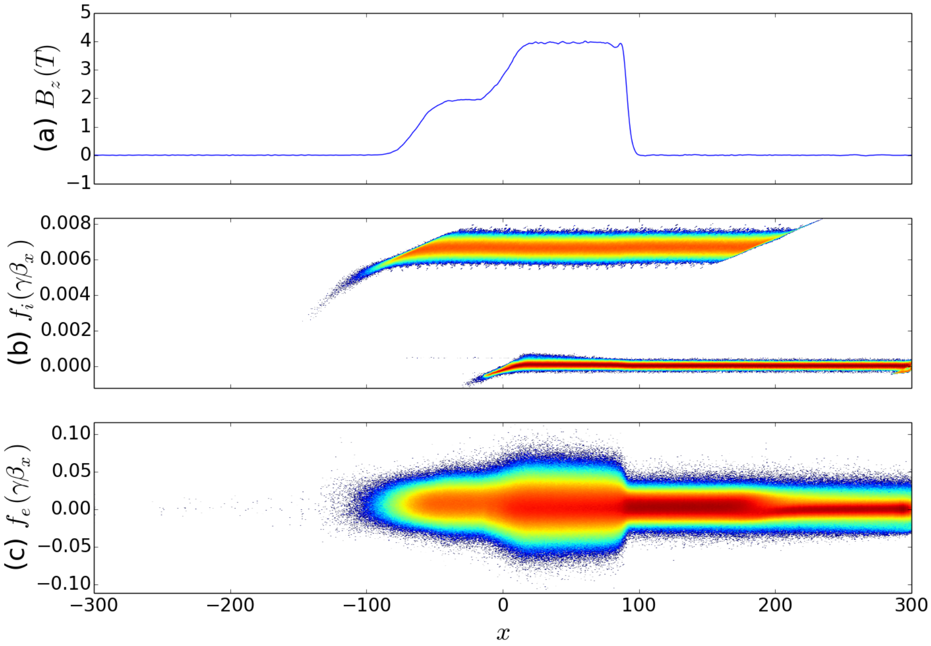

Figure 5.15 – Magnetic field spatial distribution (a) and the phase space of ions (b) and electrons (c) at the end of the simulation at $t = 3\times 10^4\omega_{pe1}^{-1}$, for R = 1.

### 5.2.5 Weibel instability

There are two ion streams in zone 4 free of magnetic field: the ions of Plasma 2 and the ions of Plasma 1 moving at a high velocity, transporting a reflected unmagnetized electron population of Plasma 2. This distribution is prone to the excitation of the ion Weibel instability as shown in Fig.5.12.

The electrons are thermalized relatively rapidly, and the ion Weibel instability is driven by the proton beam moving through the hot isotropic electron gas. Small transverse magnetic field perturbations would drive the oppositely moving protons into current layers of opposite sign, which reinforces the initial field (Medvedev and Loeb, 1999), the one scheme is similar to this presented in Chapter 2 for the electron Weibel instability. Let us consider as in (Lyubarsky and Eichler, 2006) in the electron reference system two counterpropagating proton beams along the direction x, with a waterbag distribution function to simplify the calculation, but to conserve the information on the plasma temperature. The distribution function can be written as

$$f_s(\mathbf{p}) = \frac{1}{2\pi p_{\perp 0}^2}\Big[\delta(p_x - p_{\parallel 0}) + \delta(p_x + p_{\parallel 0})\Big]\Theta(p_{\perp 0}^2 - p_\perp^2), \tag{5.22}$$

where $\Theta(x)$ is the Heaviside step function and $p_\perp = \sqrt{p_y^2 + p_z^2}$. Considering a small transverse magnetic field $\mathbf{B} = \mathrm{B}_0 e^{-i(\omega t - k_y y)}\mathbf{e}_y$. The set of Vlasov-Maxwell equations in Fourier space gives the dispersion relation

$$\mathrm{D}(\omega, k_y) = \frac{\omega^2}{k_y^2}\Big[1 + \chi_e(\omega, k_y) + \chi_i(\omega, k_y)\Big] = 0, \tag{5.23}$$

where the susceptibility $\chi_s$ for the sth species from equation (1.55) is written as

$$\chi_s = \frac{\omega_{ps}^2}{\omega^2}\int d\mathbf{p}\, v_x\left(\frac{\partial f_s}{\partial p_x} + \frac{k_y v_x}{\omega - v_y k_y}\frac{\partial f_s}{\partial p_y}\right) \tag{5.24}$$

The ion susceptibility is

$$\chi_i = -2\frac{\omega_{pi}^2}{\omega^2\gamma^2}\left[\frac{1}{m_i\gamma+\sqrt{m_i^2\gamma^2-p_{\perp 0}^2}}\times\left(m_i\gamma-\frac{p_{\parallel 0}^2}{\sqrt{m_i^2\gamma^2-p_{\perp 0}^2}}\right)+\frac{p_{\parallel 0}^2}{p_{\perp 0}^2}\left(\frac{\omega m_i\gamma}{\sqrt{\omega^2 m_i^2\gamma^2-k_y^2 p_{\perp 0}^2}}-1\right)\right] \tag{5.25}$$

For very cold plasma temperatures ($p_{\perp 0}^2 \longrightarrow 0$) equation (5.25) reduces to

$$\chi_i = -\frac{\omega_{pi}^2}{\omega^2\gamma^2}\left[\left(1-\frac{p_{\parallel 0}^2}{m_i^2\gamma^2}\right)+\frac{p_{\parallel 0}^2}{p_{\perp 0}^2}\frac{k_y^2 p_{\perp 0}^2}{\omega m_i\gamma}\right] \tag{5.26}$$

The electron susceptibility in the very low frequency limit ($\omega << kc$) can be written as

$$\chi_e = i\sqrt{\frac{\pi}{2}}\frac{\omega_{pe}^2}{\omega k_y v_{\mathrm{Te}}} \tag{5.27}$$

This conducts to the dispersion relation in the nonrelativistic approximation ($\gamma \approx 1$)

$$\mathrm{D}(\omega, k_y) = \frac{k_y^2 c^2}{\omega^2}+\frac{\omega_{pi}^2}{\omega^2}\frac{k_y^2 v_\parallel^2}{\omega^2}-i\sqrt{\frac{\pi}{2}}\frac{\omega_{pe}^2}{\omega k v_{\mathrm{T}e}}=0. \tag{5.28}$$

This equation of degree 3 can be solved analytically by the Cardan method. In the frame of reference of Plasma 2, the maximum growth rate of the Weibel instability can be estimated as

$$\delta \simeq v_0\omega_{pi}/c \tag{5.29}$$

for a wave number of

$$k_y \simeq \frac{\omega_{pe}}{c}\left(\frac{\omega_{pi}}{\omega_{pe}}\frac{v_0}{v_{\mathrm{Te}}}\right)^{1/3}. \tag{5.30}$$

The Weibel instability described in this section concerns Zone 4 where the plasma is free of magnetic field due to the adiabatic compression, the electrons in this region are thus not magnetized, and the Weibel instability grows freely. The electrons stabilize the Weibel growth, which results of the excitation of short wavelength filaments. Equations (5.29) and (5.30) give in the case of our simulation, $\delta \simeq 6.66\times 10^{-3}\omega_{pi1}$ and $k_y \sim 10\omega_{pi1}/c$. These theoretical estimations are confirmed by Figure 5.16 a, giving a dominating wavelength for the ion filaments of $\lambda_i \simeq 0.6c/\omega_{pi}$.

Furthermore, this wavelength of the unstable Weibel mode is approximately $\lambda_i \simeq 140\mu$m, which can directly be compared to the wavelength of the filaments measured in Fig.5.8f ($\sim 150\mu m$), allowing a validation of our interpretation and of our range of parameters.

The instability is developing for $t > 100\omega_{pi1}^{-1}$ immediately after the two plasmas are entering in contact, and the saturation is due to the ion trapping (Lyubarsky and Eichler, 2006), which occurs at the time $\simeq \omega_{tr}^{-1} \simeq 420\omega_{pi1}^{-1}$, where the ion trapping frequency

$$\omega_{tr} \simeq (\omega_{ci}k_y v_i)^{1/2} \simeq 0.4\delta. \tag{5.31}$$

The maximum amplitude of the magnetic filaments is so contrained by the trapping frequency and the Alfvén speed in the saturated regime can be written as

$$v_{\mathrm{A}}/v_i = \frac{\mathrm{B}_{z:max}}{\sqrt{\mu_0 n_0 m_i v_i^2}} \sim 0.4^2\left(\frac{m_e}{m_i}\frac{\mathrm{T}_e}{m_i v_i^2}\right)^{1/6}. \tag{5.32}$$

In the range of parameters of our simulation the Alfvén wave propagates at $v_{\mathrm{A}} = 33\times 10^3$km.s$^{-1}$ for a maximum value of the magnetic field $\mathrm{B}_{z:max} \simeq 1.5$T (in good agreement with figure 5.12). The field of the filaments is thus smaller the field carried by Plasma 1, and almost 3 times smaller the compressed magnetic field in zone 3. However, during the expansion of zone 3, the magnetic filaments created by the Weibel instability in the upstream region, zone 4 penetrate the magnetized

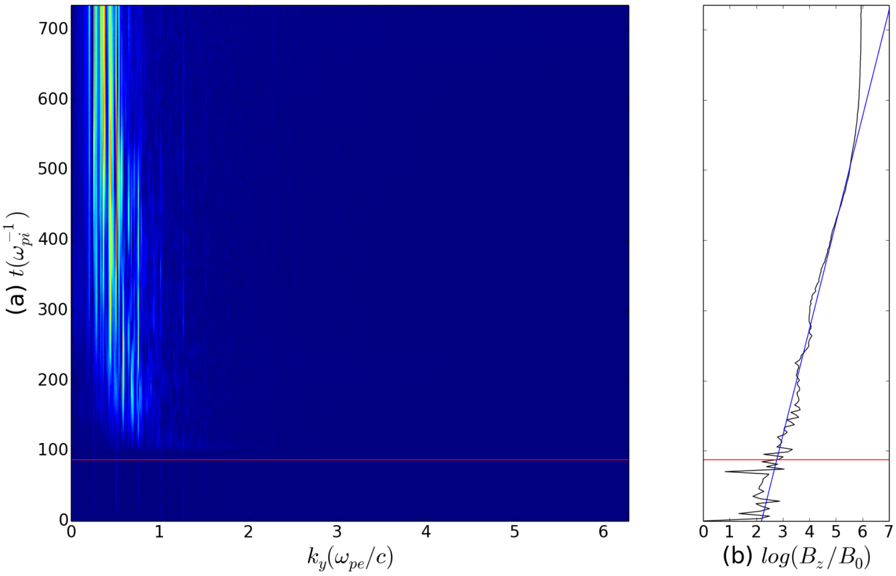

Figure 5.16 – Panel a: Time evolution of the Fourier transform of the magnetic field $\mathrm{B}_z(y)$, averaged over the interval $v_{shell} \times (t - t_0) < x < v_{shell} \times (t - t_0) + 20c/\omega_{pe}$. Panel b: The magnetic field evolution at $k_y = 0.25\omega_{pe1}/c$. The red line is the first time of interaction between the incoming flow and the gasbag $t_0$, the blue line represents a linear fit with a slope of $0.006\omega_{pi}$.

downstream region, zone 3. The magnetic modulation is visible in the front of zone 3 (cf. figure 5.12) due to the magnetic filaments. The saturation of the Weibel instability leads to filaments merging and excitation of stronger magnetic fields and larger wavelength turbulence. The latter allows the formation of an electromagnetic collisionless shock and particle acceleration via the first order Fermi mechanism. However, the present simulation is not large enough to reach this evolution time for a real ion hydrogen mass ratio.

### 5.2.6 Electromagnetic shock formation ?

As discussed in Chapter 1, collisionless shocks formation is a very long process, which presents some difficulties for numerical simulations. Electrostatic and magnetized shocks (cf. Chapters 3 and 4) can be represented in a one dimensional simulation. Electromagnetic shocks require at least a two dimensional representation, which tenfolds the number of computational resources needed to simulate them. The use of a reduced ion mass allows one to consider longer time scales and to assess the shock formation. It allows to increase the growth rate of the ion Weibel instability (in the same way as for the Buneman instability discussed in Chapter 2) and to accelerate the excitation of magnetic turbulence. Simulations with reduced a ion mass are common today to try to simulate electromagnetic shocks (Kato and Takabe, 2008; Huntington et al., 2017). It is also possible to increase the electron mass to reach the same effect, since the only important parameter is the mass ratio between ions and electrons. One interest to use a larger electron mass compared to a lower ion mass, is to let unchanged the ion acoustic speed and the Alfvén speed. In our case, the most important consideration is to conserve the electrons magnetized, and the ions unmagnetized, regarding to their mass. In particular, the electron Larmor radius defines the width of the transition zone between the states 1 and 3 in figure 5.14.

In order to model the shock formation we have decreased the ion-electron mass ratio to $m_i = 200m_e$ in our 2D PICLS simulations (changing the ion mass). This modification impacts the properties of Plasma 1 and the new plasma parameters are compiled in Table 5.5.

Plasma 1 flow is super acoustic and super Alfvénic but the Mach numbers are reduced by a

| Parameter | $\omega_{pi}(\mathrm{s}^{-1})$ | $v_{thi}(\mathrm{m.s}^{-1})$ | $\omega_{ci}(\mathrm{s}^{-1})$ | $r_i(\mathrm{m})$ |
|---|---|---|---|---|
| Numerical value | $3.93\cdot10^{12}$ | $2.96\cdot10^{5}$ | $1.75\cdot10^{9}$ | $1.14\cdot10^{-3}$ |
| Parameter | $c_s(\mathrm{m.s}^{-1})$ | $v_\mathrm{A}(\mathrm{m.s}^{-1})$ | $c_{ms}(\mathrm{m.s}^{-1})$ | $\beta$ |
| Numerical value | $6.4\cdot10^{5}$ | $1.3\cdot10^{5}$ | $6.5\cdot10^{5}$ | 20 |

Table 5.5 – Plasma parameters of the edge of the plume before its interaction with the gasbag shell for an ion-electron mass ratio of $m_i = 200m_e$, the parameters depending only of the electron mass are unchanged.

factor 3 in this case, giving $\mathrm{M}_s = 3$ and $\mathrm{M_A} = 15$, however the magnetic/thermal pressure ratio remains unchanged, $\beta = 20$. Conservation of the Mach numbers as well as of the $\beta$ parameter, would be possible by reducing linearly and squarely the temperature and the magnetic field respectively, compared to the ion mass. However, such a decrease of the electron temperature would lead to an inevitable strong numerical heating.

The initial condition for simulation of the shock formation is presented in figure 5.17 for a mass ratio of $m_i = 200m_e$, and for the same electron time scale as in figure 5.12.

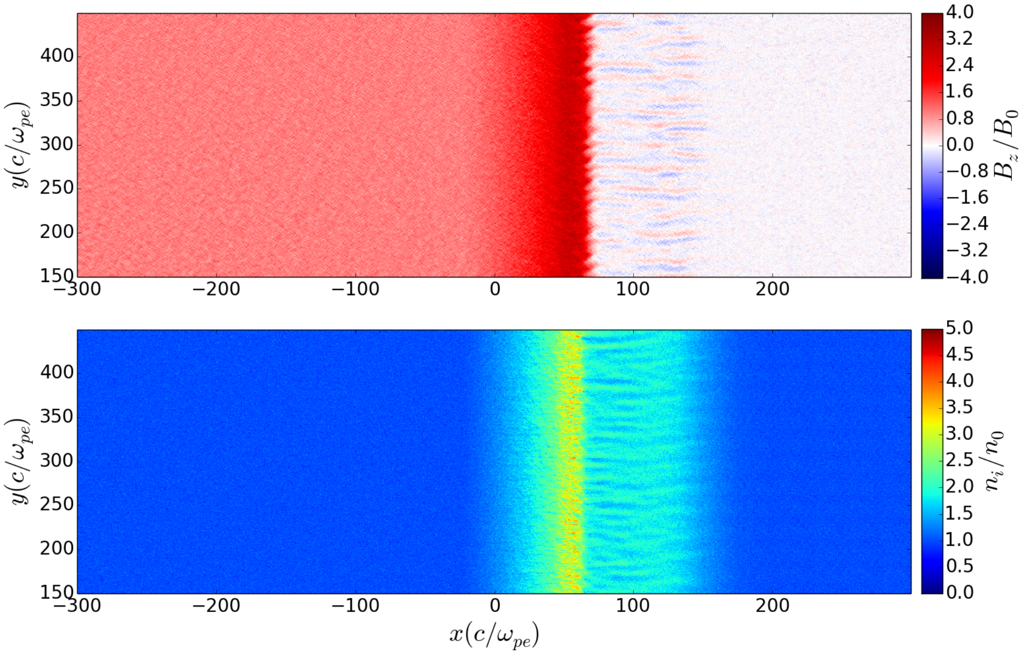

Figure 5.17 – Magnetic field (top line) and ion density (bottom line) at the time $2.25\times10^4\omega_{pe1}^{-1}$ for a mass ratio of $m_i = 200m_e$.

The reduced ion mass results in increasing of the thermal spread of the ions and in amplified the magnetic field diffusion. The transition layer between zones 1 and 3 is now 3 times larger ($30c\omega_{pe1}^{-1}$) than in the simulation with the real ion-electron mass ratio ($m_i = 1836m_e$). The magnetic field as well as the ion density are compressed in the front of zone 3 by more than a factor 2 (almost 3). The wavelength of the magnetic filaments in zone 4 have decreased to $\lambda_i = 93\mu m$ according to equation (5.30). Furthermore, the ions, after $2.25\times10^4\omega_{pe1}^{-1} \sim 1.6\times10^3\omega_{pi1}^{-1}$, are trapped into the magnetic filaments in zone 4, and penetrate zone 3, inducing a density perturbation in this region (cf. figure 5.17 bottom, red color). The shock formation has been started, but a longer simulation is needed, to see it fully formed.

The shock is presented in figure 5.18 for a mass ratio of $m_i = 200m_e$ at the time $5.4\times10^4\omega_{pe1}^{-1}$.

As figure 5.18 demonstrates, the simulation is no longer numerically stable. The magnetic field strongly diffuses in Plasma 1 generating strong numerical turbulence far from the interac-

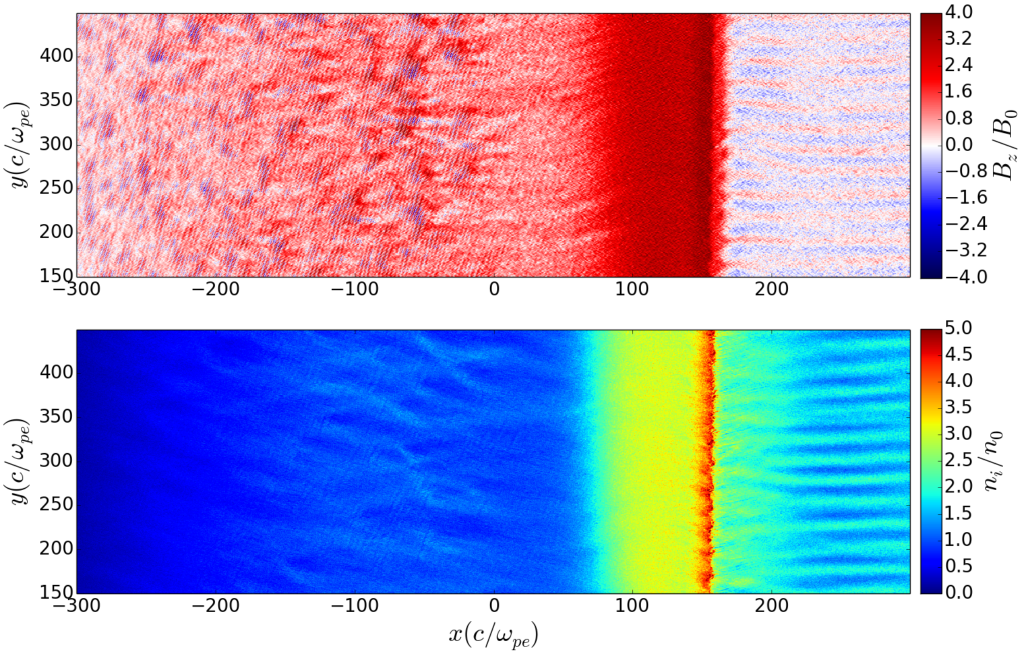

Figure 5.18 – Magnetic field (top line) and ion density (bottom line) at the time $5.4 \times 10^4 \omega_{pe1}^{-1}$ for a mass ratio of $m_i = 200 m_e$.

tion region and spatially modulates the ion density. Due to this numerical diffusion, the magnetic filaments in zone 4 are are barely above the noise. Numerical heating started to grow exponentially after $3.5 \times 10^4 \omega_{pe1}^{-1}$. Since the numerical diffusion is far from region 3, the simulation results are still representative. However, the simulation cannot be further continued, Plasma 1 would be completely disturbed by its own numerical turbulence making all the physical interpretation unfounded.

A shock is formed at the contact layer between zones 1 and 3 at $x = 80c.\omega_{pe1}^{-1}$. This shock can be identified as the reverse shock. The ions from Plasma 1 have an initial Larmor radius of $r_i \simeq 225c.\omega_{pe1}^{-1}$, however, after entering in the compressed region, the latter becomes $\simeq 75c.\omega_{pe1}^{-1}$ which is narrower than the width of zone 3. The ions of Plasma 1 are so now magnetized and slowed down in the downstream region (initially zone 3). The ion density is compressed by a factor 3 in the downstream region, as well as the magnetic field. Furthermore, as the reverse shock is mediated by Plasma 1, only a small fraction of hot ions from Plasma 2 penetrate the downstream reverse shock region as demonstrated in figure 5.19.

Most of the ions from Plasma 1 are slowed down by a factor ∼ 2.6 in the downstream region of the shock (zone 3). The ions from Plasma 1 which have passed the discontinuity region 3-4 before the shock formation, continue to propagate into Plasma 2 as a beam. The latter, continues to generate Weibel magnetic filaments (zone 4 continues to expand with the remnant beam of Plasma 1). The ramp width of the reverse shock is estimated to be $\sim 300\mu m \simeq 4c/\omega_{pi}$, and a population reflected by the ramp potential starts to appear at $x \sim 50c\omega_{pe1}^{-1}$ and propagate upstream (in zone 1).

The ion density peak (∼ 4) in figure 5.18 corresponds to a shock formed by the ions from Plasma 2. This shock can be identified as the forward shock. The mean speed of the ions of Plasma 2 in front of this shock is $\sim v_i/2.5$. This forward shock at the discontinuity between zones 3 and 4 has a narrow downstream region length $\simeq 20c/\omega_{pe1}$ at $5.4 \times 10^4 \omega_{pe1}^{-1}$ and is only composed of ions from Plasma 2 which have decelerated when crossing the ramp. The ramp width of the forward shock is estimated to be $\simeq 15c/\omega_{pe1} \simeq c/\omega_{pi}$, and the ions of Plasma 2 (in zone 4) are heated when they cross the shock ramp. Furthemore, a large ion population is reflected upstream (in zone 4) by

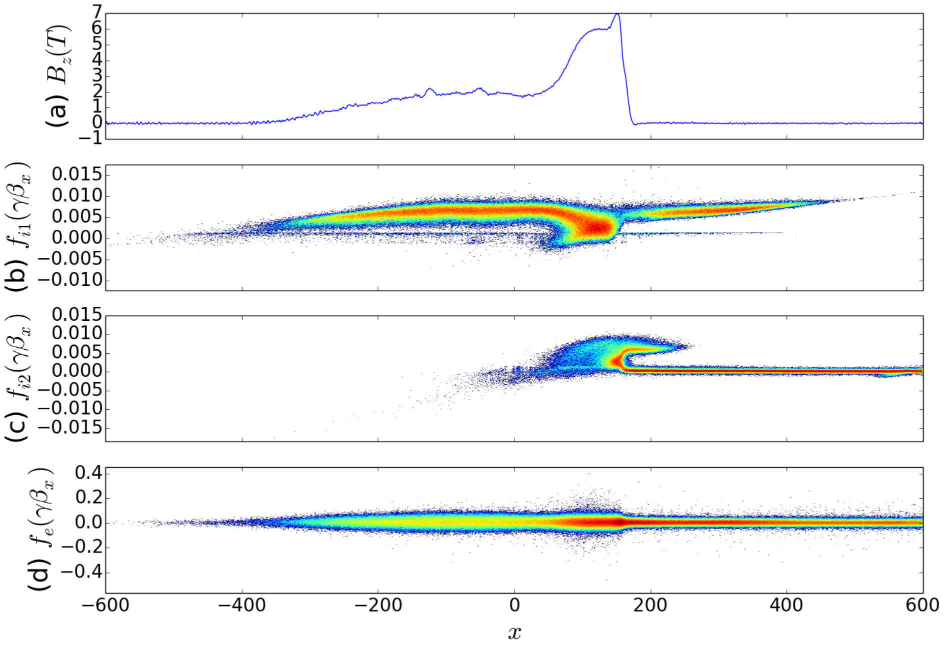

Figure 5.19 – Magnetic field spatial distribution (a) and the phase space of ions (b) and electrons (c) at the initial time at $t = 5.4 \times 10^4 \omega_{pe1}^{-1}$, for R = 1.

the potential of the ramp as demonstrated in figure 5.19, and moves at a speed slightly lower than the initial speed of Plasma 1 $v_i \sim 6. \times 10^3 \mathrm{km.s}^{-1} \sim \mathrm{v_i}/1.1$.

The electrons are heated approximately by a factor 3 in the downstream region of the reverse shock, due to the adiabatic compression of the magnetic field. The electrons in zone 4 are mostly isotropized due to the electron instabilities (two-stream instability, ...) as discussed before.

The shocks propagation (forward and reverse) is illustrated in figure 5.20 showing the time evolution of the magnetic field amplitude and ion density averaged over the transverse coordinate.

It is now important to clarify the nature of these shocks, which can be electrostatic, magnetized, or electromagnetic.

**Characterization of the reverse shock.**

The reverse shock is launched close to the initial discontinuity between zones 3 and 4 (which will become the forward shock) which moves at $u_{sh-f} \sim v_i/2.275$. Due to the motion of the discontinuity between zones 3 and 4, the downstream region of the reverse shock expands to the right in the laboratory frame of reference at $u_{sh-r} \sim v_i/13$ (dotted line), but in the discontinuity 3-4 frame of reference, the reverse shock moves to the left, in the opposite direction of the upstream plasma, Plasma 1, at $|v_i/13 - v_i/2.275| \sim v_i/2.75$. In the reverse shock frame of reference, the upstream velocity (plasma 1) $v_\mathrm{I} = v_i - u_{sh-r} \sim v_i/1.08$ and the downstream fluid velocity $v_\mathrm{II} = v_i/2.6 - u_{sh-r} \sim v_i/3.25$. Combining the jump velocity with the magnetic field and ion density jumps, $\frac{v_\mathrm{I}}{v_\mathrm{II}} = \frac{\mathrm{B_{II}}}{\mathrm{B_I}} = \frac{\rho_\mathrm{II}}{\rho_\mathrm{I}} = r \approx 3$, the Rankine-Hugoniot conditions are fulfilled. A necessary condition for being a shock is to satisfy the Rankine-Hugoniot relations, and this is the case at least semi-quantitatively, the magnetic field, density and velocity jumps are approximately of 3 between the zones 1 and 3. But this is not sufficient. One need also to demonstrate the entropy dissipation. Ideal plasma evolution including compression can generate structures such as solitary waves with adiabatic heating. But adiabatic heating is a reversible process. The required condition for a shock formation is entropy production which is an irreversible process. It can be often in the form of electron heating/acceleration and/or ion heating/acceleration beyond adiabatic heating due to

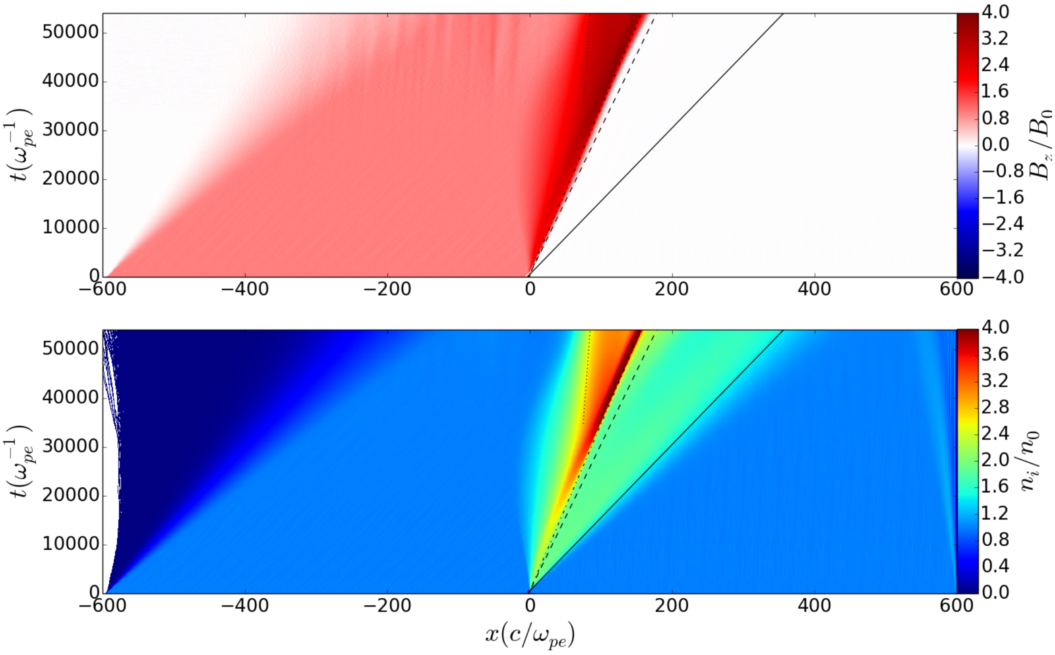

Figure 5.20 – Magnetic field (top line) and ion density (bottom line) evolution with time. The forward shock front (discontinuity between zones 3 and 4) moves at ~ $v_i/2.275$ (point-dashed line). The black line represents the intial plasma 1 velocity $v_i$, and the dashed black line the velocity of the magnetic field $v_b$ due to the adiabatic compression. The magnetic diffusion increase the initial smooth transition 1-3 which move from the left to right at ~ $v_i/6$.

compression. This is the case for this reverse shock, where the upstream ions are heated downstream by a factor ~ 1.7. The reverse shock is thus purely MHD and is a strong shock since in 2D, $r \approx 3$ corresponds to $M_I \longrightarrow \infty$, .

**Characterization of the forward shock**.

The density jump between zones 3 and 4 is $\rho_{II}/\rho_I \sim 2.6$, since the downstream ion density is ~ 4 and is only of ~ 1.5 in the upstream region due to the compression of the ions from Plasma 1 (reverse shock). The upstream ions (zone 4) are slowed down in the forward shock frame of reference to $v_{II} \sim u_{sh-f} - v_d = v_i/25$, where $v_d = v_i/2.5$ is the velocity of the ions in the downstream region of the forward shock in the laboratory frame of reference. The upstream ions of zone 4 are composed of ions from Plasma 2 at rest (~ 66%) and a fraction of reflected ions of Plasma 2 and ions from Plasma 1 (~ 33%), both propagating at ≈ $v_i/1.1$. The upstream velocity in the shock frame of reference can thus be established as $u_{sh-f} + 0.5(u_{sh-f} - v_i/1.1) = v_i/10$, where the factor 0.5 represents the density proportion of the reflected ions from Plasma 2 and the ions from Plasma 1 in upstream region, zone 4. The velocity jump can be estimated as $r = v_I/v_{II} \sim 2.5$ in agreement with the density jump. The ions are heated in the downstream region, reaching a temperature of 40 eV (4 times more than their initial temperature). Furthemore, some of these ions propagating in the downtream region of the reverse shock (connected to the downstream region of the forward shock) are strongly heated and reach the temperature equilibrium in this region (heating by a factor 17). The forward shock has a downstream region with a magnetic field ~ $4B_0$, and an upstream region dominated by the Weibel instability (two polarities, so in average $B = 0$). The shock is not MHD since the magnetic field jump is considered infinite, however the Rankine-Hugoniot relations (hydrodynamic) are satisfied at least semi-quantitatively.

The forward shock can thus be electrostatic or electromagnetic. Even if magnetic filaments are generated upstream, is it sufficient to claim that this shock is mediated by the Weibel instability, and thus that it is an electromagnetic shock ? Moderately supersonic flows may develop laminar electrostatic shocks instead of turbulent Weibel-mediated shocks.

Electrostatic shocks are mediated by the ambipolar electric field set up by the electron across a plasma (pressure) discontinuity (cf. Chapter 3). These shocks are stable in a certain range of Mach numbers. For sub-critical shock the limitation is found to be $\mathrm{M}_s \sim 3$ (Dieckmann et al., 2013), under the assumption that the electron temperature $\mathrm{T}_e$ exceeds by far the ion temperature $\mathrm{T}_i$ and that the particle velocity distributions are Maxwellian far upstream of the shock. Sub-critical shocks can convert the entire kinetic energy of the inflowing upstream plasma into heat, while the shock-reflected ion beam of super-critical shocks provides an additional energy dissipation mechanism and such shocks are stable at larger Mach numbers, $\mathrm{M}_s \sim 6.5$, than the sub-critical shocks. No stable electrostatic shocks exist under these approximations above a value $\mathrm{M}_s > 6.5$. However, an asymmetry between the colliding plasma clouds in terms of the electron temperature and density yields a double layer that can raise the maximum value of $\mathrm{M}_s$ (Sorasio et al., 2006), which is confirmed by many observations of collisionless shock waves with Mach numbers ranging between 10 and $10^3$.

In our simulation, the Mach number of the forward shock is found to be $\mathrm{M}_f = u_{sh-f}/c_s \sim 1.3$ and it is super-critical $v_d/c_{s-d} > 1$, where $c_{s-d} = v_i/3$ is the ion acoustic speed in the downstream shock region. The Mach number is thus low enough to stabilize an electrostatic shock. The super-criticality of the shock is in agreement with presence of the shock reflected ion beam shown in figure 5.19. However, this structure is also possible in electromagnetic shocks. As explained in the introduction of this Chapter, the electrostatic shock (ES) can be transformed in an electromagnetic shock (EM) when the Weibel modes time scale $t_\mathrm{W}$ starts to be equivalent to the ES formation time scale $t_{sf}$ (cf. 5.1). Furthermore, the low temperature of our flow $k_\mathrm{B}\mathrm{T}_e/m_e c^2 \sim 2\times10^{-4}$ for a drift speed of $v_i = 6.66\times10^{-3}$ puts our simulation in the configuration of a pure EM shock according to figure 5.1.

Electromagnetic shocks are mediated by the Weibel instability growing due to a strong temperature anisotropy between two interpenetrating plasmas defined as

$$a_i = \frac{m_i v_{ix}^2 + \mathrm{T}_{ix}}{\mathrm{T}_{i\perp}} - 1. \tag{5.33}$$

During the nonlinear saturation of the instability, the particles are isotropized due to the turbulent magnetic field and are accumulated in the overlap downstream region until the hydrodynamic-like jumps conditions of a stationnary shock wave are established. This consideration means that the initial anisotropy of the plasma leading to the Weibel instability must drop to approximately $a_i \sim 0$ in the downstream shock region. The plasma anisotropy can be estimated from the ion phase space in figure 5.21.

The anisotropy in the shock region at $t = 3.75\times10^4\omega_{pe1}^{-1}$ is $\sim 30$ and decreases to $\sim 5$ at $t = 5.4\times10^4\omega_{pe1}^{-1}$. This plasma isotropization is underlying signature of turbulent Weibel-mediated shocks. Electrostatic shocks are characterized by laminar deceleration/reflection of the incoming ions and they do not lead to diffusive particle acceleration. Even if the anisotropy is not close to 0, its strong decrease indicates formation of an electromagnetic shock.

The ion isotropization length defined as the length necessary for the Weibel-mediate shock formation has been estimated by (Spitkovsky, 2008a) as $\mathrm{L}_{iso} \sim 100c.\omega_{pi}^{-1} \propto m_i^{1/2}$, and by (Lyubarsky and Eichler, 2006) as $\mathrm{L}_{iso} \sim (m_i/m_e)^2 c.\omega_{pi}^{-1} \propto m_i^2$, in the relativistic regime. A global model (non / relativistic) proposed by (Ruyer et al., 2016) under the condition $\mathrm{T}_e << \mathrm{T}_i$. (Ruyer et al., 2016) finds that ion isotropization corresponds to $\mathrm{T}_i \simeq m_i v_i^2/2$, leading to a magnetic wavelength of $\lambda \sim 4\pi c.\omega_{pi}^{-1}$, and to an isotropization distance of $\mathrm{L}_{iso} \simeq 35\left(\frac{m_i}{\mathrm{Z}_i m_e}\right)^{0.4} c.\omega_{pi}^{-1}$. Considering the parameters of our simulation (protons with a reduced mass $m_i = 200m_e$), this length is found to be $\mathrm{L}_{iso} > 4000c.\omega_{pe}^{-1}$ which is 10 times larger than our simulation box. However, this isotropisation length has been estimated in a configuration of two counter-propagating ion beams without any external magnetic field.

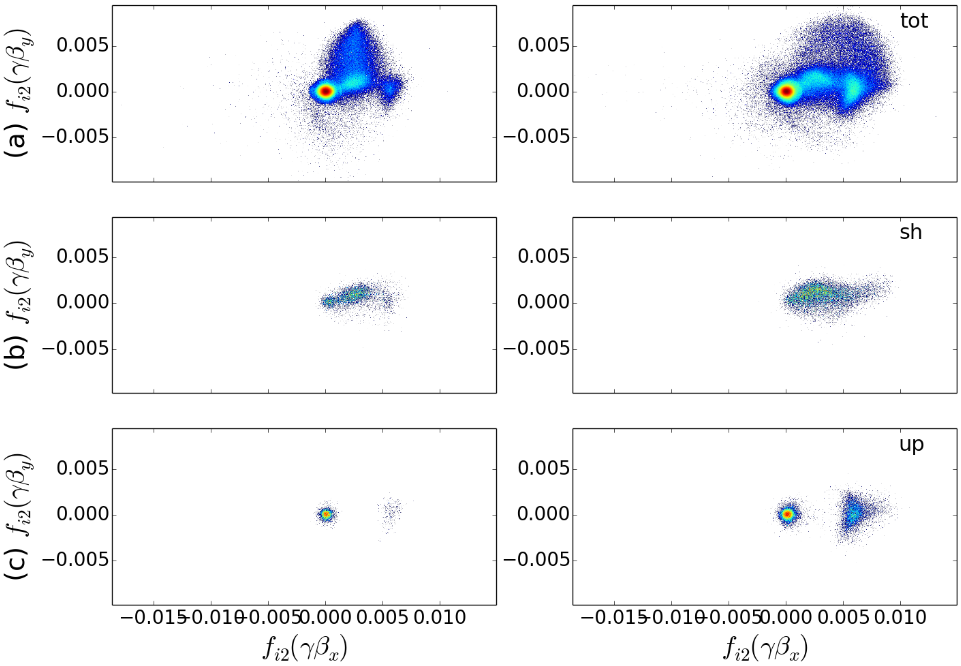

Figure 5.21 – Ion phase space from Plasma 2 at $t = 3.75\times10^4\omega_{pe1}^{-1}$ (left) and $t = 5.4\times10^4\omega_{pe1}^{-1}$ (right) integrated over the whole simulation box (top), in the downstream region of the shock (middle) and in the upstream region (bottom).

Similar simulations than those presented above but with unmagnetized electrons in Plasma 1 have been performed in order to confirm that in a symmetric configuration of magnetic field (so $B_z = 0$ everywhere at $t = 0$), no shocks have been formed on such time/space scales. Indeed, the Weibel instability is well formed and reaches its nonlinear saturation, but no shock is formed after $400c\omega_{pe}^{-1}$ of propagation as demonstrated in figure 5.22.

Our results lead to think that the configuration with an external magnetic field accelerates the isotropization of the ions and lead to a shock formation on smaller time and space scales. Two factors are able to explain the accelerated shock formation. First, the ions propagating in Plasma 1 (magnetized) carry a convected electric field $E_y = v_i B_0$. The ions from plasmas 1 and 2, when penetrating the compressed region, zone 3 (magnetic piston), are accelerated oppositely in the transverse direction according to

$$\frac{dv_{2,y}}{dt} = \frac{e}{m_i} v_i B_0 \tag{5.34a}$$

$$\frac{dv_{1,y}}{dt} = -\frac{e}{m_i} v_i B_0. \tag{5.34b}$$

These two opposite flows in the transverse direction are a seed for excitation of two-stream magnetosonic instabilities, inducing a slowing down of the fast ions, helping to generate of the shock. Furthermore, the electrons which stabilize the ion Weibel instability, are magnetized and produce a smaller current than those of equation (5.27). The electron susceptibility can be written as

$$\chi_e = i\sqrt{\frac{\pi}{2}}\frac{\omega_{pe}^2}{\omega_{ce}^2}, \tag{5.36}$$

and if $\omega_{ce} > \omega k_y v_{Te}$, the growth rate is greater and shifts of unstable wavelengths to $k_y \sim \omega_{pi}/c$ (Ryutov et al., 2014). These two effects are possible explanations to the acceleration of the shock formation process.

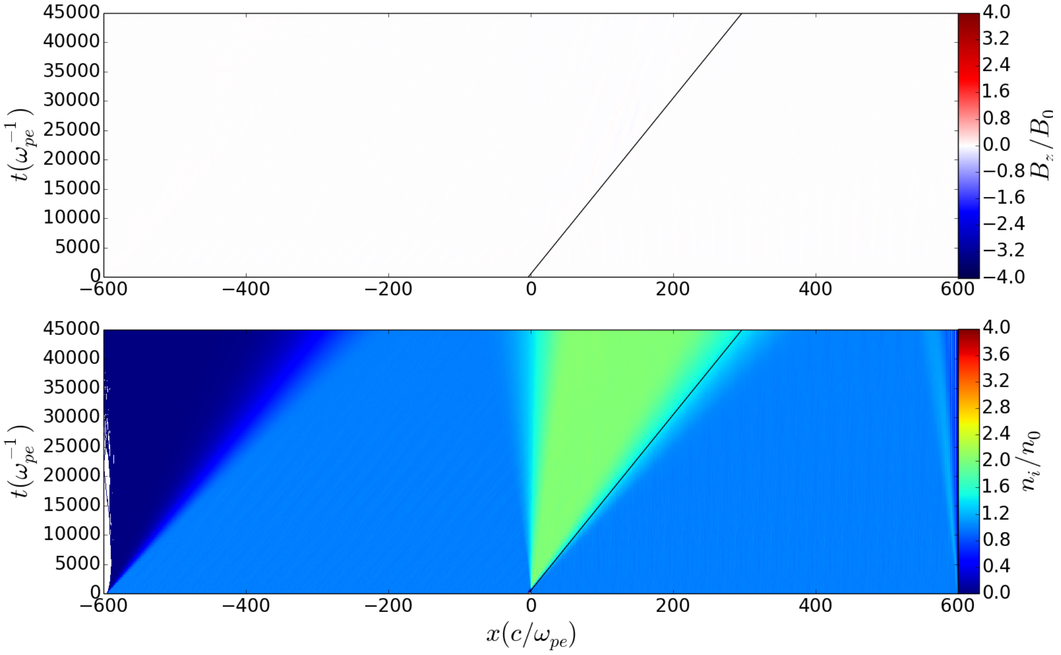

Figure 5.22 – Magnetic field (top line) and ion density (bottom line) evolution with time for two unmagnetized counterstreaming flow. The ion to electron mass ratio is $m_i = 200 m_e$. The black line represents the intial Plasma 1 velocity $v_i$.

The particularity of electromagnetic shocks is their efficiency to accelerate particles via the first order Fermi mechanism. If the forward shock is indeed of electromagnetic nature it must be able to accelerate a small fraction of the particles.

### 5.2.7 Test particles acceleration by the Fermi mechanism

Collisionless shock waves represent the final result of collective interactions involving particles and electromagnetic fields. This process cannot be described by test particle motion in prescribed fields. Test particle approach can however be applied for studies of motion of a small numbers of particles in a strongly nonlinear structure. This is used in the shock theory of charged particle acceleration which will be the subject of this last subsection.

The PICLS code possesses a particle tracking diagnostic which records the macro-particle positions and momenta at various timesteps and allows plotting particle trajectories. The simulations discussed above were equipped with particle tracking for all species (ion of Plasma 1, ions of Plasma 2, and electron). Various particle trajectories can be seen in figure 5.23.

The electrons from Plasma 1 rotate at the cyclotron frequency, and increase their gyration speed during the adiabatic compression and later when crossing the MHD reverse shock ramp. The ions from Plasma 1 perform a gyration on much larger time scales, and finally are decelerated in the downstream shock region, however, the ions from Plasma 1 which have been separated from their magnetized electrons, freely propagate through Plasma 2 without any additional momentum transfer ($p_x$ to $p_y$).

The particles are accelerated, and our goal is to understand if the aforementioned Fermi mechanism operates.

**Fermi acceleration**

(Fermi, 1949) discussed the origin of the Cosmic Rays CRs and proposed a mechanism of acceleration of charged particles based on their interaction with magnetic clouds in the ISM. If a particle

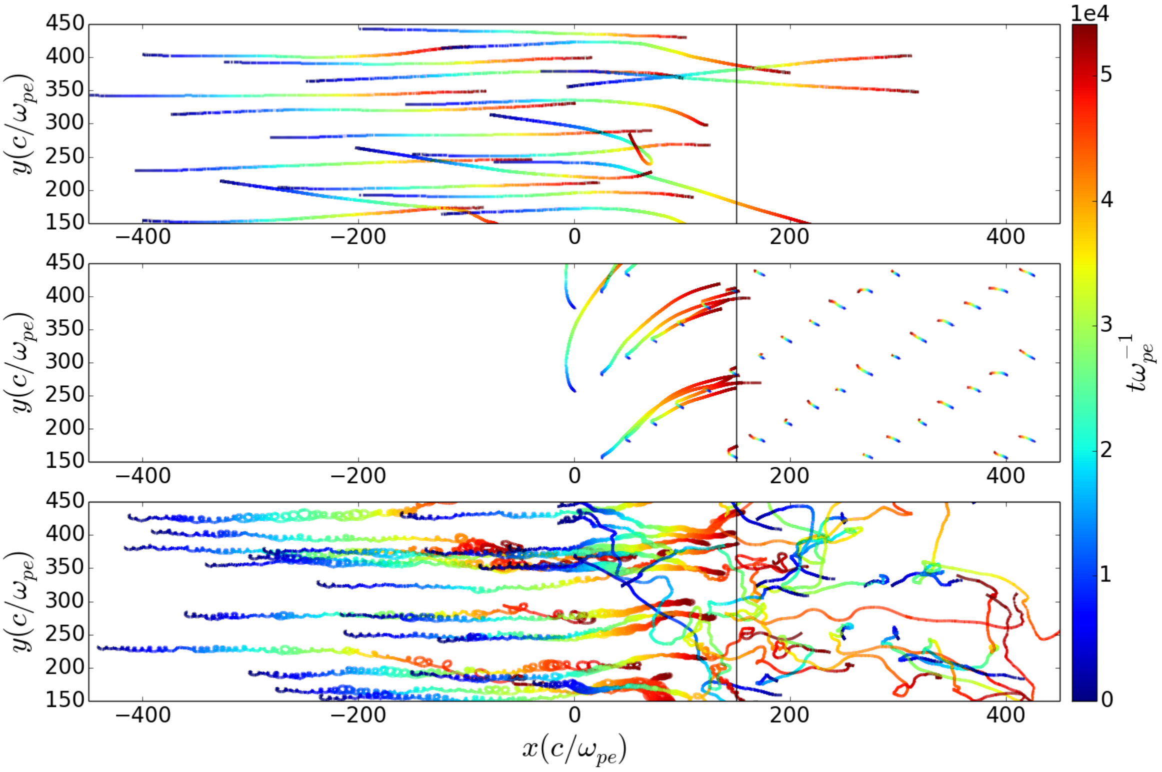

Figure 5.23 – Tracking particle trajectories (top: ion 1, middle: ion 2, bottom: electron).

penetrates a cloud with an energy $E_1$ and an angle $\theta_1$ measured in the Galactic frame of reference and escapes from this cloud with the energy $E'_2$ and the angle $\theta'_2$ measured in the cloud frame of reference, the change of reference frame can lead to

$$E'_1 = \gamma E_1(1-\beta\cos\theta_1) \tag{5.37a}$$

$$E_2 = \gamma E'_2(1+\beta\cos\theta'_2), \tag{5.37b}$$

where $\gamma$ and $\beta$ are respectively the Lorentz factor and the reduced velocity of the particle. The energy variation is thus

$$\frac{\Delta E}{E} = \gamma[\beta(\cos\theta'_2 - \cos\theta_1) + \beta(1-\cos\theta'_2\cos\theta_1)]. \tag{5.39}$$

and the average energy variation calculated on all the possible angles of penetration and extraction can be written as

$$\left\langle \frac{\Delta E}{E} \right\rangle = \frac{4}{3}\gamma\beta^2. \tag{5.40}$$

This equation presents the so-called second order Fermi acceleration mechanism, since the growth of the particle energy is $\propto \beta^2$. This acceleration is stochastic since only a small fraction of particles increases its energy. One particle can lose or gain energy in interaction with a cloud.. If the collision is frontal (particle and cloud propagate in opposite directions in the Galactic frame of reference), the particle will increase its energy. If the collision is leaking (particle and cloud propagate in the same directions at different velocities in the Galactic frame of reference), the particle will lose energy. On average the total energy of the particle grows since frontal collisions occur more often than leaking ones. However, this mechanism has some limitations, and is not able to explain the origin of the CRs. The most important problem of this mechanism is the 'injection'. At low energy, the particles propagate in the ISM and lose energy during Coulombian interaction. If the collision frequency between particles and clouds is too low, the energy gain by the second order Fermi mechanism cannot compensate the losses from the Coulombian interactions between two collisions. This is why Fermi proposed to injected very energetic particles (during solar flares, as an example), in order to not be affected by the coulombian losses, but such source of very large energy particles is not yet found.

Due to these problems of injection and a very long acceleration time by the second order Fermi mechanism, (Bell, 1978; Blandford and Eichler, 1987) have proposed a new particle acceleration process via shock waves, known as the first order Fermi mechanism. The main idea of this mechanism is that in each part of the shock front, inhomogeneous magnetic fields are able to deflect particles as in the second order mechanism and to isotropize their distribution. Each time, when a particle crosses the shock front, it penetrates in a new medium with a different velocity acting like a magnetic cloud. However, on contrary to the second order process, here the cloud has only one direction (the shock propagation), oriented toward the particle.

When a particle crosses the shock ramp upstream-downstream, the particle energy $E_1$ in the upstream frame of reference has become $E_1'$ in the downstream frame of reference regarding to equation (5.37). The particle is scattered in the downstream region and returns back in the upstream. The change of reference frame modifies the particle energy, passing from $E_1' = E_2'$ to $E_2$, as in equation (5.37) with however $\beta = \Delta v / c$, representing the reduced drift velocity between the two mediums. The energy variation is again dictated by equation (5.39), and the average energy gain is obtained by averaging on all the crossing angles $\theta_1$ (upstream-downstream) and $\theta_2$ (downstream-upstream). The net growth in energy for one cycle upstream-downstream-upstream can be written as

$$\langle \Delta E \rangle = \frac{4}{3} \beta E. \tag{5.41}$$

This acceleration is of the first order ($\propto \beta$), and depends of the shock velocity. Equation (5.41) can be written as

$$\langle \Delta E \rangle = \frac{4}{3} \frac{r-1}{r} E \frac{u_{sh}}{c}, \tag{5.42}$$

if the upstream region does not move in the laboratory frame of reference ($v_I = u_{sh}$), with $r$ the shock jump parameter.

A spectrum of the accelerated particles can be obtained (Spitkovsky, 2008b; Sironi and Spitkovsky, 2011a,b; Caprioli and Spitkovsky, 2014). For an initial number of particles $N_0$ with an energy of $E_0$, the spectrum of the accelerated particles can be written as

$$\frac{dN}{dE} = (x-1) \frac{N_0}{E_0} \left( \frac{E}{E_0} \right)^{-x}, \tag{5.43}$$

with $x = (r+2)/(r-1)$. The spectrum depends only of the compression ratio $r$, and do not depend of the shock speed, if the shock is strong ($M_I > 20$). This process also referred to as the Diffusive Shock Acceleration process (DSA), it is considerably more efficient than the second order Fermi mechanism. Due to its dependence in $\propto \beta$ and not in $\propto \beta^2$, the acceleration time of a particle is strongly reduced, which also helps to reduce considerably the problem of injection (Caprioli et al., 2015). Indeed, the injection problem consists now in finding a source particles whose radius of gyration is higher than the thickness of the shock, in order that the latter is effectively seen as a discontinuity. The DSA process has been observed around interplanetary shockwaves (like the Earth bow shock). Many space probes have thus been able to measure sudden increase in the density of energetic particles at crossing of such a shock. However, spectra of shock-accelerated particles have never been observed in laboratory experiments yet.
f

The spectra of electrons and ions obtained in our numerical simulation are shown in figure 5.24. The electron spectrum spreads out during the interaction time. The electron temperature grows from 100eV to ~ 2keV in the downstream region of the forward shock. The ions from Plasma

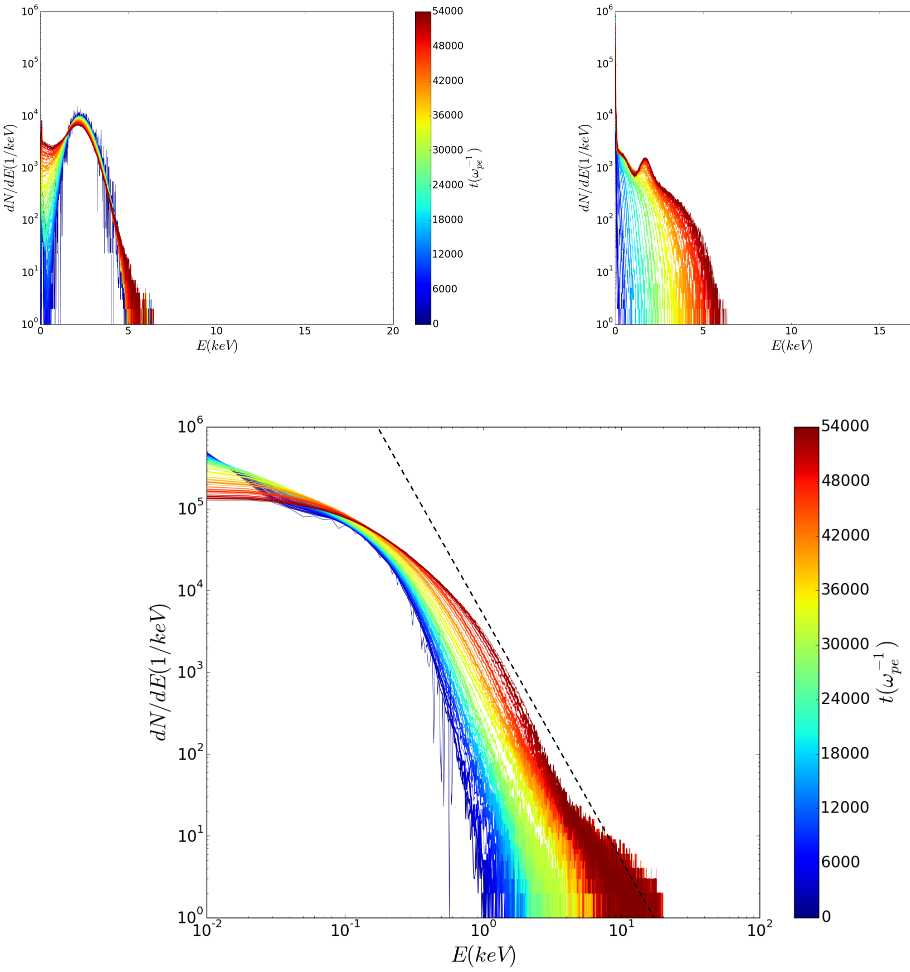

Figure 5.24 – Time evolution of the spectra of the particles in the whole simulation box (top left: ions from Plasma 1, top right: ions from Plasma 2, bottom: electrons). The black line on the bottom panel represents the spectrum from equation (5.43) for r=2.5.

2 are heated and get momentum from the Plasma 1 ions which are decelerated. A long suprathermal tail appears in the electron spectrum demonstrating an efficient acceleration via the first order mechanism. Some electrons reach energy of 20keV. The theoretical prediction of the non-thermal electron distribution by the first order Fermi mechanism for a density jump of r=2.5, from equation (5.43), is in good agreement with the electron spectrum in our simulation.

**Experimental electron spectrum**

Collisionless slowing down and reflection of the incoming ions require the ion Larmor radius to be comparable to, or smaller than the shock front width. The corresponding magnetic field (~ 150kG in our case) is much higher than the compressed Biermann field in laboratory experiments. Previous laboratory experiments (Romagnani et al., 2008; Kuramitsu et al., 2011; Niemann et al., 2014; Schaeffer et al., 2017a), including those using a laser-driven plasma flow (piston) to compress pre-existing magnetic fields in a magnetized background plasma (Niemann et al., 2014; Schaeffer et al., 2017a), led to the generation of magnetized shocks, which can be assimilated to the Earth's bow shock but have a limited interest to astrophysics. First, the laminar cross-shock potential generated by steady-state shock compression is not sufficient to decelerate and reflect the incoming ions with high Mach numbers. Second and most importantly, such magnetized shocks cannot accelerate particles due to a homogeneous distribution of the normal component of the electric field along the shock front. In contrast with previous experiments, the ion Weibel instability plays an essential role in our experiments for, as shown in figures 5.8 and 5.9, magnetic field amplification, turbulence generation and nonlinear collective wave-particle interactions. First, the compressed magnetic field amplifies the Weibel filaments to high amplitudes as the jet's free kinetic energy is converted to field energy, which is essential for forming a supercritical shock with a high value of $M_A$. Second, an inhomogeneous distribution of the magnetic field along the shock front provided by the Weibel filaments results in the generation of an inhomogeneous normal electric field. Such an inhomogeneous electric field provides a mechanism for multiple reflection of particles back and forth through the shock (between downstream and upstream), allowing particles to continuously gain kinetic energy. This is the fundamental feature of first-order Fermi acceleration by an electromagnetic collisionless shock.

The electron energy distributions measured in experiments with or without gasbags in figure 5.25 a.

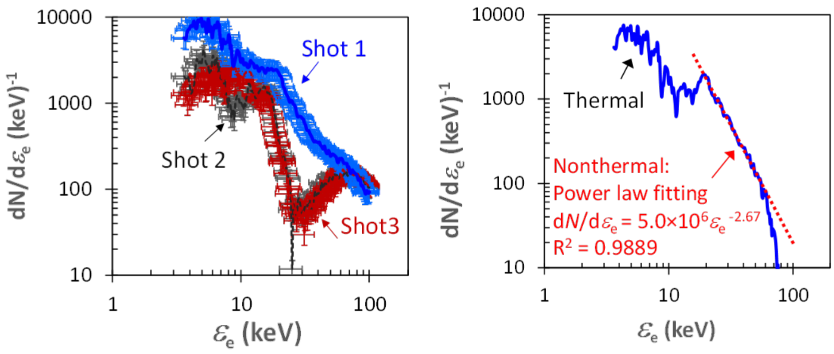

Figure 5.25 – (Left panel) Electron spectra measured at a direction perpendicular to the jet propagation with (Shot 1) and without (Shots 2 and 3) gasbags. The latter serve as null shots providing the backgrounds due to laser-plasma interaction without shocks. Error ±28% in electron number is due to the uncertainty of the imaging plate response calibration. Error ±20% in electron energy is from the uncertainties of field measurement and gyroradius estimate. (Right panel) After subtracting the average backgrounds, the electron spectrum shows a structure of two components, a thermal component with T ≈ 2keV, and a nonthermal component fitted with a power-law distribution. (Li et al., 2019)

A significant difference can be seen in the electron energy range $\epsilon_e \sim 15-60keV$. After subtracting the background, the electron spectrum in Fig.5.25 b shows a two-component structure: a thermal component and a fast electron tail component. The thermal part corresponding to a temperature $T_e \sim 2$keV shows that a significant part of the incoming ion kinetic energy $\epsilon_i = 0.5 m_i v_0^2 = 10-12$keV (with $v_0 = 1000-1500$km.s$^{-1}$) is dissipated and converted into electron thermal energy. The nonthermal part contains ~ 20% of the total electron population with an effective temperature $T_h \sim 20$keV. These hot electrons are produced in the shock via the first-order Fermi acceleration mechanism ($\propto u_{sh}/c$) or through interactions with magnetic field fluctuations, providing an efficient and irreversible shock entropy dissipation. The significantly higher electron energy ($\epsilon_e >> 1\mathrm{keV}$) excludes acceleration by a lower-hybrid wave turbulence (Rigby et al., 2018), because this mechanism can only accelerate electrons to a lower average energy ($\epsilon_e \leq 1\mathrm{keV}$) in our experimental conditions. A more detailed analysis of the energy distribution in the electron tail shows that it can be conveniently fitted by a non-thermal power law $d\mathrm{N}(\mathrm{E}_e)/d\mathrm{E}_e \propto \mathrm{E}_e^{-x} \simeq 5\times10^6\mathrm{E}_e^{-2.67}$. For the estimated jump parameter in our experiment $r \simeq 3$, the $x$ parameter from equation (5.43) is $x = (r+2)/(r-1) = 2.5$, which is comparable to the one measured in the experiment $x = 2.67$. Consequently, the obtained electron energy distribution offers a compelling experimental evidence that electromagnetic collisionless shocks are generated. During the process of shock formation, a significant fraction of the incoming-flow kinetic energy is converted to ion and electron thermal energy, and to electron acceleration mediated by strong, fluctuating, and quasi-static magnetic fields.

### 5.2.8 Conclusion

In this study we succeeded to generate high-Alfvénic-Mach-number, nonrelativistic electromagnetic collisionless shocks mediated by the ion Weibel instability in a laboratory by colliding two initially unmagnetized plasmas. The Biermann battery magnetic field generated in the jet by the exploding shell creates conditions for a faster shock formation. We showed that penetration of a plasma with magnetized electrons in another unmagnetized plasma leads to formation of a magnetic piston on electron time scales. This piston is characterized by electron compression and heating and it propagates slower than the ion front with a velocity depending on the density ratio between the two plasmas. This process allows excitation of the ion Weibel instability in the upstream region and the generation of magnetic fluctuations. Formation and evolution of the adiabatically compressed magnetic piston is demonstrated in 1D and 2D kinetic simulations. The instability generated spontaneous magnetic turbulence, regular magnetic fields, and nonlinear wave-particle interactions providing collisionless (non-Coulombian) mechanisms essential to both shock generation and energy dissipation. This study is a first hint of particle acceleration by the Fermi mechanism, and other campaigns will be important to validate these observations. This work advances our knowledge of collisionless astrophysical shocks in nonrelativistic regimes, such as in supernova remnants. Furthermore, this work provides a roadmap for studying shock physics in relativistic regimes, such as in the afterglow of cosmological $\gamma$-ray bursts, demonstrating that laser-matter interaction offers a powerful platform for quantitatively exploring collisionless shocks in a broader context.

# Chapter 6

# Collisionless plasma interpenetration in a strong magnetic field for laboratory astrophysics experiments

The last section of this thesis is dedicated to an experimental proposal which has been submitted in September 2018 for the LULI2000 laser facility, as a scaled preparatory experiment for a future experimental proposal for the LMJ laser facility. The goal of these experiments is to study collisionless sub-relativistic magnetized shocks driven by the interaction of two counter streaming fast (~ 1000km/s) plasma flows, generated by laser, and immersed in an external magnetic field leading to high plasma magnetization and high temperatures.

The magnetic field penetration into the plasma has the effect of modifying the process of shock formation according to its magnetic geometry, which depends on whether the angle the shock normal makes with the background magnetic field is larger (quasi-perpendicular) or smaller (quasi-parallel) than 45°. In particular, quasi-perpendicular shocks are the result of the non-linear steepening of a magnetosonic fast wave mode, which is characterized by its magnetosonic speed $c_{ms}$ (cf. Chapter 4). The class of supercritical ($\mathrm{M_A} \geq 3$) quasi-perpendicular magnetized collisionless shocks are of particular importance, since the dissipation mechanism of these shocks is dominated by the reflection of ions back into the upstream region (cf. Chapter 4). This process is thought to seed mechanisms (Goldenbaum, 1967) that can accelerate particles to extremely high energies (Lembege et al., 2004).

As discussed in the Introduction and in Chapter 4, collisionless magnetized shocks are ubiquitous in Space (cf Figure 3). They cover a broad range of astrophysical phenomena from the sub-relativistic regime with the solar wind, to the extremely relativistic regime with pulsar wind nebulae. Supercritical shocks have been well studied in the heliosphere within the limitations of spacecraft measurements. However, in systems such as supernovae, where remote sensing has provided compelling evidence of particle acceleration attributed to shocks, observations are too distant and too slow to resolve structural and temporal details of the shocks themselves. Consequently, laboratory experiments can complement spacecraft and remote sensing observations by providing highly resolved, reproducible, multi-dimensional datasets.

The formation of relativistic shocks is extremely difficult to conduct in experiments, since they require hot plasmas with relativistic speeds, formed by laser energy deposition on solid targets. These plasmas are for now impossible to produce due to the limitations of the current laser facilities. The sub-relativistic regime requires less laser energy and can be reached by many different laser facilities all over the world. Experiments on collisionless magnetized shocks have already been conducted in the sub-relativistic regime, with applications to supernova remnant shocks. In 2004, results from an experimental study of the collisionless interaction of two laser-produced plasmas in a magnetic field were presented (Courtois et al., 2004) using 1ns, 300J and $\mathrm{I} = 4 \times 10^{16} \mathrm{W/cm^2}$ laser beams. The dynamics of the two plasmas and their interaction were studied with and without magnetic field through spatially and temporally resolved measurements of the electron density. Experimental results showed that counter-propagating collisionless plasmas interpenetrated when no magnetic field is present. In contrast, results obtained with the addition of a 7.5T magnetic field perpendicular to plasma flow showed some steepening of the density profile with localized increases inside the interaction area that only occurred when the field is present. After an experimental study of subcritical laboratory magnetized collisionless shocks using a laser-driven magnetic piston (Schaeffer et al., 2015), Schaeffer et al. obtained evidence for the first laboratory generation of high-Mach number, magnetized collisionless shocks through the interaction of an expanding laser-driven plasma with a magnetized ambient plasma (Schaeffer et al., 2017a,b). The velocities involved were of the order of 700km.s$^{-1}$, the ambient plasma electron density was around $0.5 \times 10^{19}$cm$^{-3}$, and the ambient plasma temperature was around 15eV. The magnetization in these experiments (Courtois et al., 2004; Schaeffer et al., 2017a,b) was $\sigma \sim 3 \times 10^{-3}$.

The following proposed experiment is built on the scheme proposed in (Huntington et al., 2013) and discussed in the introduction of this section (cf. 5.2). Two ablative flows driven by high-energy nanosecond lasers collide in the center of the experimental chamber. However, compared to (Huntington et al., 2013), an external magnetic field is applied perpendicular to the direction flows. This setup is also not so far from (Schaeffer et al., 2017a,b), using an external magnetic field, but the most important difference is the significantly different electron temperature and external magnetic field levels that will be accessed. The electron temperature will be close to the one expected in SNR shocks, of the order of 100 eV to 1 keV, as estimated in our numerical simulations (see below). We propose to impose an external 10 to 40T- level magnetic field (B-field) (Albertazzi et al., 2013; Higginson et al., 2015) perpendicular to the above plasma collision, giving rise to a plasma magnetization of $\sigma \sim 10^{-1}$ much higher than (Schaeffer et al., 2015). The goal is to obtain an Alfvénic Mach number of a few tens ($M_A \simeq 10$ for a flow density $n_e \sim 10^{18}$cm$^{-3}$ and velocity $\sim$ 1000km.s$^{-1}$, see below). In this situation, PIC simulations show that instabilities distinct from the Weibel filamentation can be triggered (Korneev et al., 2014), associated with significant density and magnetic perturbations.

### 6.0.1 Experimental method and set-up

Large facilities as the NIF or the LMJ are not readily available, and each laser shot are very expensive. Scaled preparatory experiments on facilities like LULI2000 (Ecole Polytechnique, France) or Gekko XII (ILE, Japan) are so needed to access these installations in order to validate the features of the experiments. The LULI2000 and LMJ are two laser facilities of completely different scales as shown in Table 6.1 which compares the laser properties of these two installations.

| | Laser energy (J) | Pulse duration (ns) | Focal spot (µm) | Aperture |
|---|---|---|---|---|
| LMJ | $10\,10^3$ | 5 | 860 | 8.89 |
| LULI2000 | 800 | 1.5 | 500 | 4 |

Table 6.1 – Laser parameters for the LMJ and LULI2000 laser facilities

The plasma plume parameters (density, temperature, expansion speed, etc) depend of the laser properties. Indeed, an experiment on the LMJ compared to one on LULI2000 will be able to depose on the target more energy and on a longer time scale. Consequently the plasma formed on the LMJ laser facility will expand faster and will be maintained at higher temperatures on a longer time scale. However, even if the plasmas have different characteristics depending of the facility, it is possible to find some strong similarity between them.

The shock nature is defined essentially by its Mach numbers ($M_s$, $M_A$ or $M_{ms}$). These numbers possess dependence of the plasma properties, and if similar Mach numbers can be found between both experiments, it will be possible to scale them. An important parameter will be the magnetic field and its generation has some experimental constraints. The technique used for its creation will depend of the facility used.

### Setup and magnetic field generation in the LULI2000 experiment

The creation of plasmas with a high magnetization level in experiments relies in most cases on the generation of an external magnetic field.
The experiment will be carried out at the LULI2000 laser facility operating in the nano2000 configuration ("salle 2" of the facility). It will require the use of the following beams

- the North Beam, 800 J in 1.5 ns at 1 ω (1053 nm)
- the South Beam, 800 J in 1.5 ns at 1 ω (1053 nm)
- the Blue Beam in the confguration (1), 20 J in 1.5 ns at 2 ω (~ 527 nm)

Additionally, the auxiliary laser available in the target area (CFR) will be employed at 1 ω as an optical probe. This beam is small (~3 mm in diameter) and will be sent in between the N & S beams, as shown in Figure 6.1 The experimental set-up is described in Figure 6.1.

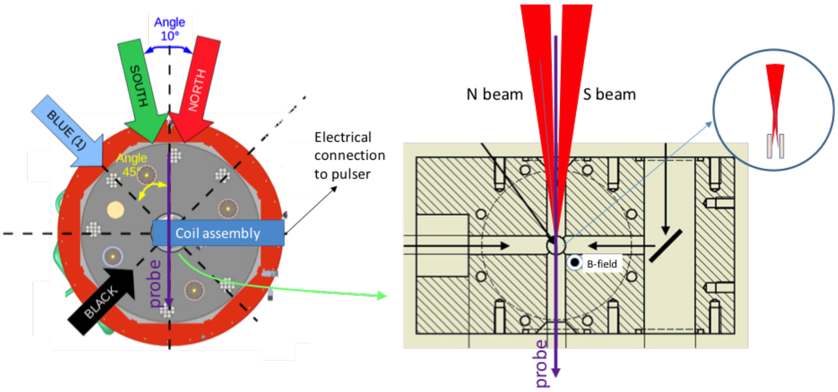

Figure 6.1 – Experimental set-up, in the nano2000 configuration ("salle 2"). on the LULI2000 laser facility. The main two beams (N & S) will come as shown and be inserted, as shown, in the coil, irradiating the two targets. The small probe beam will run in between the two main beams. The blue beam, for Thomson scattering, will be inserted in the coil from the top (see Figure 6.2). The Thomson scattered light will be collected from the same exit hole as the probe beam, using a beamsplitter to separate the probe and the Thomson scattered light. On alternate shots, we will also place along the axis used for the exit of the probe a Thomson parabola to analyse the energetic particles able to exit the coil.

Shown in Figure 6.1 is an existing coil made at LNCMI and used at ELFIE in previous experiments. The coil arrangement is shown in the equatorial (horizontal) plane of the target chamber. The coil will be arranged such that the B-field is vertical, as shown. This magnetization system has been developed in the frame the SILAMPA ANR project by coupling a 16 kV pulse-power system available at LULI (and developed by HZDR-Dresden) to split coils (developed at LNCMI). It has been shown to develop up to 40 T, repetitively and without debris in a manner compatible with a high-energy laser experiment. Several experiments at ELFIE, LULI2000 and JLF-Titan using such system have already been performed.

As shown also in Figure 6.1, the North and South Beams will be focused onto two separate targets to produce the two separate expanding plasmas that will be made to collide.
The Blue Beam will be used as a Thomson scattering probe for the plasmas created at the interaction target. This diagnostic will allow the spatially and temporally resolved measurement of the plasma density and temperature. It will be entering the target chamber and will be distributed such as entering in the coil from the top as shown in Figure 6.2. The Thomson scattered light will be collected in the horizontal axis, through the same hole where the probe beam will be exiting.
The optical probe beam (the auxiliary laser, "CFR") will be also probing the colliding plasmas in between the two targets. It will be propagated, owing to its small size, in between the N and S beams, in the horizontal plane and collected, again in between the two imaging lines of the N and

S beams, on the other side of the coil, as shown in Figure 6.1. Also on a few alternate shots, a Thomson parabola will be positioned along the axis where the probe beam will exit, in order to analyze the energy distribution of the particles exiting the coil.

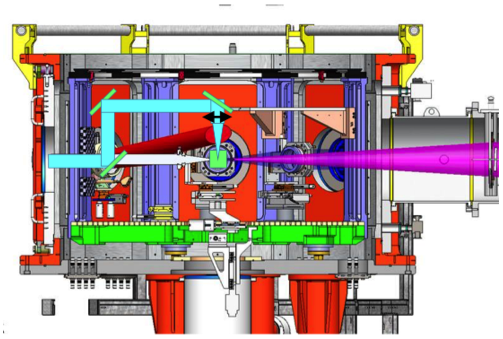

Figure 6.2 – Experimental set-up of the blue beam (schematically) in the nano2000 (“salle 2”) target chamber, showing how we plan to bring it from the top into the coil. The Thomson scattered light will be collected in the horizontal plane.

Compared to previous experiments, this project benefits from the combination of (i) the high-energy LULI2000 ns beams (enabling wider plasma plumes to be produced) and of (ii) the LULI magnetic pulser developed by the team of Julien Fuchs in collaboration with LNCMI (allowing one to use strong and pulsed external B-fields). It will allow us to perform the first experiments of fast plasma collisions in a large-volume, compressed pulsed external magnetic field with a higher plasma magnetization than previous experiments and in a well-diagnosed setup. This LULI2000 proposal is an important step to propose large scale experiments on LMJ/PETAL to confirm the role of the external magnetic field as well as the diagnostics choices envisioned for these experiments.

### Setup and magnetic field generation in the LMJ experiment

The experiment envisioned to be carried out at the LMJ laser facility is schematically represented in Figure 6.3.

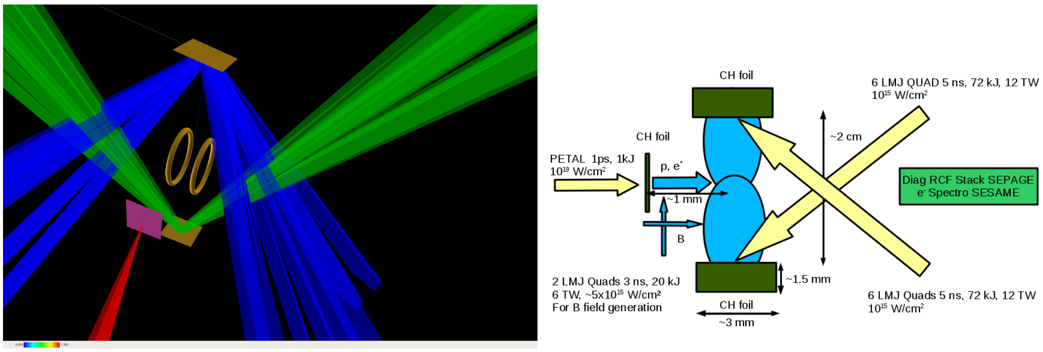

Figure 6.3 – Experimental set-up, laser-quads are used to generate the two colliding plasma plumes and the intense PETAL laser beam generates a TNSA particle beam radiograph the collision. VISRAD rendering of the experimental setup with the Helmholtz coils.

This experiment will require the use of the following beams for the formation of the two plasma plumes

- 28U-29U, 17U-18U and 10U-11U quads, first plasma plume
- 28L-29L, 17L-18L and 10L-11L quads, second plasma plume

Each quad, of 5-ns duration and 2-TW power, will pass through a type-A CCP (phase plate). The 6 LMJ bundles (12 × 10 kJ quadruplets) will be focused on ~ 1 mm diameter with type A continuous phase plates, yielding an intensity $\geq 10^{15}$W.cm$^{-2}$.

The magnetic field generation, will be ensured using the technique developed by (Fujioka et al., 2013; Santos et al., 2015). An explanation of how this technique works with one coil is shown in Figure 6.4.

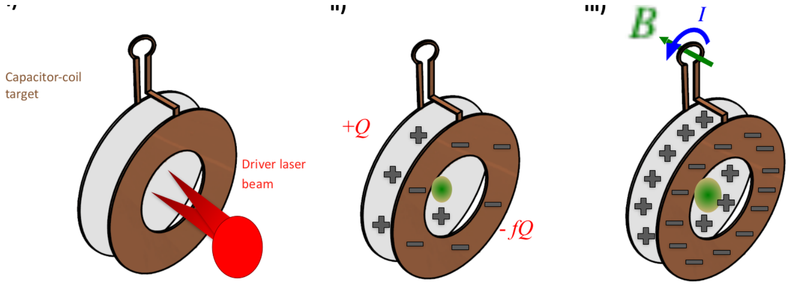

Figure 6.4 – Generation of the external magnetic field in three steps. Two nickel disks are connected by a U-turn coil. Laser pulses are focused onto the first disk through a hole in the second disk (left). A plasma is generated at the first disk, and suprathermal hot electrons are emitted from the plasma corona (middle). The hot electrons stream down the electron density gradient ahead of the expanding plasma plume and impact the second disk. The second disk acquires a negative charge, and a large electrical potential develops between the disks. That potential difference drives a current in the U-turn coil. A strong magnetic field pulse is generated in the coil (right). (Santos et al., 2015)

Two of these coils will be used to generate two current loops in a Helmoltz configuration (see Fig.6.3). The activation of these coils will require one LMJ bundle (2 × 10 kJ, 3 ns, with F type plates or ghost plates, for an intensity of $6 \times 10^{15}$W.cm$^{-2}$ ). We will use the 5U and 5L quads, of 3-ns duration and 3-TW power (10 kJ/quad). By means of the type-F CPP, the intensity will be close to $6 \times 10^{15}$W.cm$^{-2}$ on the two targets. The magnetic field in the plasma collision region is estimated to be ~ 10 T, assuming a Helmholtz configuration with 5-mm diameter coils and 1-cm separation (Fujioka et al., 2013; Santos et al., 2015). In case a ghost phase plate is used (allowing for a higher on-target intensity), a magnetic field of ~ 100 T is expected in the same configuration.

The experiment will require several diagnostics

- The laser PETAL (1 kJ, 0.5 ps) will be used to create, via TNSA, the probing proton beam for radiography. The delay of the PETAL beams relative to the 1st LMJ bundle may be varied up to a few ns.
- SEPAGE on port S26 will be used for electron and proton spectrometry, including the RCF stack module for proton-deflectometry (SESAME 1 for electron spectrometry).
- DMX on port MS8 will be used for soft X-ray spectroscopy of the plasma collision zone to evaluate the plasma temperature.

Compared to previous experiments, this project will benefit from the unique combination of (i) the radiography capability of the ps PETAL system and of (ii) the 14 high-energy LMJ quadruplets (enabling to produce wider plasma plumes, along with strong external B-field). It will allow us to perform experiments of fast plasma collisions in a large-volume, compressed pulsed external magnetic field with a high plasma magnetization. As illustrated in the next subsections, the plasma velocities before collision and the temperatures will be higher with the LMJ parameters than with the LULI2000 parameters.

### 6.0.2 Hydrodynamic representation of the plasma plumes

Similarly as in Chapter 5, the characterization of the plasma plume can be done by hydrodynamic simulations. The laser matter interaction as well as the plasma plume propagation have been simulated using the two-dimensional (2D) radiation-hydrodynamic code CHIC (Breil et al., 2011). We simulate in axisymmetric geometry the interaction of 6 laser beams with a planar plastic (CH) target. The laser beams are simulated in caustic geometry with Gaussian profiles. The wavelength of the laser is $351\,\mu\text{m}$. Two different setups have been studied corresponding to the cases of very large and intermediate energy laser facilities, the LMJ and the LULI2000 respectively. The laser pulses deliver energy to the target surface leading to the ionization and ablation of the material into an extremely hot plume, also referred to as a ‘plasma plume’. The shape of the corona is represented in Figure 6.5 for the LMJ and the LULI2000 cases, after 5 and 3.4 ns of interaction respectively.

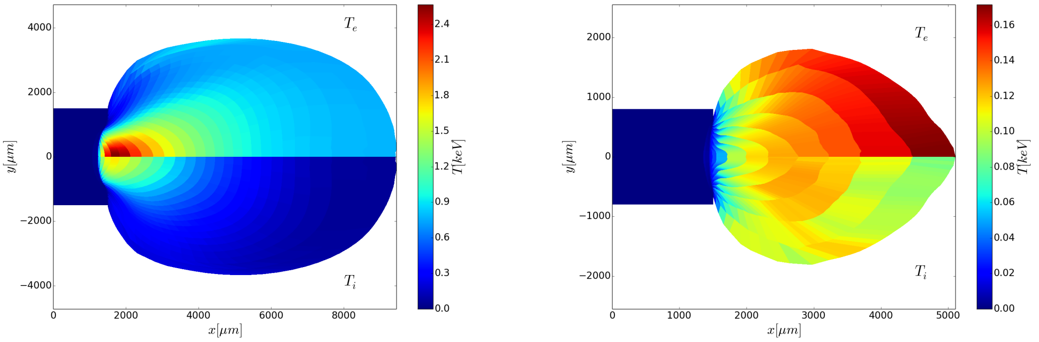

Figure 6.5 – Structure of the plasma plume. Left panel: $T_e$ (eV) and $T_i$ (eV), up and down respectively are represented at time t = 5ns in the LMJ case (left), and at time t = 3.4ns in the LULI2000 case (right).

During the expansion process, the electrons and ions cool down and a very high-Mach number flow is formed. The self-generated Biermann battery magnetic field appears as in (**?**) due to the presence of non-parallel density and temperature gradients. The typical amplitude of this frozen field is ~ 2T (not shown). However, it is stronger at the edge of the plume, far from the propagation directional axe. In the case of two counter propagating plasma plumes, they will interact first along the directional axes (where the self-generated field is weak), which implies that the Biermann battery magnetic field will not play a significant role during the plasma plumes interaction.

The evolution of the different variables at the front edge of the plasma plume (along the axis of propagation) versus time and space for the LMJ and LULI2000 laser facilities is shown in Figures 6.6 and 6.7 respectively.

The density of the plasma plume decreases exponentially during the propagation as the temperature (Atzeni and ter Vehn, 2004). The velocity of the plume remains constant (Atzeni and ter Vehn, 2004). The simulation using the laser properties of the LMJ shows a faster formation of the plasma plume compared to the one using the LULI2000 parameters. This is mostly explained by the difference of laser energy deposition on the target surface. Furthermore, the large pulse duration maintains the electrons at high temperature in the simulation using the LMJ parameters. The electrons are heated by the oscillatory field of the laser pulse via the ponderomotive force. Because of their large inertia, the ions are not sensitive to the ponderomotive force, and their temperature decreases in both simulation. The plasma plume in the LULI2000 simulation can be considered as mono-temperature, while in the LMJ simulation it is bi-temperature with $T_e/T_i \simeq 10$.

We consider that these plumes propagate in an empty space with a homogenous external magnetic field perpendicular to the propagation direction of the plasma plume with a strength of $B_0 = 10$T. These plasma parameters are sufficient to calculate at any time and at any position the ion acoustic speed $c_s = ((\gamma_e T_e + \gamma_i T_i)/m_i)^{1/2}$ and the Alfvèn speed $v_a = B_0/(\mu_0 n_0 m_i)^{1/2}$ (cf. figure 6.6, 6.7 bottom) . From these calculations, it is also possible to evaluate the magnetosonic Mach number $M_{ms} = \sqrt{\frac{1}{1+\beta_1} M_a^2} > 1$, with $\beta_1 = \mu_0 n_i \gamma_e T_e / B_0^2 = c_s^2 / v_a^2$ the Plasma-$\beta_1$ ratio and $M_a = \frac{v}{v_a}$ the Alfvènic Mach number, which give us the strength of the shock. The spatio-temporal evolutions of the magnetosonic Mach number for the two different laser facilities are shown in Figure 6.8.

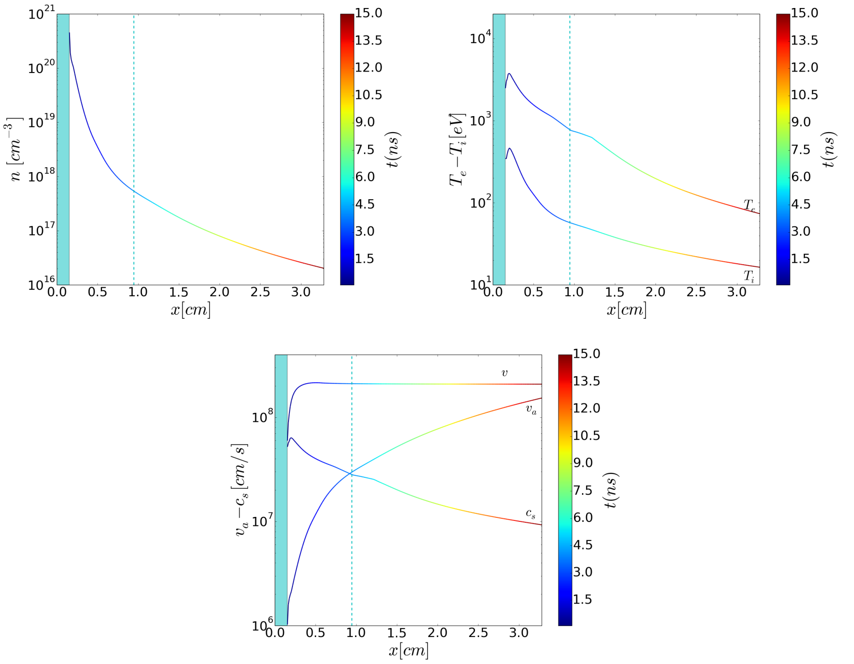

Figure 6.6 – Evolution of the density (top left), temperature (top right) and velocity (bottom) of the edge of the plasma plume versus time (color) and space (x axis) in the LMJ case.

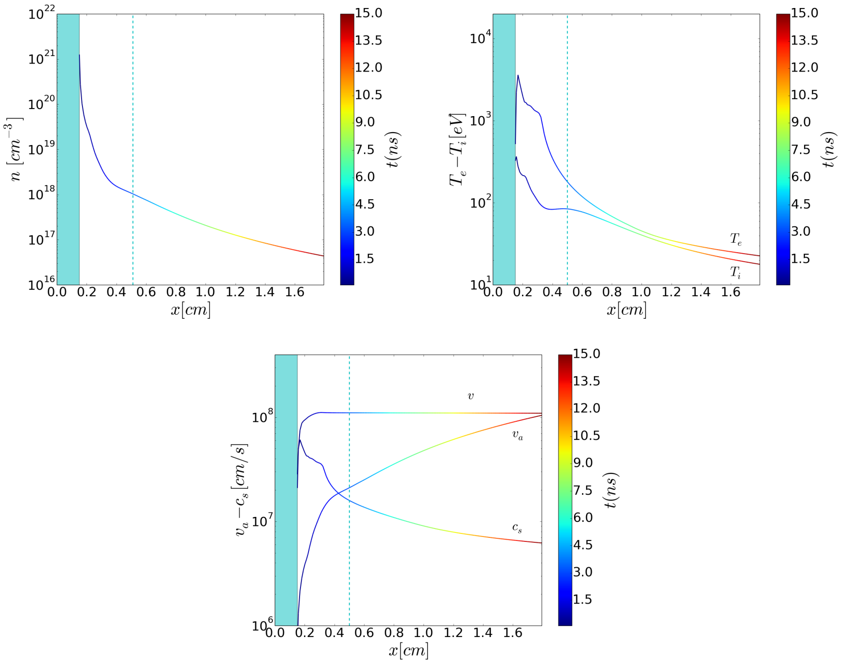

Figure 6.7 – Evolution of the density (left), temperature (middle) and velocity (right) of the edge of the plasma plume versus time (color) and space (x axis) in the LULI2000 case.

We note a similarity of the maximum value that the Mach number can reach in both cases even if the laser energies involved are very different, by more than an order of magnitude. Indeed, a lower laser energy leads to the creation of a plasma plume with a lower drift velocity as well as a lower temperature. In the end, the ratio between these two quantities does not change significantly, and it is the same for the Mach number. All the plasma parameters are computed in Table 6.2 at the time when the highest Mach number is reached (dashed line in Figure 6.8).

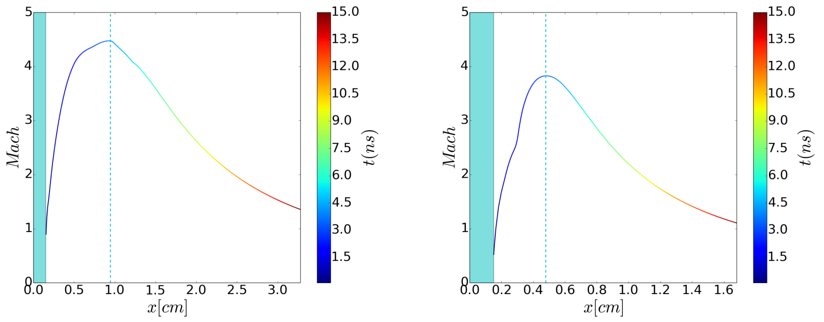

Figure 6.8 – Evolution of the magnetosonic Mach number $M_{ms}$ of the edge of the plasma plume versus time (color) and space (x axis) in the LMJ (left) and LULI2000 (right) case.

| Facility | $n_e(\mathrm{cm}^{-3})$ | $T_e(\mathrm{eV})$ | $T_i(\mathrm{eV})$ | $v(\mathrm{cm.s}^{-1})$ | $M_{ms}$ | $x_M(\mathrm{cm})$ | $t_M(\mathrm{ns})$ |
|---|---|---|---|---|---|---|---|
| LMJ | $7 \times 10^{17}$ | 965 | 65 | $2 \times 10^8$ | 4.5 | 0.9 | 4 |
| LULI2000 | $10^{18}$ | 171 | 83 | $10^8$ | 3.8 | 0.5 | 3.4 |

Table 6.2 – Plasma parameters at the edge of the plume for the LMJ and LULI2000 laser facilities at the time when the highest Mach number is reached. $x_M$ is the position of the edge of the plasma at this time $t_M$.

In order to reach the maximum Mach number, a scaling in time and space is necessary between the two laser facilities. Nevertheless, these numerical predictions of the plasma plume behavior obtained with a hydrodynamic model will have to be confronted to Thomson scattering measurements.

### 6.0.3 Collisionality aspects

One limitation of such laser facilities scalings, is the collisionnality of the created plasma plumes which also strongly depends of the plasma parameters and can destroy the collisionless nature of our shock.

As for the Mach number estimation in the previous subsection an estimate of the different mean free paths between all species is also possible. The models used to calculate these mean free paths are the same as those presented in Chapter 5.

The test particles α correspond to particles from the edge of one of the plasma plumes and the background of field particles correspond to the counter propagating plasma plume (external mean free path from eq. (5.3) (5.4) (5.5)). The evolution of all external collision mean free paths $l^{ex}_{\alpha\beta}$ versus time and space are represented in Figure 6.9.

Both plasma plumes have propagated on the same distance from their respective target, and collide at the center of the experimental setup. As a consequence, the propagation distance of the plumes to reach the maximal Mach number showed in figure 6.8 represents half of the separation distance between the two targets. A particle can be considered as collisional if its mean free path is smaller than the size of the system represented by two times the dash line value in figure 6.9. The collisions between ions in the interaction region, in the case of the LMJ, are unlikely since the lowest value of the ion-ion collision mean free path is > 2cm which is higher than the interaction region length. It is not the case for the LULI2000 parameters, the protons from one plume seem collisional with the carbon ions from the counter propagating plume (considering protons as the test particle) since at the maximum value of the Mach number the mean free path $l_{HC} \simeq 0.7 < l_{sys} \simeq 1.1$ cm. Since the temperature and drift velocity of the plasma plume is lower in the LULI2000 experiment, it is understandable that the collisions are more important. The shock formed on the LULI2000 will therefore be weakly collisional and these collisions will possibly change the shock behavior. However, even for the LMJ experiment, the mean free path linked to electron-ion and

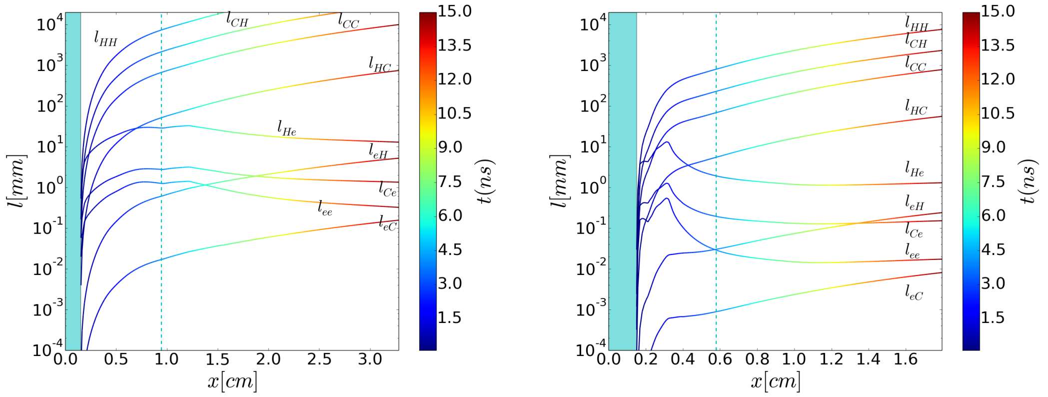

Figure 6.9 – Mean free path $l_{\alpha\beta}$ of all Coulomb collisions inter-beam versus time for LMJ (left) and LULI2000 (right). Each position corresponds to the localization of the interaction contact region, which means that at the position x=0.5 cm, the two plasma plumes would have propagated 0.5 cm each with a distance between the two targets of 1 cm, and at the position x=1 cm, the two plasma plumes would have propagated 1 cm each with a distance between the two targets of 2 cm). The dashed line corresponds to the position where the mach number $M_{ms}$ is maximum.

electron-electron collisions is lower than the size of the system, which means that the electrons will be thermalized during the interaction process. This thermalization is also a natural process of collisionless shocks driven by initial electron instabilities (cf. Chapter 2). These instabilities will possibly be affected by the electron collisionality, but the shock behavior is mainly supported by the ion dynamics.

These mean free paths have been calculated for the interactions between the species of two different plasma plumes, so when the test particles move relatively to the background of field particles. The collisions between species of the same plasma plume, the so called intra collisions, are different from the previous external collisions, and their mean free paths are calculated from equation (5.8) and (5.9). The evolution of all internal collision mean free paths $l^{in}_{\alpha\beta}$ versus time and space are represented in Figure 6.10.

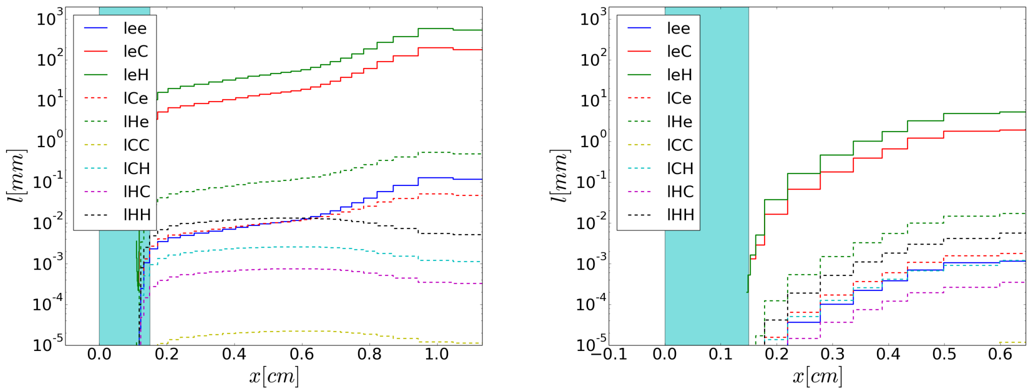

Figure 6.10 – Mean free path of all Coulomb collisions intra-beam at time t = 5ns for LMJ (left) and LULI2000 (right).

Even in the case of the LMJ, the ions and electrons in each plasma plume are highly collisional, since all the different mean-free-paths are much smaller than the size of the plume [$\lambda^{in}_{ie} << l_{sys}$]. It is interesting to note that the intra-plume collisions are more frequent for ions than for electrons. This is due to the very low thermal speed of these ions and to their charge (for carbonions). However, these collisions help to maintain the thermal equilibrium of the plasma plumes ($T_e = T_i$), and do not affect directly the shock formation. So, these collisionality calculations demonstrate that if a shock is formed in the case of the LMJ it will be collisionless and almost collisionless in the case of the LULI2000. Nevertheless, even if the external collisionality of a plasma is the first limiting effect for the collisionless shock formation, by adapting the size of the system to the laser energy capability of a laser facility, it is possible to create plasmas that are almost collisionless even for intermediate energy laser facilities.

The next subsections are dedicated to a numerical study using PIC simulations, where we have only considered the case of the LMJ laser facility. The following results will nevertheless be scalable to the LULI2000 parameters.

### 6.0.4 Species separation during plasma plume propagation

The plasma plumes are composed of ionized carbon ions and protons. As discussed previously the hydrodynamic simulations have some limitations, they consider a single fluid and cannot mix the materials. During the plasma plume expansion, the dynamics of the two ion species will depend of their mass. Indeed the carbon ions which are heavier than the hydrogen ions will be less affected by the temperature gradient, $v_{th\mathrm{P}}/v_{th\mathrm{C}} = \sqrt{m_\mathrm{C}/m_\mathrm{P}} \simeq 3.45$, and will expand with lower velocities. It is important to identify which species will interact in the overlap region of the two counter flows and will participate to the shock formation process. If the protons reach the interaction region before the carbon ions, these latter will not be involved in the shock formation process, and this species will have to be neglected. We use PIC simulations (with the code EPOCH Arber et al. (2015)), in 1D, to examine the relaxation of the thermal pressure gradient in the presence of a transverse external magnetic field.

The length $L_{0x} = 5$mm of the simulation box is subdivided into a homogenous plasma of ionized hydrogen and carbon in the interval $0 < x < 2L_{0x}/5$, and vacuum with an external magnetic field in the interval $2L_{0x}/5 < x < L_{0x}$. The initial electron density, is $n_e = 7\,10^{20}\mathrm{cm}^{-3}$ with a temperature of 1 keV, the ion temperature is 3 times lower, and the external magnetic field has a strength of 10 T. The three species densities are shown in Figure 6.11 after 0.5 ns of thermal plasma expansion.

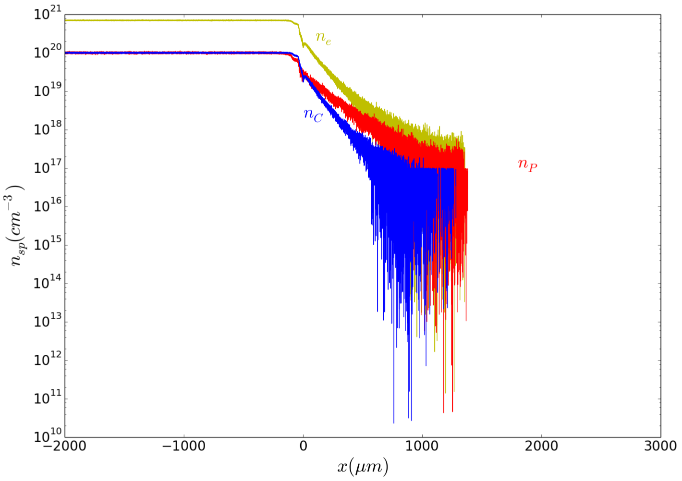

Figure 6.11 – The electron (yellow), ion carbon (blue) and proton (red) density after 0.5 ns of thermal expension.

After 0.5 ns the electrons and protons have expanded on ~ 1.4 mm and the carbon ions on ~ 1.3 mm. However, the carbon density falls dramatically and the difference of density between the carbon ions and the protons at ~ 1.3 mm is $n_\mathrm{P}/n_\mathrm{C} \sim 5$. The spatial separation of ~ 100µm between the two ion species is smaller than the typical interaction length represented by the proton Larmor radius, $r_i \simeq 300\mu\text{m}$. But, since the carbon density is much lower than the proton density, we consider the protons as the dominant ion interacting species in the next subsections. Furthermore, the electron density also falls strongly during the expansion, and reaches approximately the same density as the protons. We will therefore consider an initially neutral proton-electron plasma in what follows.

### 6.0.5 Setup of the PIC simulations for the interaction of the two plasma plumes into an external magnetic field

Due to the important computational time required to perform PIC simulations, we limit our PIC study to a small fraction of the interaction region, but we choose it large enough to be able to study the shock formation process. The box size is in this case small enough to consider the two counter streaming plasma flows as planar. A schematic representation of the localization of the PIC simulation box in the experimental setup is shown in Figure 6.12. As discussed in the previous subsection, the protons are the only ion species interacting in the simulation box, supposing in first approximation that the ionized carbon flows are much slower (cf. Figure 6.11) and reach the interpenetrating region after the protons and with a smaller density. The electron density has decreased during the expansion (cf. figure 6.11) and neutrality is fulfilled: $n_P = n_e$.

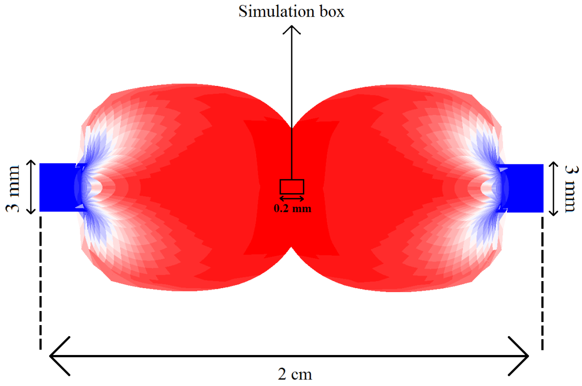

Figure 6.12 – Sketch of the plasma plumes interaction, and the localization of the PIC simulation box. The box size is small enough to consider the two counter streaming plasma flows as planar.

The simulation resolves two spatial dimensions and three particle velocity components. Reflecting and periodic boundary conditions are used in the x and y direction respectively, for the computational particles (CPs) and the fields. The lengths $L_{0x} = 200\mu\text{m}$ and $L_{0y} = 200\mu\text{m}$ of the simulation box are subdivided into evenly spaced grid cells with the lengths $\Delta_x = 7\,10^{-2}\mu\text{m}$ and $\Delta_y = 7\,10^{-2}\mu\text{m}$. The plasma in the interval $0 < x < 2L_{0x}/5$ and $0 < y < L_{0y}$ consists of protons and electrons with the number density $n_0 = 10^{24}\text{m}^{-3}$. The electron and ion temperatures in this interval are $T_e = 1\text{keV}$ and $T_i = 1\text{keV}$. The plasma in this interval has a drift velocity of $v_0 = 2\,10^6\text{m.s}^{-1}$, $\gamma_0 = 1.00002$. A symmetric plasma is located in the interval $3L_{0x}/5 < x < L_{0x}$ and $0 < y < L_{0y}$ with the same parameters but with an opposite drift velocity. We represent electrons and ions of both plasmas by $9.05 \times 10^7$CPs. A spatially uniform background magnetic field with the strength $B_0 = 10\text{T}$ is aligned with the z direction. The plasma characteristics of the plasma plumes in the PIC simulation are computed in Table 6.3, using the real proton-electron mass ratio $m_i = 1836 m_e$.

The flow is supersonic with the Mach number $M_s = v_0/c_s \simeq 3$ and super Alfvénic with the Alfvén Mach number $M_A = 10$. Figure 6.13 shows the magnetic field Bz (left), the proton density (middle), and the electron temperature (right) at the initial time.

The initial gap between the two plasmas is first chosen arbitrarily (40 μm in Figure 6.13). The size of this gap will have a crucial role in the interaction process. Indeed, the magnetic field is

| Parameter | Numerical value |
|---|---|
| $\omega_{pe} = (n_e e^2/\epsilon 0 m_e)^{1/2}$ | $5.63\,10^{13}\mathrm{s}^{-1}$ |
| $\omega_{ce} = e\mathrm{B}_0/m_e$ | $1.75\,10^{12}\mathrm{s}^{-1}$ |
| $v_{the} = (k_\mathrm{B}\mathrm{T}_e/m_e)^{1/2}$ | $1.32\,10^{7}\mathrm{m.s}^{-1}$ |
| $r_{ge} = v_{the}/\omega_{ce}$ | $7.5\,10^{-6}\mathrm{m}$ |
| $\omega_{pi} = (\mathrm{Z}^2 n_i e^2/\epsilon 0 m_i)^{1/2}$ | $1.31\,10^{12}\mathrm{s}^{-1}$ |
| $\omega_{ci} = \mathrm{Z}e\mathrm{B}_0/m_i$ | $9.56\,10^{8}\mathrm{s}^{-1}$ |
| $r_i = v_0/\omega_{ci}$ | $3.23\,10^{-4}\mathrm{m}$ |
| $c_s = ((\gamma_e\mathrm{T}_e + \gamma_i\mathrm{T}_i)/m_i)^{1/2}$ | $6.68\,10^{5}\mathrm{m.s}^{-1}$ |
| $v_a = \mathrm{B}_0/(\mu_0 n_0 m_i)^{1/2}$ | $2.18\,10^{5}\mathrm{m.s}^{-1}$ |
| $c_{ms} = (v_a^2 + c_s^2)^{1/2}$ | $7.03\,10^{5}\mathrm{m.s}^{-1}$ |

Table 6.3 – The plasma parameters of the plasma plumes in the PIC simulation.

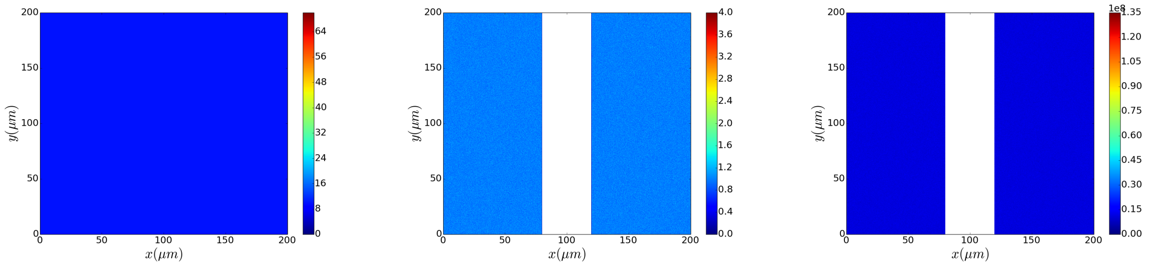

Figure 6.13 – The magnetic field Bz (left), the proton density (middle), and the electron temperature (right) at initial time. The initial gap between the two plasma flows is 40 μm.

not self-generated by the plasma as it was the case in the experiment of (**?**Huntington et al., 2017), but it is now generated by an external source (the Helmoltz coils). The magnetic field lines will therefore be pushed by the counter propagating plasma flows. The initial magnetic pressure in the simulation box is $\mathrm{P_B} = \frac{\mathrm{B}^2}{2\mu_0} \simeq 400$bars, and the initial electron thermal pressure in the plasma plumes is $\mathrm{P}_{th} = n_e k_\mathrm{B}\mathrm{T}_e \simeq 1600\mathrm{bars} \simeq 4\mathrm{P_B}$. Since the thermal pressure is much higher than the magnetic pressure the magnetic field between the two flows will be compressed until a pressure equilibrium is reached. As a consequence, the magnetic field will be higher than the initial one (10 T) when the two plasma flows will start to interact. However, it is important to note that this effect of magnetic compression can be damped by the non planar shape of the plasma plumes in the experiment. In this case, the magnetic field lines can be partially expelled in the direction transverse to the propagating flows. Nevertheless the initial ion kinetic pressure of the magnetized plasma is $\mathrm{P}_k = 0.5\, n_i m_i v_0^2 \simeq 33400$bars, which outgrows 83 times the magnetic pressure and 20 times the electron thermal pressure of the plasma. The ion Larmor radius is larger than the simulation box $r_i > \mathrm{L}_{0x}$, and the two flows will interpenetrate freely unless the electron temperature and the magnetic field compression are strongly increased. Such an increase strongly depends on the presence of an initial gap between the two colliding plasmas.

### 6.0.6 Magnetic mirror and islands formation by two magnetized counter streaming plasmas

Figure 6.14 shows the magnetic field Bz (left), the proton density (middle), and the electron temperature (right) at different times.

Each of these steps correspond to different physical processes during the interaction of the plasma flows. First the external magnetic field is compressed by the plasma flows and a magnetic mirror forms (Fig.6.14 a,b,c, 13 ps). As a second step, the magnetic mirror breaks and magnetic islands are formed (Fig.6.14 d,e,f, 18 ps) (Furth et al., 1963; Coppi et al., 1966). These latter start after their formation a period of coalescence (Fig.6.14 g,h,i, 22 ps). And finally these large magnetic

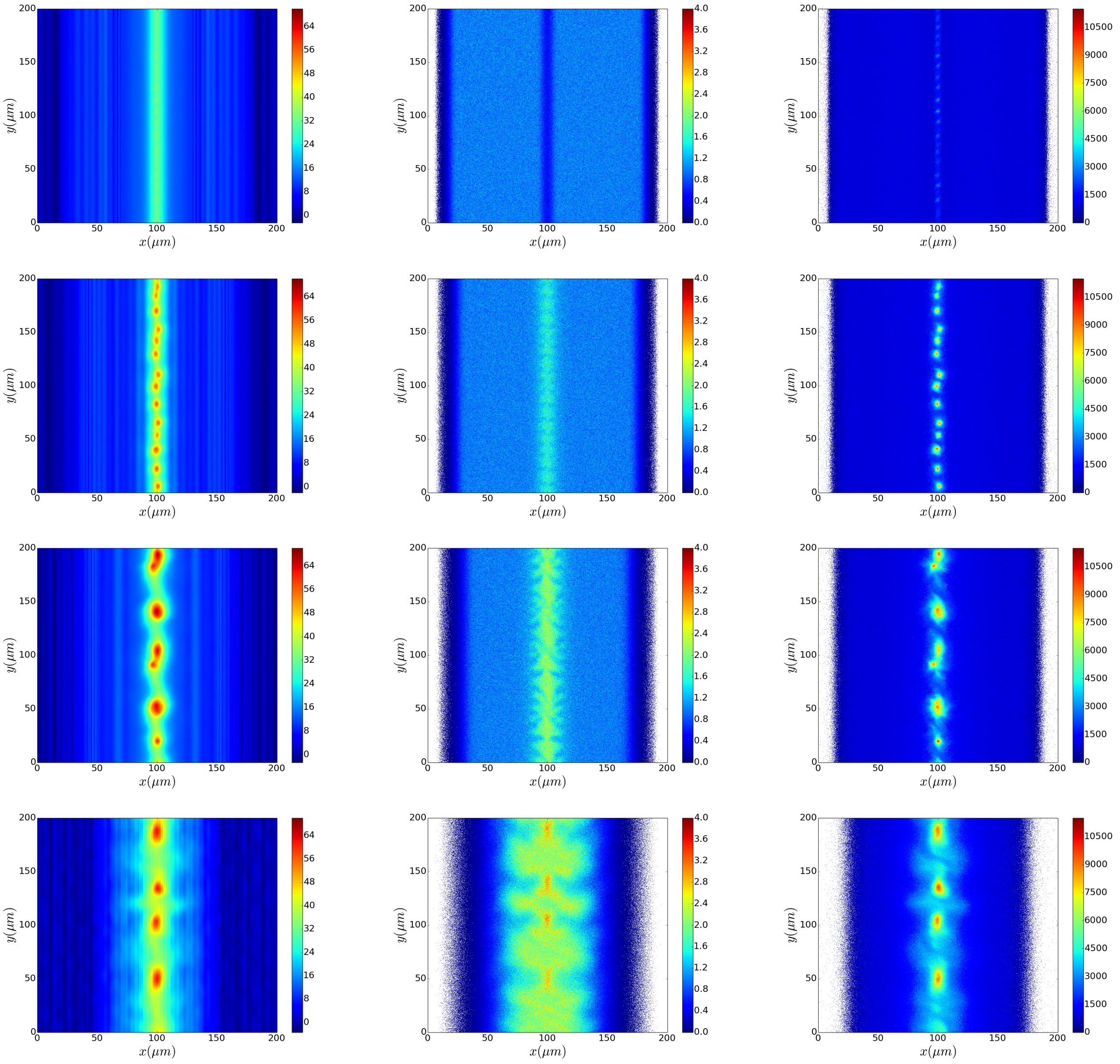

Figure 6.14 – The magnetic field Bz (left in T), the proton density (middle in $n_0$), and the electron temperature (right in eV) at 13 (magnetic compression), 18 (broken magnetic mirror), 22 (coalesceance of magnetic island) and 44 ps (magnetic island oscillation). The initial gap between the two plasma flows is 40 μm.

islands start an oscillation along the transverse direction and stop the ion flows (Fig.6.14 j,k,l, 44 ps).

### Magnetic compression: magnetic mirror

In order to explain the magnetic compression we consider a simple model, according to (Korneev et al., 2014), where two electron-ion flows propagate from one infinity to another through the magnetic field barrier ($B_z(\pm\infty) \rightarrow B_0$). The field is considered strong enough to reflect electrons back with the same velocity in an absolute value, but with an opposite sign. Considering that the magnetic part dominates in the Lorentz force $v_0 B_0 >> E_0$, which is the case of our simulation, the magnetic field amplitude after compression (Korneev et al., 2014), can be written as

$$B_{max} = \sqrt{B_0^2 + 4\gamma_0 v_0^2} \tag{6.1}$$

The predicted maximum value that the magnetic field can reach is ~ 30 T, the latter is confirmed by the simulation results (Fig.6.14 a). These results depend of an arbitrary parameter which is the width of the initial gap between the two flows. Similar simulations have been made with different gap sizes, 20 and 60µm. As demonstrated in Figure 6.15 the maximum amplitude that the magnetic mirror can reach before breaking does not depend of the initial gap width, however the width of the magnetic mirror depends on it.

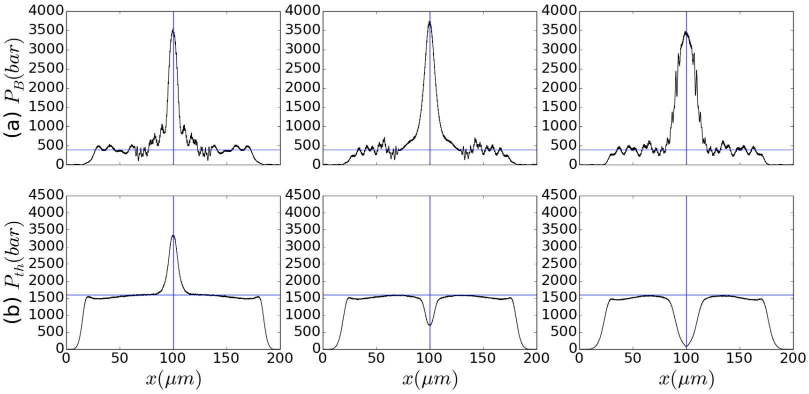

Figure 6.15 – The magnetic (a) and electron thermal pressure (b) for different widths of the initial gap between the two plasmas, shown at the time just before the magnetic mirror breaks: for a gap of 20µm at $t$ = 10ps after the beginning of the simulation (left), 40µm at $t$ = 13ps (middle), 60µm at $t$ = 16ps (right). The values are averaged over the interval $0 < y < L_{0x}$ along the y axis. The blue vertical line corresponds to the center of the simulation where the plasmas collide, and the blue horizontal line corresponds to the initial pressure value.

The plasma kinetic pressure which is much higher than the other pressures will continue to propagate the plasmas and the magnetic mirror will be broken due to current instabilities (Korneev et al., 2014). It is important to note that in the case of a small initial gap, the magnetic mirror will break after the interaction between the two flows (Fig.6.15 a), doing so the thermal pressure will be different due to the superposition of the plasmas in the overlap region and to the heating due to electron instabilities (see Chapter 2).

### Magnetic compression: broken mirror

For the first step, a stationary hydrodynamic solution was enough to represent the magnetic compression (where no particle interaction has been considered). But in the case of particle interaction, it is necessary to take a quasi-stationary hydrodynamic solution. In the case of electron-ion plasmas, the energy of the electron flow may be partially redistributed into electron-ion interactions during the process of electron slowing down. As a result, the backscattering of electrons with the same final velocities in absolute value becomes more difficult. The situation may therefore correspond to electron flows, moving along the edge of the magnetic mirror perpendicularly to the ion flows and to the magnetic field.

Considering that the electric force, created by the ions $F_c$ and the magnetic part of the Lorentz force $F_L$ are near the equilibrium, $E_x = -v_y B$ just before the breaking, the magnetic field amplitude after compression (Korneev et al., 2014), can be written as

$$B_{max} = B_0/2 + \sqrt{B_0^2/4 + 4\gamma_0^2(\gamma_0 - 1)} \tag{6.2}$$

The value of the magnetic field strength after compression in the limit $v_x \to 0$, predicted by (Korneev et al., 2014), is 25 T, which is close to the simulation results (Fig.6.15 a) and to the stationary solution (eq. (6.1)).

Considering that the electrons of the plasma edges are deflected at the border of the magnetic mirror and form now two opposite thin sheets of currents. The ions which are not deflected create a nonzero electric field between the current sheets. Small fluctuations in position, velocity and density of the current sheets will act on the fields and make the system unstable. A model of mirror edge instability has been developed by (Korneev et al., 2014). The latter analyzed the instability on the edge in three steps. It assumes first small changes of currents and densities, which modify the fields δB and δE, and then calculates the action of these perturbed fields on the currents and densities. The representation of the instability is shown in Figure 6.16.

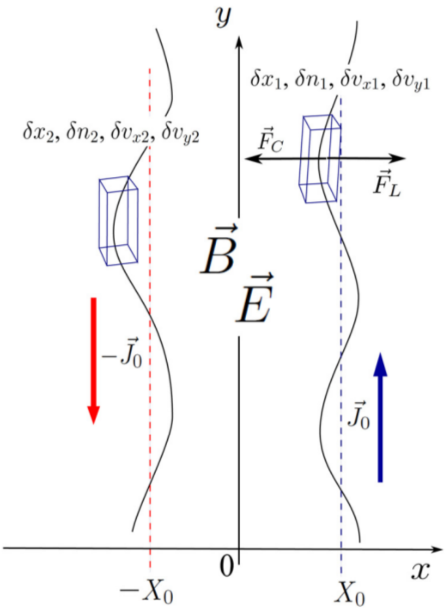

Figure 6.16 – The scheme for the linear analysis of the instability (Korneev et al., 2014). The dashed lines at $x = X_0$ correspond to the border of the mirror. The thin current $J_0$ is along this border. Fields **E** and **B** are equilibrated for these initial positions of currents according to $F_c(E_x) = F_L(v_y B_z)$. Here $\delta x_1$, $\delta v_{x1}$, $\delta U_1$, $\delta N_1$, and $\delta x_2$, $\delta v_{x2}$, $\delta U_2$, $\delta N_2$ are the small changes in positions, velocities, densities in the current sheets 1 and 2 respectively.

The solution found by (Korneev et al., 2014) uses a relativistic approximation, which is far from our experimental conditions. The model must be re-calculated, using the non-relativistic approximation $v_0 << c$. However, even the relativistic model of (Korneev et al., 2014), fails to describe the magnetic mirror dynamic when strong magnetic fields are involved, because it does not take into account the instabilities which are formed before the quasi-stationary solution (eq. (6.2)), as well as the ion density perturbations and magnetic field diffusion. An analytic study, beyond the scope of this thesis manuscript, is underway to describe the breaking mechanism of magnetic mirrors in the limits of our experiment. Nevertheless, physical properties such as the breaking wavelength of the magnetic mirror, can be estimated from PIC simulations. The thermal electron Larmor radius close to the magnetic mirror before its breaking is $r_{ge-\mathrm{MI}} \sim 2.5\mu\mathrm{m}$ (3 times less than the initial Larmor radius in Table 6.3). The breaking wavelength, corresponding to the separation between two magnetic islands, is $\lambda_{\mathrm{MI}} \simeq 12\mu\mathrm{m} \simeq 5\mathrm{r}_{\mathrm{ge-MI}}$, and the width of an island is $\Delta_{\mathrm{MI}} \simeq 5\mu m \simeq 2r_{ge-\mathrm{MI}}$. An estimation of the breaking wavelength has been found by (Pritchett, 1992) considering an equilibrium between the thermal and magnetic pressures, leading to $\lambda_{\mathrm{MI}} \sim \mathrm{T}_e / v_{\mathrm{T}h} \mathrm{B}_{max}$. The electron flows stopped initially by the mirror are now able to cross the border in the regions without strong magnetic field compression. It is important to note that the mirror can be broken even before the interpenetration of the counter streaming plasma flows (this has been observed for an initial gap of 60µm).

### Magnetic compression: island coalescence

A magnetic islands chain formed by current layers with such a periodic structure turns out to be unstable (Biskamp, 1971). The latter instability turns towards coalescence of two neighbor magnetic islands. The merging process of the magnetic islands into larger islands, called magnetic blobs, is shown in figure 6.17.

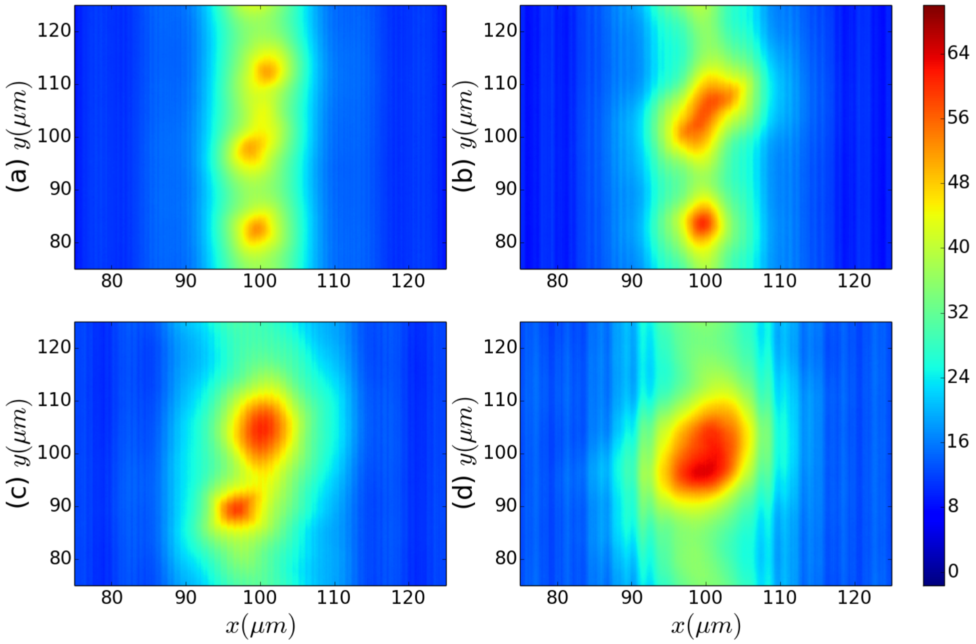

Figure 6.17 – Formation of a magnetic blob from the gyration of magnetic islands. The magnetic field $B_z$ (T) is shown at 13, 18, 22 and 27 ps. The initial gap between the two plasma flows is 40 $\mu m$.

The coalescence process has a duration estimated at $t_{mg} \sim 14$ps. Different regimes exist of the coalescence instability depending on the magnetic island width $\Delta_{\text{MI}}$ and the value of the magnetic shear $B_{\text{MI}}$ as explained in detail by (Zeleny and Taktakishvili, 1988). A solution in the MHD limit has been investigated by (Pellat, 1983). The growth rate of this instability can be written as

$$\delta \simeq 0.4(2\pi/\lambda_{\text{MI}})\, v_{\text{A}} \epsilon_{\text{MI}}^{3/4}, \qquad (6.3)$$

where $\epsilon_{\text{MI}}$ is a parameter ($0 < \epsilon_{\text{MI}} < 1$) which determines the width of the initial island chain. The growth rate is found to be equal to $\delta \simeq 10^{11}$, this value is compatible with the merging process duration in our simulation $t_{mg} \propto \delta^{-1}$.

The instability leads to four magnetic blobs possessing an amplitude of $B_{\text{BM}} \sim 70$T and a size of $\Delta_{\text{BM}} \sim 10-20\mu\text{m} \simeq 3-6r_{\text{ge-BM}}$, where $r_{ge-\text{BM}} = v_{\text{Te-BM}}/\omega_{ce-\text{BM}}$ is the electron thermal Larmor radius into a magnetic blob. The magnetic blobs are pushed by the kinetic pressure of the two flows and deformed along the transverse direction $\Delta_{\text{BM}-x} \sim 10\mu\text{m}$, $\Delta_{\text{BM}-y} \sim 20\mu\text{m}$. The blobs oscillate along the direction perpendicular to the plasma flows and the magnetic field, at the frequency $\omega_{\text{B}f} \simeq 4 \times 10^{11}\text{s}^{-1}$, as demonstrated in Figure 6.18.

Even after many oscillations, these blobs do not further merge, and the system seems stable. Simulations on larger time scales must be performed to study the lifetime of these magnetic blobs (which is beyond the scope of this thesis manuscript).

The Larmor radius of some ions, passing close to the magnetic blobs, has decreased by more than a factor of 6, reaching $r_i \sim \Delta_{\text{BM}}$. These ions are stopped on the magnetic blobs length leading to strong magnetized shocks (cf. figure 6.14 bottom). After 40 ps, the ion density has increased by a factor of 3, and the magnetic field by a factor of 6. On the contrary, the Rankine-Hugoniot relation from the set of equations (1.40) predicted the same jumps in density and magnetic field. The difference of jumps between these two plasma parameters, measured in the simulation, is due to the pre-compression of the magnetic field during the propagation of the two plasma plumes. However, shocks are formed on the length of the magnetic blobs (10 μm), and the dissipation of

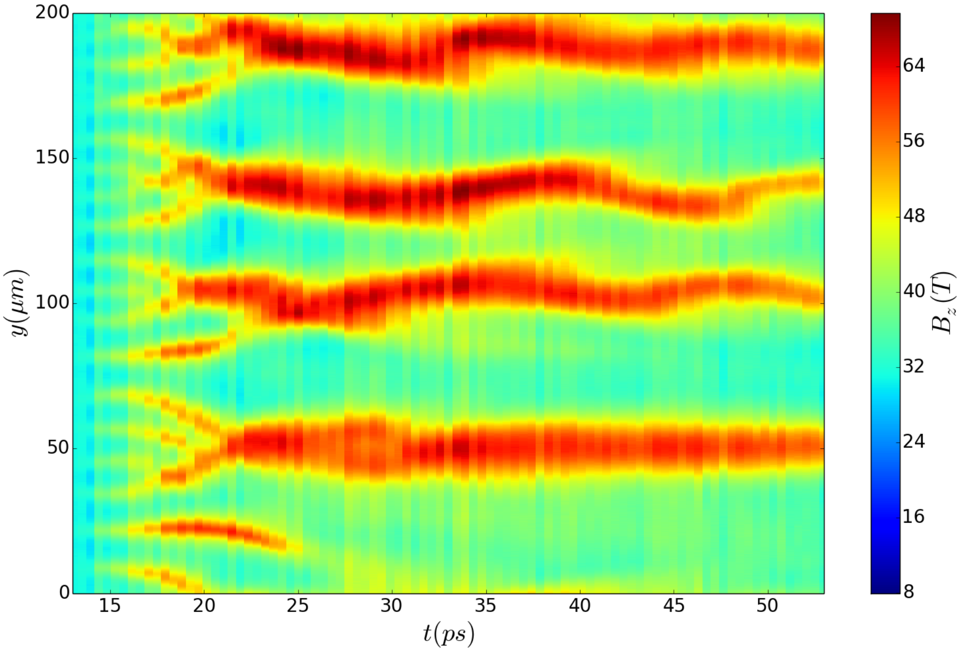

Figure 6.18 – Spatio-temporal evolution of the magnetic field $B_z(y,t)$ at the position x=100 µm (merging process between 15 and 22 ps). The initial gap between the two plasma flows is 40 µm.

the kinetic energy of the fast ions goes to electron heating. A positive radial electric field, centered on the magnetic blobs (not shown), is generated by the magnetic field gradient and slows down the ions. Electrons passing close to the blobs cannot escape from this potential and are trapped by it, leading to strong heating. These particles reach a temperature as high as 10 keV in the center of the magnetic blobs, 10 times more than their initial temperature. Furthermore, the magnetic island merging has been found to be an efficient accelerator of electrons (Tanaka et al., 2010), which has been confirmed by the electron spectra in the simulation box shown in figure 6.19.

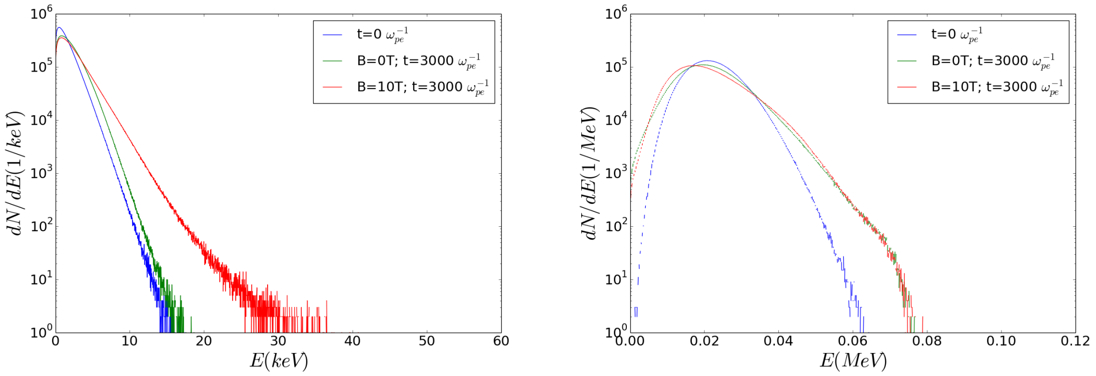

Figure 6.19 – Panel left: Electron spectrum at $t = 0\omega_{pe}^{-1}$ (blue), and $t = 3 \times 10^3 \omega_{pe}^{-1}$ with an external magnetic field (red) and without (green). The right panel shows the ion spectrum at the same times.

The green curve in figure 6.19 indicates the particle spectrum from a simulation exactly similar to the one presented here, but without external magnetic field. Figure 6.20 shows the magnetic field Bz (left), the proton density (middle), and the electron temperature (right) at different times for this simulation without external magnetic field.

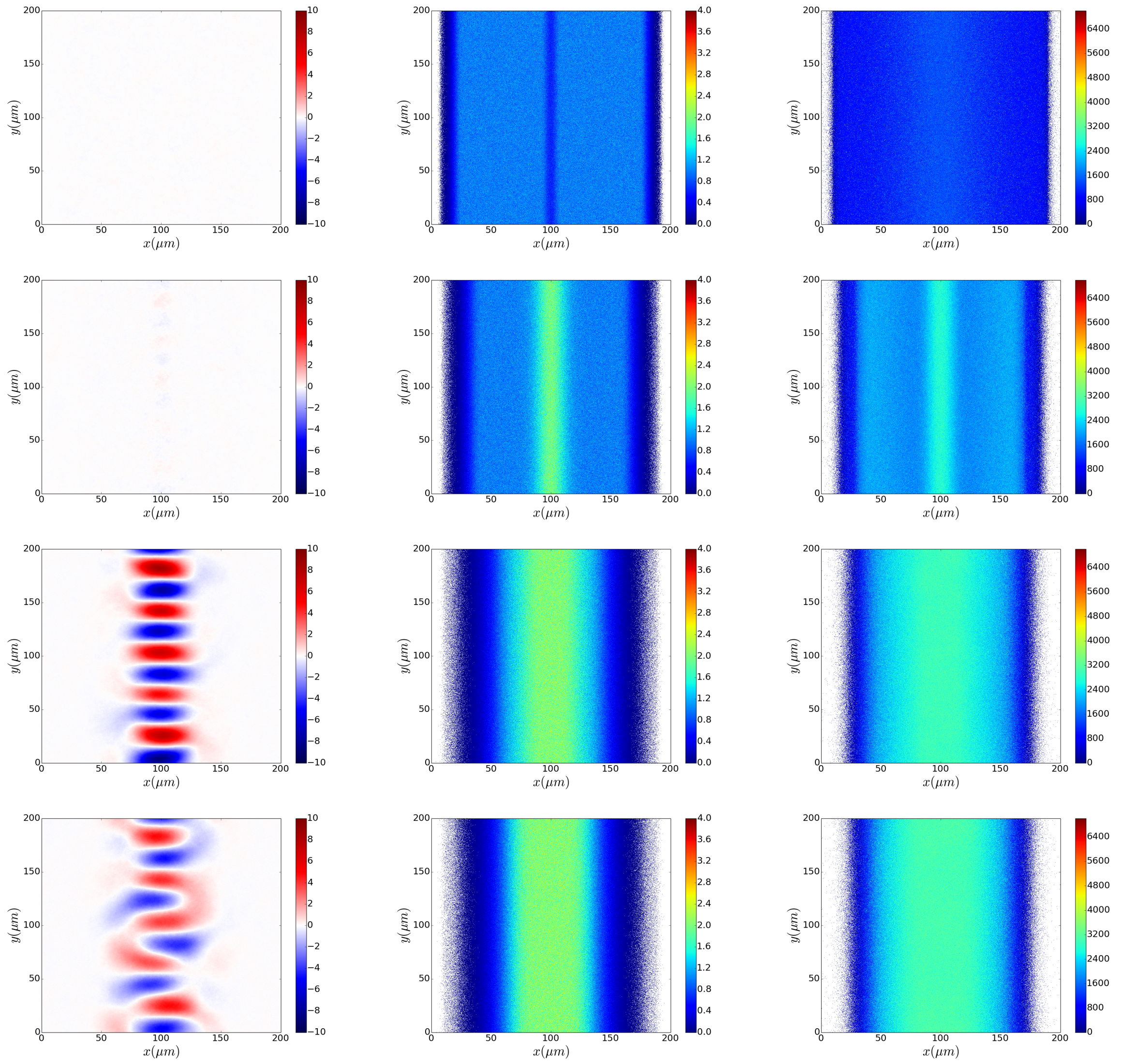

Figure 6.20 – The magnetic field Bz (left in T), the proton density (middle in $n_0$), and the electron temperature (right in eV) at 14 (no penetration yet), 22 (magnetic field perturbations appears), 35 (generation of strong magnetic filaments) and 43 ps (attenuation of the magnetic filaments). The initial gap between the two plasma flows is 40 $\mu m$ and the initial magnetic field is 0 T.

The magnetic field grows from the Weibel instability mode $k_y =\simeq \frac{\omega_{pe}}{c}\left(\frac{\omega_{pi}}{\omega_{pe}}\frac{v_0}{v_{\mathrm{Te}}}\right)^{1/3} \simeq 44\mu\mathrm{m}$ and reaches 10T after 35 ps, the growth rate is found to be $\delta \sim v_0\omega_{pi} = 6.66\times10^{-3}\omega_{pi}$. The plasma length is not large enough to sustain the Weibel instability during all its nonlinear stage, and the magnetic field decreases in amplitude after 35 ps, before reaching the saturation. The small electron heating in the interpenetration region is due to the two-stream instability. Even if the magnetic field generated by the Weibel instability is quite significant for this hot plasma, it is not capable to heat the electrons on such small time scales. The electron heating will become significant on longer time scales (taking larger plasmas for a much longer interaction time) when the magnetic field will become turbulent, turning the plasma interaction to a shock, able to accelerate particles via the Fermi first order mechanism. However, as discussed in the previous Chapter, the required time to launch such shocks is much beyond the picosecond time scale. The addition of an external magnetic field transverse to the plasma flow direction therefore allows to strongly heat electrons and decelerate ions on the blobs length.

### 6.0.7 Feasibility study

As shown in Fig.6.14, the external perpendicular magnetic field, which is compressed, allows to produce a compression zone with densities higher than three times the initial density and which is thinner than in the case with no external magnetic field. The individual magnetic vortices will not be resolved experimentally but the dislocated compressed zone which has a width growing from 20 µm after 15 ps to more than 50 µm after 30 ps can be characterized with optical probing that will allow to resolve at the same time the regions where the plasmas simply overlap (density increased by a factor of 2, so close to $2 \times 10^{18} cm^{-3}$) and the region where the magnetic mirror is broken (average density around 3 times the initial density, so close to $3 \times 10^{18}\mathrm{cm}^{-3}$). The Thomson scattering diagnostic which has a spatial resolution of 50 µm and a temporal resolution of 20 ps, will also be able to characterize the evolution of the heated zone which has a temperature evolving from 7 keV after 15 ps to 11 keV after 30 ps. We will also use a calibrated Thomson parabola to measure the spectra of energized ions escaping the magnetic field zone of the coil, and space-resolved x-ray spectroscopy.

At LULI2000, the high intensity ps beam PICO2000 cannot be used to do proton radiography when using the two 800 J ns beams. On LMJ, PETAL will be used for this purpose, allowing to obtain the spatio-temporally resolved evolution of the magnetic fields in the compressed region.

An important perspective of this work will be the use of the experimental data to determine the structure of the shock and the types of waves that develop close to the forming shock. This information can then be used to determine with Particle-In-Cell simulations and by analytic means how much the particles can get accelerated by these waves.

We also want to emphasize that this proposal is ambitious but fast plasma collisions in an external pulsed magnetic field achieved on such a scale could bring new insights in the formation of electromagnetic turbulence, in the creation of collisionless shocks and in the associated particle energization. The proposed setup would then become a new platform to propose innovative studies on collisionless shocks and particle acceleration on LMJ-PETAL and NIF.

These experiments are prepared in the framework of the MACH project funded by the Agence Nationale de la Recherche. The team involved brings together laser-plasma interaction specialists as well as experts in astrophysical collisionless shocks. The team has therefore a very strong theoretical component and this proposal is the result of several years of preparation by our theory team and several first experiments at Titan (USA), LULI and ILE (Osaka). This LULI2000 proposal is an important step in the ANR MACH project to propose large scale experiments on LMJ/PETAL to confirm the role of the external magnetic field as well as the diagnostics choices envisioned for these experiments. Further theoretical and numerical work will be performed to continue the preparation of this project.

# Conclusions

The work performed during this thesis and presented in this manuscript belongs to the general framework of High Energy Density Laboratory Astrophysics (HEDLA). Collisionless shocks of different natures have been studied in several configurations of interest for astrophysics, and often related to laser-plasma interaction.

The first work performed has been dedicated to a study of the kinetic plasma instabilities necessary for the formation of any collisionless shock. It is presented in Chapter 2. The underlying processes by which such instabilities compete with each other have been studied in details. One of the most important features is strong dependance on the ion-to-electron mass ratio during the linear and nonlinear growth phases of the instabilities. A numerical reduction of the ion-to-electron mass ratio, commonly used by the scientific community to speed up the growth of instabilities and shock formation, can overestimate some instabilities, leading to a misrepresentation of the shock processes. This study is conducted in one spatial dimension, and only a narrow range of instabilities has been investigated. This study can be extended to multi dimensional problems, representative of a larger variety of the astrophysical shocks in the Universe.

In Chapter 3, we then analyzed electrostatic collisionless shocks by investigating thermal expansion of a dense plasma, representative of a blast shell, into a dilute plasma, representative of an ambient medium, in a one-dimensional configuration. These shocks, free of magnetic field, result from the nonlinear saturation of the instabilities presented before. We performed a parametric analysis by changing the density ratio between the two plasmas and demonstrated qualitative effects of the dilute plasma on the dense plasma expansion. A double layer structure is found. The rarefaction wave pushes the dense blast shell ions, which are slowed down by the ambient dilute plasma and form a plateau. The shock speed is inversely proportional to the density ratio between the two plasmas. The shock evolution is time dependent. Ions are reflected intermittently and solitary waves are formed by the ion acoustic instability in the upstream region of the shock. These solitary waves reflect ions and form phase space holes which gradually accelerate the shock and reflect the ions from the downstream dense plasma. In the long term the shock is only mediated by the ambient medium.

In Chapter 4, we have studied the role of an external magnetic field on the development of collisionless shocks. In a magnetized plasma the ion acoustic waves are replaced by fast and slow MHD waves. Their competition depends on the angle between the shock normal and the magnetic field direction. We studied the effects of the shape of the MHD waves relation dispersion (concave/convex) on the dynamics of collisionless plasmas. Compared to a single-fluid MHD model the kinetic shocks are transient and the plasma dynamics is eventually regulated by structures that exist also in the single-fluid MHD model. Formation of magnetized shocks has been simulated in one and two dimensional configurations. The latter demonstrated that collisionless forward shocks form for all orientations of the shock normal with the ambient magnetic field direction, but their structure depends on the propagation angle of the fast or slow MHD wave. Furthermore, these shocks have been studied for heavy and light ions. Depending of the ion mass, the shocks are able to reflect more or less ions back upstream, sufficiently or not for the formation of solitary waves. This feature is not captured by the MHD model. In a supercritical regime, the magnetosonic solitary wave upstream might be responsible for perpendicular collisionless shock reformation. It is found in the subcritical regime that the shock is accelerated, possibly in a cyclic way, by fast magnetosonic solitary waves periodically created in the upstream region. These shocks are similar to the Earth's bow shock and the plasma parameters are within reach for laser-plasma experiments where our results can be tested. Further simulations with multiple ion species may help to describe a variation between MHD and kinetic structures on the ion time scale. Separation of different ion species is of great importance in laboratory experiments since most of the plasmas formed by laser-matter interaction are composed of more than one ion species.

Chapter 5 presents a study of the development of collisionless electromagnetic shocks related to recent experiments performed on the OMEGA laser facility. The interaction of a plasma jet, formed by high energy lasers illuminating the interior of an hemispherical target, and a gas bag has generated High-Alfvenic-Mach-number nonrelativistic electromagnetic collisionless shocks mediated by the ion Weibel instability. The Biermann battery magnetic field generated in the exploding shell creates conditions for a faster shock formation. We showed that penetration of a plasma with magnetized electrons in another unmagnetized plasma leads to the formation of a magnetic piston on electron time scales, characterized by an adiabatic compression. This process was demonstrated in 1D and 2D PIC simulations. The compressed hot piston propagates slower than the ion front, and the delay depends on the density ratio between the two plasmas. The difference between the velocities of the ion front and the magnetic piston allows the formation of the Weibel instability in the upstream region, and the generation of magnetic fluctuations. The initial magnetic field carried by the magnetized plasma speeds up the shock formation. Mechanisms explaining this feature are proposed. Particle acceleration has been observed in the experiment and test particle simulations have demonstrated that it can be explained by the first order Fermi process. This work advances our knowledge of collisionless astrophysical shocks in nonrelativistic regimes, such as in supernova remnants. Furthermore, this work provides a roadmap for studying shock physics in relativistic regimes, such as in the afterglow of cosmological $\gamma$-ray bursts, demonstrating that laser-matter interaction offers a powerful platform for quantitatively exploring collisionless shocks in a broader context. The importance of the magnetic field carried by only one of the colliding plasmas will be tested more accurately in experiments using two counter propagating flows and an external magnetic field localized in only one of these flows.

In Chapter 6, as one of the prospect of this thesis, we have presented detailed numerical modeling preparing laboratory experiments on collisionless magnetized shock formation. The collision of two ablative strongly magnetized flows, driven by high-energy nanosecond lasers, can trigger instabilities distinct from the Weibel filamentation. First a magnetic mirror is formed when the two flows collide. Then current instabilities lead to the breaking of this magnetic mirror and to the formation of magnetic islands. These islands can merge and locally create magnetosonic shocks responsible for an efficient electron heating. A proposal has been submitted in September 2018 to test this configuration on the LULI2000 laser facility as a scaled preparatory experiment. The proposed setup would then become a new platform to propose innovative studies on collisionless shocks and particle acceleration on LMJ-PETAL and NIF.

All these studies have been supported by Particle-in-cell codes, which, as it has been shown, have strong limitations to scale certain class of shock experiments, due to their very costly computational time. Physicists works side by side with computer scientists to improve the numerical performances of PIC codes, as it is the case for the open-source collaborative code SMILEI (Derouillat et al., 2018), which possesses, thanks to a close collaboration with the 'Maison de la simulation', an efficient load balancing. It is however evident that, except in case of huge improvements and developments of the available numerical resources, the fluid scale will not be reached by kinetic simulations in a near future, at least in 3 dimensions. But, as demonstrated in this thesis, the fluid approximation can be well representative of collisionless plasmas except for some features specific to collisionless shocks, as specular reflection and shock reformation. Some scientists are presently interested by hybrid solutions taking advantage of both models, able to simulate at the same time a thermal population, modeled by a fluid approximation, and a non-thermal one using kinetic approaches. In (van Marle et al., 2018) the MHD code describes a thermal plasma, while particles are used to represent a non-thermal component. A Boris pusher calculates the effect of electromagnetic fields on the particles. The effect of charged particles on the thermal plasma are described through an Ohm's law. There is no need for a large particle population that mimics the thermal gas, and for the particle population Maxwell's equations do not need to be solved, which reduces numerical noise. These codes are however limited by the proportion of kinetic-to-fluid particles (the condition $n_{thermal} >> n_{non-thermal}$ needs to be fulfilled), and are not suited to describe supercritical shocks, where a large number of particles are kinetic. Furthermore, the particle injection rate in the simulation is not easily determined. Nevertheless, these codes are unique tools to represent the long-time evolution of the shock propagation in order to study their radiative signature and their ability to accelerate particles to ultra-relativistic energies. This project of developing a hybrid code was one goal of the ANR MACH project, which has supported this thesis and further evidenced the new collaboration between the astrophysics and laser-plasma interaction communities.

# Publications

- Q Moreno, M E Dieckmann, X Ribeyre, S Jequier, V T Tikhonchuk and E d'Humières, Impact of the electron to ion mass ratio on unstable systems in particle-in-cell simulations, Phys. Plasmas **25**, 062125 (2018)

- Q Moreno, M E Dieckmann, X Ribeyre, and E d'Humières, Quasi-perpendicular fast magnetosonic shock with wave precursor in collisionless plasma, Phys. Plasmas **25**, 074502 (2018)

- M E Dieckmann, Q Moreno, D Doria, L Romagnani, G Sarri, D Folini, R Walder, A Bret, E d'Humières and M Borghesi, Expansion of a radially symmetric blast shell into a uniformly magnetized plasma, Phys. Plasmas **25**, 052108 (2018)

- Q Moreno, M E Dieckmann, X Ribeyre, V T Tikhonchuk, D Folini, R Walder and E d'Humières, Acceleration of a subcritical fast magnetosonic shock by magnetosonic solitary waves, To be submitted to New J. Phys. (2018)

- Q Moreno, M E Dieckmann, D Folini, R Walder, X Ribeyre and E d'Humières, Parametric simulation study of the expansion of a dense into an unmagnetized dilute plasma, To be submitted to Plasma Phys. Controll. Fusion (2018)

- C K Li, Q Moreno, A F A Bott, S Feister, H Sio, V T Tikhonchuk, E d'Humières, P Tzeferacos, G Gregori R D Petrasso, D Q Lamb, X Ribeyre, P Korneev, S Atzeni, R Betti, E M Campbell, R K Follett, J A Frenje, S X Hu, C M Huntington, M Koenig, H S Park, B A Remington, A Rigby, J S Ross, D D Ryutov, Y Sakawa, T C Sangster, F H Seguin, H Takabe, S C Wilks and S Zhang, Weibel-mediated collisionless shocks driven by supersonic plasma flows, submitted to Science (2018)

- Q, Moreno, M E Dieckmann, C K Li, Ph Korneev, L Gremillet, S Jequier, X Ribeyre, V T Tikhonchuk and E d'Humières, Formation of electromagnetic collisionless shock in interpenetration of a magnetized and unmagnetized plasma flows, To be submitted to Phys. Rev. Lett. (2018)

- D P Higginson, Ph Korneev, C Ruyer, R Riquier, Q Moreno, J Béard, S N Chen, A Grassi, M Grech, L Gremillet, H Pépin, F Perez, S Pikuz, B Pollock, C Riconda, R Shepherd, M Starodubtsev, V Tikhonchuk, T Vinci, E d'Humières and J Fuchs, Laboratory evidence of magnetic field compression and particle acceleration in collisionless colliding fast plasma flows, submitted to Nature Com. (2018)

# Presentations

- 12th HEDLA Conf., Kurashiki, Japon, 2018 (Oral Presentation)
- 5th MACH workshop, Grenoble, France, 2017 (Oral Presentation)
- 3th NWP Conf. “LaB” workshop, Volga, Russie, 2017 (Oral Presentation)
- 8th ILP Conf., Aussois, France, 2017 (Poster Presentation)
- 8th MECMATPLA winter school, Montgenèvre, France, 2017 (Poster Presentation)
- 4th MACH workshop, Paris, France, 2017 (Oral Presentation)
- 3th MACH workshop, Bordeaux, France, 2016 (Oral Presentation)
- 11th HEDLA Conf., Stanford CA, USA, 2018 (Poster Presentation)

# Appendix A

# Annexes

## A.1 Solution of a polynomial algebraic equation by the Cardan method

This method is commonly used to solve polynomial equations of 3rd degree as

$$a\Omega^3 + b\Omega^2 + c\Omega + d = 0, \tag{A.1}$$

and let us assume that : $\Omega = y - \alpha$.

Equation (A.1) can be written as :

$$y^3 + \left(\frac{b}{a} - 3\alpha y^2\right) y^2 + \left(3\alpha^2 - \frac{2b\alpha}{a} + \frac{c}{a}\right) y + \left(\frac{b\alpha^2}{a} - \frac{c\alpha}{a} + \frac{d}{a} - \alpha^3\right) = 0 \tag{A.2}$$

Assuming $b - 3\alpha = 0$ and $a = 1$ equation (A.2) can take the following form

$$y^3 + p.y + q = 0, \tag{A.3}$$

with

$$p = c - \frac{b^2}{3} \qquad q = b\left(\frac{2b^2}{27} - \frac{c}{3}\right) + d \tag{A.4}$$

The two solutions of the equation can be written as $y = u + v$, with

$$u^3 + v^3 + (3uv + p)(u + v) + q = 0 \tag{A.5}$$

where we choose $3uv + p = 0$, so $(u^3)^2 + q(u^3) - \frac{p^3}{27} = 0$

We obtain the following equation:

$$u = \sqrt[3]{-\frac{q}{2} + \sqrt{\left(\frac{q}{2}\right)^2 + \left(\frac{p}{3}\right)^3}} \qquad v = \sqrt[3]{-\frac{q}{2} - \sqrt{\left(\frac{q}{2}\right)^2 + \left(\frac{p}{3}\right)^3}} \tag{A.6}$$

Since $y = u + v$ and $\Omega = y - \alpha$, the solution can finally be written in the form (using (A.1) and (A.4)) :

$$\Omega = \sqrt[3]{-\frac{q}{2} + \sqrt{\left(\frac{q}{2}\right)^2 + \left(\frac{p}{3}\right)^3}} + \sqrt[3]{-\frac{q}{2} - \sqrt{\left(\frac{q}{2}\right)^2 + \left(\frac{p}{3}\right)^3}} - \frac{b}{3} \tag{A.7}$$

Now, depending of the discriminent $\left(\frac{q}{2}\right)^2 + \left(\frac{p}{3}\right)^3$, three different cases are possible. The one which offers complex solutions is $\left(\frac{q}{2}\right)^2 + \left(\frac{p}{3}\right)^3 < 0$, then one solution is real and the other two are complex conjugates.

$$\Omega = \sqrt[3]{g+if} + \sqrt[3]{g-if} - \frac{b}{3}$$
$$f = -\frac{q}{2} \qquad g = \sqrt{\left(\frac{q}{2}\right)^2 + \left(\frac{p}{3}\right)^3} \tag{A.8}$$

Using a trigonometric form:

$$\Omega = \sqrt[3]{\rho^3(cos\theta + isin\theta)^3} + \sqrt[3]{\rho^3(cos\theta - isin\theta)^3} - \frac{b}{3} \tag{A.9}$$

Thus the solution of (A.1) is

$$\Omega = 2\rho cos\theta - \frac{b}{3} \tag{A.10}$$

with

$$\rho = \sqrt{g^2+f^2} \qquad \theta = \frac{arctan(\frac{f}{g}) + \pi(si \quad g<0)}{3} + k\frac{2\pi}{3} \qquad k \in [0,2] \tag{A.11}$$

## A.2 Growth rate solution by the Ferrari method

This method is commonly used to solve equations of 4th degree as

$$a\Omega^4 + b\Omega^3 + c\Omega^2 + d\Omega + e = 0, \tag{A.12}$$

We first proceed to a change of variable $\Omega = z - \frac{b}{4a}$, eq. (A.12) becomes

$$z^4 + mz^2 + nz + r = 0, \tag{A.13}$$

$$m = \left(-\frac{3b^2}{8a^2} + \frac{c}{a}\right) \qquad n = \left[\left(\frac{b}{2a}\right)^3 - \frac{bc}{2a^2} + \frac{d}{a}\right] \qquad r = \left[-3\left(\frac{b}{4a}\right)^4 + \frac{c}{a^3}\left(\frac{b}{4}\right)^2 - \frac{bd}{4a^2} + \frac{e}{a}\right] \tag{A.14}$$

We assume $z^4 = (z^2+y)^2 + 2yz^2 - y^2$, where $y$ is a new parameter. Equation (A.13) becomes

$$(z^2+y)^2 - [(2y-m)z^2 - nz + y^2 - r] = 0, \tag{A.15}$$

We must determine $y$ so that the bracket can be squared in order to use the property $a^2 - b^2 = (a-b)(a+b)$, and this is possible only if

$$\Delta = (-n)^2 - 4(2y-m)(y^2-r)] = 0, \tag{A.16}$$

which leads to

$$8y^3 - 4my^2 - 8ry + 4mr - n^2 = 0, \tag{A.17}$$

The three roots of eq.(A.17) can be found by the Cardan method. We use one of the real solution $y_1$, and rewrite eq. (A.15) as

$$\left(z^2 + y_1 + \sqrt{2y_1-m}\left(z - \frac{n}{2(2y_1-m)}\right)\right)\left(z^2 + y_1 - \sqrt{2y_1-m}\left(z - \frac{n}{2(2y_1-m)}\right)\right) = 0, \tag{A.18}$$

Four different solutions for eq.(A.18) are possible (for 3 different $y_{1,2,3}$)

$$\Omega_{1,2,3,4} = \frac{1}{2}\left[\pm\sqrt{2y_1-m} \pm \sqrt{-2y_1 - m + \frac{2n}{\sqrt{2y_1-m}}}\right] - \frac{b}{4a} \tag{A.19}$$

# Bibliography

H Ahmed, M E Dieckmann, L Romagnani, D Doria, G Sarri, M Cerchez, E Ianni, I Kourakis, A L Giesecke, M Notley, R Prasad, K Quinn, O Willi, and M Borghesi. Time-Resolved Characterization of the Formation of a Collisionless Shock. *Phys. Rev. Lett.*, 110:205001, 2013. 10, 53, 115

H Ahmed, D Doria, M E Dieckmann, G Sarri, L Romagnani, A Bret, M Cerchez, A L Giesecke, E Ianni, S Kar, M Notley, R Prasad, K Quinn, O Willi, and M Borghesi. Experimental Observation of Thin-shell Instability in a Collisionless Plasma. *Astrophys. J. Lett.*, 834:L21, 2017. 56

B Albertazzi, J Beard, A Ciardi, T Vinci, J Albrecht, J Billette, T Burris-Mog, S N Chen, D Da Silva, S Dittrich, T Herrmannsdörfer, B Hirardin, F Kroll, M Nakatsutsumi, S Nitsche, C Riconda, L Romagnagni, H P Schlenvoigt, S Simond, E Veuillot, T E Cowan, O Portugall, H Pepin, and J Fuchs. Production of large volume, strongly magnetized laser-produced plasmas by use of pulsed external magnetic fields. *Rev. Scient. Instrum.*, 84:043505, 2013. 154

J E Allen and J G Andrews. A note on ion rarefaction waves. *J. Plasma Phys.*, 4:187–194, 1970. 74

T Amano and M Hoshino. Electron Injection at High Mach Number Quasi-perpendicular Shocks: Surfing and Drift Acceleration. *Astrophys. J.*, 661:190, 2007. 5

T Amano and M Hoshino. Nonlinear evolution of Buneman instability and its implication for electron acceleration in high Mach number collisionless perpendicular shocks. *Phys. Plasma*, 16:102901, 2009. 51

S Amoruso, R Bruzzese, N Spinelli, and R Velotta. Characterization of laser-ablation plasmas. *J. Phys. B: At. Mol. Opt. Phys.*, 32:R131, 1999. 119

T D Arber, K Bennett, C S Brady, A Lawrence-Douglas, M G Ramsay, N J Sircombe, P Gillies, R G Evans, H Schmitz, and A R A Bellnd C P Ridgers. Contemporary particle-in-cell approach to laser-plasma modelling. *Plasma Phys. Controll. Fusion*, 57:113001, 2015. 25, 42, 72, 98, 135, 162

S Atzeni and J Meyer ter Vehn. *The Physics of Inertial Fusion.* Oxford University, Oxford, 2004. 23, 24, 158

S Atzeni, A Schiavi, F Califano, F Cattani, F Cornolti, D Del Sarto, T V Liseykina, A Macchi, and F Pegoraro. Fluid and kinetic simulation of inertial confinement fusion plasmas. *Comput. Phys. Commun.*, 169:153 – 159, 2005. 9

S D Bale, F S Mozer, and T S Horbury. Density-Transition Scale at Quasiperpendicular Collisionless Shocks. *Phys. Rev. Lett.*, 91:265004, 2003. 6, 98

S D Bale, M A Balikhin, T S Horbury, V V Krasnoselskikh, H Kurcharek, E Mobius, S N Walker, A Balogh, D Burgess, and B Lembege. Quasi-perpendicular shock structure and processes. *Space Sci. Rev.*, 118:161–203, 2005. 6, 65, 98

M A Balikhin, M Nozdrachev, M Dunlop, V Krasnosel'skikh, S N Walker, H. St. C. K. Alleyne, V Formisano, M Andre, A Balogh, A Eriksson, and K Yearby. Observation of the terrestrial bow shock in quasi-electrostatic subshock regime. *J. Geophys. Res.*, 107(A8):SSH 1–1–SSH 1–9, 2002. 98

A Balogh and R A Treumann. Physics of collisionless shocks-space plasma shock waves. *ISSI Scientific Report Series*, 12, 2011. 2, 78

G Bardotti and S E Segre. Laminar electrostatic shock waves in a plasma. *Plasma Phys.*, 12:247, 1970. 53

W Baumjohann and R A Treumann. *Basic Space Plasma Phys.* Imperial College Press, 1997. 35, 39, 47, 61, 93, 135

F Begay and D W Forslund. Acceleration of multi-species ions in $CO_2$ laser-produced plasmas. *Phys. Fluids*, 25(9):1675–1685, 1982. 55

A R Bell. The acceleration of cosmic rays in shock fronts – I. *Mon. Not. Roy. Astron. Soc.*, 182: 147–156, 1978. 148

A R Bell, P Choi, A E Dangor, O Willi, D A Bassett, and C J Hooker. Collisionless shock in a laser-produced ablating plasma. *Phys. Rev. A*, 38:1363–1369, 1988. 10, 56, 98, 115

S T Belyaev and G I Budker. *Dokl. Akad. Nauk SSSR*, 1(807), 1956. 33

P A Bernhardt, R A Roussel-Dupre, M B Pongratz, G Haerendel, A Valenzuela, D A Gurnett, and R R Anderson. Observations and theory of the AMPTE magnetotail barium releases. *J. Geophys. Res.*, 92:5777–5794, 1987. 85, 96

L Biermann. Über den ursprung der magnetfelder auf sternen und im interstellaren raum. *Z. f. Naturf.*, 5a:65–71, 1950. 120

C Birdsall and A Langdon. *Plasma Physics via Computer Simulation.* Series in Plasma Physics and Fluid Dynamics. Taylor & Francis, 2004. 24, 25, 26

D Biskamp. Instability of two-dimensional collisionless plasmas with neutral points. *Plasma Physics*, 13:1013, 1971. 167

R Blandford and D Eichler. Particle acceleration at astrophysical shocks: A theory of cosmic ray origin. *Physics Reports*, 154:1 – 75, 1987. 148

P Blasi. The origin of galactic cosmic rays. *A & A Rev.*, 21:70, 2013. 6

S G Bochkarev, E d'Humières, Ph Korneev, V Yu Bychenkov, and V T Tikhonchuk. The role of electron heating in electromagnetic collisionless shock formation. *High Energy Density Physics*, 17: 175–182, 2015. 135

D Bohm and E P Gross. Theory of Plasma Oscillations. A. Origin of Medium-Like Behavior. *Phys. Rev.*, 75:1851–1864, 1949. 32

M Borghesi, D H Campbell, A Schiavi, O Willi, M Galimberti, L A Gizzi, A J Mackinnon, R D Snavely, P Patel, S Hatchett, M Key, and W Nazarov. Propagation issues and energetic particle production in laser–plasma interactions at intensities exceeding 1019 W/cm2. *Laser and Particle Beams*, 20: 31–38, 2002. 10

J P Boris. Relativistic plasma simulation - optimization of a hybrid code. *Proceeding of the 4th Conference on Numerical Simulation of Plasmas*, page 3–67, 1970. 27

M B Borisov, S G Zaitsev, E I Chebotareva, and E V Lazareva. Experimental investigation of the interaction of a shock wave with a magnetic field. *Fluid Dyn.*, 6:501–509, 1971. 72

A F A Bott, C Graziani, P Tzeferacos, T G White, D Q Lamb, G Gregori, and A A Schekochihin. Proton imaging of stochastic magnetic fields. *J. Plasma Phys.*, 83:905830614, 2017. 128

S Bouquet, E Falize, C Michaut, C D Gregory, B Loupias, T Vinci, and M Koenig. From lasers to the universe: Scaling laws in laboratory astrophysics. *High Energy Density Physics*, 6:368 – 380, 2010. 10

J U Brackbill, D W Forslund, K B Quest, and D Winske. Nonlinear evolution of the Lower-Hybrid drift instability. *Phys. Fluids*, 27, 1984. 93

S I Braginskii. Transport Processes in a Plasma. *Reviews of Plasma Physics*, 1:205, 1965. 24

J Breil, S Galera, and P H Maire. Multi-material ALE computation in inertial confinement fusion code CHIC. *Comput. Fluids*, 46:161 – 167, 2011. 24, 158

A Bret and M E Dieckmann. How large can the electron to proton mass ratio be in particle-in-cell simulations of unstable systems? *Phys. Plasmas*, 17:032109, 2010. 39, 40, 49, 50

A Bret, L Gremillet, and M E Dieckmann. Multidimensional electron beam-plasma instabilities in the relativistic regime. *Phys. Plasmas*, 17:120501, 2010. 15, 39, 49

A Bret, A Stockem, F Fiuza, C Ruyer, L Gremillet, R Narayan R, and L O Silva. Collisionless shock formation, spontaneous electromagnetic fluctuations, and streaming instabilities. *Phys. Plasmas*, 20:042102, 2013. 40

M Brio and C C Wu. An upwind differencing scheme for the equations of ideal magnetohydrodynamics. *J. Comput. Phys.*, 75:400 – 422, 1988. 72

O Buneman. Instability, Turbulence, and Conductivity in Current-Carrying Plasma. *Phys. Rev. Lett.*, 1:8–9, 1958. 33, 39, 60

J M Burgers. A Mathematical Model Illustrating the Theory of Turbulence. volume 1 of *Advances in Applied Mechanics*, pages 171 – 199. Elsevier, 1948. 2

D Burgess and M Scholer. Shock front instability associated with reflected ions at the perpendicular shock. *Phys. Plasmas*, 14:012108, 2007. 85, 100

D Burgess, E A Lucek, M Scholer, S D Bale, M A Balikhin, A Balogh, T S Horbury, V V Krasnoselskikh, H Kucharek, B Lembege, E Mobius, S J Schwartz, M F Thomsen, and S N Walker. Quasi-parallel shock structure and processes. *Space Sci. Rev.*, 118:205–222, 2005. 6, 65, 98

R A Cairns, R Bingham, P Norreys, and R Trines. Laminar shocks in high power laser plasma interactions. *Phys. Plasmas*, 21:022112, 2014. 54, 55

F Califano, R Prandi, F Pegoraro, and S V Bulanov. Nonlinear filamentation instability driven by an inhomogeneous current in a collisionless plasma. *Phys. Rev. E*, 58:7837–7845, 1998. 39

D Caprioli and A Spitkovsky. Simulations of Ion Acceleration at Non-relativistic Shocks. I. Acceleration Efficiency. *Astrophys. J.*, 783:91, 2014. 6, 148

D Caprioli, A R Pop, and A Spitkovsky. Simulations and Theory of Ion Injection at Non-relativistic Collisionless Shocks. *Astrophys. J. Lett.*, 798:L28, 2015. 148

S C Chapman. Shocklike behaviour exhibited at early times by the AMPTE solar wind/magnetosheath releases. *Planet. Space Sci.*, 37:1227–1247, 1989. 85

S C Chapman, R E Lee, and R O Dendy. Perpendicular Shock Reformation and Ion Acceleration. *Space Sci. Rev.*, 121:5, 2005. 85

C Z Cheng and G Knorr. The integration of the vlasov equation in configuration space. *J. Comput. Phys.*, 22:330–351, 1976. 24

B Coppi, G Laval, and R Pellat. Dynamics of the Geomagnetic Tail. *Phys. Rev. Lett.*, 16:1207–1210, 1966. 164

C Courtois, R A D Grundy, A D Ash, D M Chambers, N C Woolsey, R O Dendy, and K G McClements. Experiment on collisionless plasma interaction with applications to supernova remnant physics. *Phys. Plasmas*, 11:3386–3393, 2004. 115, 153, 154

J Cronin, T Gaisser, and S Swordy. Cosmic Rays at the Energy Frontier. *Scientific American*, 276: 44–49, 1997. 6

J E Crow, P L Auer, and J E Allen. The expansion of a plasma into a vacuum. *J. Plasma Phys.*, 14: 65–76, 1975. 74

W Daughton, G Lapenta, and P Ricci. Nonlinear Evolution of the Lower-Hybrid Drift Instability in a Current Sheet. *Phys. Rev. Lett.*, 93:105004, 2004. 93

W Daughton, V Roytershteyn, B J Albright, H Karimabadi, L Yin, and K J Bowers. Influence of Coulomb collisions on the structure of reconnection layers. *Phys. Plasmas*, 16:072117, 2009. 122

R C Davidson, D A Hammer, I Haber, and C E Wagner. Nonlinear Development of Electromagnetic Instabilities in Anisotropic Plasmas. *Phys. Fluids*, 15:317–333, 1972. 37

S O Dean, E A McLean, J A Stamper, and H R Griem. Demonstration of Collisionless Interactions Between Interstreaming Ions in a Laser-Produced- Plasma Experiment. *Phys. Rev. Lett.*, 27:487–490, 1971. 10, 98

J Denavit. Collisionless plasma expansion into a vacuum. *Phys. Fluids*, 22:1384–1392, 1979. 55

J Derouillat, A Beck, F Pérez, T Vinci, M Chiaramello, A Grassi, M Flé, G Bouchard, I Plotnikov, N Aunai, J Dargent, C Riconda, and M Grech. Smilei : A collaborative, open-source, multi-purpose particle-in-cell code for plasma simulation. *Comput. Phys. Commun.*, 222:351 – 373, 2018. 174

M E Dieckmann, P Ljung, and A A Ynnermannd K G McClements. Large scale numerical simulations of ion beam instabilities in unmagnetized astrophysical plasmas. *Phys. Plasmas*, 7: 5171–5181, 2000a. 40, 45

M E Dieckmann, K G McClements, S C Chapman, R O Dendy, and L O C Drury. Electron acceleration due to high frequency instabilities at supernova remnant shocks. *Astron. Astrophys.*, 365 (377), 2000b. 93

M E Dieckmann, A Ynnerman, S C Chapman, G Rowlands, and N Andersson. Simulating Thermal Noise. *Phys. Scripta*, 69:456, 2004. 77

M E Dieckmann, G Sarri, L Romagnani, I Kourakis, and M Borghesi. Simulation of a collisionless planar electrostatic shock in a proton–electron plasma with a strong initial thermal pressure change. *Plasma Phys. Control. Fusion*, 52:025001, 2010. 55, 56, 57, 58, 61, 64

M E Dieckmann, G Sarri, G C Murphy, A Bret, L Romagnani, I Kourakis, M Borghesi, and A A Ynnermannd L O'C Drury. PIC simulation of a thermal anisotropy-driven Weibel instability in a circular rarefaction wave. *New J. Phys.*, 14:023007, 2012. 85

M E Dieckmann, H Ahmed, G Sarri, D Doria, I Kourakis, L Romagnani, M Pohl, and M Borghesi. Parametric study of non-relativistic electrostatic shocks and the structure of their transition layer. *Physics of Plasmas*, 20(4):042111, 2013. 144

M E Dieckmann, G Sarri, D Doria, and A A Ynnermannd M Borghesi. Particle-in-cell simulation study of a lower-hybrid shock. *Phys. Plasmas*, 23:062111, 2016. 74, 78, 85

M E Dieckmann, D Doria, H Ahmed, L Romagnani, G Sarri, D Folini, R Walder, A Bret, and M Borghesi. Expansion of a radial plasma blast shell into an ambient plasma. *Phys. Plasmas*, 24:094501, 2017a. 59, 87

M E Dieckmann, D Folini, R Walder, L Romagnani, E d'Humieres, A Bret, T Karlsson, and A Ynnerman. Emergence of MHD structures in a collisionless PIC simulation plasma. *Phys. Plasmas*, 24:094502, 2017b. 12, 75, 78, 81, 85, 97, 100, 101, 112

M E Dieckmann, D Doria, G Sarri, L Romagnani, H Ahmed, D Folini, R Walder, A Bret, and M Borghesi. Electrostatic shock waves in the laboratory and astrophysics: similarities and differences. *Plasma Phys. Control. Fusion*, 60:014014, 2018a. 56

M E Dieckmann, Q Moreno, D Doria, L Romagnani, G Sarri, D Folini, R Walder, A Bret, E d'Humieres, and M Borghesi. Expansion of a radially symmetric blast shell into a uniformly magnetized plasma. *Phys. Plasmas*, 25:052108, 2018b. 12, 81, 100

K Dolder and R Hide. Experiments on the Passage of a Shock Wave through a Magnetic Field. *Rev. Mod. Phys.*, 32:770–779, 1960. 72

R P Drake. The design of laboratory experiments to produce collisionless shocks of cosmic relevance. *Phys. Plasmas*, 7:4690–4698, 2000. 117

R P Drake. *High-Energy-Density Physics: Fundamentals, Inertial Fusion, and Experimental Astrophysics*. Springer Verlag, 2006. 124

L O Drury and J H Voelk. Hydromagnetic shock structure in the presence of cosmic rays. *Astrophys. J.*, 248:344–351, 1981. 21

T H Dupree. Growth of phase-space density holes. *Phy. Fluids*, 26:2460–2481, 1983. 62

J P Eastwood, E A Lucek, C Mazelle, K Meziane, Y Narita, J Pickett, and R A Treumann. The Foreshock. *Space Sci. Rev.*, 118:41, 2005. 71

J W Eastwood. The virtual particle electromagnetic particle-mesh method. *Comput. Phys. Commun.*, 64:252–266, 1991. 25

M J Edwards, P K Patel, J D Lindl, L J Atherton, S H Glenzer, S W Haan, J D Kilkenny, O L Landen, E I Moses, A Nikroo, R Petrasso, T C Sangster, P T Springer, S Batha, R Benedetti, L Bernstein, R Betti, D L Bleuel, T R Boehly, D K Bradley, J A Caggiano, D A Callahan, P M Celliers, C J Cerjan, K C Chen, D S Clark, G W Collins, E L Dewald, L Divol, S Dixit, T Doeppner, D H Edgell, J E Fair, M Farrell, R J Fortner, J Frenje, M G Gatu Johnson, E Giraldez, V Yu Glebov, G Grim, B A Hammel, A V Hamza, D R Harding, S P Hatchett, N Hein, H W Herrmann, D Hicks, D E Hinkel, M Hoppe, W W Hsing, N Izumi, B Jacoby, O S Jones, D Kalantar, R Kauffman, J L Kline, J P Knauer, J A Koch, B J Kozioziemski, G Kyrala, K N LaFortune, S Le Pape, R J Leeper, R Lerche, T Ma, B J MacGowan, A J MacKinnon, A Macphee, E R Mapoles, M M Marinak, M Mauldin, P W McKenty, M Meezan, P A Michel, J Milovich, J D Moody, M Moran, D H Munro, C L Olson, K Opachich, A E Pak, T Parham, H S Park, J E Ralph, S P Regan, B Remington, H Rinderknecht, H F Robey, M Rosen, S Ross, J D Salmonson, J Sater, D H Schneider, F H Séguin, S M Sepke, D A Shaughnessy, V A Smalyuk, B K Spears, C Stoeckl, W Stoeffl, L Suter, C A Thomas, R Tommasini, R P Town, S V Weber, P J Wegner, K Widman, M Wilke, D C Wilson, C B Yeamans, and A Zylstra. Progress towards ignition on the National Ignition Facility. *Phys. Plasmas*, 20:070501, 2013. 9

B Eliasson. Ion shock acceleration by large amplitude slow ion acoustic double layers in laser-produced plasmas. *Phys. Plasmas*, 21:023111, 2014. 97

B Eliasson and P K Shukla. Formation and dynamics of coherent structures involving phase-space vortices in plasmas. *Phys. Rep.*, 422:225 – 290, 2006. 56, 106

E Esarey, C B Schroeder, and W P Leemans. Physics of laser-driven plasma-based electron accelerators. *Rev. Mod. Phys.*, 81:1229–1285, 2009. 40

T Zh Esirkepov. Exact charge conservation scheme for Particle-in-Cell simulation with an arbitrary form-factor. *Comput. Phys. Commun.*, 135:144 – 153, 2001. 27

É Falize, C Michaut, and S Bouquet. Similarity Properties and Scaling Laws of Radiation Hydrodynamic Flows in Laboratory Astrophysics. *Astrophys. J.*, 730:96, 2011. 10

S A E G Falle, S S Komissarov, and P Joarder. A multidimensional upwind scheme for magnetohydrodynamics. *Mon. Not. R. Astron. Soc.*, 297:265–277, 1998. 72

E Fermi. On the Origin of the Cosmic Radiation. *Phys. Rev.*, 75:1169–1174, 1949. 146

D Forslund, R Morse, and C Nielson. Electron Cyclotron Drift Instability and Turbulence. *Phys. Fluids*, 15:1303–1318, 1972. 93

D W Forslund and J P Freidberg. Theory of Laminar Collisionless Shocks. *Phys. Rev. Lett.*, 27: 1189–1192, 1971. 55, 78, 85

D W Forslund and C R Shonk. Formation and Structure of Electrostatic Collisionless Shocks. *Phys. Rev. Lett.*, 25:1699–1702, 1970. 53, 55, 116

W Fox, G Fiksel, A A Bhattacharjeend P Y Chang, K Germaschewski, S X Hu, and P M Nilson. Filamentation instability of counterstreaming laser-driven plasmas. *Phys. Rev. Lett.*, 111(22), 2013. 117, 118

B D Fried and R W Gould. Longitudinal Ion Oscillations in a Hot Plasma. *Phys. Fluids*, 4:139–147, 1961. 35

D H Froula. *Plasma Scattering of Electromagnetic Radiation*. Academic Press Burlington, 2011. 121

D H Froula, J S Ross, L Divol, and S H Glenzer. Thomson-scattering techniques to diagnose local electron and ion temperatures, density, and plasma wave amplitudes in laser produced plasmas (invited). *Rev. Sci. Instrum.*, 77:10E522, 2006. 121

S Fujioka, Z Zhang, K Ishihara, K Shigemori, Y Hironaka, T Johzaki, A Sunahara, N Yamamoto, H Nakashima, T Watanabe, H Shiraga, H Nishimura, and H Azechi. Kilotesla magnetic field due to a capacitor-coil target driven by high power laser. *Sci. Rep.*, 3(1170), 2013. 157

H P Furth, J Killeen, and M N Rosenbluth. Finite-Resistivity Instabilities of a Sheet Pinch. *Phys. Fluids*, 6:459–484, 1963. 164

S Galera, P H Maire, and J Breil. A two-dimensional unstructured cell-centered multi-material ALE scheme using VOF interface reconstruction. *J. Comput. Phys.*, 229:5755 – 5787, 2010. 24

W Gekelman, H Pfister, Z Lucky, J Bamber, D Leneman, and J Maggs. Design, construction, and properties of the large plasma research device-The LAPD at UCLA. *Rev. Sci. Instrum.*, 62:2875–2883, 1991. 115

W Gekelman, S Vincena, B V Compernolle, G J Morales, J E Maggs, P Pribyl, and T A Carter. The many faces of shear Alfvén waves. *Phys. Plasmas*, 18:055501, 2011. 90

D O Gericke and M Schlanges. Beam-plasma coupling effects on the stopping power of dense plasmas. *Phys. Rev. E*, 60:904–910, 1999. 124, 125

S J Gitomer, R D Jones, F Begay, A W Ehler, J F Kephart, and R Kristal. Fast ions and hot electrons in the laser–plasma interaction. *Phys. Fluids*, 29(8):2679–2688, 1986. 55

G C Goldenbaum. Experimental Study of Collision-Free Shock Waves and Anomalous Electron Heating. *Phys. Fluids*, 10:1897–1904, 1967. 153

M L Goldstein, J P Eastwood, R A Treumann, E A Lucek, J Pickett, and P Decreau. The near-earth solar wind. *Space Sci. Rev.*, 118:7–39, 2016. 5, 74, 98

J T Gosling and A E Robson. *Collisionless Shocks in the Heliosphere: Reviews of Current Research*, volume 35. American Geophysical Union, 1985. 100

A Grassi. *Collisionless shocks in the context of Laboratory Astrophysics*. PhD thesis, 2017. 6

L Gremillet, D Bénisti, E Lefebvre, and A Bret. Linear and nonlinear development of oblique beam-plasma instabilities in the relativistic kinetic regime. *Phys. Plasmas*, 14:040704, 2007. 15

T Grismayer and P Mora. Influence of a finite initial ion density gradient on plasma expansion into a vacuum. *Phys. Plasmas*, 13:032103, 2006. 85

T Grismayer, P Mora, J C Adam, and A Héron. Electron kinetic effects in plasma expansion and ion acceleration. *Phys. Rev. E*, 77:066407, 2008. 85

R Gueroult and N J Fisch. Practicality of magnetic compression for plasma density control. *Phys. Plasmas*, 23:032113, 2016. 100

R Gueroult, Y Ohsawa, and N J Fisch. Role of Magnetosonic Solitons in Perpendicular Collisionless Shock Reformation. *Phys. Rev. Lett.*, 118:125101, 2017. 71, 74, 78, 84, 85, 100

D N Gupta, K P Singh, A K Sharma, and N K Jaiman. Nonlinear saturation of laser driven plasma beat wave by oscillating two-stream instability. *Phys. Plasmas*, 11:5250–5255, 2004. 47

A L Gurevich, L I Pariiskaya, and L P Pitaevskii. Self-similar Motion of a Low-density Plasma. II. *JETP*, 27:476–482, 1968. 55

A V Gurevich and A P Meshcherkin. Expanding self-similar discontinuities and shock waves in dispersive hydrodynamics. *Eksp. Teor. Fiz.*, 87(1277), 1984. 88

D Haberberger, S Tochitsky, F Fiuza, C Gong R A Fonseca, L O Silva, W B Mori, and C Joshi. Collisionless shocks in laser-produced plasma generate monoenergetic high-energy proton beams. *Nature Physics*, 8:95–99, 2011. 116

T Hada, M Oonishi, B Lembège, and P Savoini. Shock front nonstationarity of supercritical perpendicular shocks. *J. Geophys. Res.*, 108:148–227, 2003. 100

A V Haeff. Space-Charge Wave Amplification Effects. *Phys. Rev.*, 74:1532–1533, 1948. 32

L Hartmann, G Herczeg, and N Calvet. Accretion onto Pre-Main-Sequence Stars. *A R A & A*, 54: 135–180, 2016. 10

N Hershkowitz. Double layers and electrostatic shocks. *J. Geophys. Res.*, 86:3307–3310, 1981. 74

D P Higginson, Ph Korneev, J Béard, S N Chen, E d'Humières, H Pépin, S Pikuz, B Pollock, R Riquier, V T Tikhonchuk, and J Fuchs. A novel platform to study magnetized high-velocity collisionless shocks. *High Energy Density Physics*, 17:190 – 197, 2015. 154

C W Hirt, A A Amsden, and J L Cook. An arbitrary Lagrangian-Eulerian computing method for all flow speeds. *J. Comput. Phys.*, 14:227 – 253, 1974. 24

M Honda, J Meyer ter Vehn, and A Pukhov. Collective Stopping and Ion Heating in Relativistic-Electron-Beam Transport for Fast Ignition. *Phys. Rev. Lett.*, 85:2128–2131, 2000. 39

T S Horbury, P J Cargill, E A Lucek, J Eastwood, A Balogh, M W Dunlop, K H Fornacon, and E Georgescu. Four spacecraft measurements of the quasiperpendicular terrestrial bow shock: Orientation and motion. *J. Geophys. Res.*, 107(A8), 2002. 98

M Hoshino and J Arons. Preferential positron heating and acceleration by synchrotron maser instabilities in relativistic positron–electron–proton plasmas. *Phys. Fluids B*, 3:818–833, 1991. 5

M Hoshino and N Shimada. Nonthermal Electrons at High Mach Number Shocks: Electron Shock Surfing Acceleration. *Astrophys. J.*, 572:880, 2002. 5, 85

S M Hosseini-Jenab and F Spanier. Kinetic-Simulation Study of Propagation of Langmuir-Like Ionic Waves in Dusty Plasma. *IEEE Trans. Plasma Sci.*, 45:193–199, 2017. 47

J D Huba. *NRL Plasma Formulary.* Naval Research Laboratory, 2009. 122

C M Huntington, F Fiuza, J S Ross, A Zylstra, R P Drake, D Froula, G Gregori, N L Kugland, C Kuranz, M Levy, C K Li, J Meinecke, T Morita, R Petrasso, C Plechaty, B A Remington, D D Ryutov, Y Sakawa, and A A Spitkovskynd H S Park. Observation of magnetic field generation via the Weibel instability in interpenetrating plasma flows. *Nat. Phys.*, 11:173–176, 2013. 11, 117, 118, 120, 121, 123, 154

C M Huntington, M J E Manuel, J S Ross, S C Wilks, F Fiuza, H G Rinderknecht, H S Park, G Gregori, D P Higginson, J Park, B B Pollock, B A Remington, D D Ryutov, C Ruyer, Y Sakawa, H Sio, A Spitkovsky, G F Swadling, H Takabe, and A B Zylstra. Magnetic field production via the Weibel instability in interpenetrating plasma flows. *Phys. Plasmas*, 24:041410, 2017. 11, 117, 139, 164

O Ishihara, A Hirose, and A B Langdon. Nonlinear evolution of Buneman instability. *Phys. Fluids*, 24:452–464, 1981. 34

C H Jaroschek, H Lesch, and R A Treumann. Ultrarelativistic Plasma Shell Collisions in Gamma-Ray Burst Sources: Dimensional Effects on the Final Steady State Magnetic Field. *Astrophys. J.*, 618:822, 2005. 39

F Jüttner. Das Maxwellsche Gesetz der Geschwindigkeitsverteilung in der Relativtheorie. *Annalen der Physik*, 339:856–882, 1911. 15

H Karimabadi, N Omidi, and K B Quest. Two-dimensional simulations of the ion/ion acoustic instability and electrostatic shocks. *Geophys. Res. Lett.*, 18:1913–1816, 1991. 53, 56

T N Kato and H Takabe. Collisionless shock experiments on the NIF. *Astrophys. J. Lett.*, 681:L93, 2008. 115, 117, 123, 139

T N Kato and H Takabe. Electrostatic and electromagnetic instabilities associated with electrostatic shocks: Two-dimensional particle-in-cell simulation. *Phys. Plasmas*, 17:032114, 2010. 53

Y Kazimura, J I Sakai, T Neubert, and S V Bulanov. Generation of a Small-Scale Quasi-Static Magnetic Field and Fast Particles during the Collision of Electron-Positron Plasma Clouds. *Astrophys. J.*, 498:L183, 1998. 39

K L Klein, S Krucker, G Trottet, and S Hoang. Coronal phenomena at the release of solar energetic electron events. *Astron. Astrophys.*, 431:1047–1060, 2005. 40

Yu L Klimontovich. *Statistical Theory of Non-Equilibrium Processes in a Plasma.* Pergamon Press Oxford, 1967. 13

M Koenig, A Benuzzi-Mounaix, A Ravasio, T Vinci, N Ozaki, S Lepape, D Batani, G Huser, T Hall, D Hicks, A MacKinnon, P Patel, H S Park, T Boehly, M Borghesi, S Kar, and L Romagnani. Progress in the study of warm dense matter. *Plasma Phys. Controll. Fusion*, 47:B441, 2005. 10

E P Kontar. Dynamics of electron beams in the inhomogeneous solar corona plasma. *Solar Phys.*, 202:131–149, 2001. 40

Ph Korneev, E d'Humières, and V T Tikhonchuk. Collisionless plasma interpenetration in a strong magnetic field for laboratory astrophysics experiments. *Phys. Plasmas*, 21:022117, 2014. 154, 165, 166, 167

D J Korteweg and G de Vries. On the change of form of long waves advancing in a rectangular canal, and on a new type of long stationary waves. *The London, Edinburgh, and Dublin Philosophical Magazine and Journal of Science*, 39:422–443, 1895. 2

Y Kuramitsu, Y Sakawa, T Morita, C D Gregory, J N Waugh, S Dono, H Aoki, H Tanji, M Koenig, N Woolsey, and H Takabe. Time Evolution of Collisionless Shock in Counterstreaming Laser-Produced Plasmas. *Phys. Rev. Lett.*, 106:175002, 2011. 53, 150

M Lampe and P Sprangle. Saturation of the relativistic two stream instability by electron trapping. *Phys. Fluids*, 18:475–481, 1975. 33

L D Landau. On the vibrations of the electronic plasma. *Jour. Phys. USSR*, 10:25, 1946. 38

J S Lazendic, P O Slane, B M Gaensler, S P Reynolds, P P Plucinsky, and J P Hughes. A High-Resolution Study of Nonthermal Radio and X-Ray Emission from Supernova Remnant G347.3–0.5. *Astrophys. J.*, 602:271, 2004. 4

M A Lee, V D Shapiro, and R Z Sagdeev. Pickup ion energization by shock surfing. *J. Geophys. Res.*, 101:4777, 1996. 107

R E Lee, S C Chapman, and R O Dendy. Ion acceleration processes at reforming collisionless shocks. *Phys. Plasmas*, 12:012901–012901–8, 2005. 85

B Lembege and P Savoini. Nonstationarity of a two dimensional quasiperpendicular supercritical collisionless shock by self reformation. *Phys. Fluids B*, 4:3533 – 3548, 1992. 85, 100

B Lembege and F Simonet. Hybrid and particle simulations of an interface expansion and of collisionless shock: A comparative and quantitative study. *Phys. Plasmas*, 8:3967–3981, 2001. 85

B Lembege, J Giacalone, M Scholer, T Hada, M Hoshino, V Krasnoselskikh, H Kucharek, P Savoini, and T Terasawa. Selected Problems in Collisionless-Shock Physics. *Space Sci. Rev.*, 110:161–226, 2004. 153

C K Li, F H Séguin, J A Frenje, J R Rygg, R D Petrasso, R P J Town, P A Amendt, S P Hatchett, O L Landen, A J MacKinnon, P K Patel, V A Smalyuk, T C Sangster, and J P Knauer. Measuring E and B Fields in Laser-Produced Plasmas with Monoenergetic Proton Radiography. *Phys. Rev. Lett.*, 97:135003, 2006. 127

C K Li, Q Moreno, A F A Bott, S Feister, H Sio, V T Tikhonchuk, E D'Humieres, P Tzeferacos, G Gregori, R D Petrasso, D Q Lamb, X Ribeyre, P Korneev, S Atzeni, R Betti, E M Campbell, R K Follett, J A Frenje, S X Hu, C M Huntington, M Koenig, H S Park, B A Remington, A Rigby, J S Ross, D D Ryutov, Y Sakawa, T C Sangster, F H Seguin, H Takabe, S C Wilks, and S Zhang. Weibel-mediated collisionless shocks driven by supersonic plasma flows. *Phys. Rev. Lett.*, 2019. 119, 120, 121, 127, 128, 130, 150

M Lobet, C Ruyer, A Debayle, E d'Humières, M Grech, M Lemoine, and L Gremillet. Ultrafast Synchrotron-Enhanced Thermalization of Laser-Driven Colliding Pair Plasmas. *Phys. Rev. Lett.*, 115:215003, 2015. 11

V V Lobzin, V V Krasnoselskikh, J M Bosqued, J-L Pincon, S J Schwartz, and M Dunlop. Nonstationarity and reformation of high-Mach-number quasiperpendicular shocks: Cluster observations. *Geophys. Res. Lett.*, 34:L05107, 2007. 100

R V Lovelace and R N Sudan. Plasma Heating by High-Current Relativistic Electron Beams. *Phys. Rev. Lett.*, 27:1256–1259, 1971. 39, 49

E A Lucek, D Constantinescu, M L Goldstein, J Pickett, J L Pincon, F Sahraoui, R A Treumann, and S N Walker. The magnetosheath. *Space Sci. Rev.*, 118:95–152, 2005. 6, 98

N Lugaz, C J Farrugia, C-L Huang, R M Winslow, H E Spence, and N A Schwadron. Earth's magnetosphere and outer radiation belt under sub-Alfvénic solar wind. *Nat. Commun.*, 7:13001, 2016. 74, 98

Y Lyubarsky and D Eichler. Are Gamma-Ray Burst Shocks Mediated by the Weibel Instability? *Astrophys. J.*, 647:1250, 2006. 137, 138, 144

Y E Lyubarsky. The termination shock in a striped pulsar wind. *Mon. Not. R. Astron. Soc.*, 345: 153–160, 2003. 5

A Macchi, M Borghesi, and M Passoni. Ion acceleration by superintense laser-plasma interaction. *Rev. Mod. Phys.*, 85:751–793, 2013. 8

E Mach and J Wentzel. Anzeiger kaiserl akad wiss wien. *Math-Naturw Classe*, 21:121–122, 1884. 1

P H Maire, R Abgrall, J Breil, and J Ovadia. A Cell-Centered Lagrangian Scheme for Two-Dimensional Compressible Flow Problems. *SIAM J. Sci. Comput.*, 29:1781–1824, 2007. 24

A Maksimchuk, S Gu, K Flippo, D Umstadter, and V Yu Bychenkov. Forward Ion Acceleration in Thin Films Driven by a High-Intensity Laser. *Phys. Rev. Lett.*, 84:4108–4111, 2000. 55

M A Malkov, R Z Sagdeev, G I Dudnikova, T V Liseykina, P H Diamond, K Papadopoulos, C S Liu, and J J Su. Ion-acoustic shocks with self-regulated ion reflection and acceleration. *Phys. Plasmas*, 23:043105, 2016. 63

A Marcowith and F Casse. Postshock turbulence and diffusive shock acceleration in young supernova remnants. *A&A*, 515:A90, 2010. 4

A Marcowith, A Bret, A Bykov, M E Dieckmann, L O'C Drury, B Lembège, M Lemoine, G Morlino, G Murphy, G Pelletier, I Plotnikov, B Reville, M Riquelme, L Sironi, and A S Novo. The microphysics of collisionless shock waves. *Rep. Prog. Phys.*, 79:046901, 2016. 85, 99

W Marshall. The structure of magneto-hydrodynamic shock waves. *Proceedings of the Royal Society of London A: Mathematical, Physical and Engineering Sciences*, 233:367–376, 1955. 70, 100

S F Martins, R A Fonseca, L O Silva, and W B Mori. Ion Dynamics and Acceleration in Relativistic Shocks. *Astrophys. J.*, 695:L189, 2009. 116

S Matsukiyo, Y Ohira, R Yamazaki, and T Umeda. Relativistic Electron Shock Drift Acceleration in Low Mach Number Galaxy Cluster Shocks. *Astrophys. J.*, 742:47, 2011. 5

K G McClements, R O Dendy, R Bingham, J G Kirk, and L O'C Drury. Acceleration of cosmic ray electrons by ion-excited waves at quasiperpendicular shocks. *Mon. Not. R. Astron. Soc.*, 291: 241–249, 1997. 74

M V Medvedev and A Loeb. Generation of Magnetic Fields in the Relativistic Shock of Gamma-Ray Burst Sources. *Astrophys. J.*, 526:697, 1999. 116, 137

P Mora. Thin-foil expansion into a vacuum. *Phys. Rev. E*, 72:056401, 2005. 74

P Mora and T Grismayer. Rarefaction Acceleration and Kinetic Effects in Thin-Foil Expansion into a Vacuum. *Phys. Rev. Lett.*, 102:145001, 2009. 55

Q Moreno, M E Dieckmann, D Folini, R Walder, X Ribeyre, and E D'Humieres. Parametric simulation study of the expansion of a dense plasma into an unmagnetized dilute plasma. *Plasma Phys. Control. Fusion*, 2018a. 12

Q Moreno, M E Dieckmann, C K Li, Ph Korneev, L Gremillet, S Jequier, X Ribeyre, V T Tikhonchuk, and E D'Humieres. Formation of electromagnetic collisionless shocks in the interpenetration of magnetized and unmagnetized plasma flows. *Phys. Rev. Lett.*, 2018b. 12

Q Moreno, M E Dieckmann, X Ribeyre, and E d'Humières. Quasi-perpendicular fast magnetosonic shock with wave precursor in collisionless plasma. *Phys. Plasmas*, 25:074502, 2018c. 12, 59, 85

Q Moreno, M E Dieckmann, X Ribeyre, S Jequier, V T Tikhonchuk, and E d'Humières. Impact of the electron to ion mass ratio on unstable systems in particle-in-cell simulations. *Phys. Plasmas*, 25:062125, 2018d. 11, 31, 100, 101, 112

Q Moreno, M E Dieckmann, X Ribeyre, V T Tikhonchuk, D Folini, R Walder, and E D'Humieres. Parametric simulation study of the expansion of a dense plasma into an unmagnetized dilute plasma. *New J. Phys.*, 2018e. 12

T Morita, Y Sakawa, K Tomita, T Ide, Y Kuramitsu, K Nishio, K Nakayama, K Inoue, T Moritaka, H Ide, M Kuwada, K Tsubouchi, K Uchino, and H Takabe. Thomson scattering measurement of a shock in laser-produced counter-streaming plasmas. *Phys. Plasmas*, 20:092115, 2013. 121

D L Morse, W W Destler, and P L Auer. Nonstationary Behavior of Collisionless Shocks. *Phys. Rev. Lett.*, 28:13–16, 1972. 98

L Muschietti. Electron beam formation and stability. *Solar Phys.*, 130:201–228, 1990. 40

R S Myong and P L Roe. Shock waves and rarefaction waves in magnetohydrodynamics. Part 2. The MHD system. *J. Plasma Phys.*, 58:521–552, 1997. 72, 101

C Niemann, C G Constantin, D B Schaeffer, A Tauschwitz, T Weiland, Z Lucky, W Gekelman, E T Everson, and D Winske. High-energy Nd:glass laser facility for collisionless laboratory astrophysics. *J. Instrum.*, 7:P03010, 2012. 115

C Niemann, W Gekelman, C G Constantin, E T Everson, D B Schaeffer, A S Bondarenko, S E Clark, D Winske, S Vincena, B V Compernolle, and P Pribyl. Observation of collisionless shocks in a large current free laboratory plasma. *Geophys. Res. Lett.*, 41:7413–7418, 2014. 150

K I Nishikawa, J Niemiec, P E Hardee, M Medvedev, H Sol, Y Mizuno, B Zhang, M Pohl, M Oka, and D H Hartmann. Weibel Instability and Associated Strong Fields in a Fully Three-Dimensional Simulation of a Relativistic Shock. *Astrophys. J.*, 698:L10, 2009. 39

K Noguchi, C Tronci, G Zuccaro, and G Lapenta. Formulation of the relativistic moment implicit particle-in-cell method. *Phys. Plasmas*, 14:042308, 2007. 25

Rachel Nuter, Mickael Grech, Pedro Gonzalez de Alaiza Martinez, Guy Bonnaud, and Emmanuel d'Humières. Maxwell solvers for the simulations of the laser-matter interaction. *Eur. Phys. J. D*, 68:177, 2014. 26

T M O'Neil, J H Winfrey, and J H Malmberg. Nonlinear Interaction of a Small Cold Beam and a Plasma. *Phys. Fluids*, 14:1204–1212, 1971. 45

H S Park, D D Ryutov, J S Ross, N L Kugland, S H Glenzer, C Plechaty, S M Pollaine, B A Remington, A Spitkovsky, L Gargate, G Gregori, A Bell, C Murphy, Y Sakawa, Y Kuramitsu, T Morita, H Takabe, D H Froula, G Fiksel, F Miniati, M Koenig, A Ravasio, A Pelka, E Liang, N Woolsey, C C Kuranz, R P Drake, and M J Grosskopf. Studying astrophysical collisionless shocks with counterstreaming plasmas from high power lasers. *High Energy Density Physics*, 8:38 – 45, 2012. 117, 123

H S Park, C M Huntington, F Fiuza, R P Drake, D H Froula, G Gregori, M Koenig, N L Kugland, C C Kuranz, D Q Lamb, M C Levy, C K Li, J Meinecke, T Morita, R D Petrasso, B B Pollock, B A Remington, H G Rinderknecht, M Rosenberg, J S Ross, D D Ryutov, Y Sakawa, A Spitkovsky, H Takabe, D P Turnbull, P Tzeferacos, S V Weber, and A B Zylstra. Collisionless shock experiments with lasers and observation of Weibel instabilities. *Phys. Plasmas*, 22:056311, 2015. 115

H S Park, J S Ross, C M Huntington, F Fiuza, D D Ryutov, D Casey, R P Drake, G Fiksel, D Froula, G Gregori, N L Kugland, C C Kuranz, M C Levy, C K Li, J Meinecke, T Morita, R D Petrasso, C Plechaty, B A Remington, Y Sakawa, A Spitkovsky, H Takabe, and A B Zylstra. Laboratory astrophysical collisionless shock experiments on Omega and NIF. *J. Phys. Conf. Ser.*, 688(1), 2016. 115

M Passoni, L Bertagna, and A Zani. Target normal sheath acceleration: theory, comparison with experiments and future perspectives. *New J. Phys.*, 12:045012, 2010. 8

R Pellat. Coalescence of magnetic islands. *Fizika Plasmy*, 9:204, 1983. 168

J R Pierce. Possible Fluctuations in Electron Streams Due to Ions. *Journal of Applied Physics*, 19: 231–236, 1948. 33

I M Podgorny. Collisionless shocks: Simulation and laboratory experiments. *Il Nuovo Cimento C*, 2:834–853, 1979. 115

O A Pokhotelov and O A Amariutei. Quasi-linear dynamics of Weibel instability. *Annales Geophysicae*, 29:1997–2001, 2011. 37

P L Pritchett. The coalescence instability in collisionless plasmas. *Plasma Physics*, 4:3371–3381, 1992. 167

I Pusztai, J M TenBarge, A N Csapó, J Juno, A Hakim, L Yi, and T Fülöp. Low Mach-number collisionless electrostatic shocks and associated ion acceleration. *Plasma Phys. Control. Fusion*, 60: 035004, 2018. 55, 60

K Quinn, L Romagnani, B Ramakrishna, G Sarri, M E Dieckmann, P A Wilson, J Fuchs, L Lancia, A Pipahl, T Toncian, O Willi andR J Clarke, M Notley, A Macchi, and M Borghesi. Weibel-Induced Filamentation during an Ultrafast Laser-Driven Plasma Expansion. *Phys. Rev. Lett.*, 108:135001, 2012. 85, 93

M A Raadu and J J Rasmussen. Dynamical aspects of electrostatic double layers. *Astrophys. Space Sci.*, 144:43–71, 1988. 53

A K Ram, A Bers, and C N Lashmore-Davies. Emission of electron Bernstein waves in plasmas. *Phys. Plasmas*, 9:409–418, 2002. 96

A S Hamish Reid and E P Kontar. Solar Wind Density Turbulence and Solar Flare Electron Transport from the Sun to the Earth. *Astrophys. J.*, 721:864, 2010. 40

H A S Reid and H Ratcliffe. A review of solar type III radio bursts. *Res. Astron. Astrophys.*, 14:773, 2014. 40

B A Remington, D Arnett, R P Drake, and H Takabe. Modelling astrophysical phenomena in the laboratory with intense lasers. *Science*, 284:1488–1493, 1999. 10, 85

G Revet, C N Sophia, R Bonito, B Khiar, E Filippov, C Argiroffi, D P Higginson, S Orlando, J Béard, M Blecher, M Borghesi, K Burdonov, D Khaghani, K Naughton, H Pépin, O Portugall, R Riquier, R Rodriguez, S N Ryazantsev, Y I Skobelev, A Soloviev, O Willi, S Pikuz, A Ciardi, and J Fuchs. Laboratory unraveling of matter accretion in young stars. *Sci Adv.*, 3, 2017. 10

X Ribeyre, E d'Humières, O Jansen, S Jequier, V T Tikhonchuk, and M Lobet. Pair creation in collision of $\gamma$-ray beams produced with high-intensity lasers. *Phys. Rev. E*, 93:013201, 2016. 10

X Ribeyre, E d'Humières, S Jequier, and V T Tikhonchuk. Effect of differential cross section in Breit–Wheeler pair production. *Plasma Phys. Controll. Fusion*, 60:104001, 2018. 10

A Rigby, F Cruz, B Albertazzi, R Bamford, A R Bell, J E Cross, F Fraschetti, P Graham, Y Hara, P M Kozlowski, Y Kuramitsu, D Q Lamb, S Lebedev, J R Marques, F Miniati, T Morita, M Oliver, B Reville, Y Sakawa, Kar SarS, C Spindloe, R Trines, P Tzeferacos, L O Silva, R Bingham, M Koenig, and G Gregori. Electron acceleration by wave turbulence in a magnetized plasma. *Nature. Physics*, 14:475–479, 2018. 151

B H Ripin and R L Stenzel. Electron Cyclotron Drift Instability Experiment. *Phys. Rev. Lett.*, 30: 45–48, 1973. 96

B H Ripin, J D Huba, E A McLean, C K Manka, T Peyser, H R Burris, and J Grun. Sub-Alfvénic plasma expansion. *Phys. Fluids B*, 5:3491–3506, 1993. 93

K V Roberts and H L Berk. Nonlinear Evolution of a Two-Stream Instability. *Phys. Rev. Lett.*, 19: 297–300, 1967. 45, 47

L Romagnani, S V Bulanov, M Borghesi, P Audebert, J C Gauthier, K Löwenbrück, A J MacKinnon, P Patel, G Pretzler, T Toncian, and O Willi. Observation of Collisionless Shocks in Laser-Plasma Experiments. *Phys. Rev. Lett.*, 101:025004, 2008. 53, 55, 115, 150

I N Ross, P Matousek, and J L Collier. Optical parametric chirped pulse amplification. page CWC1, 2000. 8

J S Ross, S H Glenzer, P Amendt, R Berger, L Divol, K L Kugland, O L Landen, C Plechaty, B Remington, D Ryutov, W Rozmus, D H Froula, G Fiksel, C Sorce, Y Kuramitsu, T Morita, Y Sakawa, H Takabe, R P Drake, M Grosskopf, C Kuranz, G Gregori, J Meinecke, C D Murphy, M Koenig, A Pelka, A Ravasio, T Vinci, E Liang, R Presura, A Spitkovsky, F Miniati, and H S Park. Characterizing counter-streaming interpenetrating plasmas relevant to astrophysical collisionless shocks. *Phys. Plasmas*, 19:056501, 2012. 121

J S Ross, D P Higginson, D Ryutov, F Fiuza, R Hatarik, C M Huntington, D H Kalantar, A Link, B B Pollock, B A Remington, H G Rinderknecht, G F Swadling, D P Turnbull, S Weber, S Wilks, D H Froula, M J Rosenberg, T Morita, Y Sakawa, H Takabe, R P Drake, C Kuranz, G Gregori, J Meinecke, M C Levy, M Koenig, A Spitkovsky, R D Petrasso, C K Li, H Sio, B Lahmann, A B Zylstra, and H-S Park. Transition from Collisional to Collisionless Regimes in Interpenetrating Plasma Flows on the National Ignition Facility. *Phys. Rev. Lett.*, 118:185003, 2017. 11, 118, 122

R Ruffini, G Vereshchagin, and S-S Xue. Electron–positron pairs in physics and astrophysics: From heavy nuclei to black holes. *Physics Reports*, 487(1):1 – 140, 2010. 10

H Ruhl. *Classical Particle Simulations with the PSC code.* Ruhr-Universität Bochum, 2005. 27

C Ruyer. *Kinetic instabilities in plasmas : from electromagnetic fluctuations to collisionless shocks*. PhD thesis, 2014. 6

C Ruyer, L Gremillet, G Bonnaud, and C Riconda. Analytical Predictions of Field and Plasma Dynamics during Nonlinear Weibel-Mediated Flow Collisions. *Phys. Rev. Lett.*, 117:065001, 2016. 144

D Ryutov, R P Drake, J Kane, E Liang, B A Remington, and W M Wood-Vasey. Similarity Criteria for the Laboratory Simulation of Supernova Hydrodynamics. *Astrophys. J.*, 518(2):821, 1999. 10

D D Ryutov, N L Kugland, H S Park, C Plechaty, B A Remington, and J S Ross. Basic scalings for collisionless-shock experiments in a plasma without pre-imposed magnetic field. *Plasma Phys. Control. Fusion*, 54:105021, 2012. 10

D D Ryutov, F Fiuza, C M Huntington, J S Ross, and H S Park. Collisional effects in the ion Weibel instability for two counter-propagating plasma streams. *Phys. Plasmas*, 21:032701, 2014. 122, 123, 145

Ch Sack and H Schamel. Plasma expansion into vacuum — A hydrodynamic approach. *Phys. Rep.*, 156:311 – 395, 1987. 85

R Z Sagdeev. Cooperative phenomena and shock waves in collisionless plasmas. *Rev. Plasma Phys.*, 4(23), 1966. 13, 53, 68, 69, 78, 79, 84, 105

R Z Sagdeev, D A Usikov, and G M Zaslavsky. *Nonlinear Physics —From the Pendulum to Turbulence and Chaos*. Harwood Academic Publishers, 1988. 135

J I Sakai, R Schlickeiser, and P K Shukla. Simulation studies of the magnetic field generation in cosmological plasmas. *Phys. Lett. A*, 330:384 – 389, 2004. 39

J J Santos, M Bailly-Grandvaux, L Giuffrida, P Forestier-Colleoni, S Fujioka, Z Zhang, Ph Korneev, R Bouillaud, S Dorard, D Batani, M Chevrot, J E Cross, R Crowston, J L Dubois, J Gazave, G Gregori, E d'Humières, S Hulin, K Ishihara, S Kojima, E Loyez, J R Marquès, A Morace, P Nicolaï, O Peyrusse, A Poyé, D Raffestin, J Ribolzi, M Roth, G Schaumann, F Serres, V T Tikhonchuk, P Vacar, and N Woolsey. Laser-driven platform for generation and characterization of strong quasi-static magnetic fields. *New J. Phys.*, 17:083051, 2015. 157

G Sarri, G C Murphy, M E Dieckmann, A Bret, K Quinn, I Kourakis, M Borghesi, L O C Drury, and A Ynnerman. Two-dimensional particle-in-cell simulation of the expansion of a plasma into a rarefied medium. *New J. Phys.*, 13:073023, 2011. 53

G Sarri, K Poder, J M Cole, W Schumaker, A Di Piazza, B Reville, T Dzelzainis, D Doria, L A Gizzi, G Grittani, S Kar, C H Keitel, K Krushelnick, S Kuschel, S P D Mangles, Z Najmudin, N Shukla, L O Silva, D Symes, A G R Thomas, M Vargas, J Vieira, and M Zepf. Generation of neutral and high-density electron–positron pair plasmas in the laboratory. *Nat. Commun.*, 6:6747, 2015. 11

D B Schaeffer, E T Everson, A S Bondarenko, S E Clark, C G Constantin, D Winske, W Gekelman, and C Niemann. Experimental study of subcritical laboratory magnetized collisionless shocks using a laser-driven magnetic piston. *Phys. Plasmas*, 22:113101, 2015. 98, 154

D B Schaeffer, W Fox, D Haberberger, G Fiksel, A Bhattacharjee, D H Barnak, S X Hu, and K Germaschewski. Generation and Evolution of High-Mach Number, Laser-Driven Magnetized Collisionless Shocks in the Laboratory. *Phys. Rev. Lett.*, 119:025001, 2017a. 10, 11, 85, 98, 115, 150, 154

D B Schaeffer, W Fox, D Haberberger, G Fiksel, A Bhattacharjee, D H Barnak, S X Hu, K Germaschewski, and R K Follett. High-Mach number, laser-driven magnetized collisionless shocks. *Phys. Plasmas*, 24:122702, 2017b. 10, 11, 115, 154

H Schamel. Electron holes, ion holes and double layers: electrostatic phase space structures in theory and experiment. *Phys. Rep.*, 140:161–191, 1986. 62

H Schmitz, S C Chapman, and R O Dendy. Electron preacceleration mechanisms in the foot region of High Alfvenic Mach number shocks. *Astrophys. J.*, 579:327–336, 2002. 98, 100

M Scholer and D Burgess. The role of upstream waves in supercritical quasiparallel shock reformation. *J. Geophys. Res.*, 97:8319 – 8326, 1992. 85

M Scholer, I Shinohara, and S Matsukiyo. Quasiperpendicular shocks: Length scale of the cross-shock potential, shock reformation, and implication for shock surfing. *J. Geophys. Res.*, 108: 1014, 2003. 85, 98, 100

G P Schurtz, Ph D Nicolaï, and M Busquet. A nonlocal electron conduction model for multidimensional radiation hydrodynamics codes. *Phys. Plasmas*, 7:4238–4249, 2000. 24

Y Sentoku and A J Kemp. Numerical methods for particle simulations at extreme densities and temperatures: Weighted particles, relativistic collisions and reduced currents. *J. Comput. Phys.*, 227:6846 – 6861, 2008. 25, 131

J Sheffield, D Froula, S H Glenzer, and N C Luhmann. *Plasma Scattering of Electromagnetic Radiation: Theory and Measurement Techniques*. Academic Press Inc., 2010. 121

N Shimada and M Hoshino. Strong Electron Acceleration at High Mach Number Shock Waves: Simulation Study of Electron Dynamics. *Astrophys. J.*, 543:L67, 2000. 85, 98, 100

L O Silva, R A Fonseca, J W Tonge, J M Dawson, W B Mori, and M V Medvedev. Interpenetrating Plasma Shells: Near-Equipartition Magnetic Field Generation and Nonthermal Particle Acceleration. *Astrophys. J. Lett.*, 596:L121, 2003. 39

L Sironi and D Giannios. Relativistic Pair Beams from TeV Blazars: A Source of Reprocessed GeV Emission rather than Intergalactic Heating. *Astrophys. J.*, 787:49, 2014. 40

L Sironi and A Spitkovsky. Particle Acceleration in Relativistic Magnetized Collisionless Electron-Ion Shocks. *Astrophys. J.*, 726:75, 2011a. 5, 116, 148

L Sironi and A Spitkovsky. Acceleration of Particles at the Termination Shock of a Relativistic Striped Wind. *Astrophys. J.*, 741:39, 2011b. 5, 148

G Sorasio, M Marti, R Fonseca, and L O Silva. Very High Mach-Number Electrostatic Shocks in Collisionless Plasmas. *Phys. Rev. Lett.*, 96:045005, 2006. 144

A Spitkovsky. On the Structure of Relativistic Collisionless Shocks in Electron-Ion Plasmas. *Astrophys. J. Lett.*, 673:L39, 2008a. 116, 144

A Spitkovsky. Particle Acceleration in Relativistic Collisionless Shocks: Fermi Process at Last? *Astrophys. J. Lett.*, 682:L5, 2008b. 5, 148

K. Stasiewicz, M. Longmore, S. Buchert, P. K. Shukla, B. Lavraud, and J. Pickett. Properties of fast magnetosonic shocklets at the bow shock. *Geophys. Res. Lett.*, 30(24):2241, 2003. 71

A Stockem, E Boella, F Fiuza, and L O Silva. Relativistic generalization of formation and ion-reflection conditions in electrostatic shocks. *Phys. Rev. E*, 87:043116, 2013. 116

A Stockem, T Grismayer, R A Fonseca, and L O Silva. Exploring the nature of collisionless shocks under laboratory conditions. *Sci. Rep.*, 4(3934), 2014. 53, 116

A Stockem, A A Bret, R A Fonseca, and L O Silva. Physics of collisionless shocks: theory and simulation. *Plasma Phys. Control. Fusion*, 58(014005), 2016. 116

RG Stone and BT Tsurutani. Collisionless shocks in the heliosphere: a tutorial review. *Geophysical Monograph Series*, 34:120, 1985. 99

D Strickland and G Mourou. Compression of amplified chirped optical pulses. *Opt. Commun.*, 55 (6):447 – 449, 1985. 7

M Tabak, J Hammer, M E Glinsky, W L Kruer, S C Wilks, J Woodworth, E M CampA Bellnd M D Perry, and R J Mason. Ignition and high gain with ultrapowerful lasers. *Phys. Plasmas*, 1:1626–1634, 1994. 40

A Taflove, S C Hagness, and M Piket-May. 9 - computational electromagnetics: The finite-difference time-domain method. In *The Electrical Engineering Handbook*, pages 629 – 670. Academic Press, 2005. 25

K G Tanaka, T Yumura, M Fujimoto, I Shinohara, S V Badman, and A Grocott. Merging of magnetic islands as an efficient accelerator of electrons. *Phys. Plasmas*, 17:102902, 2010. 169

D J Tetreault. Growing ion holes as the cause of auroral double layers. *Geophys. Res. Lett.*, 15: 164–167, 1988. 62

C Thaury, P Mora, A Héron, J C Adam, and T M Antonsen. Influence of the Weibel instability on the expansion of a plasma slab into a vacuum. *Phys. Rev. E*, 82:026408, 2010. 85

L E Thode and R N Sudan. Two-Stream Instability Heating of Plasmas by Relativistic Electron Beams. *Phys. Rev. Lett.*, 30:732–735, 1973. 40

L E Thode and R N Sudan. Plasma heating by relativistic electron beams. II. Return current interaction. *Phys. Fluids*, 18:1564–1573, 1975. 39, 50

R A Treumann. Fundamentals of collisionless shocks for astrophysical application, 1. Non-relativistic shocks. *Astron. Astrophys. Rev.*, 17:409–535, 2009. 20, 99, 105, 107, 117

B A Trubnikov. Particle interactions in a fully ionized plasma. *Reviews of Plasma Physics*, 1:105, 1965. 122

P Tzeferacos, M Fatenejad, N Flocke, C Graziani, G Gregori, D Q Lamb, D Lee, J Meinecke, A Scopatz, and K Weide. FLASH MHD simulations of experiments that study shock-generated magnetic fields. *High Energy Density Physics*, 17:24–31, 2015. 119

M Tzoufras, C Ren, F S Tsung, J W Tonge, W B Mori, M Fiore, R A Fonseca, and L O Silva. Space-Charge Effects in the Current-Filamentation or Weibel Instability. *Phys. Rev. Lett.*, 96:105002, 2006. 40

A J van Marle, F Casse, and A Marcowith. On magnetic field amplification and particle acceleration near non-relativistic astrophysical shocks: particles in MHD cells simulations. *Mon. Not. Roy. Astron. Soc.*, 473:3394–3409, 2018. 174

A L Verdon, I H Cairns, D B Melrose, and P A Robinson. Properties of lower hybrid waves. *Proceedings of the International Astronomical Union*, 4:569–573, 2008. 73, 78, 79

A L Verdon, I H Cairns, D B Melrose, and P A Robinson. Warm electromagnetic lower hybrid wave dispersion relation. *Phys. Plasmas*, 16:052105, 2009. 73

D Daniel Verscharen, C H K Chen, and R T Wicks. On Kinetic Slow Modes, Fluid Slow Modes, and Pressure-balanced Structures in the Solar Wind. *Astrophys. J.*, 840:106, 2017. 78

J Villasenor and O Buneman. Rigorous charge conservation for local electromagnetic field solvers. *Comput. Phys. Commun.*, 69:306 – 316, 1992. 27

A A Vlasov. On the kinetic theory of an assembly of particles with collective interaction. *Russ. Phys. J.*, 9:25–40, 1945. 13

S N Walker, M A Balikhin, and M N Nozdrachev. Ramp nonstationarity and the generation of whistler waves upstream of a strong quasiperpendicular shock. *Geophys. Res. Lett.*, 26:1357–1360, 1999. 98, 99

J S Warren, J P Hughes, C Badenes, P Ghavamian, C F McKee, D Moffett, P P Plucinsky, C Rakowski, E Reynoso, and P Slane. Cosmic-Ray Acceleration at the Forward Shock in Tycho's Supernova Remnant: Evidence from Chandra X-Ray Observations. *Astrophys. J.*, 634:376, 2005. 4

J Warwick, T Dzelzainis, M E Dieckmann, W Schumaker D, Doria, L Romagnani, K Poder, J M Cole, A Alejo, M Yeung, K Krushelnick, S P D Mangles, Z Najmudin, B Reville, G M Samarin, D D Symes, A G R Thomas, M Borghesi, and G Sarri. Experimental Observation of a Current-Driven Instability in a Neutral Electron-Positron Beam. *Phys. Rev. Lett.*, 119:185002, 2017. 40

E S Weibel. Spontaneously Growing Transverse Waves in a Plasma Due to an Anisotropic Velocity Distribution. *Phys. Rev. Lett.*, 2:83–84, 1959. 5, 11, 35, 85

S C Wilks, A B Langdon, T E Cowan, M Roth, M Singh, S Hatchett, M H Key, D Pennington, A MacKinnon, and R A Snavely. Energetic proton generation in ultra-intense laser–solid interactions. *Phys. Plasmas*, 8:542–549, 2001. 8, 55

D Winske. Short wavelength modes on expanding plasma clouds. *J. Geophys. Res.*, 93:2539–2552. 93

D Winske and N Omidi. A nonspecialist's guide to kinetic simulations of space plasmas. *J. Geophys. Res.*, 101:17287–17303, 1996. 98

R Wood. *Laser-Induced Damage of Optical Materials*. Boca Raton: CRC Press, 2003. 7, 8

L C Woods. On the structure of collisionless magneto—plasma shock waves at super—critical Alfvén—Mach numbers. *J. Plasma Phys.*, 3:435–447, 1969. 98

N C Woolsey, Y A Ali, R G Evans, R A D Grundy, S J Pestehe, P G Carolan, N J Conway, R O Dendy, P Helander, K G McClements, J G Kirk, P A Norreys, N M Notley, and S J Rose. Collisionless shock and supernova remnant simulations on Vulcan. *Phys. Plasmas*, 8:2439–2445, 2001. 56

H Yamaguchi, A E Kristoffer, C Badenes, J P Hughes, N S Brickhouse, A R Foster, D J Patnaude, R Petre, P O Slane, and R K Smith. New Evidence for Efficient Collisionless Heating of Electrons at the Reverse Shock of a Young Supernova Remnant. *Astrophys. J.*, 780:136, 2014. 4

K Yee. Numerical solution of inital boundary value problems involving Maxwell's equations in isotropic media. *IEEE Trans. Antennas Propag.*, 14:302–307, 1966. 25

X Yuan, I H Cairns, L Trichtchenko, R Rankin, and D W Danskin. Confirmation of quasi-perpendicular shock reformation in two-dimensional hybrid simulations. *Geophys. Res. Lett.*, 36(5):L05103, 2009. 100

Y P Zakharov. Collisionless laboratory astrophysics with lasers. *IEEE Trans. Plasma Sci.*, 31:1243–1251, 2003. 85

P Zarka, D Le Quéau, and F Genova. The maser synchrotron instability in an inhomogeneous medium: Determination of the spectral intensity of auroral kilometric radiation. *J. Geophys. Res.*, 91:13542–13558, 1986. 5

L M Zeleny and A L Taktakishvili. A kinetic theory of the magnetic islands merging instability. *Plasma Phys. Control. Fusion*, 30:663, 1988. 168